AD-A057 411 AIR FORCE GEOPHYSICS LAB HANSCOM AFB MASS F/G 4/1
COMPILATION OF PAPERS PRESENTED BY THE SPACE PHYSICS DIVISION A--ETC(U)
APR 78

UNCLASSIFIED AFGL-TR-78-0080 NL

1 OF 2
AD A057411



AD A057411

LEVEL II

AFGL-TR-78-0080
SPECIAL REPORTS, NO. 212

Compilation of Papers Presented by the Space Physics Division at the Ionospheric Effects Symposium (IES 1978)

SPACE PHYSICS DIVISION

AD No.
DDC FILE COPY

5 APRIL 1978

Approved for public release; distribution unlimited.

DDC
RECEIVED
AUG 11 1978
D

SPACE PHYSICS DIVISION PROJECT 4643
AIR FORCE GEOPHYSICS LABORATORY
HANSCOM AFB, MASSACHUSETTS 01731

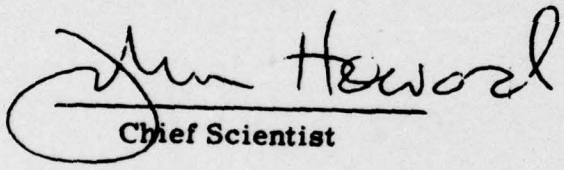
AIR FORCE SYSTEMS COMMAND, USAF

78 08 10 017

This report has been reviewed by the ESD Information Office (OI) and is releasable to the National Technical Information Service (NTIS).

This technical report has been reviewed and is approved for publication.

FOR THE COMMANDER



Chief Scientist

Qualified requestors may obtain additional copies from the Defense Documentation Center. All others should apply to the National Technical Information Service.

LEVEL II

(1)

Unclassified

SECURITY CLASSIFICATION OF THIS PAGE (When Data Entered)

REPORT DOCUMENTATION PAGE	READ INSTRUCTIONS BEFORE COMPLETING FORM
(14) 1. REPORT NUMBER AFGL-TR-78-0080 / AFGL-SR-212	2. GOVT ACCESSION NO. / 3. RECIPIENT'S CATALOG NUMBER
(6) 4. TITLE (and Subtitle) Compilation of Papers presented by the Space Physics Division at the Ionospheric Effects Symposium (IES 1978) held 24-26 January, Arlington, Virginia	5. TYPE OF REPORT & PERIOD COVERED Scientific. Interim. (9) 6. PERFORMING ORG. REPORT NUMBER Special Reports, No. 212
7. AUTHOR(s) Space Physics Division	8. CONTRACT OR GRANT NUMBER(s)
9. PERFORMING ORGANIZATION NAME AND ADDRESS Air Force Geophysics Laboratory(PH) Hanscom AFB Massachusetts 01731	10. PROGRAM ELEMENT, PROJECT, TASK AREA & WORK UNIT NUMBERS (16) 62101F 46430503 (17) 05
11. CONTROLLING OFFICE NAME AND ADDRESS Air Force Geophysics Laboratory(PH) Hanscom AFB Massachusetts 01731	(11) 12. REPORT DATE 5 April 1978 13. NUMBER OF PAGES 161
14. MONITORING AGENCY NAME & ADDRESS(if different from Controlling Office) (12) 153p.	15. SECURITY CLASS. (of this report) Unclassified 15a. DECLASSIFICATION/DOWNGRADING SCHEDULE

16. DISTRIBUTION STATEMENT (of this Report)

Approved for public release; distribution unlimited.

17. DISTRIBUTION STATEMENT (of the abstract entered in Block 20, if different from Report)

18. SUPPLEMENTARY NOTES

19. KEY WORDS (Continue on reverse side if necessary and identify by block number)

Equatorial F-region irregularities
Ionospheric scintillations
Ionospheric time delay
Ionospheric trough
Radar range correction

20. ABSTRACT (Continue on reverse side if necessary and identify by block number)

This is a compilation of seventeen (17) papers presented by the Space Physics Division at the 1978 Symposium on the Effect of the Ionosphere on Space and Terrestrial Systems. The symposium was jointly sponsored by the Naval Research Laboratory and the Office of Naval Research, January 24-26, 1978. The emphasis is on the occurrence of ionospheric irregularities and their effect on communication, radar and navigation systems.

DD FORM 1 JAN 73 1473 EDITION OF 1 NOV 65 IS OBSOLETE

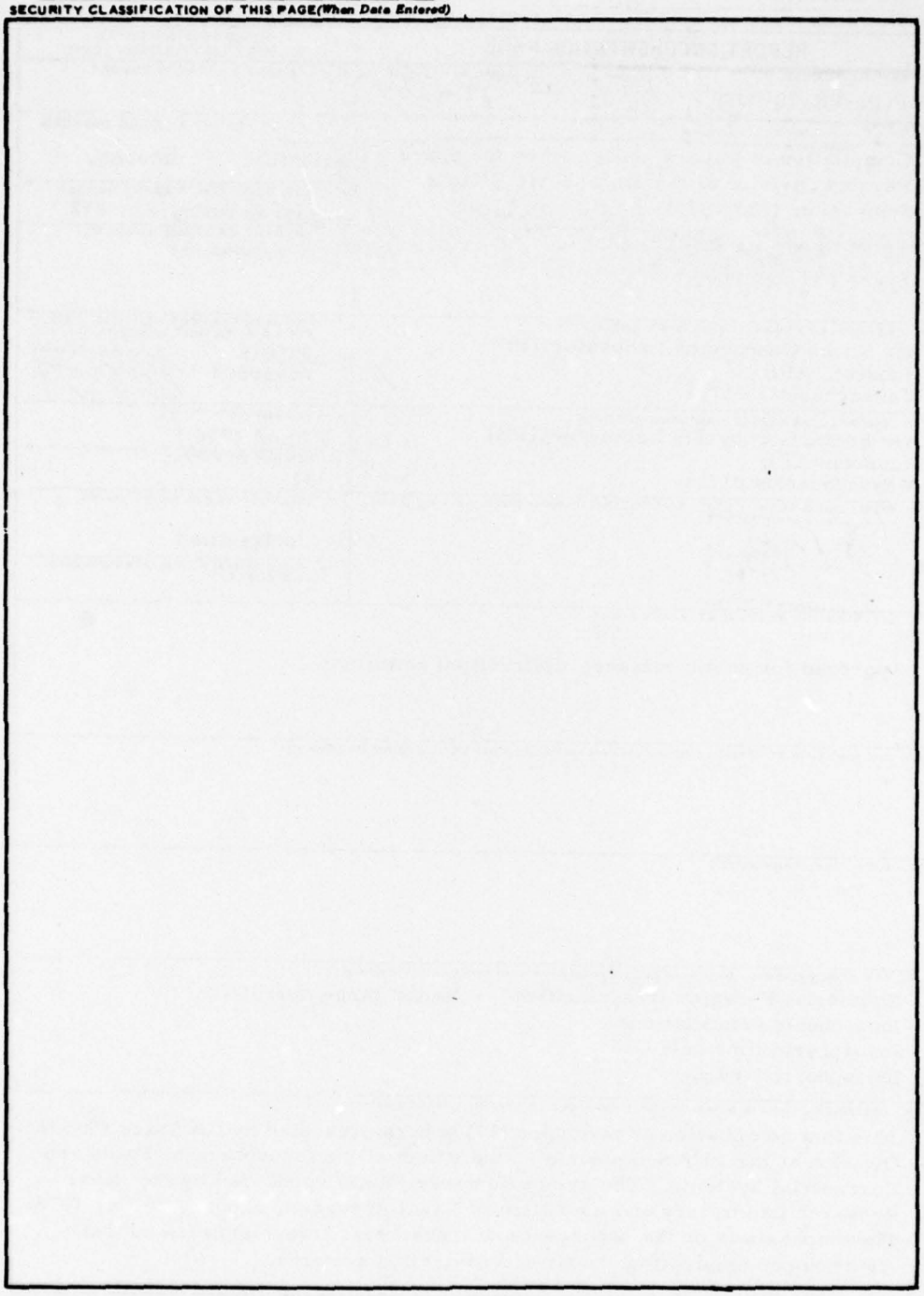
Unclassified

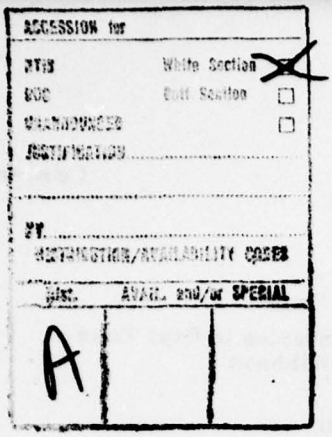
SECURITY CLASSIFICATION OF THIS PAGE (When Data Entered)

DDC
RECEIVED
AUG 11 1978
D

409578

78 08 10 017





Contents

IES Papers for In-House Report:

INTRODUCTION
A.S. Jursa, Director Space Physics Division 5

Equatorial Ionospheric Scintillations in the Indian Zone
R.G. Rastogi, M.R. Deshpande and Hari Om Vats 7

Amplitude Scintillation Studies in the Polar Region on 250 MHz
J. Buchau, J. Aarons, J. Mullen, E. Weber, J.A. Whalen, H.E. Whitney and E.E. Crampton 11

Gigahertz Scintillation at the Magnetic Equator
J. Mullen, A. Bushby, J. Lanat and J. Pantaja 19

Spaced Receiver Measurements of Intense Equatorial Scintillations
H.E. Whitney 25

A Review of Recent Studies of Equatorial F-Region Irregularities and their Impact on Scintillation Modeling
Sunanda Basu and M.C. Kelley 37

Large and Small Scale Properties of Nighttime Equatorial Irregularities from Scintillations and Radar Backscatter Measurements
S. Basu, H. Whitney, J. Aarons and J. McClure 55

Radio and Optical Diagnostics Applied to an Isolated Equatorial Scintillation Event
J. Buchau, E. Weber and J. McClure 65

Topside Ionospheric Trough Morphology at Mid and High Latitudes
M. Ahmed and R.C. Sagalyn 75

ATS-6 Observations of Ionospheric/Protonospheric Electron Content and Flux
L. Kersley, H. Hajeb-Hossenieh and K. Edwards 85

Contents

Remote Ionospheric Monitoring
J. Buchau and W. Hall, B. Reinisch and S. Smith 95

Attempts to Predict Trough/Plasmapause Boundaries in Real Time
M. Mendillo, C. Chacko, F. Lynch and P. Wildman 105

The Variability of Ionospheric Time Delay
J. Johanson, M. Buonsanto and J. Klobuchar 117

The Contribution of the Plasmasphere to Total Time Delay
J. Klobuchar, M. Buonsanto, M. Mendillo and J. Johanson 125

Temporal Variability of Ionospheric Refraction Correction
D. Donatelli and R.S. Allen 129

Adaptive Correction of the Effect of the Ionosphere on Range Determination by Terrestrial Radars
A. Katz, M. Grossi, R. Allen and D. Donatelli 137

Adaptive Mapping of Ionospheric Features
R. Leitinger, R. Allen, D. Donatelli and G. Hartmann 147

Effects of Ionospheric Scintillations on Satellite Communication
Banshidhar, N.M. Vadher, Hari Om Vats, M.R. Deshpande and R. Rastogi 155

Introduction

A.S. Jursa, Director Space Physics Division

The 1978 Symposium on the Effect of the Ionosphere on Space and Terrestrial Systems was held at Arlington, Virginia from 24 to 26 January 1978, under the auspices of the Naval Research Laboratory and the Office of Naval Research.

The conference was divided into six sections, with a large number of presentations in a tight time frame. The Space Physics Division of Air Force Geophysics Laboratory has a primary interest in each subject area, since many different Air Force systems are affected by the ionospheric structure and its dynamical behavior. Various disturbances within the ionosphere cause amplitude and phase variations which limit the performance of radar, navigation and communication systems. Long term statistical studies from ground based stations or in-situ probes are usually necessary to understand the ionospheric effects and describe them in terms that can be used to develop error-correction or forecasting schemes. The following papers which were presented at the IES-78 represent the results of ongoing studies within the Space Physics Division which are directed toward increasing our knowledge of ionospheric behavior and provide techniques for mitigation of the effects on system performance.

(Received for publication 5 April 1978)

EQUATORIAL IONOSPHERIC SCINTILLATIONS IN THE INDIAN ZONE

R.G. RASTOGI* M.R. DESHPANDE and HARI OM VATS
Physical Research Laboratory
Ahmedabad 380009
India.

TEXT

The phenomenon of scintillation is now well known as being the occasional changes in the amplitude, phase and angle of arrival of radio waves propagating through the ionosphere. These changes are known to be due to ionization irregularities present in the ionosphere. Earlier studies showed that these changes are more severe in equatorial and two auroral zones. The equatorial scintillation is basically a nighttime phenomenon with its maximum before midnight for any longitude and is largely due to spread F irregularities (Koster 1972, Mullen 1973, Chandra and Rastogi 1974). At high latitudes some scintillations are observed during daytime hours (Munro 1966, Frihagen 1971, Nielson and Aarons 1974). Recently Deshpande et al. (1977) reported that during a magnetic storm scintillations are found to be caused by the F region irregularities in the early hours of the day i.e., at post sunrise. McClure (1964) estimated the height of the irregularities responsible for the daytime scintillations to be embedded in the E region. Association of scintillations and Es patches has been noted at middle and low latitudes (Aarons and Whitney 1968, Rastogi and Iyer 1976).

Fig.1 shows some of the examples of the amplitude records of radio beacons (40, 140 and 360 MHz) from ATS-6 recorded at Ootacamund and simultaneous ionograms from a nearby equatorial station Kodaikanal. Note that whenever there is Es-q present in the ionograms the amplitudes do not show appreciable variation, whereas during Es-h type reflections severe scintillations have been observed. Chandra et al. (1977) have shown that daytime scintillations are caused by each of the irregularities responsible for Es-b, Es-h, Es-l, M-reflections and G-layer and never by Es-q irregularities. Similarly nighttime scintillations are caused either by spread F irregularities or by Es irregularities (Rastogi et al. 1977, Chandra et al. 1977).

Fig.2 shows the diurnal occurrence of ionospheric scintillations at 40, 140 and 360 MHz during two periods, i.e. Oct-Nov 1975 and May 1976. It can be noticed that during Oct-Nov 1975 there is a major peak occurrence of scintillations at night between 2000 hr and 2300 hr and two minor peaks during daytime around 0900 hr and 1400 hr. On the contrary May 1976 occurrence has a broader maximum during daytime than at night. Although at 40 MHz there seems to be appreciable scintillations at all times with a slight decrease in percentage around sunset and sunrise. The difference of daytime and nighttime occurrence of scintillations is quite clear at 140 and 360 MHz. This broader maximum during daytime in a summer month (May) is probably because of frequent occurrence of non q type of Es irregularities. A detailed study of this in comparison with ionosonde data seems to be necessary.

Acknowledgements

Authors are thankful to Dr.Kenneth Davies and his group for collaboration and to Professor G.Swarup for facilities for ATS-6 RBE project at Ootacamund. This project was partially supported by DOS and NASA.

References

Aarons J. and Whitney H.E., Planet. Space Sci., 16, 21 (1968).

* At present: NRC/NAS Senior Resident Research Associate,
Air Force Geophysics Laboratory, Hanscom AFB, MA 01731
U.S.A.

Chandra H. and Rastogi R.G., Curr. Sci. 43, 567 (1974).
Chandra H. et al., Ann. Geophys.(1977) (in press).
Deshpande M.R. et al., Nature, 268, 6 614 (1977).
Frihagen J., J. Atmos. Terr. Phys., 33, 21 (1971).
Koster J.R., Planet. Space Sci., 20, 1999 (1972).
McClure J.P., J. Geophys. Res., 69, 2774 (1964).
Mullen J.P., J. Atmos. Terr. Phys., 35, 1187 (1973).
Munro H., Rad. Sci., 1, 1186 (1966).
Nielson E. and Aarons J., J. Atmos. Terr. Phys., 36, 159 (1974).
Rastogi R.G. and Iyer K.N., Curr. Sci., 45, 685 (1976).
Rastogi R.G. et al., Pramana, 8, 1 (1977).

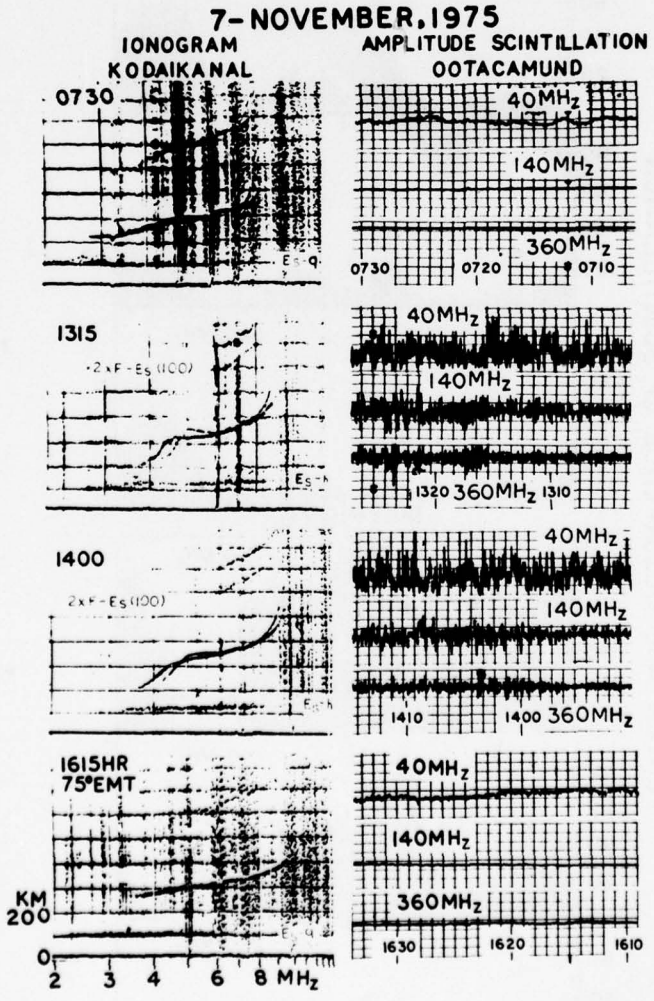

7-NOVEMBER,1975
IONOGRAM
KODAIKANAL
AMPLITUDE SCINTILLATION
OOTACAMUND
0730
40MHz
140MHz
360MHz
0730
0720
0710
1315
2xF-Es(100)
40MHz
140MHz
1320
360MHz
1310
1400
2xF-Es(100)
40MHz
140MHz
1410
1400
360MHz
1615HR
75°EMT
40MHz
140MHz
360MHz
KM
200
0
2
3
4
6
8 MHz
1630
1620
1610

Figure 1

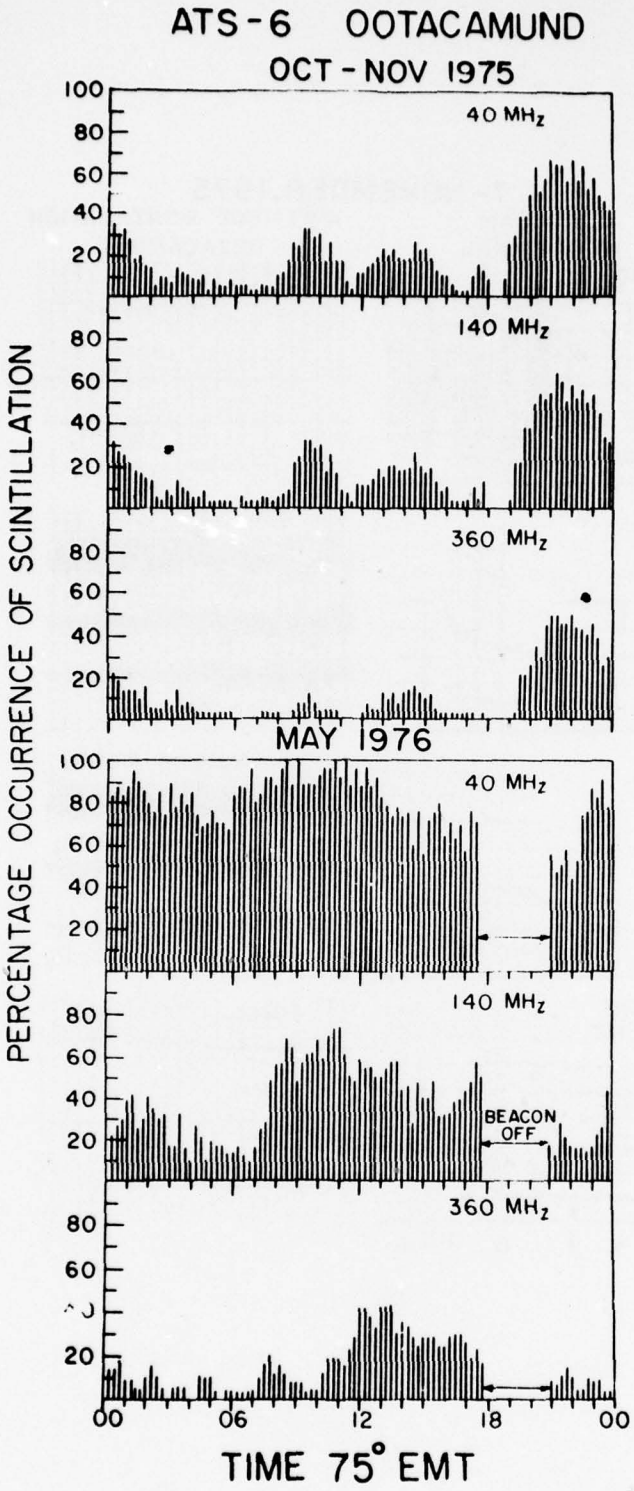

ATS-6 OOTACAMUND
OCT - NOV 1975
40 MHz
140 MHz
360 MHz
MAY 1976
40 MHz
140 MHz
BEACON OFF
360 MHz
PERCENTAGE OCCURRENCE OF SCINTILLATION
100
80
60
40
20
00
06
12
18
00
TIME 75° EMT

Figure 2

AMPLITUDE SCINTILLATION STUDIES IN THE POLAR REGION ON 250 MHz

By

J. Buchau, J. Aarons, J.P. Mullen, E.J. Weber
J.A. Whalen and H.E. Whitney
Air Force Geophysics Laboratory
Hanscom AFB, MA 01731

And

E.E. Crampton, Jr.
MITRE Corporation
Bedford, MA 01731

ABSTRACT

In April, July and September 1975 twelve C-141 flights (28 hours of data) were conducted to measure amplitude scintillations on VHF satellite transmissions in the polar region, under auroral conditions. A second aircraft, a KC-135, instrumented for ionospheric/auroral research, monitored the conditions of the auroral ionosphere in the ray path to relate scintillation events to auroral conditions in the April and September tests. Simultaneous ground measurements were made at Thule, Greenland; Goose Bay, Labrador, Canada; and Sagamore Hill, Massachusetts. For the first time in the polar region satellite 250 MHz transmissions could be monitored for an extended period (up to 4 hours) at high elevation angles.

The observed aircraft scintillations were separated into groups, describing the ionospheric situation along the ray path (trough, oval, or polar cap). The spatial distribution of the occurrence probability of scintillations indicates, that scintillations are more likely to occur in the northern half of the auroral oval (29% of the time) and in the polar cap (21%) than in the region of continuous (diffuse) aurora (17%). Scintillations were almost completely absent in the F-layer trough (4%). Even though aurora was present throughout most of the flights (with Kp ranging from 0+ to 4o) only weak to moderate scintillations were observed (mostly <9 dB).

Over 200 hours (34 during flights) of observations were made at each of three ground stations: Thule (polar cap), Goose Bay (auroral oval), and Sagamore Hill (mid-latitude ionosphere). For any distinct time period of simultaneous observations, there was considerable scatter of which station recorded maximum activity. During magnetically quiet periods (Kp = 0-3) the ground data show good latitudinal ordering. The highest probability of occurrence of scintillations and the strongest scintillations are found in the polar cap. During periods of moderate magnetic activity (Kp = 4-6) the probability of scintillations strongly increases at Goose, at times above the Thule level, which is not significantly changed by the increase in magnetic activity. In general, Sagamore Hill for moderate magnetic activity showed lower scintillation levels than either Thule or Goose Bay.

INTRODUCTION

In April, July and September 1975, a comprehensive program (Figure 1) was conducted to assess ionospheric and auroral conditions during AFSATCOM scintillation test flights and to determine the effects of the aurora on satellite communications. In this program coordinated flights were made by an Air Force 4950th Test Wing C-141, carrying an AFSATCOM communications terminal and by the AFGL Airborne Ionospheric Observatory, an NKC-135 instrumented for ionospheric and auroral research and VHF field-strength measurements. The Sagamore Hill Observatory at Hamilton, Massachusetts, the Goose Bay Ionospheric Observatory at Goose Bay, Labrador and the Geopole Observatory at Thule, Greenland, all operated by AFGL and equipped for routine satellite observations, enhanced their observation programs during the test period.

The AFSATCOM satellite, in a polar orbit and transmitting at 250 MHz, provided the signal source for the scintillation studies. These experiments resulted in a body of data that allowed the determination of the effects that auroral ionization and the high latitude ionosphere have on trans-ionospheric VHF signal propagation at relatively high elevation angles.

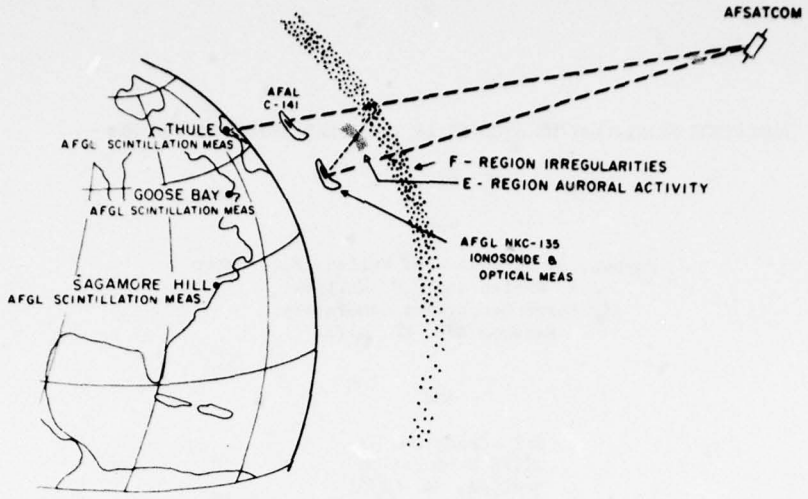


Figure 1. 250 MHz Scintillation Studies during April, July and September 1975 Involved Two USAF Research/Test Aircraft and Three AF Geophysics Laboratory Ground Stations.

The goal of these experiments was to determine the relation between ionospheric and auroral conditions and VHF scintillations, and to compare the results of the airborne experiments with results from the considerably more extensive ground observations.

AIRBORNE EXPERIMENTS

The purpose of the AFGL aircraft flights was to monitor the ionospheric environment in the region where the VHF signal path from satellite to receiver (C-141 aircraft) traversed the ionosphere. To enhance the scintillation data base, a satellite receive capability was installed in the AFGL aircraft for the September 1975 missions.

The high latitude ionospheric/auroral environment can be separated into 3 distinctly different regions, the F-layer trough region, the auroral oval and the polar cap (see Figure 2). The auroral oval is the location of a band of auroral forms around the magnetic pole, which separates the two other regions and provides the ordering frame for various ionospheric and auroral phenomena. VHF scintillations have been observed over the entire polar cap, in the auroral oval and at subauroral latitudes down to the scintillation boundary (Aarons and Allen, 1971; Aarons, 1973), also shown in Figure 2. It was the goal of the airborne studies to investigate the effects of irregularities in the different regions on the VHF signals. A flight track, shown in Figure 2, was chosen which permitted the consecutive scanning of F-layer trough, oval and polar cap regions in a single flight and also allowed for the known variability of the oval size. Since during the April missions only weak scintillations were observed in the trough the flights in September focused only on the study of oval and polar cap effects. Figure 3 shows schematically a cross-section of the ionospheric structures along the flight track and identifies the five possible ray path configurations. The path can encounter pure trough-, oval- or polar cap conditions and in addition two transition regions, where E-layer effects of one region and F-region effects of another jointly affect the ray path. Data were grouped

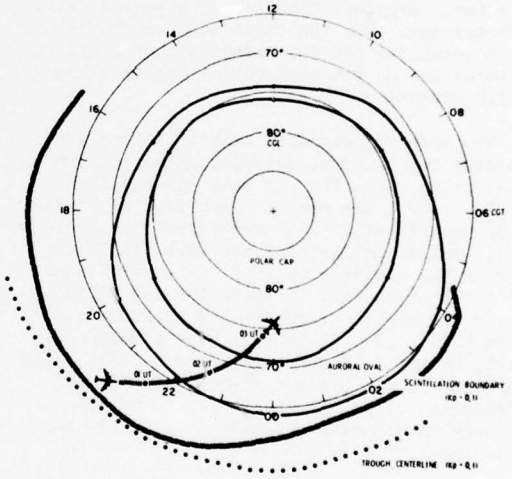


Figure 2. Corrected Geomagnetic/Local Time View of the Test Aircraft Flight Track in Relation to the Q=3 Auroral Oval, the Scintillation Boundary, the Mid-Latitude F-layer Trough, and the Polar Cap.

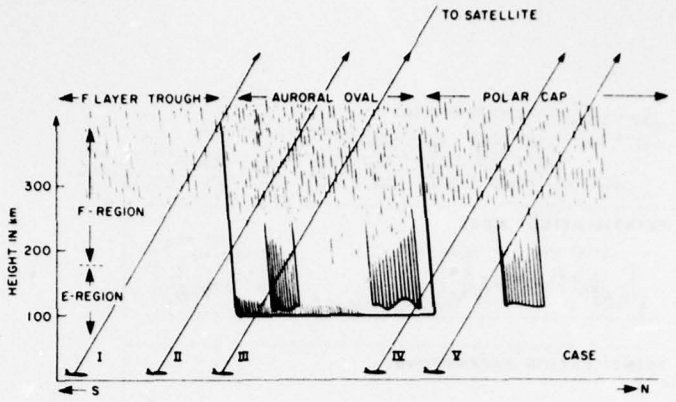


Figure 3. Schematic Cross-Section Through the High-Latitude Ionosphere/Auroral Structure along the Flight Track. The data are grouped according to the propagation conditions encountered: Trough (I), Oval (III), Polar Cap (V), and two Transition Regions (II and IV).

according to these five cases to assess the dependence of scintillations of the various morphological regions.

The Airborne Ionospheric Observatory's instrumentation consisting of ionospheric sounders, all sky cameras, photometers and spectrometers (Gowell and Whidden, 1968), was used to establish the location of the major geophysical boundaries previously described, with respect to the satellite ray path and also to assess the specific conditions, such as presence of auroral forms, in the ray path. These efforts were enhanced by vertical and backscatter soundings at the Goose Bay Ionospheric Observatory.

Figure 4 shows a typical flight track, along the 60°W meridian, flown by the C-141 carrying the satellite communications receiver. The majority of all flights discussed here followed this track. All September flights were made only to the North of Goose Bay concentrating on oval and polar cap studies.

In addition to the flight track the figure shows the observed scintillations given as scintillation index (SI) in dB (Whitney et. al., 1969). The scintillation index was determined for each one-minute interval. Following the international convention the ground data are analyzed using 15 minutes as time base for the data samples. The more dense determination of SI of the airborne data is required since geophysical conditions change rapidly due to the aircraft motion. The SI (in dB) is obtained by measuring the dB difference between the third peak down from the highest and the third fade up from the minimum within each time sample.

The satellite was in a northeasterly direction from the aircraft during the April flight tests and in a northeasterly direction in September. As Figure 4 (data taken on 23 April 1975) shows, scintillations tended to be enhanced when the aircraft was over water. Small land masses close by and in the direction to the satellite also reduced the scintillation level

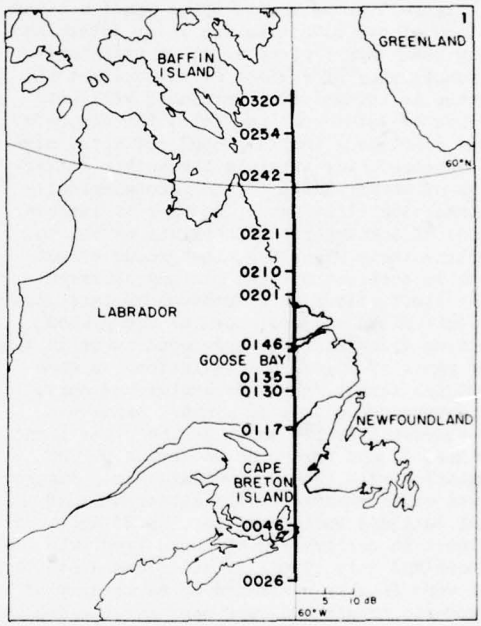


Figure 4. Flight Track of 23 April 1975. Times in UT. Scintillation Index (in dB) is plotted to the right of the track. Scintillations are enhanced over water due to ground reflected propagation mode.

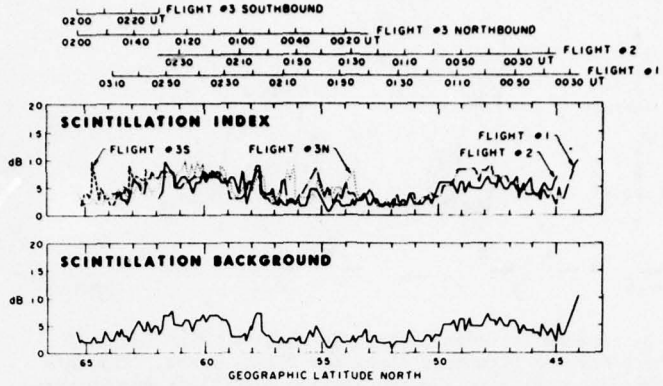


Figure 5. Superposition of Scintillation Data from Flights in April 1975 vs Geographic Latitude (upper panel). Minimum Scintillations (lower panel) derived from the superposed curves.

when the aircraft was over water. Land close to the flight track but not within the azimuth to the satellite did not affect the scintillation levels.

Figure 5 shows in its upper panel a superposition of the scintillation index determined during three April missions along this track. The consistency of regions of enhancement and decrease is evident and correlates well with presence of water and land below the aircraft. It was concluded, that a ground reflected signal, enhanced over water by the better reflectivity of water, added to the ionospherically produced scintillations. In order to isolate periods of ionospheric scintillations and to determine their magnitude, the ground effect had to be subtracted. The minimum observed signal fluctuations as a function of latitude were determined and are shown as the ground effect or scintillation background curve in the lower panel of Figure 5. Deviations on each individual flight from this background curve were determined minute by minute, using the time-reference scales shown in the upper part of Figure 5, and were plotted versus UT for correlation with the geophysical data. Figure 6 gives as an example of the differences of flight data and background for the 23 April 75 mission. An arbitrary 2 dB noise level was introduced and only signal fluctuations above this level were finally considerd to be clearly of ionospheric origin and were used for the analysis.

The scintillation data determined from the September 1975 C-141 flights showed similar behavior and thus were treated identically. The AFGL aircraft was equipped for the September missions with a Dorne Margolin VHF/UHF wide band antenna designed to reject ground reflected propagation modes and the data resulting from this instrumentation was free of a background-component.

The Table shown in Figure 7 gives the % of occurrence of scintillations by region for each flight which scanned through at least 3 adjacent regions, transition regions included. Even though the average conditions as indicated in the average column giving % of the total observing time during each mission that the signal was scintillated, changed over a wide range (6% to 71%), the individual flights show (with the exception of Flight 1) a clear similarity. The highest percentage of scintillations is found in region IV, the transition between oval and polar cap. This result is also seen in the data averaged by expedition and shown in the top section of Figure 7. The graph shows the % of occurrence of scintillations by region, derived separately for the April 75 and the September 75 expeditions. The occurrence in the trough is a low 4% (small data base) and a moderate 14% in the auroral oval region, where both discrete and continuous auroras re generally present. (Discrete auroras are the well known curtains, folds and rays, visible to the eye. Continuous auroras is a more uniform glow, generally just above

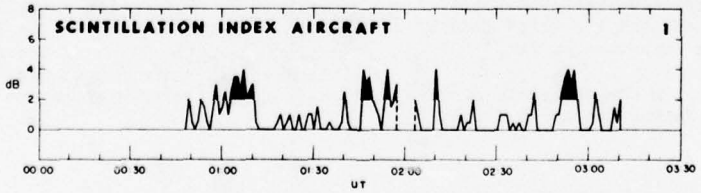
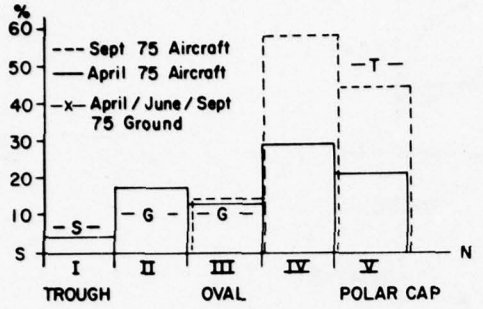


Figure 6. Example of Corrected Aircraft Scintillation Index vs UT for 23 April 1975 Flight. The black regions indicate scintillation peaks >2 dB.



INDIVIDUAL FLIGHTS

FLIGHT NO.	Regions I	II	III	IV	V	Average
1	0	26	12	23	—	15
2	7	0	7	10	—	6
3			23	26	21	23
4			4	38	—	22
5			33	100	87	71
6			19	63	16	30
7			2	54	27	18

Figure 7. Occurrence of Scintillations in % by Region Given Separately for the April and September Expedition (Top Panel) and by Flight (Bottom Table). Ground Results from the same period, measured at Sagamore Hill (S), Goose Bay (G) and Thule (T) are shown for comparison.

the level of visibility, in which discrete forms may be embedded.)' The poleward edge of the oval belt, characterized by discrete auroras in the absence of continuous aurora, is the most probable region of scintillations (29% in April and 58% in September). Polar cap measurements show 21 and 44 percent scintillations respectively.

The conclusions on the relation between the occurrence of substantial scintillations and discrete auroral forms is summarized in Figure 8. This generalization is based on the somewhat

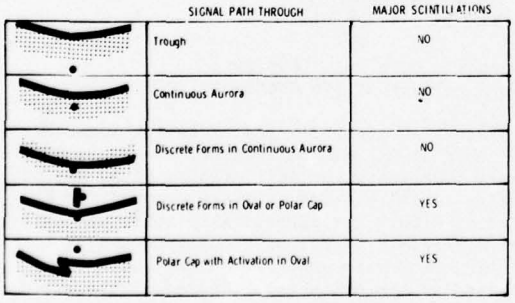


Figure 8. Schematic Representation of the Signal Ray Path (dot) and the Auroral/Ionospheric Features Leading to Scintillations. Shaded: Continuous Aurora. Heavy Lines: Discrete Auroral Forms.

subjective description of the nature of auroral forms by observers, onboard the AFGL aircraft, who made continuous visual observations in the satellite azimuth, and is supported by the statistical data shown in Figure 7. The only auroras definitely associated with high SI are the auroral arcs at the high-latitude edge of the auroral oval - hence at the oval-polar cap transition. Definitely not associated with high SI are the continuous aurora and discrete auroras embedded within the continuous aurora - even though this type of aurora was at times active and bright. The highest SI has been observed in the polar cap, even though the observe probability of scintillations is lower than in the oval/polar cap transition region.

GROUND BASED EXPERIMENTS

The limited amount of airborne measurements served to complement the ground based observations which were made throughout the test periods and resulted in a 34 hour data base from each station, compared to a total of 19.5 hours of data taken by both aircraft in the various regions. The recording equipment used was similar to the equipment used onboard the Airborne Ionospheric Observatory and consisted of Spectrum International Converters and R-390/URR receivers used as IF amplifiers. Signal strength was recorded both on strip charts and analog magnetic tapes. 10-element yagis with a gain of 12 dB and a 45° horizontal/58° vertical beamwidth were used. As an example of the results obtained during the flight tests the results of the ground observations for September 75 are shown in Figure 9. Intense scintillations were observed initially (5 dB on 1 September, 8 dB on 2 September), however the SI did not exceed 4 dB for the remainder of the measurements. Thule generally showed stronger scintillations than Goose Bay. Sagamore Hill except for 1 September is completely quiet. This behavior is typical for magnetically quiet (Kp = 0 to 3) conditions as will be shown later in the discussion of results from the complete ground data base. Inspection of individual days shows that the behavior of the scintillations is far from consistent. There are instances in the test series wherein the highest SI can be found at any of the three stations.

The levels of occurrence of scintillations >3 dB (in percent) at each of the three ground stations Sagamore Hill (S), Goose Bay (G) and Thule (T) determined as averages over the three test periods, April, July and September, are indicated for comparison with the airborne data in the bar graph in Figure 7. Results from each station are indicated by their respective symbols. They show general qualitative agreement with the airborne measurements considering the fact, the Sagamore Hill encounters trough-like conditions only occasionally, while Goose Bay's situation may vary from experiencing trough conditions to pure oval conditions depending on the time of day of the measurements.

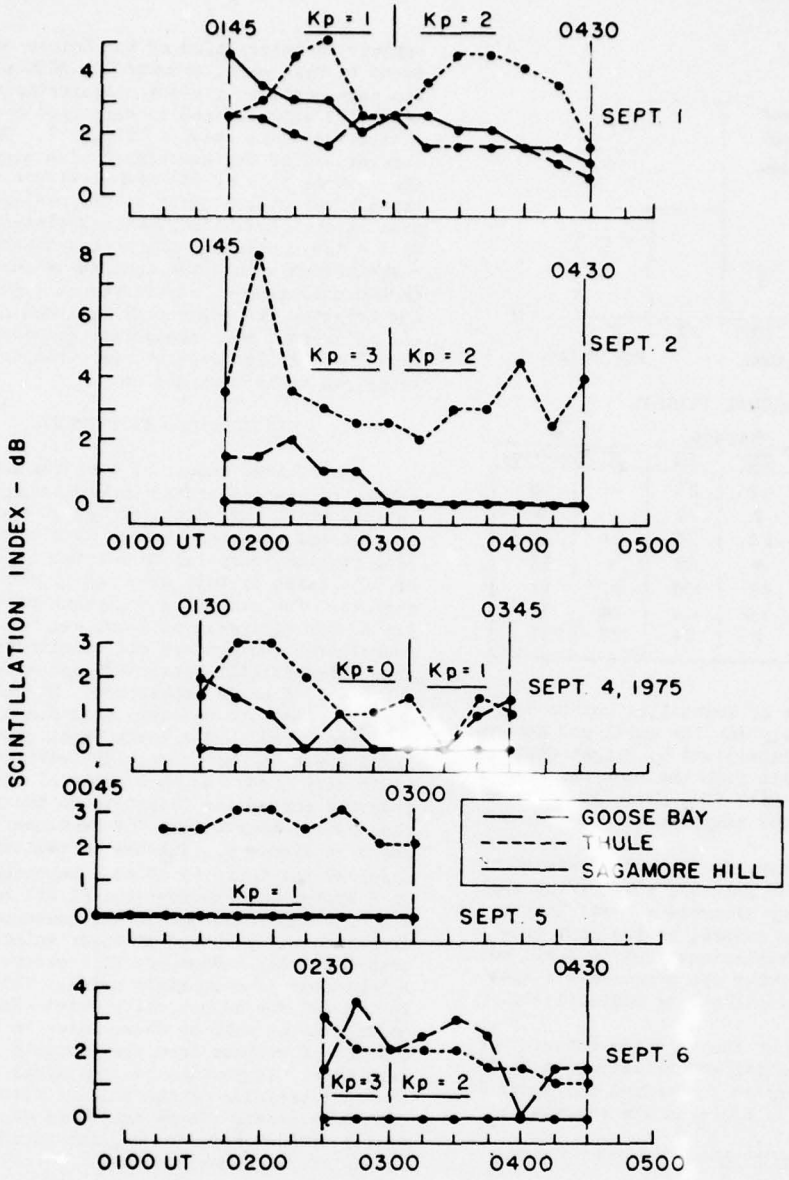


Figure 9. Ground Observed Scintillation as Seen at Goose Bay, Labrador, Thule, Greenland, and Sagamore Hill, Mass., During Tests of 1-6 September 1975.

A more consistent picture evolves if one considers the complete ground data base available. Besides transmissions during the airborne campaign there were many transmissions outside the flight schedule and every transmission was recorded at all three stations. This data base not only allows determination of the latitudinal dependence, but it is also sufficiently large to permit the assessment of the influence of magnetic activity on the occurrence of scintillations.

Figure 10 gives for the three stations the dependence of all scintillations, SI >2 dB, and of more substantial scintillations, SI >4 dB, on magnetic activity. The data are grouped for Kp ranges of 0 to 3 for magnetically quiet and 4 to 6 for moderately disturbed conditions and by 4 hour time intervals centered on the local times indicated on the ordinates. The data base for Kp = 4 to 6 in the time interval centered on 04 LMT was not large enough to be statistically significant and no value for the percentage

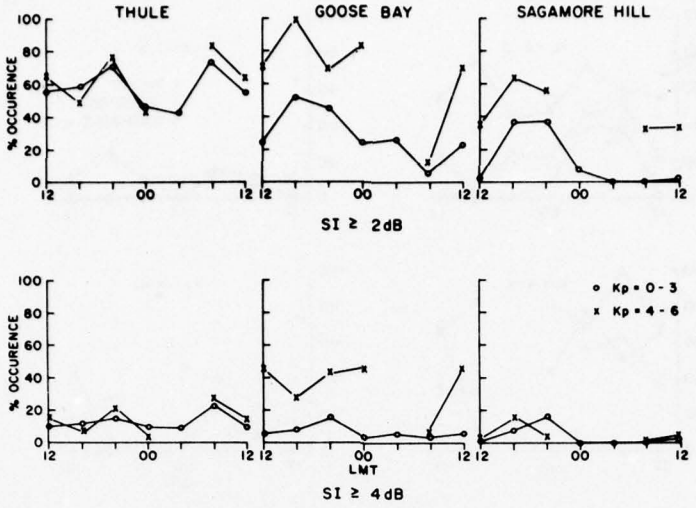


Figure 10. Scintillation Data Base April-September 1975. Grouped for magnetically quiet and moderately disturbed conditions, they show strong magnetic control at Goose Bay, moderate magnetic control at Sagamore Hill and independence at Thule.

occurrence was established. The graphs show a clear dependence of occurrence of scintillations with SI >2 dB on the magnetic activity for Sagamore Hill and Goose Bay, with the occurrence increasing by approximately 50% at Sagamore Hill and by 100% at Goose Bay. The local time dependence shows a well defined maximum in the afternoon to evening sector, which is evidence of the time asymmetry of the scintillation boundary shown in Figure 2. This result increases the confidence in the statistical significance of the accumulated data base. The Thule data show complete lack of magnetic control and a rather flat occurrence versus time distribution. Only a weak minimum in the post midnight sector is indicated. If one considers only stronger scintillations, SI >4 dB, the graphs show no evidence for magnetic control at Sagamore Hill and Thule, but a significant increase at Goose Bay. This may be the result of the oval being enlarged during Kp = 4 to 6 conditions bringing Goose Bay more often under the influence of discrete aurora. The continuous aurora with its lesser effects on VHF signals may under these conditions be found to the south of the station. Goose Bay and Sagamore Hill again show evidence of the afternoon to evening maximum with Thule again showing no temporal variability for the larger scintillations.

The latitudinal dependence of scintillations as a function of Kp is shown in Figure 11, a replot of the data shown in the previous figure. Scintillations with SI >2 dB show under quiet magnetic conditions a clear south to north increase in occurrence, a trend also evident though not quite as clear, if only scintillations with SI >4 dB are considered. Under more disturbed magnetic conditions the auroral oval station Goose Bay shows a strong enhancement, reaching 100% occurrence in the afternnon sector, while the scintillations at Sagamore Hill reach approximately the generally unchanged Thule levels except for a morning maximum. The same behavior is shown if only stronger scintillations with SI $\geq$4dB are considered.

CONCLUSIONS

Airborne and ground based scintillation measurements on 250 MHz signals conducted in 1975, a year of very low solar activity (smoothed sunspot numbers varied from a high of 18.6 in April to a low of 14.5 in September 1975), showed only small to moderate scintillations at subauroral, auroral and polar cap latitudes. Scintillations observed by the ground-stations rarely exceeded 10 dB and generally were in the order of 4 dB. The ground data base showed under quiet conditions good latitudinal ordering, the highest probability and the strongest SI was found in the polar cap. During magnetic disturbances, which were only moderate during the test period, Goose Bay scintillation occurrence increased strongly, and moderately at Sagamore Hill, with both stations showing large afternoon maxima in the occurrence distribution under all conditions. The Thule data show neither magnetic nor local time dependence. The aircraft data confirm that polar cap scintillations under magnetically quiet to moderately disturbed conditions are more prevailing than those in the oval. They do not corroborate the strong enhancement seen under magnetically disturbed conditions at Goose Bay, most likely since the aircraft data collected in the oval under disturbed conditions fell with Kp = 4o and 4- just above the lower limit of the disturbance criterion, encompassed

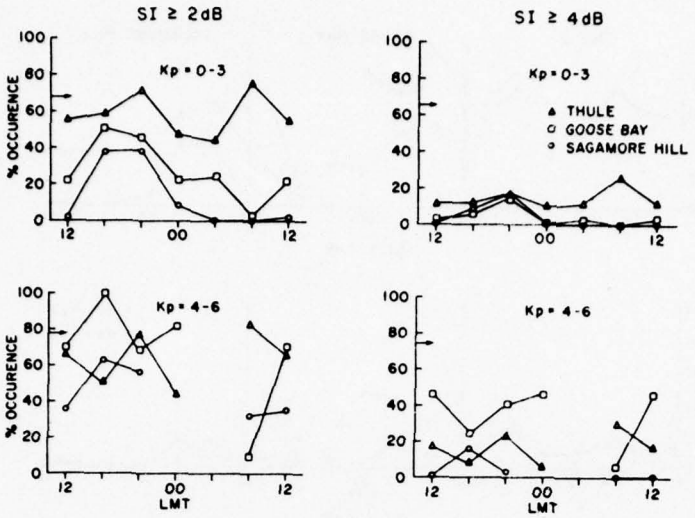


Figure 11. Scintillation Data Base April-September 1975. Presentation shows good latitudinal ordering for quiet magnetic conditions.

less than 3 hours of data and were not taken in the most disturbed 14-18 LT sector. The scintillation amplitude probability distributions determined from aircraft data for the various regions show good agreements with those determined from the ground data base, validating generalizations derived from the small airborne data base. The following are the major findings from the airborne data: The strongest scintillations (>9 dB) were found in the polar cap. During airborne measurements in the oval the highest occurrence of scintillations was consistently found in the poleward half of the auroral oval, at least twice as much as found in the southern half of the oval. Since no station has previously operated in a suitable location, this enhancement so far has been overlooked. The most surprising result is the lack of scintillations associated with that discrete aurora which is embedded in continuous aurora, a condition which is routinely found in the southern half of the oval. Even during auroral disturbances aurora in this location did not affect the signals. Even though the behavior described is not clearly understood, it is likely, that large-scale F-region irregularities are more prevalent at the poleward boundary of the oval, piled up there by convection of F-region ionization from the oval noon sector across the polar cap, and that the possibly more uniform F-region ionization in the southern half of the oval has little effect on the satellite signals.

ACKNOWLEDGEMENTS

All tests were conducted under the auspices of Lt Col R. Bothwell, ESD Test Director for the AFSATCOM System Evaluation, and without his support, this research could not have been performed. Major O.W. Hoering, SAMSO System Program Office, was responsible for the space segment during these tests. His help and interest are gratefully acknowledged. Engineering support by Messrs. C. Galanis, R.W. Gowell, L.J. James, J. Knapick, C. Perkins, P. Pickell, L. Ross, J.C. Spor, and J.B. Waaramaa was instrumental in providing this unique data base, collected under difficult airborne and ground arctic conditions. We thank Mr. Waaramaa especially for his strong efforts to establish a satellite receive capability on board the AFGL aircraft. The data analysis of Ms. A. Pauline Krukonis and Mr. W.N. Hall aided in the interpretation of the airborne and ground based ionospheric data. The support of Airborne Engineering groups and flight crews from the USAF 4900th Test Wing, Kirtland AFB, NM and the USAF 4950th Test Wing, Wright-Patterson AFB, OH is gratefully acknowledged. We also acknowledge the assistance of the staff of the AFGL Goose Bay Ionospheric Observatory and the AFGL Geopole Station.

REFERENCES

Aarons, J. and R.S. Allen (1971), Scintillation Boundary During Quiet and Disturbed Magnetic Conditions, J.G.R. 76, 1, 170-177.

Aarons, J. (1973), A Descriptive Model of F-Layer High Latitude Irregularities as Shown by Scintillation Observations, J.G.R. 78, 31, 7441-7450.

Gowell, R.W. and R.W. Whidden (1968), Ionospheric Sounders in Aircraft, AFCRL-68-0369, Instrumentation Papers, No. 144.

Whitney, H.E., C. Malik and J. Aarons (1969), A Proposed Index for Measuring Ionospheric Scintillations, Planet. Space Sci., 17, 1069-1073.

GIGAHERTZ SCINTILLATION AT THE MAGNETIC EQUATOR

J. P. Mullen
Air Force Geophysics Laboratory
Hanscom AFB, MA 01731

A. Bushby, J. Lanat and J. Pantoja
Instituto Geofisico Del Peru
Apartado 3747, Lima, Peru

BACKGROUND

When a radio wave is propagated through the irregular ionosphere it is diffracted and caused to fluctuate in amplitude and phase. A wealth of experimental and theoretical analysis has been performed on this phenomenon; early experiments began in the high frequency range (≈ 20 MHz) and have progressed to the gigahertz region. It is the purpose of this note to consider results obtained at or near 1.5 GHz, the band to be used by the DoD NAVSTAR (Global Positioning System). Early observations of equatorial GHz scintillation were made by Golden (1970) who found 5 dB scintillation on 1.5 GHz at Quito, Ecuador. Skinner et al. (1971) reported 4 dB fading at SHF (6.3 GHz) at Kenya. Christiansen (1971) measured 20 and 25 dB at 2.2 GHz from Guam, Canary Islands and Ascension Island. Craft (1971) found up to 8 dB scintillation at 4 and 6 GHz at a number of equatorial locations. Other equatorial gigahertz scintillation measurements were reported by Crampton and Sessions (1971), Sessions (1972), Taur (1973 and 1976) and Mullen et al. (1977). Much of the early work was done using the ATS-5 satellite, which carried VHF and L Band (1.5 GHz) transmitters, the Intelsat space vehicles which transmitted at 4 and 6 GHz while more recent work (Mullen et al., 1977 and Paulson and Hopkins, 1977) used the UHF and 1541.5 MHz beacons on Marisat I and II. A very strong tool for investigation of scintillation at a number of coherent frequencies (137, 378, 390, 401, 413, 424, 435, 447, 1239, 2891 MHz) was provided by the DNA Wideband satellite (Fremouw, 1976).

THE DATA

Observations of scintillation at L Band (1.5 GHz) and at UHF (254.15 and 257.55 MHz) using the transmitters of MARISAT were begun at Huancayo in April 1976, and have continued without substantial interruption. Figure 1 shows the probability of occurrence of L Band scintillation greater than 2 dB. The month of October 1976 saw unusual activity, and it is shown separately, as well as lumped together with the months of April and December, 1976, January, February and March 1977. This shows that the scintillation occurs for the most part between 1900 and 2300 LMT, with a maximum at 2100 LMT. Figure 2, taken from recently published work (Mullen et al., 1977) shows the cumulative distribution function of a 15 minute period in which the L Band scintillation exceeded 7 dB. While this is far from a worst case, it does illustrate the problem of the systems designer. These results show that for operation at the 99th percentile, a system would require a fade margin of 2 dB at 1541 MHz. Figure 3 shows a common event; strong scintillation begins on the UHF signal, and L Band scintillation commences simultaneously. The UHF signal remains strongly scintillated after the L Band scintillation ceases. In this illustration is also seen one of the rare instances of substantial UHF daytime scintillation. Figure 4 shows an instance in which UHF scintillation begins, shortly thereafter follows L Band scintillation which quiets while the UHF strong scintillation continues for another two hours. Two hours later UHF scintillation re-

commences, followed by L Band, which ceases within an hour and finally the UHF scintillation ends. Figure 5 is an example of strong UHF scintillation associated with only moderate (≈ 2 dB) L Band scintillation. In these illustrations, L Band scintillation is found to vary from a nightly maximum of about 2 dB to a nightly maximum of about 8 dB. This last is the maximum L Band scintillation measured at Huancayo, where the elevation angle to the satellite is 21°. The occurrence pattern is of some interest; the UHF scintillation begins either before or at the same time as the L Band. It is also noteworthy that intense scintillation can develop at UHF with little or no activity at L Band (Figs. 3 and 5).

DISCUSSION

The Naval Ocean System Center (Paulson and Hopkins, 1977) has recently completed simultaneous observations of the L Band and UHF transmitters of Marisat II over a 6 months period. They found significant levels of amplitude scintillation (up to 5 dB) during the tests. From this they inferred that large phase scintillations also occurred.

One view of the causative mechanism for the gigahertz scintillation producing ionospheric irregularities is a thick layer (≈ 200 kilometers) extending upward from the base of the F region and containing irregularities varying from a few meters to several kilometers in size having density fluctuations on the order of 50-75% (Basu and Basu, 1976). This is corroborated by observations made at Huancayo, Jicamarca and Ancon, Peru in 1976 and 1977 by a joint task force which included personnel of AFGL, SRI, AFAL and University of Texas at Dallas. The program included participation by the Jicamarca radar, the AFGL flying laboratory and the AFAL airborne communications terminal as well as ground observations at Ancon and Huancayo.

The morphology of the irregular equatorial ionosphere has been explored first by bottomside soundings (Wright, 1959) by topside sounder (Calvert and Schmid, 1964) by transiting satellites (Sinclair and Kelleher, 1969), by a combination of in-situ and geostationary observations (Basu et al., 1976), by a world wide network of earth stations (Taur, 1973) and most recently by the combination of ground and airborne multi-media observations supplemented by an ionospheric backscatter radar (Aarons et al., 1977). The findings are in general agreement; the zone of maximum equatorial scintillation extends from about 20° geomagnetic north to 20° geomagnetic south.

The longitudinal morphology of equatorial scintillation has also been explored by Basu et al. (1976). Their findings suggest a pronounced longitude variation, with the scintillation zone width and percentage occurrence maximizing over the African sector. In the American sector, the width of the zone decreases without appreciable change in scintillation occurrence. In the Indian sector, both width and occurrence probability are decreased. The model based on in-situ measurements is consistent with ground based observations during the December solstice.

CONCLUSION

The nighttime equatorial ionosphere has been found to cause scintillation up to approximately 8 dB at L Band. Geographically, this occurs most frequently within ± 20° geomagnetic. Timewise, it can occur just about anytime between sunset and sunrise, with midnight ± 2 hours being most likely. Cumulative amplitude distributions have been reported earlier and found to correspond to the Nakagami distribution with m=22. It was found that the corresponding UHF distribution was a good fit to the Nakagami distribution where m=1.3, which is very close to a Rayleigh distribution, and which in our experience has been the limiting case.

REFERENCES

Aarons, J., J. Buchau, S. Basu and J. P. McClure, "The Localized Origin of Equatorial F-region Irregularity Patches", submitted for publication in J. Geophys. Res., 1977.

Basu, Sunanda, S. Basu and B. K. Khan, "Model of Equatorial Scintillations from In-Situ Measurements", Radio Sci., 11, 821, 1976.

Basu, Sunanda and S. Basu, "Correlated Measurements of Scintillations and In-Situ F-region Irregularities from Ogo-6", Geophys. Res. Lett., 3, 681, 1976.

Calvert, W. and C. W. Schmid, J. Geophys. Res., 69, 1839, 1965.

Christiansen, R. M., "Preliminary Report of S-Band Propagation Disturbance During ALSEP Mission Support", November 19, 1969 - June 30, 1976) Report X861-71-239, Goddard Space Flight Center, June, 1971.

Craft, H. D., Jr., "Investigation of Satellite Link Propagation Anomalies at 4 and 6 GHz, Preliminary Report", Comsat Laboratories, CL-9-71, 9 Feb 1971.

Crampton, E. E., Jr., and W. B. Sessions, "Experimental Results of Scintillation Measurement of Ionospheric Amplitude Variations of 136 and 1550 MHz signals at the Geomagnetic Equator", Report to the ASTRA Panel, International Civil Aviation Organization, 7 Jan 1971.

Fremouw, E. J., "Wideband Satellite Observations", Bimonthly Progress Report #2, Contract DNA 001-75C-0111, SRI Project 3793, Stanford Research Institute, Menlo Park, CA, 13 August 1976.

Golden, T. S., "A Note on Equatorial Ionospheric Scintillation at 136 MHz and 1550 MHz", Report X520-70-397, Goddard Space Flight Center, Greenbelt, MD, October, 1970.

Mullen, J. P., H. E. Whitney, Santimay Basu, A. Bushby, J. Lanat and J. Pantoja, "Statistics of VHF and L Band Scintillation at Huancayo, Peru", To be published in JATP, September, 1977.

Paulson, M. R., and R. U. F. Hopkins, "Spatial Diversity Characteristics of Equatorial Scintillation", Technical Report No. 3, Naval Ocean Systems Center, San Diego, CA, 2 May 1977.

Sessions. W. B., "Amplitude Fading of Simultaneous Trans-Ionospheric L Band and VHF Signals Received at the Geomagnetic Equator", NAS Report X810-72-282 GSFC, June, 1972.

Skinner, N. J., R. F. Kelleher, J. B. Hacking and C. W. Benson, "Scintillation Fading of Signals in the SHF Band", Nature (Phys. Sci.), 232, 19-21, 1971.

Sinclair, J. and R. F. Kelleher, "The F-region Irregularity Belt as Observed from Scintillation of Satellite Transmissions", JATP, 31, 201-206, 1969.

Taur, R., "Ionospheric Scintillation at Frequencies Above 1 GHz", Technical Memorandum CL-29-73, COMSAT Laboratories, Clarksburg, MD.

Taur, R. R., "Ionospheric Scintillation at 4 and 6 GHz", COMSAT Technical Review, 3, #1, Spring, 1973.

Taur, R., "Simultaneous 1.5 and 4 GHz Ionospheric Scintillation Measurement, Radio Sci., 11, 1029-1036, 1976.

Wright, R. W. H., J. Geophys. Res., 64, 2203, 1959.

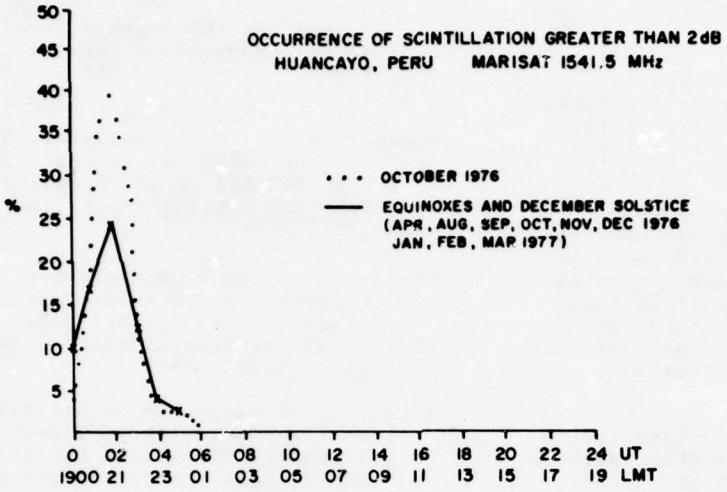

OCCURRENCE OF SCINTILLATION GREATER THAN 2dB
HUANCAYO, PERU MARISAT 1541.5 MHz
• • • OCTOBER 1976
EQUINOXES AND DECEMBER SOLSTICE
(APR., AUG., SEP., OCT., NOV., DEC. 1976
JAN., FEB., MAR. 1977)
%
50
45
40
35
30
25
20
15
10
5
0 02 04 06 08 10 12 14 16 18 20 22 24 UT
1900 21 23 01 03 05 07 09 11 13 15 17 19 LMT

fig 1

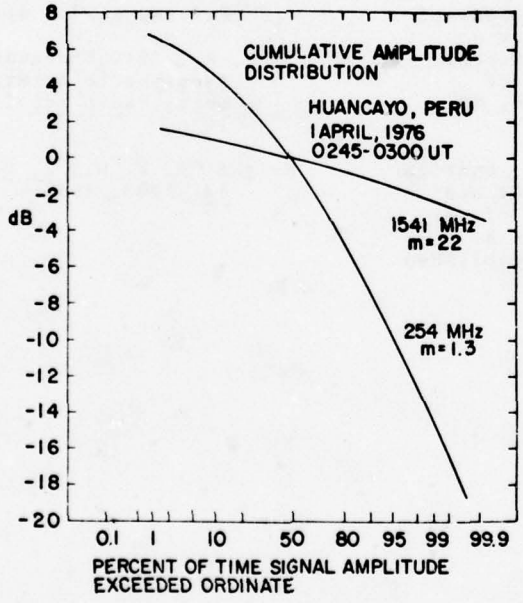

CUMULATIVE AMPLITUDE
DISTRIBUTION
HUANCAYO, PERU
1 APRIL, 1976
0245-0300 UT
1541 MHz
m=22
254 MHz
m=1.3
dB
8
6
4
2
0
-2
-4
-6
-8
-10
-12
-14
-16
-18
-20
0.1 1 10 50 80 95 99 99.9
PERCENT OF TIME SIGNAL AMPLITUDE
EXCEEDED ORDINATE

fig 2

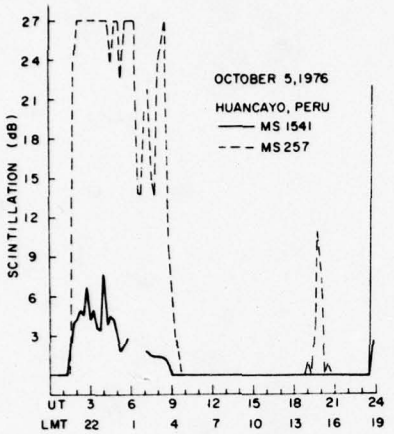


fig 3

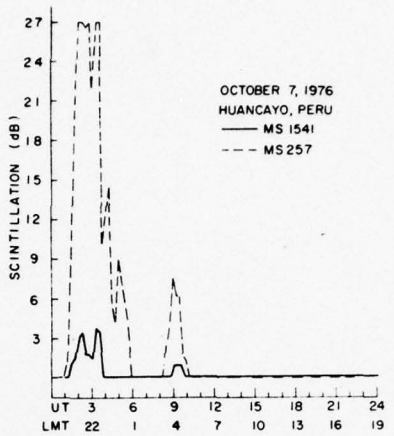


fig 4

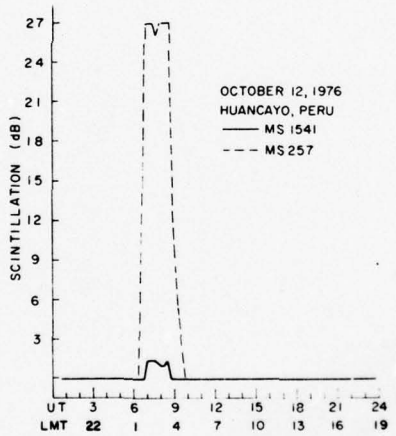


fig 8

SPACED RECEIVER MEASUREMENTS OF INTENSE EQUATORIAL SCINTILLATIONS

Herbert E. Whitney
Air Force Geophysics Laboratory
Hanscom AFB, MA 01731

INTRODUCTION

Satellite communication links can be affected by ionospheric scintillations particularly at frequencies less than 400 MHz and in the equatorial region. During the equatorial scintillation campaign of October 1976 and March 1977, spaced receiver measurements were made at Ancon, Peru to investigate several facets of scintillations which included a determination of the signal statistics of the scintillation events and a measurement of the temporal and spatial correlation functions. The signal statistics are necessary for evaluating the performance of communication links when affected by scintillations and the correlations functions are used to determine the effectiveness of diversity and coding techniques. The aim of this paper is to present some results which were obtained from the analysis of one of the tests, 19-20 Oct. 1976.

AMPLITUDE DATA

F-region irregularities develop shortly after local sunset in the equatorial ionosphere and show up as backscatter on the Jicamarca radar operating at 50 MHz and fluctuations of the LES-9 signal at 249 MHz as shown in fig. 1. The top panel is a reproduced range-time-intensity plot of backscatter of 3 m scale size irregularities detected by the Jicamarca radar. After sunset a localized depletion of electron density may form in the lower F layer and then rise and move into the middle and upper F layers. This upwelling results in "plumes" on the radar map and two "plumes" can be observed in fig. 1. The middle panel shows the time variation of scintillation index recorded on the propagation path from Ancon to the LES-9 satellite and the lower panel is the scintillation index recorded at Huancayo. The scintillation index was scaled in two minute intervals from the strip chart records. Once formed, the irregularity structure drifts eastward. Since the scintillations occurred first at Huancayo and then at Ancon, prior to the first "plume" on the radar map, irregularity structures must have formed first between Huancayo and Ancon, and then between Ancon and Jicamarca prior to the appearance of backscatter over Jicamarca.

SIGNAL STATISTICS

Magnetic tape recordings were made at Ancon and the results of the computer analysis for signal statistics during the time period 0030-0340 UT will be described. The strip chart record in fig. 2 shows the rapid development of scintillations at 0050 UT on two receivers spaced 366 meters on an east-west baseline. From an essentially undisturbed level, fluctuations reached more than 20 dB in about a one minute interval.

The data on magnetic tape was analyzed in 1.5 minute segments to obtain information on the S_4 index (square root of the variance of received power divided by the mean value of the received power), cumulative amplitude distribution (cdf), power spectrum, autocorrelation function and cross correlation function. To show examples of the analysis, the 1.5 minute section of input data shown in fig. 3 which occurred just after the developing phase of scintillations, will be used. Fading of the signal below the mean level was greater than 15 dB.

The cumulative amplitude distribution (cdf) for this period is shown in fig. 4. The cdf is a first order

statistic and is useful for defining the minimum margin requirements for the communications link of nondiversity systems. The S_4 index for this period was 1.17. Generally the S_4 index does not exceed unity except under foccusing conditions. The solid line is the experimental data and the dots are calculated for a Rayleigh distribution. Based on the analysis to date the Rayleigh distribution function provides a good fit to the observed data under the limiting conditions of intense scintillation. It can be noted that approximately 1% of the time the signal fades exceed 15 dB.

In addition to the information on the amplitude of the fades which is given by the cdf, a statistical description of the fading rate is needed to fully characterize the effects of scintillation on the communications channel. Information on the fading rate can either be produced by level-crossing techniques or by Fourier techniques which produce the power spectra and time correlation functions. The power spectrum for this data sample is shown in fig. 5. Generally the spectral shape consists of a relatively flat low frequency spectrum and a high frequency roll-off with a slope of approximately f^{-4} to f^{-5} for intense scintillations. The slope for the data in this sample period was -3.7

Fig. 6 shows the related autocorrelation function for this data sample. The autocorrelation function is another means of characterizing the rate of scintillation fading. It is the Fourier transform of the power spectrum and therefore has a width of the main lobe which is inversely proportional to the bandwidth of the power spectrum. The correlation interval or delay is listed in fig. 6 for various values of the correlation coefficient. The correlation interval was approximately 0.9 seconds for a correlation coefficient of 0.5. This parameter can be used to evaluate the effectiveness of time diversity techniques. Coding or interleaving can be an effective means of achieving time diversity improvement.

Since two antennas spaced on a 366 meter east-west baseline were used to record scintillation at Ancon, the spatial correlation function and drift velocity of the irregularities can be measured. A typical crosscorrelation plot is shown in fig. 7 for the same data sample on 20 Oct. 1977. The maximum coefficient was 0.88 at a delay of 2.39 seconds. Since the scintillation pattern at the west antenna leads the east antenna the velocity is eastward and has a value of 153 meters per second. While this is a typical value the drift velocity can vary from approximately 50 to 200 meters per second.

The variations with time of the S_4 index, autocorrelation interval (ρ=0.5), and the crosscorrelation coefficient for a 3¼ hour period (0030-0345) are shown in fig. 8. The S_4 index shows an abrupt rise at the onset of scintillations, and indicates the drift of several irregularity regions thru the antenna beam. The S_4 index reaches unity during the passage of the first two regions.

The autocorrelation interval was low ($\sim$ 0.5 seconds) following the onset of scintillations, but in general varied between 1 and 2 seconds. The bandwidth or rate of scintillation varied by more than a factor of 4. Generally the autocorrelation interval was lowest during the most intense scintillations. The data indicates that time diversity techniques would have to provide delays of a few seconds to significantly reduce the effects of scintillation.

The crosscorrelation coefficient also showed great variability, ranging from a low of approximately 0.2 following the onset of scintillations to almost unity under conditions of very intense scintillations. While the antenna spacing of 366 meters is sufficient to provide significant space diversity improvement for some periods of intense scintillation, a much larger spacing would be required to provide the necessary decorrelation for the entire period.

DIVERSITY TECHNIQUES

When correlation data are available it can be used to determine the advantages of using diversity techniques. Diversity techniques combine two or more signals that are fading independently to reduce the effects of scintillation fading. Autocorrelation data can be used to evaluate time diversity techniques; crosscorrelation data from multifrequency measurements can be used to evaluate the effectiveness of frequency diversity; and the crosscorrelation data from spaced receivers can be used to evaluate the effectiveness of space diversity.

When scintillations follow a Rayleigh distribution the signal will fade approximately 20 dB for one percent of the time. Depending on the degree of correlation between diversity signals some protection can be provided against the fading. Most of the diversity improvement is achieved by the time the correlation coefficient reaches 0.6. For example, the improvement at the 1% point is approximately 8 dB for $\rho=0.6$ and 10 dB for $\rho=0$ or complete decorrelation.

From a large collection of observations a limited amount of data has been presented on the amplitude and rate characteristics of intense scintillations in the equatorial region. Typical autocorrelation and crosscorrelation data was given which shows the feasibility of reducing the effects of intense scintillations.

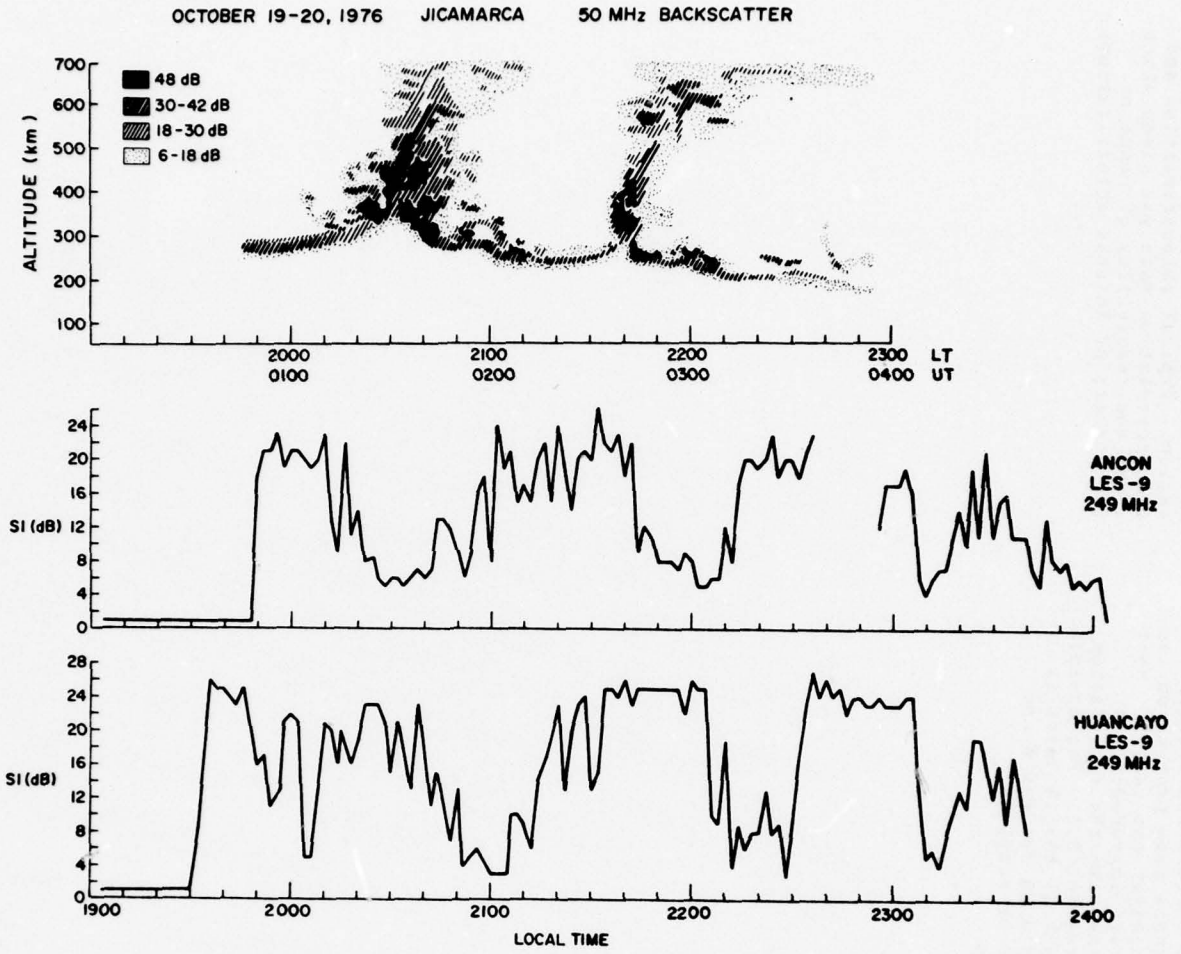


Fig. 1. Jicamarca radar backscatter map and corresponding amplitude scintillations observed at Ancon and Huancayo.

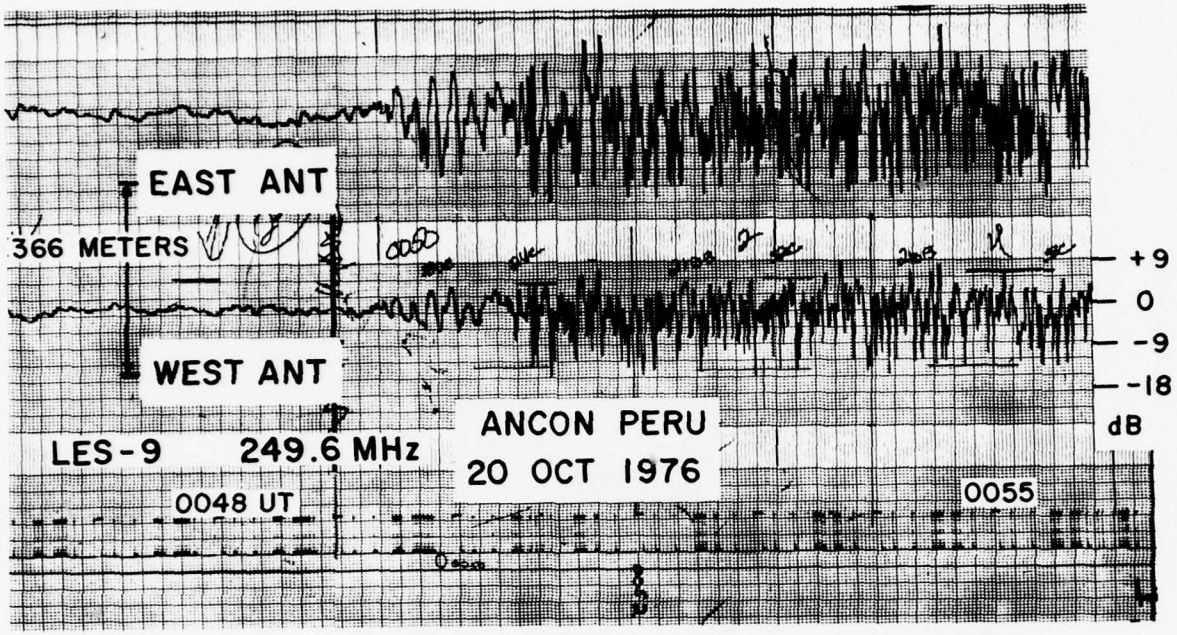


Fig. 2. Signal strength recording from spaced receivers at Ancon of LES-9 scintillations.

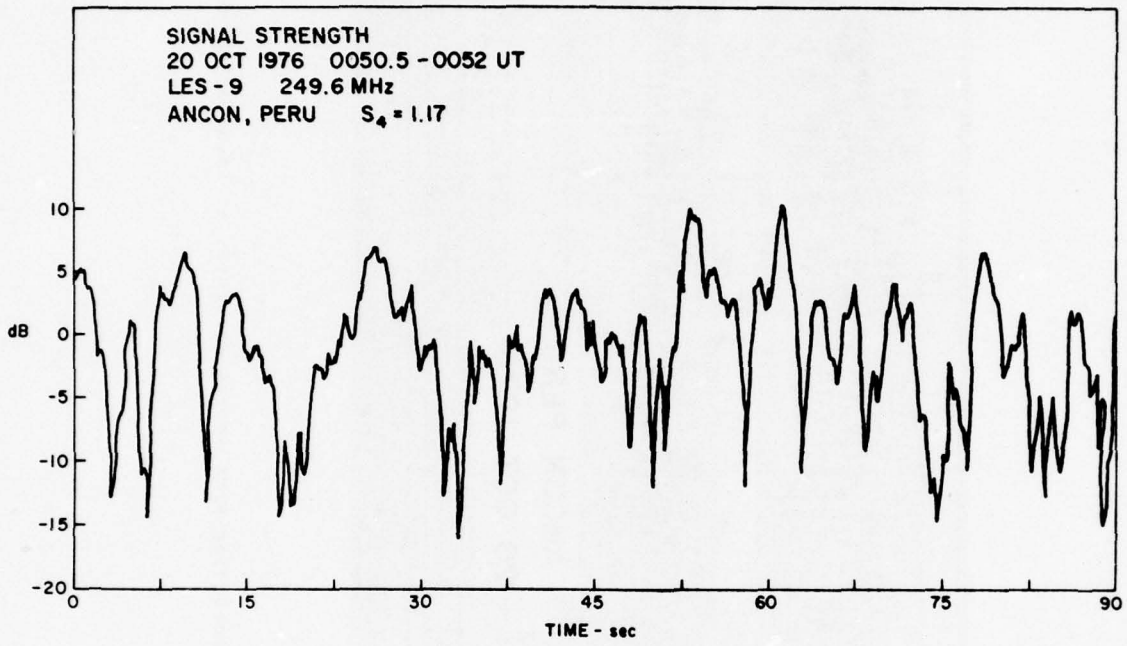


Fig. 3. Signal strength sample at start of scintillations.

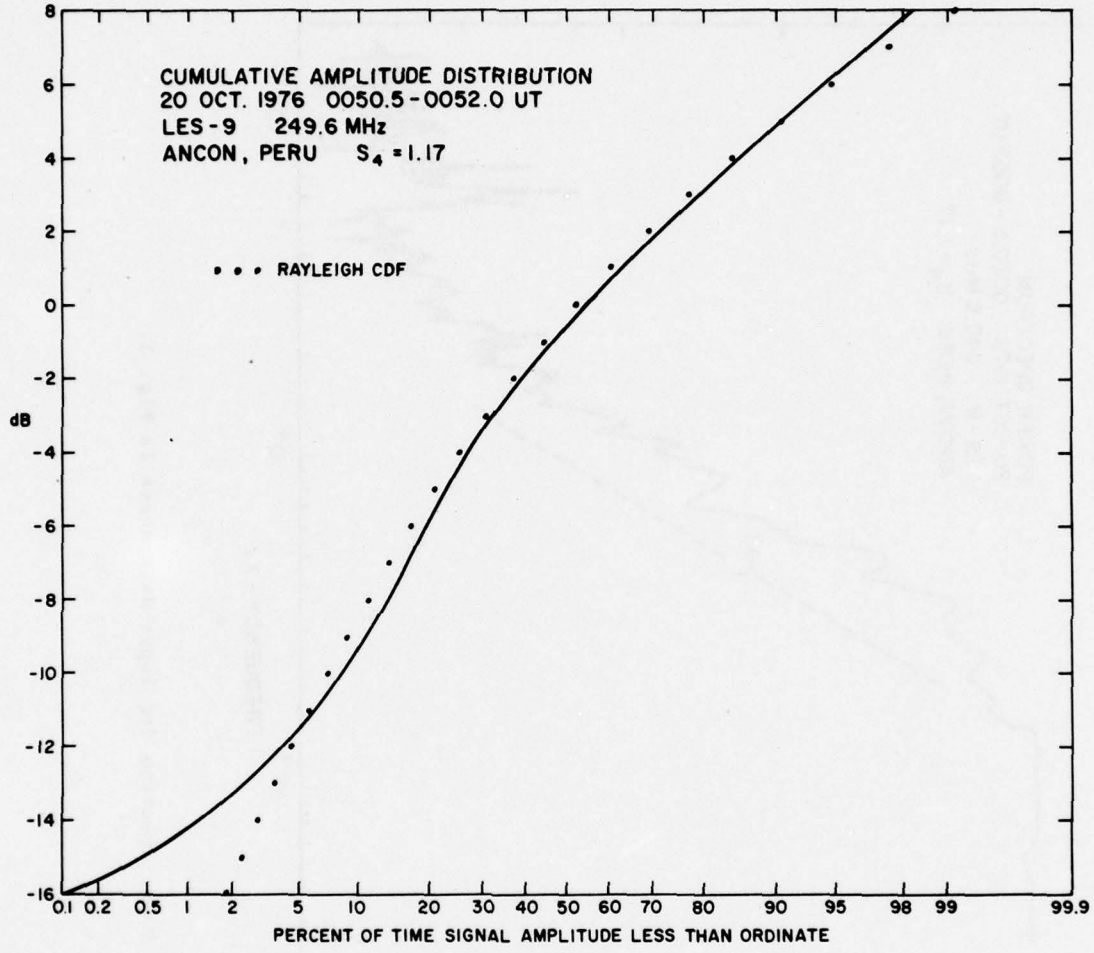


Fig. 4. Cumulative Amplitude distribution for input data shown in Fig. 3.

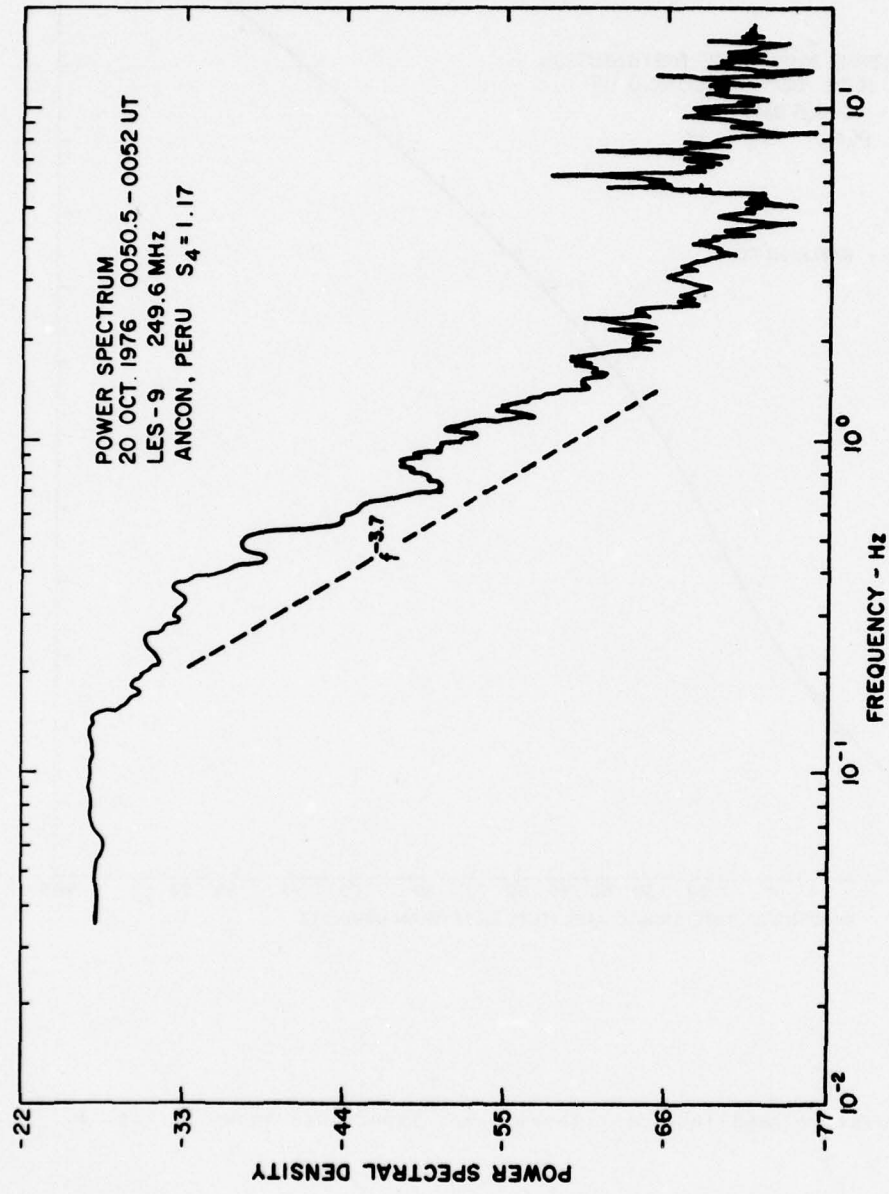


Fig. 5. Power spectrum for input data shown in Fig. 3.

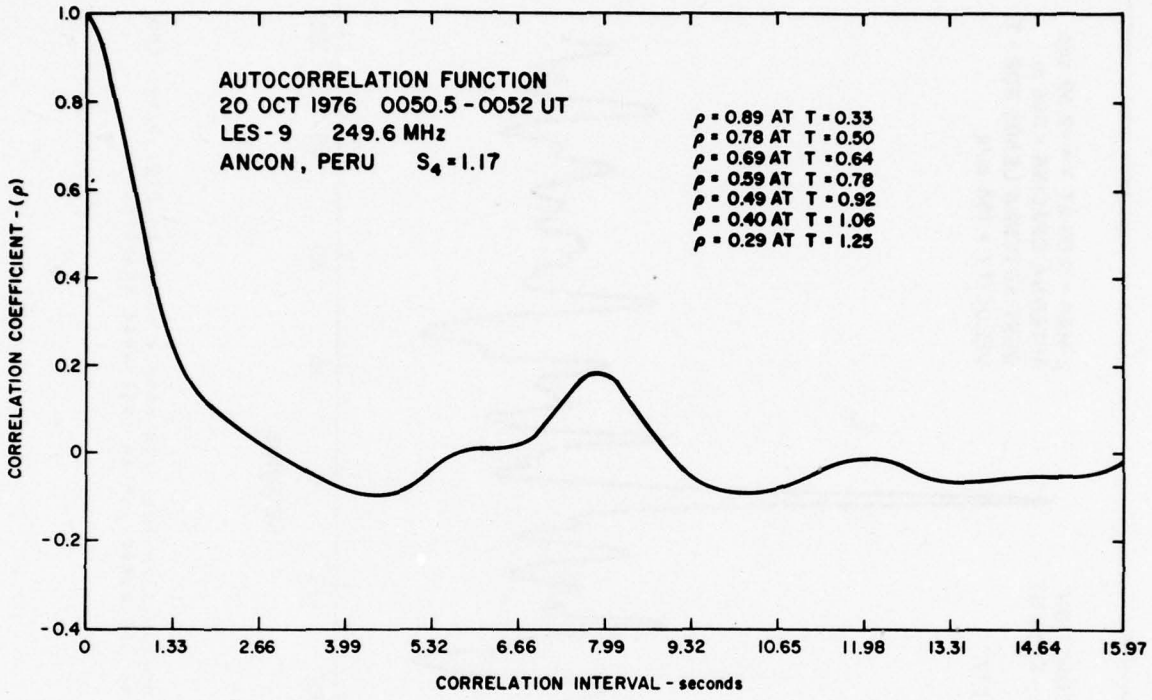


Fig. 6. Autocorrelation function for input data shown in Fig. 3.

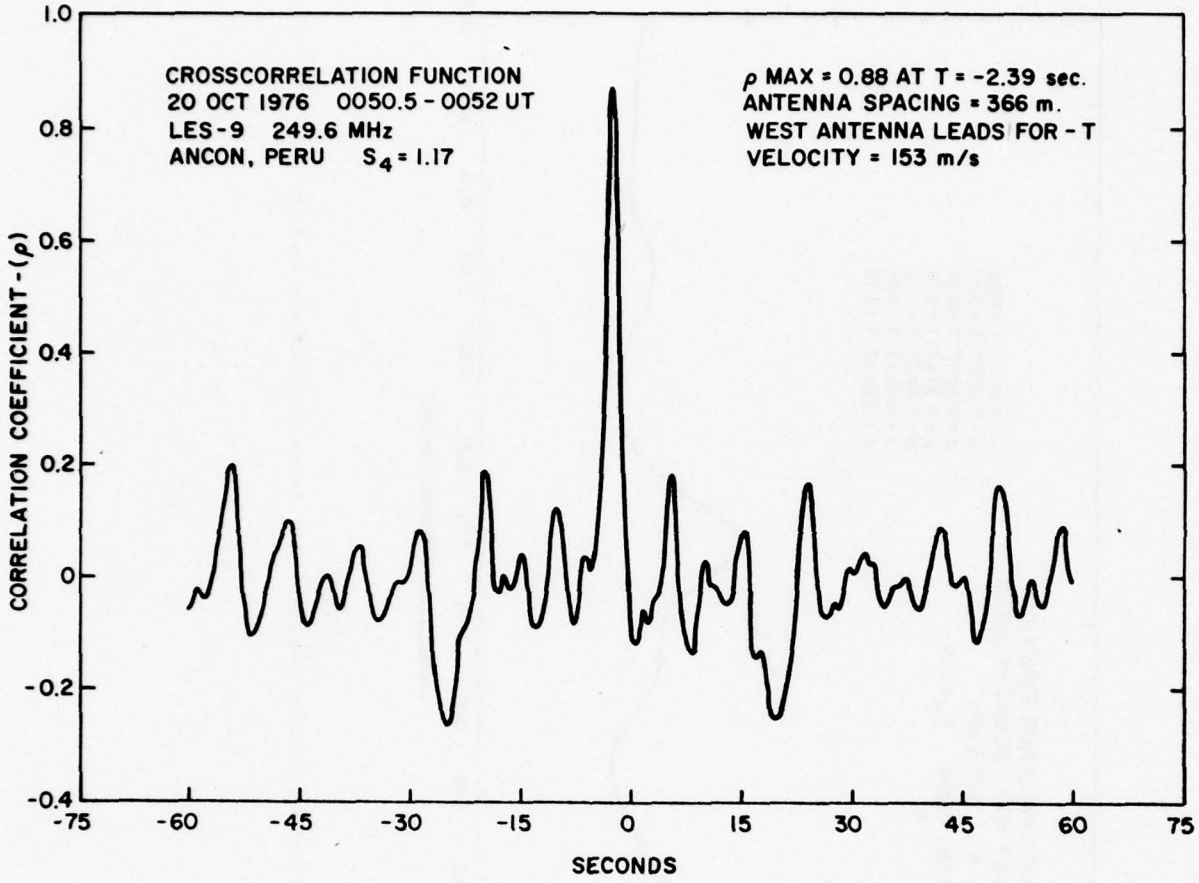


Fig. 7. Crosscorrelation function for data sample shown in Fig. 3 for two receivers spaced 366 meters on an east-west baseline.

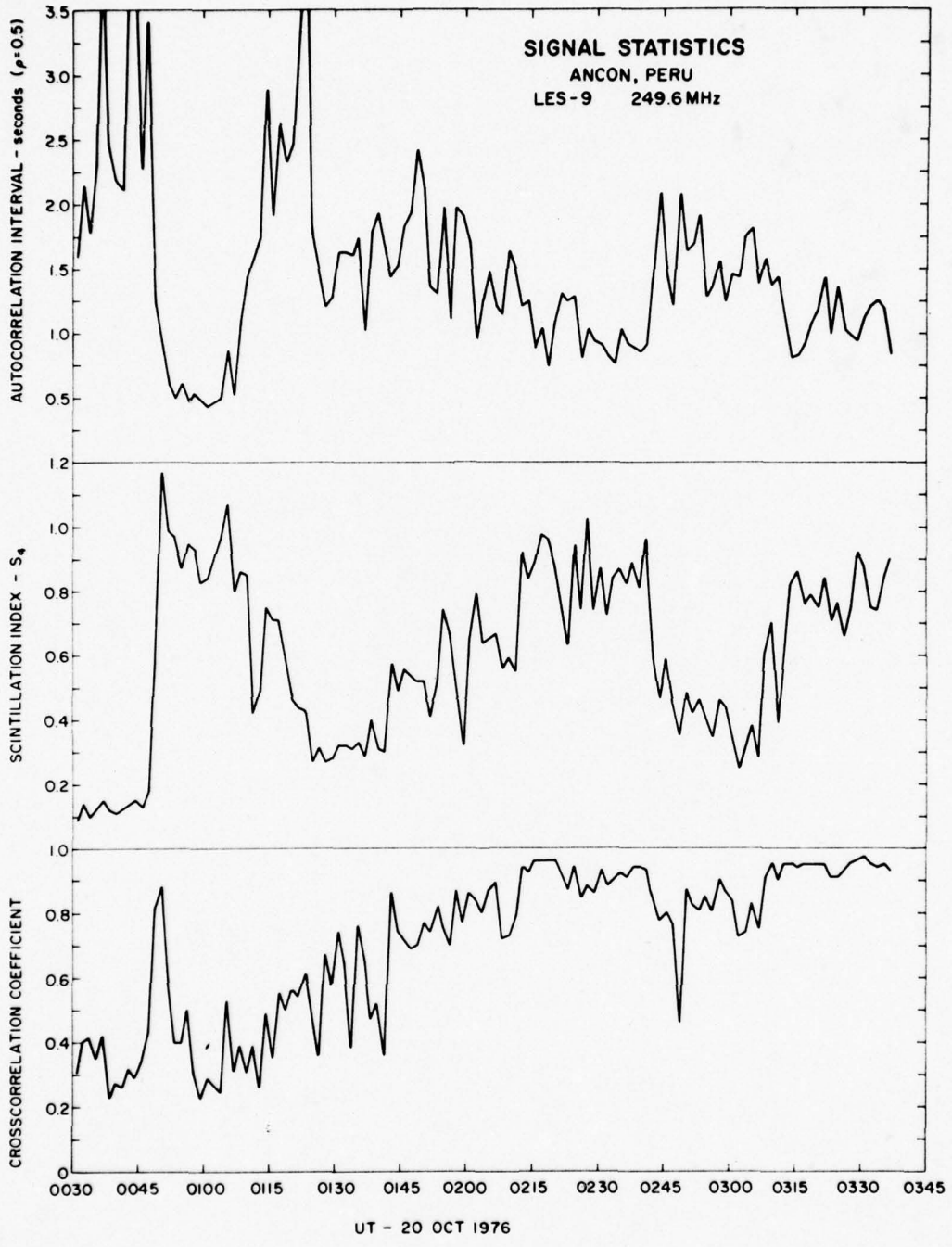


Fig. 8. Variation of S_4, autocorrelation interval, and crosscorrelation coefficient for an extended period of scintillations on 20 Oct. 1977.

A REVIEW OF RECENT STUDIES OF EQUATORIAL F-REGION IRREGULARITIES AND THEIR IMPACT ON SCINTILLATION MODELING

Sunanda Basu *
Air Force Geophysics Laboratory
Hanscom AFB, MA 01731

M.C. Kelley
School of Electrical Engineering, Cornell University
Ithaca, N.Y. 14853

Abstract Our understanding of the various plasma instabilities that cause nighttime equatorial F-region irregularities and their effects upon radio wave propagation has grown enormously since the last IES Symposium three years ago. This has been achieved through the combined use of ground-based, aircraft and in-situ measurements in the radio and optical domains. Analytical and computer simulation investigations have kept pace with the experimental results. In this review we shall outline the present state of both experiment and theory. A realistic modeling of the irregular medium must precede effective communications channel modeling. We shall thus endeavor to bring to the attention of the systems engineer those aspects of scintillation modeling most affected by the new understanding of equatorial spread-F.

1. INTRODUCTION

Four decades after the discovery of the phenomenon called 'equatorial spread-F' (Booker and Wells, 1938), the general problem of nighttime equatorial F-region irregularities has remained a fascinating one to theoretical and experimental geophysicists. This problem has also been one of serious concern to communications engineers as it is well known that these irregularities cause amplitude scintillation which can degrade the performance of satellite communication links. More recently, it has become clear that naturally occurring phase scintillation can impair the performance of satellite surveillance systems that use synthetic aperture processing to achieve high range resolution.

* NRC Resident Research Associate

A variety of different techniques, such as, in-situ rocket and satellite measurements, radar and airglow observations as well as numerical and analytical investigations have, on one hand, enlarged vastly the scope of the problem and, on the other, contributed greatly to our understanding of equatorial F-region irregularities. It is also interesting to note how our improved understanding of the characteristics of equatorial irregularities has influenced the development of more realistic models of equatorial scintillations. For instance, soon after in-situ measurements revealed that the irregular medium is best represented by a power-law *type* irregularity power spectrum (Dyson et al., 1974) over a wide range of scale lengths (~10 km to 10 m) rather than by a gaussian spectrum characterized by a single scale size (Briggs and Parkin, 1963), modeling of ionospheric scintillation was tailored to reflect this change (Rufenach, 1975; Costa and Kelley, 1977). It is also being recognized that saturated amplitude scintillations (>20 dB) in the VHF/UHF band and moderate fadings (4-8 dB) in the GHz band over the equatorial region can only be modelled in terms of large amplitude irregularities distributed in thick layers having a power-law type irregularity power spectrum with large, ill-defined outer scale sizes (Basu and Basu, 1976). These large scale size irregularities can contribute substantially to phase scintillation even under conditions of weak amplitude scatter (Fremouw et al., 1978) as we shall be discussing later.

In our last review on the subject presented at the 5th International Symposium of Equatorial Aeronomy in August, 1976 and recently published

(Basu and Kelley, 1977, hereafter to be referred to as Paper I), we discussed the latest information, available at the time, on equatorial irregularities obtained by the various techniques and presented a model of equatorial scintillations consistent with these observations. Since then considerable new information has become available as a result of the Air Force Geophysics Laboratory (AFGL) equatorial irregularity campaigns in Peru in October, 1976 and March, 1977, and the analysis by Stanford Research Institute (SRI) of the data obtained with DNA Wideband satellite which was launched in May, 1976. In addition, considerable theoretical work on plasma instability and fluid turbulence has been conducted during the past year. Most of the papers resulting from such current experimental and theoretical efforts are under various stages of publication and the present review will be an appropriate forum to bring such material to the attention of the ionospheric community.

As in Paper I, we shall limit the scope of the present review to cover only the irregularity generation mechanisms and their effects on both amplitude and phase scintillation as well as VHF radar backscatter. Worldwide equatorial scintillation morphology has been adequately reviewed by Aarons (1977). Since Paper I has recently been published, we intend to deal very briefly, in Section 2, with the topics mentioned in the earlier paper. The two major experimental efforts by AFGL and SRI are described in Sections 3 and 4 and current theoretical efforts are discussed in Section 5. A brief summary is given in Section 6.

2. BRIEF REVIEW

In Paper I we pointed out that for scintillation effects in the equatorial region we are primarily interested in the properties of the disturbed equatorial ionosphere near or above the peak in electron density. This is due to the fact that scintillations are controlled by the absolute fluctuations in electron density. Thus even though equatorial irregularities originate below the F peak and result in very intense fluctuations in electron density there, the scintillation effects are modest. This has been discussed in detail by Costa and Kelley (1976) who calculated the scintillation effects of the observed plasma density profiles shown in Figure 1 and concluded that only modest scintillation would result at VHF frequencies with negligible effect at GHz frequencies. On the other hand, using topside in-situ irregularity data from Ogo-6 shown in Figure 2, Basu and Basu (1976) showed that saturated VHF scintillation and moderate GHz scintillation can be explained on the basis of large amplitude irregularities in an environment of high electron density (McClure and Hanson, 1973) distributed in thick layers as observed by radar studies (Basu et al., 1977a). Nonetheless we need to briefly review the bottomside processes since they are the origin for the high altitude disturbances.

Several mechanisms have been proposed as the initial source for the bottomside structures. The Rayleigh-Taylor gravitational instability has been invoked as an explanation for observed irregular structure of the equatorial F-region ionosphere (Dungey, 1956; Haerendel, 1974; Hudson and Kennel, 1975). The growth rate is small, however, and it is possible that some other seed mechanism might actually initiate the bottomside structure. Beer (1974), and more recently, Booker and Ferguson (1977) have strongly argued that the seat of the primary instability is in the neutral medium. Martyn (1959) and Cole (1974) have suggested that neutral winds in the E region play a role in creating F region structure. The drift instability (Hudson and Kennel, 1975) and partial reflections from the steep unperturbed gradient (Balsley and Farley, 1975) have also been invoked to explain weak bottomside spread F at short wavelengths.

Whatever the initial process, there is strong evidence that regions of low plasma density rise into the high density topside region. Evidence for this comes from rocket (Kelley et al., 1976; Morse et al., 1977), radar studies (Woodman and La Hoz, 1976), satellite (McClure et al., 1977) and indirectly from airglow observations (Weber et al., 1977). As an example consider the rocket data in Figure 1 where a "hole" in plasma density is indicated just below the F peak. Less than two minutes after the rocket passed through this low density region, a ground based 50 MHz radar detected a patch of 3 m irregularities rising rapidly from the same region. The Jicamarca radar maps showing the existence of intense regions of 3 m backscatter high above the F peak and the airglow evidence will be discussed in Section 3. Satellite data in Figure 3 taken from McClure et al., (1977) shows low density topside "holes" or

"bubbles" in which the plasma drift velocity is upward and westward with respect to the background medium. Moreover these depletions have ion composition typical of low altitude regions, that is, significant numbers of molecular and metallic ions (Hanson and Sanatani, 1973; McClure et al., 1977).

Scannapieco and Ossakow (1976) have performed computer simulations of a Rayleigh-Taylor unstable ionosphere in the collision dominated case. They showed that an initial 3 km wavelength finite amplitude sinusoidal perturbation on the bottomside eventually formed a bubble-like structure which rose into the topside such as was seen by the experimental techniques mentioned earlier. The development time of 10^4 sec determined by Scannapieco and Ossakow was considerably longer than that observed but factors not included in the simulation could act to speed up the process. First, the observed zero order vertical gradient is considerably steeper than that used in the simulation. Second, the observed bottomside structures (Kelley et al., 1976; Morse et al., 1977; see also Figure 16) are of larger amplitude than the initial perturbation used in the computer simulation and were already highly nonlinear steepened structures. Attempts at treating analytically the nonlinear Rayleigh-Taylor instability in the collisionless regime have been presented by Chaturvedi and Kaw (1975) and Hudson (1977). Further recent analytical treatment of the problem will be presented in Section 5.

With this brief review of experimental and theoretical efforts made to understand the nature of equatorial irregularities we will present various recent coordinated scintillation and irregularity studies which give us a better idea of scintillation modeling in the equatorial region.

3. AFGL EQUATORIAL IRREGULARITY CAMPAIGNS

An intensive study of nighttime electron density irregularities in the equatorial ionosphere was performed in October, 1976 and March, 1977 by conducting simultaneous radar and scintillation measurements near the magnetic dip equator in Peru. The 50 MHz radar observations were made at Jicamarca and scintillation measurements were performed at the nearby ground stations of Ancon and Huancayo by receiving VHF transmissions from geostationary and orbiting satellites. In addition, the AFGL aircraft was employed to make on board scintillation, ionosonde and airglow measurements to provide spatial configuration of irregularity patches as well as to determine the existence of density depletions indicated by in-situ measurements. The multi-station scintillation measurements were used to study the localized origin of large scale irregularity patches, their drift speed, spatial extent and lifetime in the equatorial ionosphere. The simultaneous radar and scintillation observations also provided information on the relationship between the meter and kilometer sized irregularities giving rise to the radar backscatter and VHF-UHF scintillations respectively. Much new information became available as a result of this major effort and many publications and presentations have been made based on these correlated data sets. These are summarized below with specific references.

1) There is great variability of irregularity occurrence from one night to another. On certain nights, such as on October 16-17, 1976 a single irregularity patch may evolve at a particular location and then drift eastwards for a period dictated by its lifetime as discussed by Aarons et al., 1977. Figure 2 of the paper by Basu et al., 1978 in this volume gives the irregularity configuration for this night probably the simplest that was seen during the campaign periods. On some other nights, a series of irregularity patches with a large scale quasi-periodicity is observed. A good example of such a configuration was obtained on October 19-20 as shown in Figure 4 taken from the detailed report on the October campaign done by Basu and Aarons (1977). Figure 5 also taken from the report shows the respective positions for the observations. The important point to note from the radar map kindly provided by J.P. McClure is that a relatively thin layer of bottomside irregularities appeared at 1950 LT which by 2015 developed into a plume structure extending several hundred km into the topside. A second plume developed at 2140 LT. The drifting plume structures caused severe scintillations (>20 dB) at the ground stations with periods of 4 - 6 dB scintillation caused by the bottomside structures observed in between the plumes. It is interesting to note that HF forward scatter experiments in the equatorial region had earlier obtained evidence

of irregularity patches existing in quasi-periodic patterns (Röttger, 1976). On yet other nights there were no irregularities within the 900 km E-W coverage provided by the Jicamarca radar and various satellites as shown in Figure 5.

2) Although the irregularity patches occur after local sunset, these are found to evolve either to the west or the east of any specific station signifying that local conditions rather than local time dictate the generation of irregularities (Basu and Aarons, 1977).

3) The large scale irregularity patches are found to consistently drift eastwards between 1900 - 2400 LT with a speed ranging between 90-140 m/sec. Combining the temporal variation of scintillation with the drift speed, the E-W dimensions of the patches are found to range typically between 200-400 km, although some are larger (Basu and Aarons, 1977).

4) Another important aspect of the campaign was the determination of the relationship between the relatively large scale irregularities that cause scintillation ($\sim$ km to 100 m) and the small scale irregularities that cause 50 MHz backscatter (3m). Woodman and Basu (1977) using the simultaneous backscatter and scintillation data obtained from nearly common ionospheric volume on October 29, 1976 shown in Figure 6 found that both these types co-existed in the developing phase of the irregularities. However, they showed in a quantitative manner that in view of the 8 dB scintillation at 360 MHz, backscatter echo strength of approximately 80 dB above incoherent scatter levels is expected if the commonly observed monotonic power law spectrum (Dyson et al., 1974) extends upto 3m. There is thus a discrepancy of 4 orders of magnitude between the observed 40 dB enhancement and that computed. To bring computations and observations into agreement they postulated a Gaussian type of cut-off near the O^+ ion gyroradius which is on the order of 3m in the topside ionosphere. The existence of such a cut-off can be considered to be an effective inner scale of turbulence. This point is discussed further in Section 5. Recently, Booker and Ferguson (1977) have postulated an inner scale near the ionic gyroradius to explain spread-F signatures on equatorial ionograms in the HF band and Booker and Miller (1977) have discussed the importance of the inner scale in scintillation modeling. The existence of an inner scale has interesting practical implications for pulse propagation within the ionosphere. For instance if the ionic gyroradius is considered to be the effective inner scale rather than the Debye length, computations show that pulse broadening due to scattering in the 100 - 300 MHz will be 2 orders of magnitude smaller (Yeh and Liu, 1977).

As a result of further co-located scintillation and radar observations during the March, 1977 campaign, Basu et al., (1977b) have come to the conclusion that km and m scales co-exist only during the developing phase in the early evening hours whereas later at night it is possible to have equally large km scale irregularities (as monitored by scintillation observations) without any associated backscatter. It is important to note that even L-band scintillations are possible without appreciable backscatter leading Basu et al., (1977b) to speculate that the cut-off scale length at this time is probably of the order of few tens of m. Further details and diagrams are given in paper by Basu et al., (1978) in this volume.

5) The AFGL aircraft scintillation observations have helped separate spatial and temporal behaviour of irregularities while the on-board ionosonde and optical imaging system have found evidence of electron density depletions in the bottomside F-region. Figure 7 using data kindly made available by J. Buchau shows the locus of the subionospheric point as the aircraft flew between ground stations on Oct 19-20, 1976. The thin lines signify the absence of scintillations while the thick lines signify their presence. The top panel shows that during 2247 UT (October 19) to 0015 UT (October 20), when the ground stations at Ancon and Huancayo did not record any scintillations as may be observed from Figure 4, the aircraft did not detect any irregularities in the entire latitude range of 11°S to 13°S and longitude interval of 72°W to 75°W. The bottom panel shows that from 0015 UT onwards the aircraft detected three irregularity patches with distinct boundaries indicating spatially localized irregularity generation after UT midnight (i.e., 1900 LT). The imaging system provided all-sky pictures of the 6300 Å OI airglow emission, which results from dissociative recombination of O_2^+ in the F region. Initial observations show the existence of north-south aligned regions of airglow depletion (Weber

et al., 1977). An isolated airglow depletion band observed on March 17, 1977 is modelled in Figure 8 as a troughlike bottomside electron density depletion which explains the observed airglow and ionosonde features. Further details regarding the association of the airglow depletion with scintillations and 3m backscatter are provided in the paper by Buchau et al., (1978) in this volume.

6) The scintillation data obtained from the various ground stations, in particular, spaced receiver measurements made at Ancon, and the data obtained from the AFGL aircraft as well as the Air Force Avionics Laboratory (AFAL) aircraft have been used to determine various diversity techniques to mitigate the effects of intense amplitude scintillation at 250 MHz (Whitney et al., 1977). In particular it was found that the high degree of decorrelation over a baseline of 366 m associated with rapid, severe intensity fluctuations ($S_4 \sim 1$) make space diversity techniques useful. Further details are given in paper by Whitney (1978) in this volume.

4. WIDEBAND SATELLITE OBSERVATIONS

The Wideband satellite was launched into a sun-synchronous near polar orbit on May 22, 1976 carrying a multifrequency coherent radio beacon on-board. The mutually coherent signals, which range from VHF to S-band are being recorded by SRI at ground stations in Poker Flat, Alaska and two equatorial stations, namely Ancon, Peru and Kwajalein in the Pacific sector. The second equatorial station at Kwajalein was set up to determine longitudinal differences in equatorial scintillation first pointed out by Basu et al., (1976) on the basis of in-situ irregularity data. We shall primarily discuss the equatorial data but point out certain basic differences with auroral scintillation structure that have been reported by the SRI group. The following information has been taken from Rino et al., (1977) and Fremouw et al., (1978).

1) The most important aspect of these observations has been the realization that ionospheric radio-wave propagation is dominated by large slowly varying phase scintillations. These can be large even in the absence of significant amplitude scintillations. The latter statement is particularly true for the auroral zone. Indeed, the measurement of simultaneous phase and amplitude scintillation has shown that computations of phase deviation based on the weak scatter theory using the observed amplitude scintillation would grossly underestimate the actual phase scintillation level. Based on these observations the SRI group has developed a multiplicative two-component model to characterize the joint first-order statistics of amplitude and phase. This model is discussed in detail by Fremouw et al., (1976). Briefly, the idea is to separate two components of the total (complex) scintillating signal by filtering. Because of the power-law nature of the irregularity spectrum the low frequency cut-off had to be somewhat arbitrarily defined. Thus using a double detrending process it was possible to separate a 'focus' component having fluctuations with periods between 2.5 and 10 seconds and a 'scatter' component having fluctuation periods smaller than 2.5 secs. If one considers the scan velocity of the satellite in the F-layer of 3 km/sec then the focus component can be considered to be caused by refractive focusing and defocusing by irregularities between 30 km and 7.5 km acting as lenses. The scatter component is caused by smaller irregularities comparable to and smaller than the first Fresnel zone through the diffraction process. The focus component gives rise to the large slow phase fluctuations while the scatter component causes the fast intensity fluctuations. Figure 9 taken from Fremouw et al., (1978) contains one VHF data set showing these two components obtained from each of the three latitudinal regions (initially the Wideband observations were started at Stanford, the equipment being moved to Kwajalein in October, 1976) where SRI had ground stations. It is interesting to note that for the same value of the S_4 index (a measure of the scatter component), the standard deviation of phase (a measure of the focus component) varies substantially at different locations being the smallest at the equator. Later this has been found to be a consistent feature (Fremouw, 1977) and may be of importance for irregularity generation mechanisms. For communications purposes it is important to note that in the equatorial region the scatter component displays a very Rician characteristic while that obtained at midlatitude is highly nonRician. Whitney and Basu (1977) have reported earlier a difference in the slope of the intensity spectrum between an equatorial and auroral station.

2) The SRI group has categorized scintillations qualitatively into seven groups ranging from 'extremely quiet' to 'extremely active' categories. It is interesting to note that equatorial stations provide the majority of cases in both these extreme situations as compared to the auroral station where a 'modestly active' behavior is most frequent. This equatorial scintillation behavior is probably caused by the great day-to-day variability in irregularity occurrence discussed in Section 3.

3) During extremely active conditions, scintillations are found to persist in the gigahertz range such as shown in Figure 10. The observations of GHz scintillations with a low orbiting satellite proved that weak irregularities all the way upto the plasmasphere are not necessary as suggested by Booker (1975). Indeed, Booker and Miller (1977) have recently point out that weak irregularities persisting over the entire plasma envelope cannot explain GHz scintillations for which large amplitude irregularities at the F-region peak is necessary. Basu and Basu (1976) had earlier proposed such a model on the basis of in-situ and radar data.

4) The multifrequency Wideband observations have shown that the standard deviation of phase in general shows an f^{-1} behavior even under conditions of strong diffractive scatter. Occasional violation of the law has been observed in conjunction with strong scintillations in the GHz range. Figure 11 shows the frequency dependence of phase scintillation during two 20-second periods of the pass shown in Figure 10. The L-band point has been corrected for the S-band phase perturbations which were seen to be present at the beginning of the pass. In the less disturbed interval the f^{-1} law is generally followed whereas in the more disturbed sample the VHF departs significantly and even the UHF points show some scatter. At such times the slope P of the phase spectrum also flattens with values of $P > -2$ being observed at VHF and UHF.

5) The frequency dependence of intensity scintillations observed during the same periods is shown in Figure 12. The fully developed or saturated nature of the intensity scintillations at VHF and the five UHF frequencies analyzed during the more disturbed period is apparent in the departure of these six data points from a $f^{-1.5}$ dependence (Rufenach, 1974) that holds between L band and S band. Such a reduction in frequency dependence of intensity scintillations in the multiple scatter regime had been discussed earlier by Whitney and Basu (1977) and Mullen et al., (1977). Figure 12 also shows that under extremely active conditions it is possible to have intensity decorrelation across the UHF comb of frequencies. In this regard it should be noted that during the March, 1977 AFGL campaign it was found that most Wideband passes, even those showing GHz scintillation, were not associated with 3m radar backscatter (Basu et al., 1977b). This point has been discussed in Section 3. Thus whether intensity decorrelation during the developing phase of equatorial irregularities will be still greater is not yet known.

6) The SRI group on the basis of their observations at Kwajalein (9°N geog; 8°N dip) and Ancon (11°S geog; 2°N dip) have indicated that there is a local summer maximum of equatorial scintillations. On the other hand, Ghana observations (5°N geog; 8°S dip) over a five year period show a local summer minimum (Koster, 1976) in Figure 13. We are of the opinion that there is probably a longitudinal control over equatorial scintillations with differences being observed between the Atlantic and Pacific sectors as discussed by Basu et al., (1976) rather than a seasonal control. The reason for such a longitudinal variation is yet unclear.

7) There is strong indication from simultaneous scintillation and total electron content (TEC) measurements at Ghana over a 42 month period (excluding the June solstice) that scintillations in the premidnight period are associated with a decrease in TEC (Koster, 1976). The largest TEC depletion is noted at 2100 LT a time that is closely associated with the development of plumes on radar maps. This agrees well with current theoretical ideas and in-situ observations of equatorial irregularities being associated with density depletions. It is rather interesting to note that one instance of such a "hole" with 90% TEC depletion was observed in Kwajalein in August, 1977 (Fremouw and Lansinger, 1977). The fact that such a behavior has been reported only once during a year's observation probably indicates the close relationship between density depletions and the developing stage of equatorial irregularities which the Wideband satellite because of orbital constraints is in general unable to

sample.

5. RECENT THEORETICAL RESULTS

Theoretical efforts have kept pace with the multi-technique experimental efforts described above. The successful attempt to numerically simulate the rising bubbles have been described in Section 2. These computer simulations are strongly supported by an analytic treatment due to Ott (1977) who, assuming the experimental validity of the bubble concept, calculated their shape and velocity as a function of altitude and size. At low altitudes he found that the bubbles should be cylindrical (circular cross sections and uniform along $\underline{B}$) and that they rise with the velocity

$$u = (1 - \frac{n_b}{n_o})\, g/(2\nu_{in}) \qquad (1)$$

where n_b is the density inside the bubble, n_o is the density outside, g is the gravitational constant and ν_{in} the ion neutral collision frequency. At high altitudes where ion neutral collisions can be neglected, Ott showed that the equations governing the motion are identical to the equations of two dimensional ordinary fluids (for example, a liquid constrained between two planes with separation distance much less than the size of the planes). Considerable theoretical and experimental work has already been done on such fluids and can thus be directly applied to the present problem. The observed bubble shape is shown in Figure 14 and the velocity is given by

$$u \simeq .5\,(Rg)^{1/2} \qquad (2)$$

where R is the radius of the circular 'cap'. (It should be noted that all statements concerning velocity fields or velocity turbulence can be replaced by discussions of electric fields or electrostatic turbulence since $\underline{V} = \underline{E} \times \underline{B}/B^2$).

From our previous discussions we know that an outstanding feature of equatorial spread F on the topside is the presence of large scale ($\sim$ 10 km scale) regions of low plasma density with very sharp gradients at the edges. The source of energy for this interchange of low and high density plasma is the excess gravitational potential energy which resides in the F region plasma supported against gravity by the magnetic field. From a plasma physics standpoint the zero upward density gradient is disrupted by the electrostatic fields in the instability process. The second most important feature of equatorial spread F is the wide range of wavelengths exhibited by spread F irregularities as discussed in Sections 3 and 4. For instance, the 3 m scalelength is 3-4 orders of magnitude smaller than the primary process described above. Two processes have been recently suggested which may well accunt both for the wide range of wavelengths as well as the extended spatial extent of spread F.

Costa and Kelley (1978a,b) have considered the steep gradients in plasma density associated with bottomside irregularities (see Figure 16) and presumably also with topside bubbles, and have shown that drift waves should grow rapidly on the observed gradients. The normalized growth rate is plotted in Figure 15 as a function of the parameter $b = k_\perp^2 \rho_i^2/2$ where $k_\perp$ is the wavenumber perpendicular to $\underline{B}$ and ρ_i is the ion gyroradius. For reference, b at the Jicamarca backscatter wavelength is 100. The growth rate peaks at $k_\perp \rho_i = 1.5$ which corresponds to wavelengths of about 20 m. The growth rate is linearly proportional to the gradient scale length, L, at the bubble edge and is 1 sec^{-1} for L = 125 m under typical ionospheric conditions. These drift waves should not only contribute to backscatter but play a role in the eventual merging of bubbles into the background (via destruction of the steep gradient).

A second and perhaps more important process from the standpoint of scintillations is the generation of a thick irregularity layer as suggested by Kelley and Ott (1978). Again use was made of Ott's results that in the collisionless case the equations of motion are identical to a two dimensional fluid. In the fluid case, the upward buoyancy force is balanced by emission of vortices in the background fluid. This injects velocity turbulence into the background fluid in a wake which trails behind the bubble. In the plasma case each vortex corresponds to a line charge surrounded by a circular $\underline{E}\underline{x}\underline{B}$ drift of the plasma. Since there is a background density gradient this vortex will create density irregularities with the same scale size as the velocity turbulence.

Numerous theoretical studies of turbulence in two dimensional fluids (Kraichnan, 1967; Lilly, 1969) have shown that velocity injected into such a fluid at some characteristic wave number k_o will cascade to wavenumbers both higher and lower than k_o. In the space domain this 'inverse cascade' to lower k implies that the velocity

(and density) turbulence will spread into the largest volume available in the system. Evidence for this dual cascade in two dimensional turbulence has been found in the Earth's atmosphere (Kao and Wendell, 1970) and magnetosphere (Kelley and Kintner, 1978).

Kelley and Ott (1978) suggest that the vortices emitted by upwelling bubbles not only form the wake but tend to fill the between bubble regions (i.e., in an E-W direction) with velocity and density irregularities via this cascade to lower k values. Cascade to higher k also occurs with the ultimate spectral cutoff occurring at some large wavenumber where ion viscosity plays a role. This dissipation is most effective near the ion gyroradius and hence it seems likely that the 3 m scale (Jicamarca backscatter) lies in the dissipative subrange. Such a 'cutoff' in the amplitude of irregularities at short wavelengths was postulated by Woodman and Basu (1977) as discussed in Section 3.

In the intermediate range of wavenumbers $L_s^{-1} < k < L_d^{-1}$, where L_s is the stirring length (bubble size) and L_d is the dissipation scale, Kelley and Ott (1978) predicted a k^{-3} spectrum for velocity or electric field fluctuations and a k^{-1} spectrum for density irregularities. This seems in contradiction to numerous reports of one dimensional k^{-2} density spectrum associated with equatorial spread F. However, Costa and Kelley (1978a) have shown that at least in the case of bottomside non-linear structures, the k^{-2} spectrum is due to the steep edges in density encountered. Several examples of the steep edges are clear in the data presented in the top panel of Figure 16, obtained during the passage of a sounding rocket through bottomside spread F. The relative density ($\delta n/n$) is plotted for an 8 second interval ($\sim$ 16 km along trajectory). As an illustration of the steep edge effect, Costa and Kelley (1978a) performed a fourier transform of the data in panel 1, then randomized the phase in each fourier component and reassembled the data in the time domain. Two such random phase runs were made and are plotted in the lower two panels. The power spectrum of all three sets of data is identical and varies as f^{-2} over most of the spectrum,

It is interesting to note that R. F. Woodman (private communication, 1976) had first suggested a phase coherence test as a way of distinguishing between the dominance of steep structures or turbulence in equatorial spread -F. More recently Chaturvedi and Ossakow (1977) have considered the non-linear development of bottomside spread -F. They conclude that steepened structures should evolve in time and in fact a k^{-2} spectrum would result due to the steep edges. They also suggested a phase coherence test to distinguish between such process and a turbulence like mechanism proposed earlier by Chaturvedi and Kaw (1976). The results of Costa and Kelley (1978a) described above seem to agree with the sharp edge hypothesis.

6. SUMMARY

The following picture evolves from the discussion above. Bottomside spread-F occurs in a widespread region (at least $\pm 10°$ latitude) centered on the magnetic equator in the post sunset hours. Some of the resulting low density regions rise into the topside leaving being a trail of counter rotating vortices which mix the background density gradient and create irregularities in density. Since the whole flux tubes partake in this upwelling a two dimensional bubble originating anywhere in this latitude range will have effects in the topside. The dual cascade of velocity turbulence tends to fill the E-W region between bubbles with both velocity and density irregularities. The density gradients in the bubbles themselves will eventually dissipate possibly via the "universal" drift wave instability.

Radio waves incident upon the equatorial ionosphere under these conditions are thus subject to at least three different types of scintillating environment: 1. Just after sunset during the development phase, the bottomside irregularitiies cause modest amplitude scintillation effects due to the low absolute fluctuations in electron density. It is not known whether large phase fluctuations accompany such weak amplitude scintillations as the Wideband satellite does not have equatorial crossings at this time. 2. In the fully developed stage bubbles are continually emitted into the topside over a wide range of latitudes. These bubbles continually stir the medium at wavelengths comparable to the bubble dimensions ($\sim$10km). Two dimensional dual cascade spreads the velocity and density irregularities to larger and smaller k values. The cascade to smaller k combined with the vertical wake formation tends to fill a large volume with density irregularities. Incident radio waves thus are subject to sharp discontinuities in electron

density in the bubbles as well as very thick (in altitude) regions of power law type density irregularities. Very intense amplitude scintillations have been observed during such times as discussed in Section 3 and it is expected that large phase fluctuations will also be present. 3. In the decay phase (later local time) the velocity turbulence injected by the bubbles as well as the bubble gradients themselves decay via dissipation at large k. In this phase the dissipation scale moves to smaller k values (Kelley and Ott, 1978) so the smallest scale structures disappear first. Thus significant kilometer scale structures will still exist in the medium and strongly affect scintillation even though backscatter measurements become less intense. This is probably the phase of irregularity evolution most often sampled by the Wideband satellite as discussed by Basu et al., (1977b). However these authors have pointed out that they are as yet unable to conclude in a definitive manner, whether these non-backscatter associated irregularities are drifting 'fossil' structures of irregularities generated after sunset or freshly generated structures appearing later in the evening having little or no power at 3m scalelength.

It has to be pointed out that two-dimensional models of irregularity bubbles do not explain why density depletions are observed to rise more frequently than enhancements fall (Hudson, 1977). G. Haerendel (private communication, 1977) has noted that density enhancements may be tied to the E-region, whereas density depletions are free to interchange and drift up. Alternatively, McClure et al., (1977) have suggested that density enhancements may spread out over a broader E-W extent than depletions, thereby producing a smaller relative enhancement. More extensive experiments are required during which both velocity and density irregularities are measured simultaneously as a function of k to solve the three-dimensional problem. Electric field measurements of the velocity fields are easier to perform on technical grounds and are equivalent since $\underline{V} = \underline{E} \times \underline{B}/B^2$.

From the scintillation point of view, it would be highly desirable to have a geostationary satellite with the capabilities of the present Wideband one to monitor the focus and scatter components during the developing phase of irregularities. Such measurements in conjunction with the Jicamarca radar observations would provide valuable information on spectral characterisitics of equatorial irregularities. The finding of Costa and Kelley (1978a) and Chaturvedi and Ossakow (1977) regarding steepened bottomside structures and the associated k^{-2} spectrum is an important one. It is thus quite crucial to determine whether steepened structures also dominate topside irregularity behavior. This may have far-reaching implications in scintillation modeling.

ACKNOWLEDGMENTS

Numerous people have contributed to the development of the ideas expounded in this paper and it is hoped that the reference list adequately recognizes their contribution. We also thank the various authors who made their diagrams available to us for reproduction. We wish to thank Santimay Basu for many helpful comments and a careful reading of the manuscript. The AFGL equatorial irregularity campaigns were conducted under the guidance of J. Aarons to whom Sunanda Basu is indebted for many constructive suggestions. She extends her thanks to the National Research Council for the award of an Associateship. M.C. Kelley acknowledges helpful discussions with E. Costa and D.T. Farley. The work at Cornell University was sponsored by ONR under N00014-75-C-0780.

REFERENCES

Aarons, J., Equatorial scintillations: A review, IEEE Trans. Ant. & Propagat. AP 25, 729, 1977.

Aarons, J., J. Buchau, Santimay Basu and J.P. McClure. The localized origin of equatorial F-region irregularity patches, J. Geophys. Res., in press, 1977.

Balsley, B.B. and D.T. Farley, Partial reflections: A source of weak VHF equatorial spread-F echoes, J. Geophys. Res, 80, 4735, 1975.

Basu, Sunanda and Santimay Basu, Correlated maesurements of scintillations and in -situ F-region irregularites from Ogo-6, Geophys. Res. Lett., 3, 681, 1976.

Basu, Sunanda, Santimay Basu and B.K. Khan, Model of equatorial scintillations from in -situ measurements, Radio Sci., 11, 821, 1976.

Basu, Sunanda and M.C. Kelley, Review of equatorial scintillation phenomena in the light of recent developments in the theory and measurement of equatorial irregularities, J. Atmos. Terr. Phys., 39 (9), 1977.

Basu, Sunanda, J. Aarons, J.P. McClure, C. LaHoz, A. Bushby and R.F. Wood-, man, Preliminary comparisons of VHF radar maps of F-region irregularities with scintillations in the equatorial region, J. Atmos. Terr. Phys., 39(9), 1977a.

Basu, Santimay and J. Aarons, Equatorial irregualrity campaigns: Part I, Correlated scintillation and radar backscatter measurements in October, 1976 Air Force Geophysics Laboratory Technical Report, under preparation, 1977.

Basu, Santimay, Sunanda Basu, J. Aarons, J.P. McClure and M.D. Cousins, On the coexistence of km and m scale irregularities in the nighttime equatorial F-region, Submitted to J. Geophys. Res., 1977b.

Basu, Santimay, H. Whitney, J. Aarons, J.P. McClure, Large and small scale properties of nighttime equatorial irregularities from scintillations and radar backscatter measurements, presented at the Symposium on "The Effect of the Ionosphere on Space and Terrestrial Systems", Washington, D.C., Jan. 24-26, 1978.

Beer, T., On the dynamics of equatorial spread-F, Aust. J. Phys., 27, 391, 1974.

Booker, H.G. and H.W. Wells, Scattering of radio waves by the F-region of the ionosphere, Terres. Magn., 43, 249, 1938.

Booker, H.G., The role of the magnet-osphere in satellite and radio-star scintillation, J. Atmos, Terr. Phys., 37, 1089, 1975.

Booker, H.G. and J.A. Ferguson, A theoretical model for equatorial ionospheric spread-F echoes in the HF and VHF bands, Submitted to J. Atmos. Terr. Phys., 1977.

Booker, H.G. and D.C. Miller, A theoretical model for iono-spheric scintillation caused by weak irregularities of ioniza-tion density, Submitted to Radio Science, 1977.

Briggs,B. H. and I. A. Parkin, On the variation of radio star and sat-ellite scintillation with zenith angle, J. Atmos. Terr. Phys., 25, 339, 1963.

Buchau, J., E.J. Weber and J.P. McClure, Radio and optical diagnostics applied to an isolated equatorial scintillation event, presented at the Symposium on "The Effect of the Ionosphere on Space and Terrestrial Systems", Washington, D.C., Jan. 24-26, 1978.

Chaturvedi, P.K. and P.K. Kaw, Steady state finite amplitude Rayleigh Taylor modes in Spread-F, Geophys. Res. Lett., 2, 381, 1975.

Chaturvedi, P.K. and P.K. Kaw, An inter-pretation for the power spectrum of spread-F irregularities, J. Geophys. Res., 81, 3257, 1976.

Chaturvedi, P.K. and S.L. Ossakow, Nonlinear theory of the collisional Rayleigh-Taylor instability in equatorial spread-F, NRL Report 3604, Naval Research Laboratory, Washington, D.C. August, 1977.

Cole, K.D., Energetics of and a source of energy for equatorial spread-F events, J. Atmos. Terr. Phys., 36, 1099, 1974.

Costa, E. and M.C. Kelley, Calculations of equatorial scintillations at VHF and gigahertz frequencies based on a new model of the disturbed equatorial ionosphere, Geophys. Res. Lett., 3, 677, 1976.

Costa, E. and M.C. Kelley, Ionospheric scintillations based on in situ irregularity spectra, Radio Sci., 12, 797, 1977.

Costa, E. and M.C. Kelley, Evidence for and development of a 2-step theory for equatorial spread-F, submitted to J. Geophys. Res., 1978a.

Costa, E. and M.C. Kelley, Linear theory for collisionless drift mode waves with wavelengths near the ion gyro-radius, Submitted to J. Geophys. Res., 1978b.

Dungey, J.W., Convective diffusion in the equatorial F-region, J. Atmos. Terr. Phys., 9, 304, 1956.

Dyson, P.L., J.P. McClure and W.B. Hanson, In-situ measurements of the spectral characteristics of ionospheric irregularities, J. Geophys. Res., 79, 1497, 1974.

Fremouw, E.J., C.L. Rino and R.C. Livingston, "A two-component model for scintillation," in Proc. Symp. Cospar Satellite Beacon Group, June 1-4, 1976, Boston University, Boston, MA., 1976.

Fremouw, E.J., Examination of data from the Wideband Satellite experiment, Report PD-N-77-118-R01, Physical Dynamics, Inc., Seattle, Washington 98109, August 1, 1977.

Fremouw, E.J. and J.M. Lansinger, Examination of data from the Wideband Satellite experiment, Report PD-NW-118-R02, Physical Dynamics, Inc., Seattle, Washington 98109, October 15, 1977.

Fremouw, E.J., B.C. Fair, R.T. Tsunoda, R.A. Long and A.A. Burns, Design considerations for a microwave scintillation experiment, Report DNA 4092F, Stanford Research Institue, Menlo Park, CA 94025, March 15, 1977.

Fremouw, E.J., R.L. Leadabrand, R.C. Livingston, M.D. Cousins, C.L. Rino, B.C. Fair and R.A. Long, Early results from the DNA Wideband satellite experiment-complex signal scintillation, Radio Sci., 13 (1), 1978.

Haerendel, G., Theory of equatorial spread-F, preprint, Max-Planck-Institut fur Physik und Astrophysik, Garching, West Germany, 1974.

Hanson, W.B. and S. Sanatani, Large Ni gradients below the equatorial F peak, J. Geophys. Res., 78, 1167, 1973.

Hudson, M.K. and C.F. Kennel, Linear theory of equatorial spread-F, J. Geophys. Res., 80, 4581, 1975.

Hudson, M.K., Spread-F bubbles: Nonlinear Rayleigh-Taylor mode in two dimensions, preprint, University of California, Berkeley, CA 94720, January, 1977.

Kao, S.K. and L.L. Wendell, The kinetic energy of the large scale atmosphere motion in wavenumber frequency space, J. Atmos. Sci., 27, 359, 1970.

Kelley, M.C., G. Haerendel, H. Kappler, A. Valenzuela, B.B. Balsley, D.A. Carter, W.L. Ecklund, C.W. Carlson, B. Hausler and R. Torbert, Evidence for a Rayleigh-Taylor type instability and upwelling of depleted density regions during equatorial spread-F, Geophys. Res. Lett., 3, 448, 1976.

Kelley, M.C. and P.M. Kintner, Evidence for two-dimensional inertial turbulence in a cosmic scale low β plasma, Astrophys. J., in press, 1978.

Kelley, M.C. and E. Ott, On the role of two-dimensional turbulence in equatorial spread-F, submitted to J. Geophys. Res., 1978.

Koster, J.R., Study of the equatorial ionosphere, Report AFGL-TR77-0165, University of Ghana, Legon, Ghana, November, 1976.

Kraichnan, R.H., Inertial ranges in two-dimensional turbulence, Phys. Fluids, 10, 1417, 1967.

Lilly, D.K., Numerical simulation of two-dimensional turbulence, Phys. Fluids, Supplement II, II-240, 1969.

Martyn, D.F., Large-scale movements of ionization in the ionosphere, J. Geophys. Res., 64, 2178, 1959.

McClure, J.P. and W.B. Hanson, A catalog of ionospheric F-region irregularity behavior based on Ogo-6 retarding potential analyzer data, J. Geophys. Res., 78, 7431, 1973.

McClure, J.P., W.B. Hanson and J.H. Hoffman, Plasma bubbles and irregularities in the equatorial ionosphere, J. Geophys. Res., 82, 2650, 1977.

Morse, F.A., B.C. Edgar, H.C. Koons, C.J. Rice, W.J. Heikkila, J.H. Hoffman, B.A. Tinsley, J.D. Winningham, A.B. Christensen, R.F. Woodman, J. Pomalaza and N.R. Teixeira, Equion: An ionospheric irregularity experiment, J. Geophys. Res., 82, 578, 1977.

Mullen, J.P., H.E. Whitney, Santimay Basu, A. Bushby, J. Lanat and J. Pantoja, Statistics of VHF and L band scintillation at Huancayo, Peru, J. Atmos. Terr. Phys., 39(9), 1977.

Ott, E., Theory of Rayleigh-Taylor bubbles in the equatorial ionosphere, submitted to J. Geophys. Res., 1977.

Rino, C.L., E.J. Fremouw, R.C. Livingston, M.D. Cousins and B.C. Fair, Wideband satellite observations, Report DNA4399F, SRI International, Menlo Park, Calif. 94025, June, 1977.

Röttger, J., The macroscale structure of equatorial irregularities, J. Atmos. Terr. Phys., 38, 97, 1976.

Rufenach, C.L., Wavelength dependence of radio scintillation: Ionosphere and interplanetary irregularities, J. Geophys. Res., 79, 1562, 1974.

Rufenach, C.L., Ionospheric scintillation by a random phase screen: Spectral approach, Radio Sci., 10, 155, 1975.

Scannapieco, A.J. and S.L. Ossakow, Nonlinear equatorial spread-F, Geophys. Res. Lett., 3, 451, 1976.

Weber, E.J., J. Buchau, R.H. Eather and S.B. Mende, North/south aligned equatorial airglow depletions, J. Geophys. Res. (in press), 1977.

Whitney, H.E. and Santimay Basu, The effect of ionospheric scintillation on VHF/UHF satellite communications, Radio Sci., 12, 123, 1977.

Whitney, H.E., J.P. Mullen, J. Buchau, E.J. Weber and A. Johnson, Report on Peru scintillation tests, October 1976 and March, 1977, AFGL Technical Report, under preparation, 1977.

Whitney, H.E., Spaced receiver measurements of intense equatorial scintillations, presented at the Symposium on "The Effect of the Ionosphere on Space and Terrestrial Systems", Washington, D.C., Jan. 24-26, 1978.

Woodman, R.F. and C. LaHoz, Radar observations of F-region equatorial irregularities, J. Geophys. Res., 81, 5447, 1976.

Woodman, R.F. and Sunanda Basu, Comparison between in-situ spectral measurements of equatorial F-region irregularities and backscatter observations at 3m wavelength (abstract), EOS Trans. AGU, 58, 49, 1977, submitted to Geophys. Res. Lett., 1977.

Yeh, K.C. and C.H. Liu, Pulse delay and pulse distortion by random scattering in the ionosphere, presented at AGARD Meeting, Cambridge, MA, Oct. 3-7, 1977.

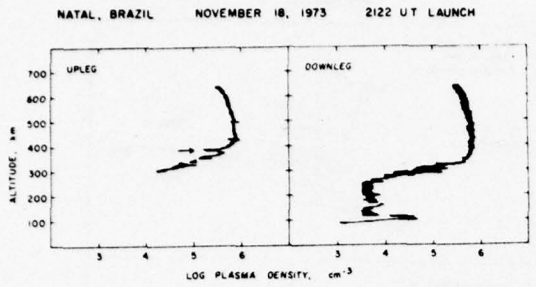


Fig. 1. Upleg and downleg plasma density profiles obtained on a sounding rocket during equatorial spread-F. The arrow shows the location of a deep depression in plasma density (after Kelley et al., 1976).

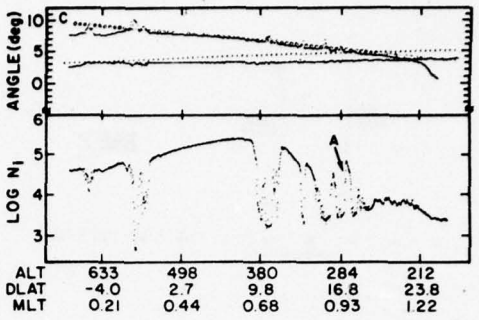


Fig. 3. Ion drift meter data from AE-C orbit 2282. The observed pitch and yaw angles are shown in the upper and lower curves of the top panel and the total density on the bottom. Positive angles correspond to ions moving up or left with respect to spacecraft (after McClure et al., 1977).

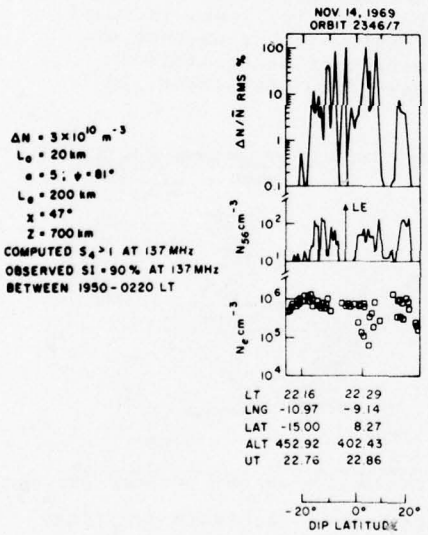


Fig. 2. Ogo-6 orbit in Legon, Ghana longitude sector during a strong VHF scintillation event. The scintillation model parameters are also indicated (after Basu and Basu, 1976).

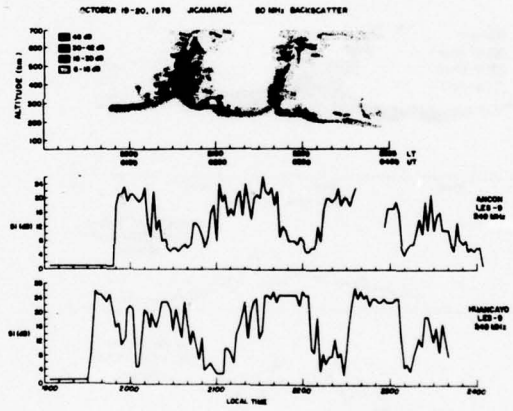


Fig. 4. Temporal variation of the 50 MHz radar backscatter observed at Jicamarca and scintillation index, SI(dB), of the 249 MHz transmissions from LES-9 satellite recorded at Ancon and Huancayo on October 19-20, 1976 (after Basu and Aarons, 1977).

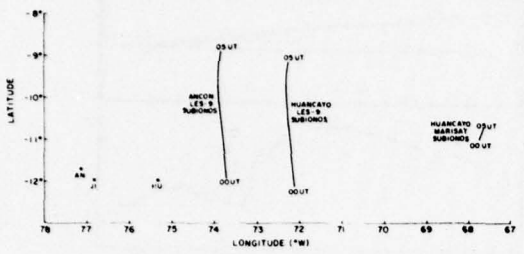


Fig. 5. The geometry of radar backscatter and scintillation measurements during AFGL equatorial campaign in October, 1976. The ground locations for various observatories and subionospheric (400 km) locations for LES-9 are shown (after Basu and Aarons, 1977).

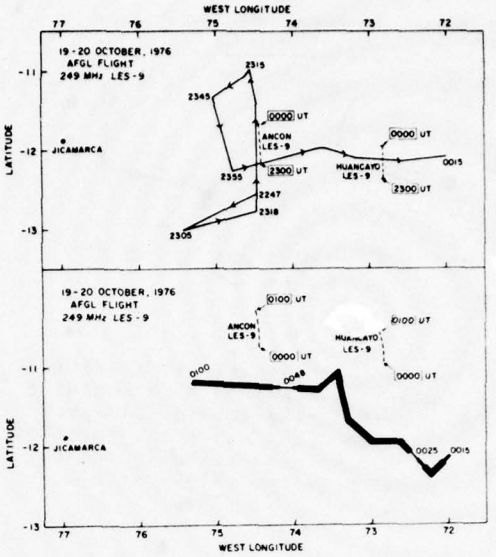


Fig. 7. Subionospheric flight path of the AFGL aircraft making 249 MHz scintillation observations with LES-9 on October 19-20, 1976. Thin and thick lines indicate respectively the absence or presence of scintillations (after Basu and Aarons, 1977).

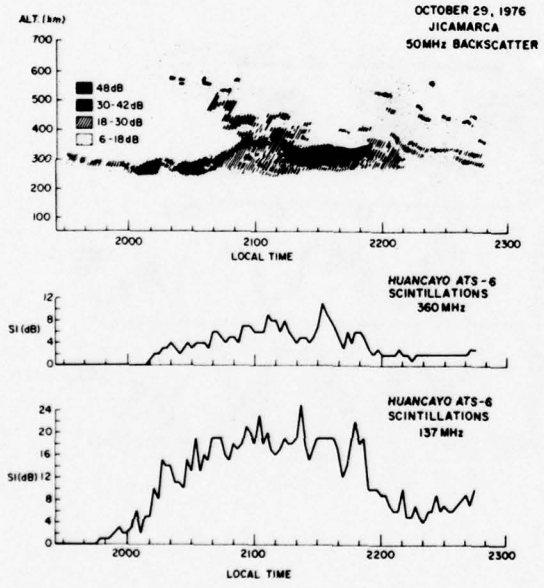


Fig. 6. Comparison of backscattered power map from Jicamarca and ATS-6 scintillation data corresponding to a nearly common ionospheric volume on October 29-30, 1976 (after Woodman and Basu, 1977).

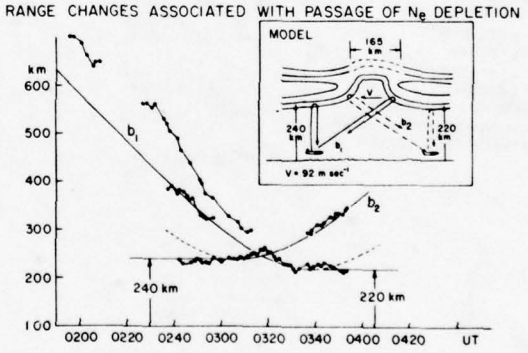


Fig. 8. Model of an eastward drifting, bottomside N_e depletion based on observed ionosonde and airglow parameters. The measured ranges of oblique returns and the virtual height of overhead F-region are compared with range/height changes expected from the passage of the model bottomside structure over the ionosonde (after Weber et al., 1977).

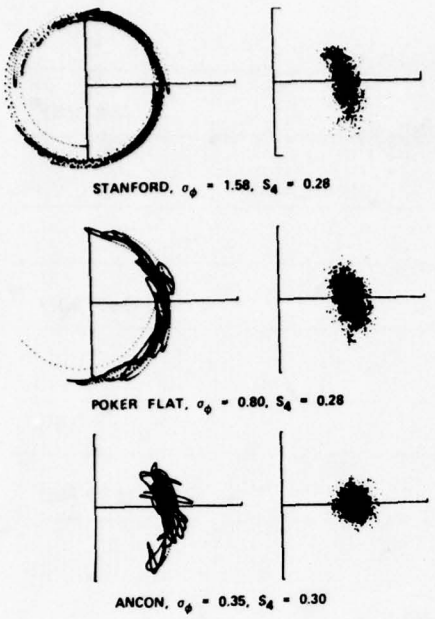


Fig. 9. Scatter diagrams for the focus (left) and scatter (right) components isolated from segments of VHF records obtained at a midlatitude (top), auroral (center) and equatorial (bottom) station (after Fremouw et al., 1978).

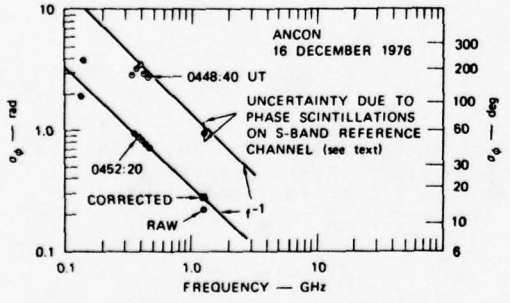


Fig. 11. Frequency dependence of phase-scintillation index during two 20-second periods of pass shown in Figure 10, compared with an f^{-1} dependence arbitrarily passed through the 413 MHz data point (after Fremouw et al., 1978).

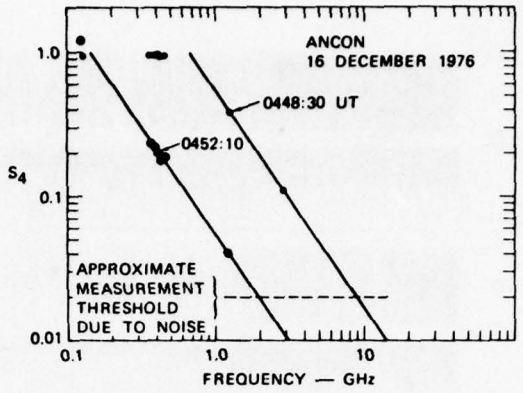


Fig. 12. Frequency dependence of intensity-scintillation index during two 20-second periods of the pass shown in Figure 10, compared with an $f^{-1.5}$ dependence (after Fremouw et al., 1978).

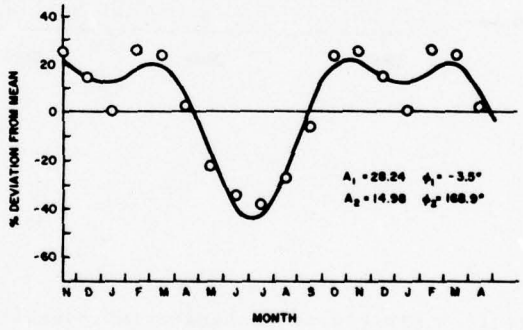


Fig. 13. Seasonal variation of 136 MHz scintillation from ATS-3 at Legon, Ghana during the period Sept. 71 to Dec. 75. Note that the annual component (with a minimum in the June solstice) has twice the amplitude of the semi-annual component (after Koster, 1976).

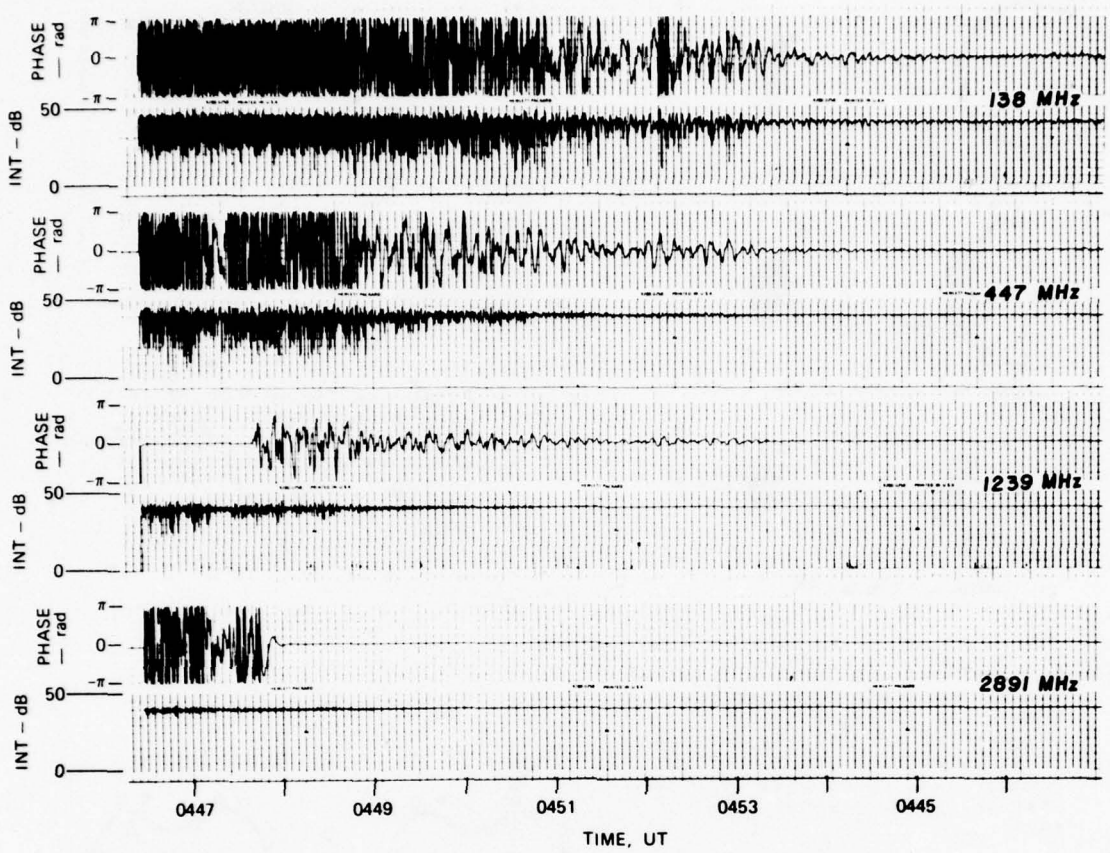


Fig. 10. Example of an equatorial Wideband pass at Ancon on December 16, 1976 showing phase and intensity scintillations at VHF, UHF, L band and S band. Note change of phase reference from L band to S band just before 0448 UT (after Fremouw et al., 1977).

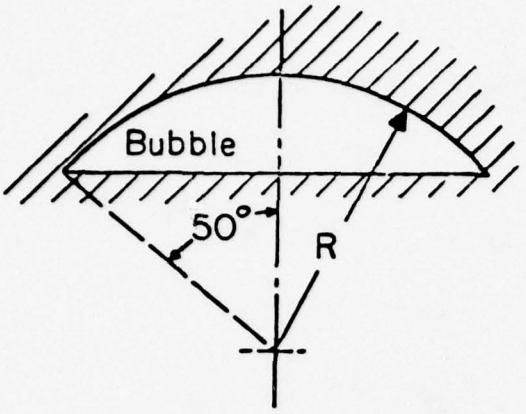


Fig. 14. Shape of bubbles in fluids (after Ott, 1977).

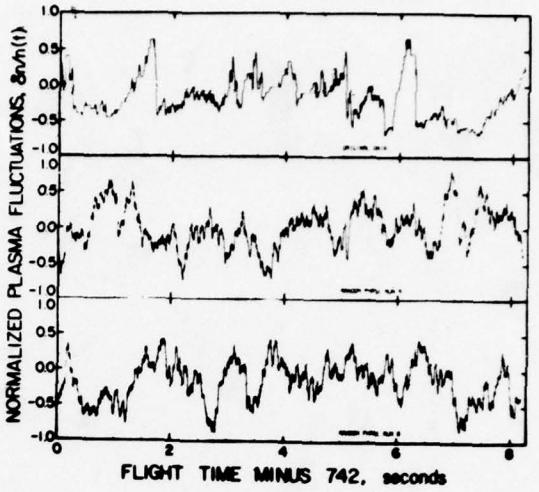


Fig. 16. The upper plot is a detrended data stream obtained on the bottomside of the F-peak during equatorial spread-F. The lower two plots are reconstructed time domain samples using the same data, but with the addition of a random phase in the FFT before reconstruction (after Costa and Kelley, 1978a).

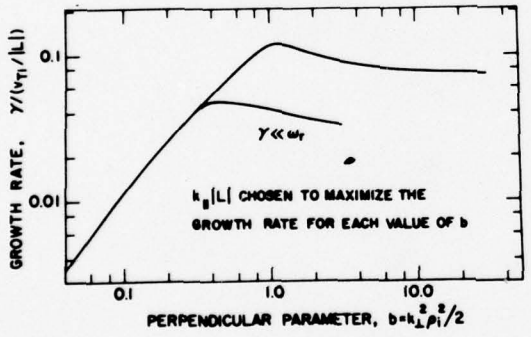


Fig. 15. Growth rate γ as function of the parameter b. The curve labeled $\gamma << \omega_r$ is obtained from the 'small growth rate' expression while the unlabeled curve is obtained from the 'generalized' expressions (after Costa and Kelley, 1978b).

LARGE AND SMALL SCALE PROPERTIES OF NIGHTTIME EQUATORIAL IRREGULARITIES FROM SCINTILLATIONS AND RADAR BACKSCATTER MEASUREMENTS

Santimay Basu
Emmanuel College
Boston, MA 02115

H. Whitney and J. Aarons
Air Force Geophysics Laboratory
Hanscom AFB, MA 01731

J.P. McClure
University of Texas at Dallas
Richardson, TX 74080

INTRODUCTION

The nighttime F-region irregularities of electron density at equatorial latitudes have been studied for several decades by observing the spread-F signature in ionograms and scintillations in transionospheric communication links (Booker and Wells, 1938; Aarons et al., 1971; Skinner and Kelleher, 1971). In recent years, these studies have been supplemented by a variety of new and powerful experimental techniques, such as, in-situ measurements by rockets and satellites, HF forward scatter and VHF radar backscatter measurements (Farley et al., 1970; Dyson et al., 1974; Kelley et al., 1976; Röttger, 1976; Woodman and LaHoz, 1976; McClure et al., 1977). These experimental investigations have been supported by computer simulations and analytic work on the formation of equatorial irregularities (Scannapieco and Ossakow, 1976; Haerendel, 1974; Hudson and Kennel, 1975).

Basu and Kelley (1977) have reviewed the recent advances in our knowledge of equatorial irregularities but point out that some of the basic questions remain unresolved. For example, it has not been established if the generation of nighttime irregularities is related to the passage of the terminator (or sunset line) or to the existence of suitable conditions in certain spatial locations. The nighttime equatorial irregularities also exhibit a marked day-to-day variability; a night indicating the presence of strong irregularities may be followed by another without any irregularities within the detectable limit. The question of co-existence of large and small scale irregularities also remains unexplored. Nevertheless, it has important implications in regard to the irregularity power spectrum and hence of importance in communications channel modelling and the development of theories of irregularity generation.

In order to explore some of these unresolved questions, we performed simultaneous VHF radar backscatter and scintillation measurements near the magnetic equator during October, 1976 and March, 1977 (Basu and Aarons, 1977). The 50 MHz radar backscatter measurements were performed at Jicamarca, Peru (11.97°S, 76.86°W) and scintillation measurements were made at two nearby ground stations Ancon (11.7°S, 77.15°W) and Huancayo (11.97°S, 75.34°W). The VHF-UHF scintillations are sensitive to irregularities within the scale length range of about one kilometer to a hundred meter whereas the 50 MHz radar backscatter is caused by 3 meter irregularities. Thus simultaneous radar and scintillation measurements allowed a study of irregularity development over a three decade range of scale lengths. The scintillation measurements made at the two stations with various geostationary satellites made it possible to track the irregularity patches and thereby determine their drift and lifetime.

RESULTS AND DISCUSSIONS

Figure 1 shows the results of simultaneous 50 MHz radar backscatter observations performed at Jicamarca and scintillation measurements made at Huancayo with the 137 and 360 MHz transmissions from ATS-6 satellite on October 29. 1976. During the October period, the ATS-6 satellite was being moved to its new location and on the night of October 29, 1976, the 400 km intersection point from the satellite to Huancayo was only 30 km to the east of the ionospheric volume illuminated by the radar beam. The top panel of Figure 1 exhibits the backscattered power map. This map has been redrawn from the original digital power map which is difficult to reproduce. The radar map shows the temporal variation of the range of backscattering region and the strength of the echo power in decibels above the approximate maximum incoherent scatter level. A description of the digital power mapping technique has been outlined in Woodman and LaHoz (1976). The second and third panels represent the temporal variation of scintillation index, SI(dB), as recorded at 360 and 137 MHz respectively. It may be noted that the radar backscatter and scintillation measurements are very well correlated. The onset of scintillations at 20 LT is coincident with the radar detecting moderately strong (18-30 dB) irregularities in a thin layer. Later, the intensity of 137 MHz scintillations attained saturated levels when the 3 m irregularity layer thickened. The measurements indicate that, in the early evening period, the 3 meter irregularities detected by the radar co-existed with large scale irregularities (1 km - 100 m) causing scintillations over a nearly common ionospheric volume. Woodman and Basu (1977) have made a quantitative comparison of the backscattered power level and 360 MHz scintillation level indicated in Figure 1 and found that a monotonic power law form of the 3-dimensional irregularity power spectrum with spectral index 4 cannot explain the backscatter observations. The in-situ irregularity data suggested such a spectra between scale lengths of several kilometers to tens of meters. These authors have indicated that a sharper roll-off of the irregularity power spectrum at irregularity scale lengths of several meters due to finite ion gyro-radius can explain the observations.

Figure 2 shows the radar and scintillation measurements performed on October 16-17, 1976. The top panel shows the 50 MHz radar backscattered power map. The second panel shows the temporal variation of scintillation recorded at Ancon by receiving the 249 MHz transmissions from LES-9 satellite. The 400-km intersection of Ancon scintillation observations was located at a distance of 350 km to the east of Jicamarca radar observations. The third panel illustrates the results of 249 MHz scintillation measurements made at Huancayo. The 400 km intersection of Huancayo measurements was located 175 km to the east of the ionospheric location probed by the Ancon measurements. In contrast to the measurements presented in Figure 1, the different panels of Figure 2 represent observations at different locations. From Figure 2, it may be observed that the Jicamarca radar exploring the westernmost location first detected the 3 meter irregularities as early as 19 LT but an extended irregularity structure termed as 'plume' evolved later at 1950 LT. The panel 2 of the figure shows that the onset of scintillations at Ancon occurred at about 2050 LT. Considering that the plume structure drifted towards east and traversed 350 km distance to cause the onset of Ancon scintillation, an eastward drift speed of 97 m/sec is obtained. From panel 3, it is found that the sharp onset of strong scintillations at Huancayo was delayed from that at Ancon by about 25 minutes. This delay is again consistent with a drift speed of about 116 m/sec. Thus the results illustrated in Figure 2 shows that an irregularity structure evolved first in the west possibly due to the existence of suitable background conditions and the structure drifted eastwards at a speed of approximately 100 m/sec to cause delayed onsets of scintillations on two propagation paths (Aarons et al., 1977). Considering the onset time of plume structure at Jicamarca and decay of scintillations at Huancayo a total lifetime of at least 3 hours for the irregularity structure is obtained.

The results of October 16, 1976 and October 29, 1976, indicated that large scale irregularities ($\sim$1 km - .1 km) co-existed with 3 m irregularities. The above fact did not, however, hold in all cases. It was found that scintillation measurements detected larger number of irregularity patches than did the radar. In Figure 3, we illustrate the radar maps, in schematic form, and results of scintillation measurements performed at Ancon and Huancayo, on seven nights in

RESULTS AND DISCUSSIONS

Figure 1 shows the results of simultaneous 50 MHz radar backscatter observations performed at Jicamarca and scintillation measurements made at Huancayo with the 137 and 360 MHz transmissions from ATS-6 satellite on October 29. 1976. During the October period, the ATS-6 satellite was being moved to its new location and on the night of October 29, 1976, the 400 km intersection point from the satellite to Huancayo was only 30 km to the east of the ionospheric volume illuminated by the radar beam. The top panel of Figure 1 exhibits the backscattered power map. This map has been redrawn from the original digital power map which is difficult to reproduce. The radar map shows the temporal variation of the range of backscattering region and the strength of the echo power in decibels above the approximate maximum incoherent scatter level. A description of the digital power mapping technique has been outlined in Woodman and LaHoz (1976). The second and third panels represent the temporal variation of scintillation index, SI(dB), as recorded at 360 and 137 MHz respectively. It may be noted that the radar backscatter and scintillation measurements are very well correlated. The onset of scintillations at 20 LT is coincident with the radar detecting moderately strong (18-30 dB) irregularities in a thin layer. Later, the intensity of 137 MHz scintillations attained saturated levels when the 3 m irregularity layer thickened. The measurements indicate that, in the early evening period, the 3 meter irregularities detected by the radar co-existed with large scale irregularities (1 km - 100 m) causing scintillations over a nearly common ionospheric volume. Woodman and Basu (1977) have made a quantitative comparison of the backscattered power level and 360 MHz scintillation level indicated in Figure 1 and found that a monotonic power law form of the 3-dimensional irregularity power spectrum with spectral index 4 cannot explain the backscatter observations. The in-situ irregularity data suggested such a spectra between scale lengths of several kilometers to tens of meters. These authors have indicated that a sharper roll-off of the irregularity power spectrum at irregularity scale lengths of several meters due to finite ion gyro-radius can explain the observations.

Figure 2 shows the radar and scintillation measurements performed on October 16-17, 1976. The top panel shows the 50 MHz radar backscattered power map. The second panel shows the temporal variation of scintillation recorded at Ancon by receiving the 249 MHz transmissions from LES-9 satellite. The 400-km intersection of Ancon scintillation observations was located at a distance of 350 km to the east of Jicamarca radar observations. The third panel illustrates the results of 249 MHz scintillation measurements made at Huancayo. The 400 km intersection of Huancayo measurements was located 175 km to the east of the ionospheric location probed by the Ancon measurements. In contrast to the measurements presented in Figure 1, the different panels of Figure 2 represent observations at different locations. From Figure 2, it may be observed that the Jicamarca radar exploring the westernmost location first detected the 3 meter irregularities as early as 19 LT but an extended irregularity structure termed as 'plume' evolved later at 1950 LT. The panel 2 of the figure shows that the onset of scintillations at Ancon occurred at about 2050 LT. Considering that the plume structure drifted towards east and traversed 350 km distance to cause the onset of Ancon scintillation, an eastward drift speed of 97 m/sec is obtained. From panel 3, it is found that the sharp onset of strong scintillations at Huancayo was delayed from that at Ancon by about 25 minutes. This delay is again consistent with a drift speed of about 116 m/sec. Thus the results illustrated in Figure 2 shows that an irregularity structure evolved first in the west possibly due to the existence of suitable background conditions and the structure drifted eastwards at a speed of approximately 100 m/sec to cause delayed onsets of scintillations on two propagation paths (Aarons et al., 1977). Considering the onset time of plume structure at Jicamarca and decay of scintillations at Huancayo a total lifetime of at least 3 hours for the irregularity structure is obtained.

The results of October 16, 1976 and October 29, 1976, indicated that large scale irregularities ($\sim$1 km - .1 km) co-existed with 3 m irregularities. The above fact did not, however, hold in all cases. It was found that scintillation measurements detected larger number of irregularity patches than did the radar. In Figure 3, we illustrate the radar maps, in schematic form, and results of scintillation measurements performed at Ancon and Huancayo, on seven nights in

October, 1976. It may be noted that the irregularity patches detected in scintillation experiments were more preponderant than 3 m plume structures. Based on the October measurements, a definite conclusion regarding the above fact could not be made because, except for October 29, 1976, the radar and scintillation experiments were probing different ionospheric volumes with a minimum separation of 350 km. The problem of co-existence of large and small scale irregularities can only be investigated if the measurements refer to a common volume.

During March, 1977, scintillation measurements with a host of geostationary satellites were so organized that ionospheric locations to the west, the east and in close proximity to the volume illuminated by the radar backscatter observations could be probed. As in October, the ground stations at Ancon and Huancayo performed scintillation measurements. The geostationary satellites LES-8 (abbreviated as L-8), ATS-3 (A-3), GOES-1 (G), LES-9 (L-9) and MARISAT were used. The 400 km subionospheric positions of all these measurements are shown in Figure 4, each location being specified by the station name (A for Ancon, H for Huancayo) followed by the abbreviated name of the satellite. Owing to finite orbital inclination, some of these vary considerably with time. The ground stations have been indicated by dotted circles. It may be noted that scintillation measurements performed at Ancon with the GOES-1 satellite probed an ionospheric location which was only 20 km to the east of the magnetic field line passing through the radar illuminated volume.

We shall illustrate only one night's observation (March 20, 1977) to indicate the nature of co-existence of small and large scale irregularities. Figure 5 shows the results of all scintillation measurements on this night, the panels from top to bottom being arranged in the order of increasing east longitude. The exact subionospheric locations corresponding to these different panels can be obtained from Figure 4. It is found that the onset of scintillations on this night occurred between 00 UT - 01 UT. When referred to the local time of these various subionospheric locations, the onset seems to have occurred within 4 minutes of 19h 40m LT. Thus unlike the results of October 16-17, 1976, when the irregularities evolved first in the west and were localized spatially, the irregularities seem to be under temporal control on March 20, 1977. It is to be noted that panels 2-5 of Figure 5 exhibit two discrete irregularity structures to which we shall have occasion to discuss again. Figures 6 and 7 represent the results of simultaneous radar observations at Jicamarca and scintillation measurements at Ancon with the GOES-1 satellite which, as mentioned earlier, refer to approximately a common ionospheric volume. From Figure 6 we find that during the early evening hours, the onset of scintillations occurred precisely when a plume evolved in the radar map. However, later (after 2045 LT) when the radar backscatter became weak, the scintillations maintained a high level. This indicates that the relative spectral powers of large scale and meter scale irregularities varied considerably during a two hour period (20 LT - 22 LT). In Figure 7 we show that the scintillation experiment detected another irregularity structure on this night between 23 LT - 01 LT (bottom panel) but virtually no radar backscatter was detected during this time (top panel). Referring to Figure 5, it may be noted that this second irregularity structure having negligible spectral power at 3 m was detected in panels 2 through 5, corresponding to the longitude interval of 78°W - 74°W. The reason for the absence of any signature of this event in panel 1 (79°W position) may be due to the evolution of the irregularity to the east of 79°W location. The significant fact regarding the second irregularity structure evolving an hour before midnight is a cut-off in the irregularity power spectrum at meter wavelengths. By performing power spectral analysis of amplitude scintillations recorded in the post sunset and near midnight period, we find no difference in the spectral form over the frequency interval of 0.2 - 2 Hz. The spaced receiver scintillation measurements made on this night at Ancon with LES-9 indicated that the eastward drift speed was about 75 m/sec at 1900 LT which increased to about 125 m/sec around 2300 LT. Considering an approximate drift speed of 100 m/sec, the frequency interval of 0.2 - 2 Hz may be translated to irregularity scale lengths of 2 km - 200 m. Thus the irregularity power spectrum between the scale lengths 2 km - 200 m remained unaltered between the post sunset and near midnight periods although their associations with 3 m irregularities was markedly different.

CONCLUSIONS

We have shown that on certain nights the equatorial irregularities are generated in particular spatial locations. On other nights, the irregularity generation is predominantly controlled by local time. The measurements of October, 1976 and March, 1977 indicate that between 1900 - 0100 LT the irregularity patches drift eastwards at speeds ranging from 85 - 140 m/sec. By tracking the irregularity patches with multisatellite scintillation measurements, it is found that the patches have typical lifetimes of several hours. Thus the temporal variation of scintillations recorded at an equatorial station, is dictated by spatial or temporal localization of irregularity generation, subsequent drift and lifetime of irregularity patches.

The equatorial irregularities that evolve in the post-sunset period are found to have a wide scale length range between several kilometers to a few meters. Such a scale length range can give rise to both scintillations and radar backscatter. The irregularity structures that arise around midnight are found to have little spectral powers at meter scale lengths. Such irregularity structures give rise to scintillation but no radar backscatter. For both these types, the irregularity power spectrum between a few kilometers to several hundred meters remain unaltered. Thus the major difference between these two types of irregularity power spectrum lies at scale lengths of tens of meters.

REFERENCES

Aarons, J., H.E. Whitney, R.S. Allen, Global morphology of ionospheric scintillation, Proc. I.E.E.E., 59, 159-172, 1971.

Aarons, J., J. Buchau, Santimay Basu, and J.P. McClure, The localized origin of equatorial F-region irregularity patches, to appear in J. Geophys. Res., 1977.

Basu, Sunanda, and M.C. Kelley, Review of equatorial scintillation phenomena in the light of recent developments in the theory and measurement of equatorial irregularities, to appear in J. Atmos. Terr. Phys., 1977.

Basu, Santimay and J. Aarons, Equatorial irregularity campaigns: Part I. Correlated scintillation and radar backscatter measurements in October, 1976, Air Force Geophysics Laboratory Scientific Report, 1977 (in press).

Booker, H.G., and H.W. Wells, Scattering of radio waves by the F-region of the ionosphere, J. Terres. Magn., 43, 249-256, 1938.

Dyson, P.L., J.P. McClure, W.B. Hanson, In-situ measurements of the spectral characteristics of F-region ionospheric irregularities, J. Geophys. Res., 79, 1495-1502, 1974.

Farley, D.T., B.B. Balsley, R.F. Woodman, and J.P. McClure, Equatorial spread-F: Implications of VHF radar observations, J. Geophys. Res., 75, 7199-7216. 1970.

Haerendel, G., Theory of equatorial spread-F, Preprint, Max-Planck-Institut für Physik und Astrophysik, Garching, West Germany, 1974.

Hanson, W.B. and S. Sanatani, Large N_i gradients below the equatorial F-peak, J. Geophys. Res., 78, 1167-1173, 1973.

Hudson, M.K., and C.F. Kennel, Linear theory of equatorial spread-F, J. Geophys. Res., 80, 4581-4590, 1975.

McClure, J.P., W.B. Hanson, and J.H. Hoffman, Plasma bubbles and irregularities in the equatorial ionosphere, J. Geophys. Res., 82, 2650-2656, 1977.

Röttger, J., The macroscale structure of equatorial irregularities, J. Atmos. Terr. Phys., 38, 97-101, 1976.

Skinner, N.J., and R.F. Kelleher, Studies of F-region irregularities at Nairobi, I - From spread-F on ionograms 1964-1970, Ann. Geophys. 27, 181-194, 1971.

Scannapieco, A.J., and S.L. Ossakow, Nonlinear equatorial spread-F, Geophys. Res. Lett., 3, 451-454, 1976.

Woodman, R.F., and C. LaHoz, Radar observations of F-region equatorial irregularities, J. Geophys. Res., 81, 5447-5466, 1976.

Woodman, R.F., and Sunanda Basu, Comparison between in-situ spectral measurements of equatorial F-region irregularities and backscatter observations at 3 m wavelengths (abstract), EOS Trans. AGU, 58, 449, 1977.

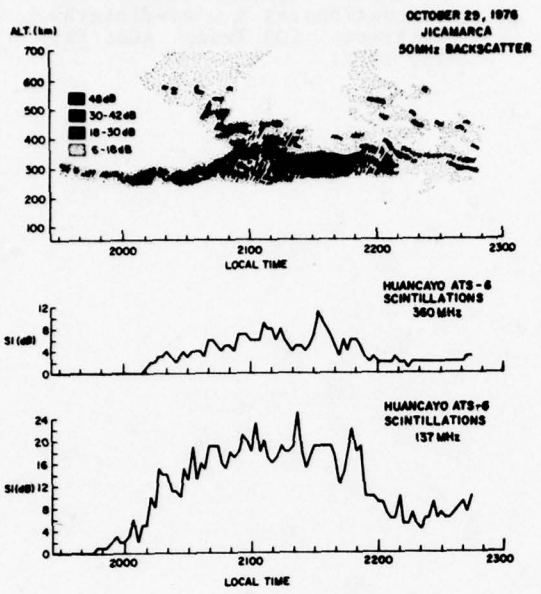


Figure 1. Radar (50 MHz) backscattered power maps of F-region irregularities obtained at Jicamarca and results of simultaneous scintillation measurements performed at Huancayo on October 29, 1976, with 137 and 360 MHz transmissions from the ATS-6 satellite. The east-west separation between the ionospheric locations explored by the radar and scintillation experiments was only 30 km at an ionospheric height of 400 km.

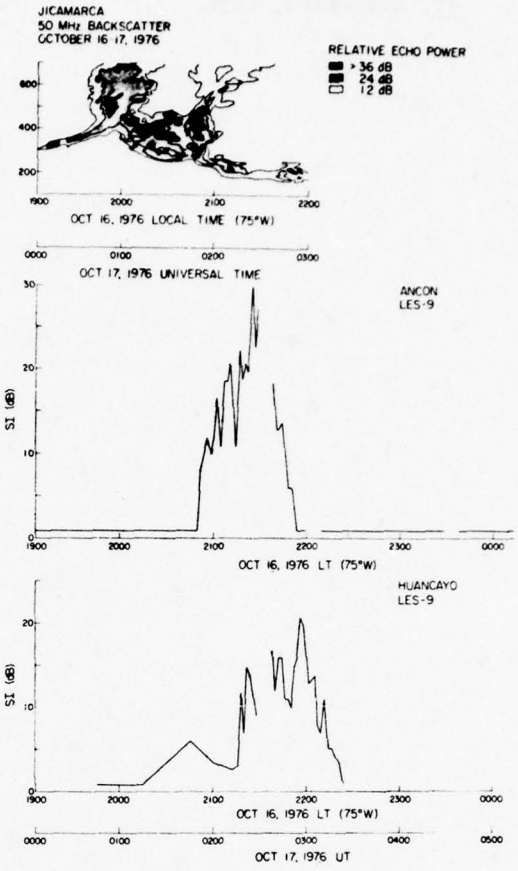


Figure 2. Results of simultaneous radar backscatter and 249 MHz scintillation observations performed on October 16-17, 1976. The ionospheric volumes pertaining to the results in the top and middle panels were separated by 350 km whereas those pertaining to the middle and the lower panels by 175 km.

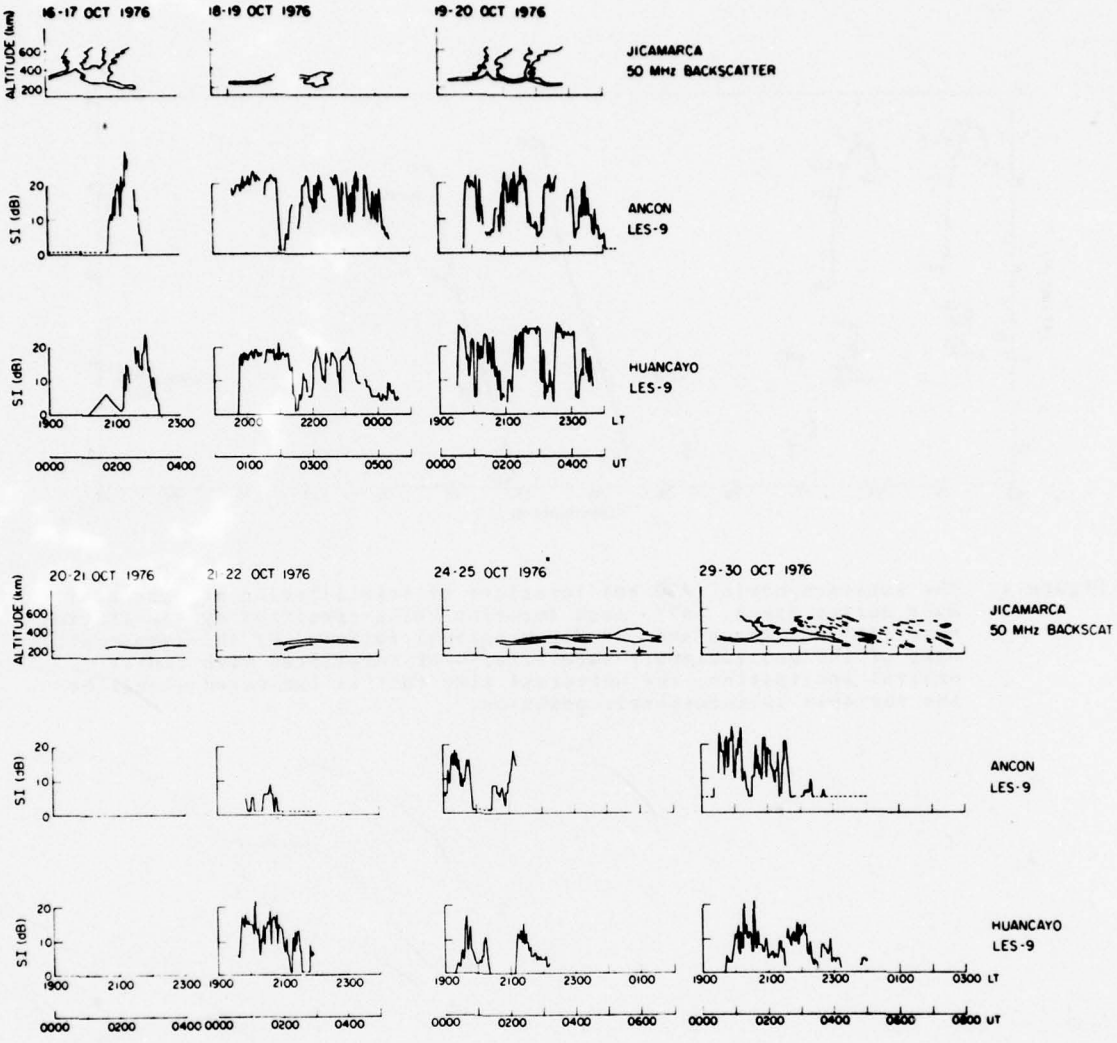


Figure 3. Comparison of radar power maps, in schematic form, and results of simultaneous scintillation measurements made at Ancon and Huancayo on seven nights in October, 1976.

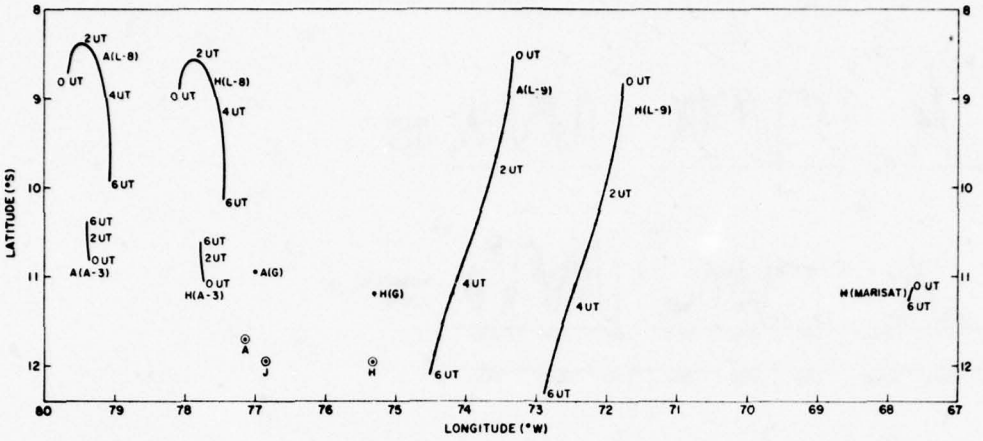


Figure 4. The subionospheric (400 km) locations of scintillation measurements made during March, 1977, each location being specified by the station name ('A' for Ancon and 'H' for Huancayo) followed by the abbreviated name of the geostationary satellite. For satellites with finite orbital inclination, the universal time (UT) is indicated alongside the variable subionospheric position.

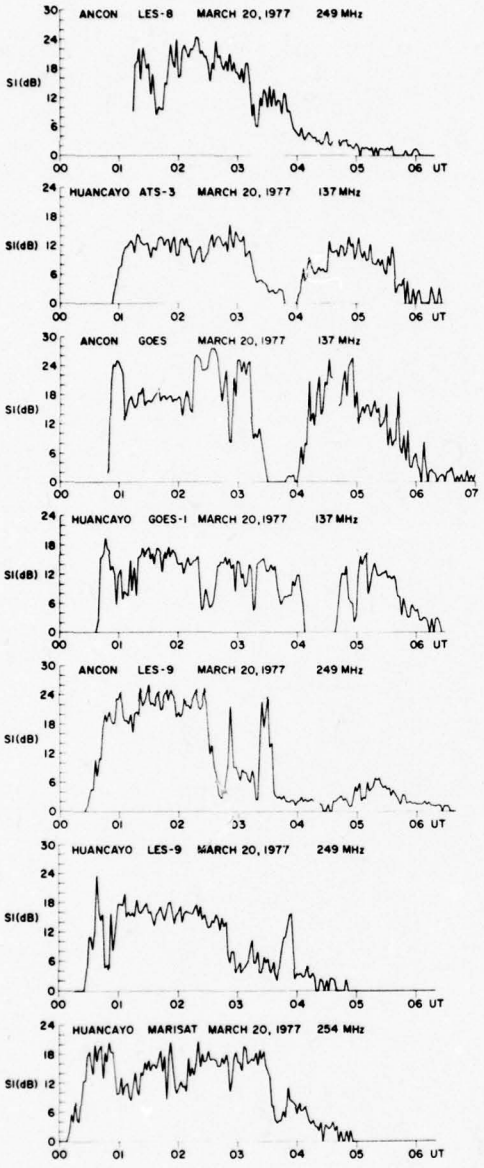


Figure 5. The results of simultaneous scintillation measurements performed on March 20, 1977. The subionospheric (400 km) location corresponding to each panel may be obtained from Figure 4.

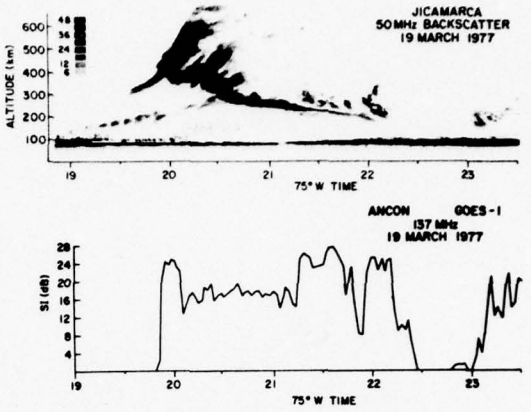


Figure 6. Comparison of radar power map and simultaneous 137 MHz scintillation measurements over a nearly common ionospheric volume during the development phase of irregularity generation on March 20, 1977.

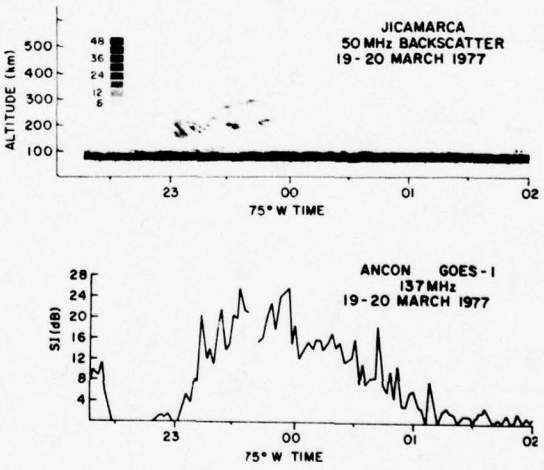


Figure 7. Comparison of radar power map and simultaneous 137 MHz scintillation measurements obtained on March 20, 1977, in the late phase of irregularity generation.

Radio and Optical Diagnostics Applied to ah Isolated Equatorial Scintillation Event

By

J. Buchau and E.J. Weber
Air Force Geophysics Laboratory
Hanscom AFB, MA 01731

And

J.P. McClure
The University of Texas at Dallas
Richardson, TX 74080

ABSTRACT

During equatorial scintillation studies carried out in March 1977 a new all-sky spectrophotometric imaging system and an ionospheric sounder, both onboard a USAF research aircraft and the Jicamarca Backscatter Radar were operated to monitor the development, structure and motion of F region irregularities leading to scintillations on satellite signals. The imaging system provided all-sky pictures of the 6300 Å OI airglow emission, which results from dissociative recombination of O_2^+ in the F region. This technique provided minute by minute images of the large scale structure of the bottomside F-layer. Initial observations show the existence of north-south aligned regions of airglow depletion. These bands often extend more than 1200 km in the north-south direction and from a few km to several hundred km in the east-west direction. They drift eastward at ~100 m sec^{-1}. Their presence is detected by the ionospheric sounder as oblique echoes or spread F and they correlate with scintillation events.

An isolated airglow depletion band was observed during a flight on 17 March 1977 and is described here in detail. The depletion drifted east at 92 m sec^{-1} and was observed for three hours during which time it moved from the western to the eastern observational horizon. The ionospheric sounder showed strong electron density gradients associated with the eastern and western edges of the airglow depletion. Substantial raising of the bottom height of the F-layer and strong spread F characteristics were associated with the passage of the depletion over the aircraft. The Jicamarca Backscatter radar observed a patch of irregularities in the 175 to 700 km height range, drifting eastward over the radar, in good correlation with the passage of the airglow depletion.

250 MHz signals from the LES-9 satellite exhibit 6-14 dB scintillations during passage of the disturbance through the ray path. Geometrical considerations suggest that irregularities between 275 and 800 km, collocated with the airglow depletion, are responsible for the observed scintillations.

A troughlike bottomside electron density depletion, extending for more than 1200 km in N/S direction with an E/W width varying between 100 and 200 km and with a base height of the F-layer around 300 km, collocated and moving with the 6300 Å depletion, explains both the observed 6300 Å airglow structure and the sounder observations. The backscatter and scintillation measurements indicate the simultaneous presence of F-region irregularities of scale sizes ranging from 3 m to several km. We suggest that the at times rapidly rising and at times stationary strong electron density bite outs (plasma bubbles) observed by satellites in the equatorial ionosphere are the topside signature of disturbances such as the one we describe.

INTRODUCTION

An intensive experimental campaign was conducted in March 1977 in Peru to investigate the development, dynamic behavior and lifetime of equatorial nighttime F-layer irregularities and to determine their relation to scintillations observed on trans-ionospherically propagated rf-signals. Participating in this campaign were two USAF research aircraft conducting communication and environmental studies, Air Force Geophysics Laboratory (AFGL) ground stations for satellite reception and the large VHF radar at Jicamarca.

Out of a total of seven flights, we have selected one, flown on 17 March 1977, during

which an intense isolated scintillation event was observed on a 250 MHz signal transmitted from the LES 9 satellite. This event permitted the detailed correlation of various airborne and ground based geophysical and propagation measurements for a unique description of the F-layer irregularities responsible for the observed scintillations. From these investigations we obtained both a three-dimensional model of the irregularity region and a description of its temporal behavior. Our results are representative of other strong equatorial scintillation events.

EXPERIMENTS

Figure 1 shows the flight track flown on 17 March 1977. The objective was to have the ray path from the LES 9 satellite to the AFGL Airborne Ionospheric Observatory intersect the Jicamarca magnetic meridian at a height of 400 km. During the flight the LES 9 satellite, stationed nominally at 40°W, moved from 17°40'N at 00:40 UT to 14°55'S at 06:10 UT (subsatellite points) and the elevation/azimuth angles to the satellite changed from 29°/52° East of North to 51°/101° East of North respectively. The intersection of the satellite-to-aircraft ray path with the Jicamarca magnetic meridional plane was at all times within 250 km of the ground station. Considering the field alignment of F-layer irregularities, it was assumed that the occurrence of backscatter over Jicamarca and the simultaneous observation of scintillations on the satellite-to-aircraft path were the result of the formation or arrival of F-layer irregularities belonging to the same event, at the Jicamarca meridian.

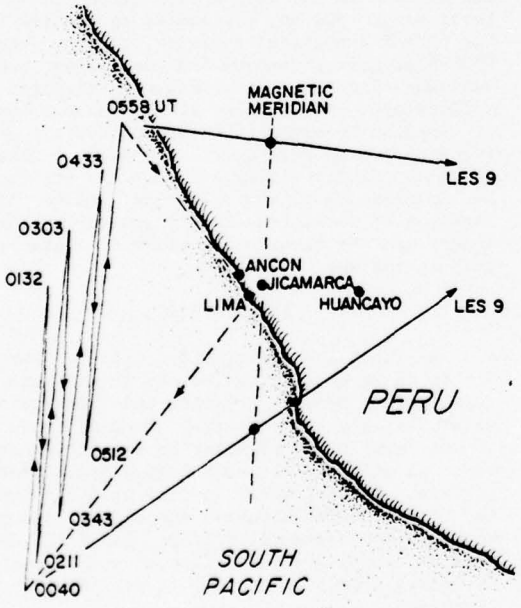


Figure 1. Flight track of 17 March 1977. Arrows labelled LES 9 are ground projections of ray paths to the satellite at the beginning and at the end of the measurements.

The aircraft carried satellite beacon radio receivers, vertically looking spectrometers and a new all-sky spectrophotometric imaging system (Mende and Eather, 1976; Weber et al., 1977). The ionospheric sounder used for these studies was a modified Granger 3905-I sounder (Gowell and Whidden, 1968), recording three ionograms every five minutes. The satellite receive system consisted of a Dorne-Margolin VHF/UHF wide band circularly polarized antenna, a Spectrum International preamplifier converter and a modified Collins R-390 HF receiver used as an IF amplifier. The AGC was recorded on a strip chart recorder and magnetic tape, as a measure of field strength with a post-detection bandwidth of 20 Hz. For the purpose of this study, the scintillation index, SI, in dB (Whitney et al., 1969) was determined by measuring the dB difference between the third peak down from the maximum and the third fade up from the minimum in each 2 minute time interval.

Significant airborne measurements were made with the all-sky photometer, a new spectrophotometric imaging system added to the instrumentation of the Airborne Ionospheric Observatory. The instrument is a wide field of view (155°), narrow spectral bandwidth TV system designed to operate in a time exposure mode. All-sky images of the equatorial airglow were made through 6300 Å and 5577 Å narrow band (30 Å) interference filters, using alternate 2.5 sec exposures to produce an image at each wavelength every 30 seconds. The resulting TV frames were then recorded on video tape and by photographing a TV monitor. An example of an all-sky photometer 6300 Å image is shown in the left half of Figure 2. The grid lines are magnetic meridians in 1° increments, assuming a 250 km emission height. The 6300 Å airglow emission originates in the F-region primarily as a result of dissociative recombination of molecular ionized oxygen. This emission feature is a sensitive indicator of F-region height and electron density changes; decreased intensity is associated with regions of low density or increased height of F-layer ionization. The bright airglow filling the portion of the sky from overhead to the western horizon and a second bright region extending from 2° east of the aircraft to the eastern horizon are indicative of substantial F-layer ionization below 300 km. The dark field aligned band or airglow depletion between these two bright regions is a phenomenon which was routinely observed during these equatorial flights and is the result of decreased ionization below 300 km. The ground projection on the right side of Figure 2 gives an indication of the size of the field of view, and the dimensions of this airglow depletion.

Care must be exercised in the interpretation of features near the edge of the field of

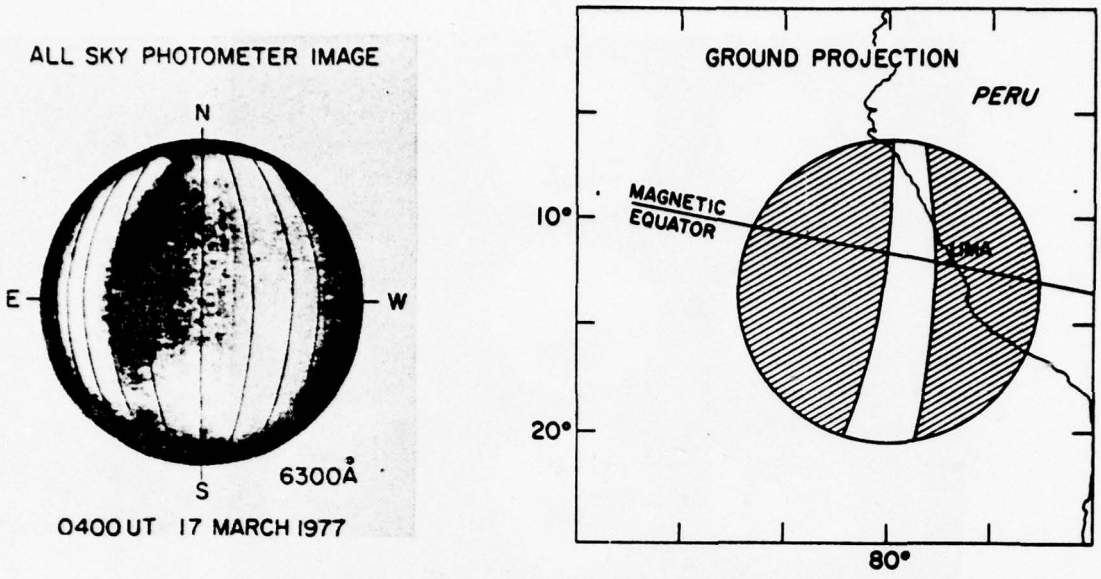


Figure 2. Example of an All-Sky Photometer Image and Its Ground Projection Assuming a 250 km Emission Height. The superimposed grid indicates the projection of corrected geomagnetic longitudes, at one degree intervals.

view. The van Rhijn effect and vignetting act in opposition, but vingetting exceeds van Rhijn enhancement at the edges, often resulting in a perceptable dark band around the image for the weak airglow features under consideration. The narrow north-south striations about ½° to the west of zenith are the ionosonde antennas which stretch above the all-sky lens.

The Jicamarca 50 MHz radar has been used for the study of equatorial irregularities for several years. The observed "plumes" resulting from backscatter due to 3 meter irregularities have been described in detail and tentatively modelled elsewhere (Woodman and La Hoz, 1976). These plumes are thought to result from the development and upward propagation of low electron density bubbles in the equatorial F-region. During these experiments the Jicamarca radar was operated to record the development and structure of the irregularities for subsequent correlation with the airborne and ground based data observations.

As discussed by Basu et al. (1977), VHF scintillations are the result of F-region irregularities with scale sizes on the order of 1 km, while the radar measures irregularities of 3 m scale size. Based on other measurements and theoretical calculations, Basu et al. (and references therein) established that the smaller irregularities are sometimes but not always observed in conjunction with the larger ones. Comparison of the radar maps with scintillation and airglow data will permit us to further elucidate the relation of the larger and smaller-scale irregularities.

OBSERVATIONS ON 17 MARCH 1977

All-Sky Photometer

Figure 3 presents a series of 6300 Å images (photographs of the tape recorded video frames) obtained during the flight on 17 March 1977, at 15 minute intervals between 0100 and 0545 UT. For the discussions in this paper, only the 6300 Å images were considered. All images have been reoriented with magnetic north to the top as shown in Figure 1.

The images between 0100 UT and 0200 UT show a low-level, unstructured glow with some enhancement towards the South, probably enhanced emission from the maximum of the Appleton anomaly. The Milky Way is visible in the 0100-0145 UT images as a slight enhancement aligned in the southeast-northwest direction. The 0215 UT image shows a prominent depletion in the 6300 Å airglow in the form of a dark band which extends from south to north along much of the western horizon. The formation of this dark band can

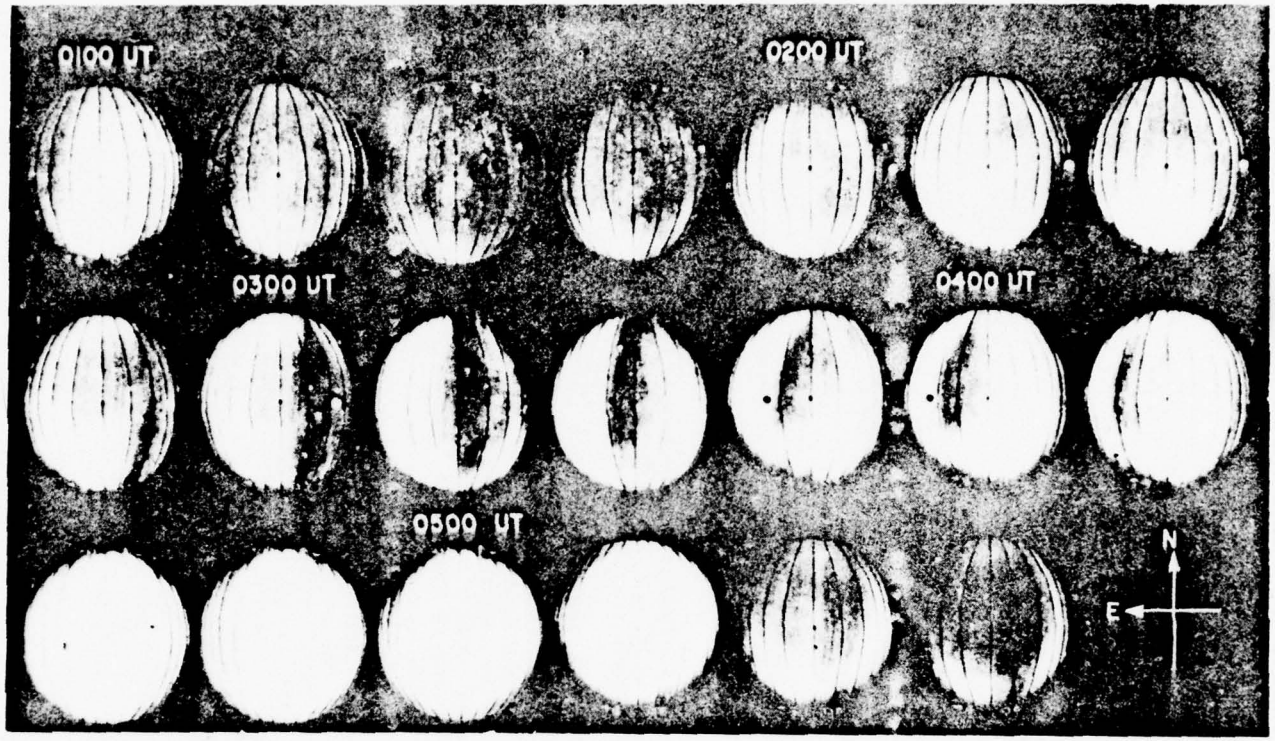


Figure 3. All sky (155° field of view) 6300 Å OI airglow images at 15 minute intervals, from 0100 UT to 0545 UT, 17 March 1977. The superposed grid indicates the projection of C.G. longitudes, at one degree intervals, for an assumed emission height of 250 km. The black and white dots represent respectively the location of approaching and receeding oblique F-region ionosonde backscatter returns.

be seen as early as 0200 UT. Within the next 2.5 hours, this band travels across the sky, leaving the instrumental field of view on the eastern horizon by approximately 0445 UT. Generally the images show that the eastern or leading edge of the airglow depletion is closely aligned in the magnetic North/South direction, (best seen in the 0330 UT image). The leading edge displays a sharp intensity gradient in the east-west direction while the western edge of the depletion region shows a somewhat more gradual, structured transition to the adjacent bright airglow region. The width of the depletion when directly overhead at 0330 UT is approximately 150-200 km. In the north-south direction, these regions extend across the entire field of view to include a horizontal distance of more than 1200 km, assuming a 250 km emission height.

Unstructured airglow covers (most of) the observable sky until 0515 UT and then rapidly falls in intensity, leaving only minor enhancements towards the southern and western horizons.

Drifts

The Corrected Geomagnetic (C.G.) longitudes of the eastern and western edges of the airglow depletion, measured on an east-west great circle through the aircraft zenith, are shown in Figure 4. The depletion drifted eastward with a relatively constant velocity of approximately 92 m/sec, while maintaining on almost constant east-west size of approximately 165 km. Eastward drifts from 50 to 100 m/sec were observed for similar depletions on other evenings.

Ionosonde Measurements

Figure 5 presents results of the ionospheric soundings conducted simultaneously onboard the aircraft. The virtual height of the observed F layer and the virtual range of oblique F-layer echoes are shown as a function of time. The oblique echoes are first observed at a virtual range of 800 km at 0157 UT, almost coincident with the initial observation of the airglow depletion on the western horizon. These oblique returns decrease in range, consistent with the approach of a reflecting or scattering region, and merge with the overhead F-layer by 0317 UT.

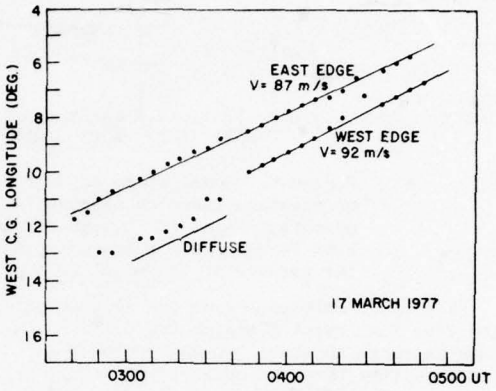


Figure 4. The Corrected Geomagnetic Longitudes of the Eastern and Western Edges of the Airglow Depletion Shown in Figure 3.

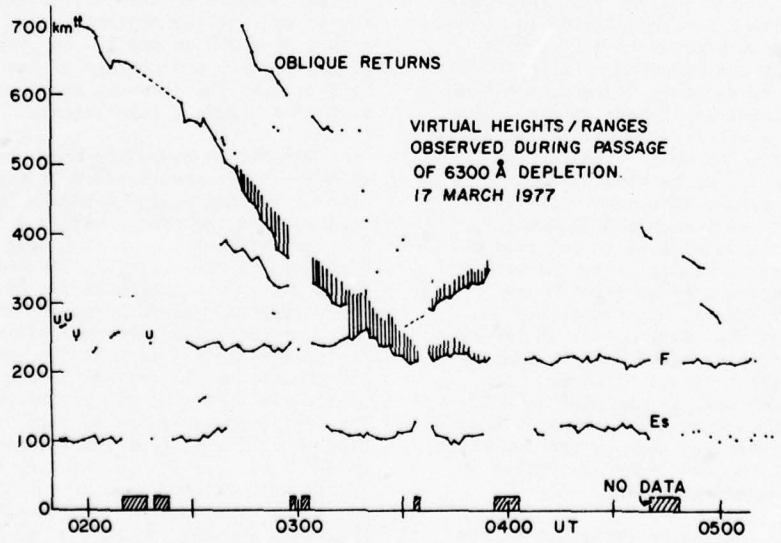


Figure 5. Virtual Heights/Ranges of Ionosonde Returns Observed During Passage of 6300 Å Depletion. The shaded areas represent range spread on backscatter returns or overhead spread F conditions.

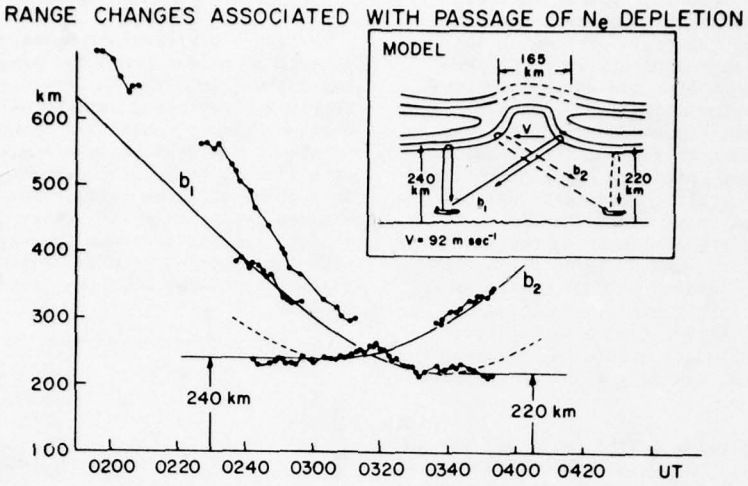


Figure 6. Model of an eastward drifting, bottomside Ne depletion or corrugation based on observed ionosonde and airglow parameters. The measured ranges of oblique returns and the virtual height of the overhead F-region are compared with range/height changes expected from the passage of the model bottomside structure over the ionosonde.

By 0335 UT oblique echoes are seen to separate from the lowest F-region trace and to increase in range to about 350 km by 0354 UT. After this time they are obscured by other returns and cannot be further identified. Even though the omnidirectional sounder antenna does not permit determination of the angle of arrival of the oblique echoes, the coinciding time histories of the airglow depletion movement and the backscatter range change suggest that the sounder observes the motion of ionospheric scattering regions associated with the motion of the depletion. To verify the identity of airglow depletion edges and backscatter regions, the location of the backscattering irregularities was superimposed on the all-sky images. Assuming a height of 250 km for the scattering region, ranges of the approaching backscatter front were converted to ground distances. The estimated locations of these approaching scattering regions are shown as white dots in the respective airglow images in Figure 3, to the west of zenith. Ground ranges derived from the receding backscatter branch, observed after the overhead passage of the leading edge of the depletion, were entered as black dots to the east of the zenith of the respective images. As Figure 3 shows, best seen in the 0245 to 0315 UT images, the approaching backscatter is tracking the trailing (western) edge of the depletion, while the leading (eastern) edge is tracked by the receding echoes observed after 0330 UT.

A model of an ionization depletion in the bottomside of the ionosphere, shown in the upper right of Figure 6, produces a sequence of approaching and receding echo traces (branch b_1 and b_2) as well as a variation in h'F, which closely resemble the observations. With the aircraft located to the east of the structure, returns are received vertically and via ray path b_1; after passage of the structure to the east of the aircraft, returns are received vertically and via ray path b_2. As mentioned above the width of the structure has been taken as 165 km and the velocity as 92 m sec^{-1}. The time of passage of the eastern edge through the aircraft zenith was determined as 0308 UT. The virtual heights of the F-layer before and after the passage of the depletion were taken from Figure 3 as 240 km and 220 km respectively. Figure 6 shows the results of the model computations with the relevant sections of the h' plot from Figure 3 superimposed.

The fit is generally good, but additional strong returns associated with the trailing edge of the depletion at ranges larger than derived from the simple model, and approaching at a greater speed suggest a more complex structure of the trailing edge than assumed for the model. Examination of the 16 mm all-sky photometer photographic record, having 30 second time resolution, reveals diffuse structure having turbulent motion at the western edge of the depletion, in contrast to the smooth and stable features observed at the eastern edge. The east-west asymmetry is also visible in Figure 3. The 0300 UT image shows diffuse and patchy structure at the trailing edge compared to the well defined leading edge. In-situ satellite observations of presumably similar depletion regions (McClure et al., 1977) show similar variations in the structure of the edges of the depletions. The structural differences may be responsible for the differences in the ionosonde backscatter associated with the leading and trailing edge.

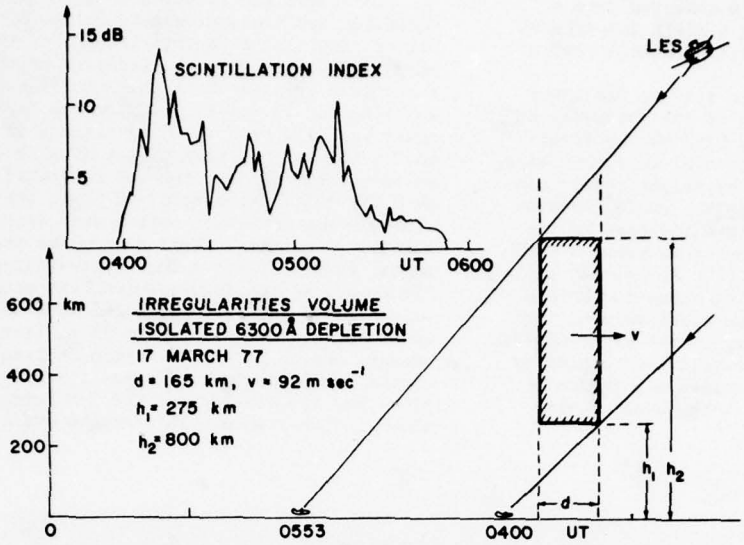


Figure 7. Isolated Scintillation Event Observed on 17 March 1977 and Estimated Irregularities Volume Cross-Section.

After the approaching trace merged with the overhead trace, strong unstructured spread F developed, and persisted for the period of passage of the depletion. Throughout the evening, the F-layer had come down, from initially 275 km (0000 UT) to 230 km (0300 UT) just prior to the overhead arrival of the leading edge of the depletion. The layer rapidly moved upwards by 35 km, reaching a maximum virtual height (h') of 265 km by 0319 UT, the time of strongest spread F. After this, the layer again rapidly moved down to 215 Km (0332 UT) and fluctuated around this level for the remainder of the observations.

Determination of foF2 between 0100 and 0500 UT is somewhat uncertain because of spread conditions and high nighttime HF noise levels. Sporadic ionograms from this time interval showing clear traces indicate that foF2 fluctuated between 8.5 and 9.5 MHz. After 0500 UT the spread and noise conditions improved and a clear decrease of the foF2 from 9.2 MHz (0503 UT) to 8.0 MHz (0523 UT) and finally to 5.8 MHz (0549 UT) is observed, which follows the decrease of the overall brightness of the 0500 UT to 0545 UT all-sky photometer images. Since h'F does not change appreciably (from 212 km at 0503 to 226 km at 0549 UT) this change in airglow level is directly attributable to the Ne decay.

Scintillations

Three clearly separated scintillation events were observed in the aircraft during this flight lasting from 0104 UT to 0242 UT, from 0215 UT to 0317 UT and the last one from 0400 UT to 0553 UT. Here we are concerned only with the last event, since it occurred during the time when the previously described depletion moved through the LES 9 ray path. The eastward drift in effect moved the ray path from lower to higher altitudes through the region. The scintillations observed during this last event are shown in the upper left of Figure 7. The scintillations start with SI showing a strong 14 dB peak; after that they fluctuate for about one hour between 5 and 10 dB and decay towards the end to weak 2 dB scintillations.

If we assume, that the irregularities responsible for the observed scintillations reside in a volume coincident with and extending vertically above the airglow depletion shown by the all-sky photometer, we can determine a minimum and a maximum height for the volume containing the irregularities. Using the width of 165 km and the eastward velocity of 92 m sec^{-1} determined from the all-sky photometer measurements, the minimum height can be estimated as 275 km and the maximum height as 800 km. The geometry of the ray paths at the start and the end of the isolated scintillation event and the cross-section of the volume defined by these rays and the depletion is shown in the lower right of Figure 7. It has to be pointed out, however, that neither the all-sky photometer nor the sounder measurements allow any inference about the ionospheric structure above 300 km.

Jicamarca Backscatter Measurements

The 50 MHz backscatter measurements (Figure 8) show the time history of the development or drift of 3 m irregularities above Jicamarca. The picture can be understood either as the time history of an eastward

drifting irregularity region observed from a fixed location or, assuming a rigid ionosphere, as an east-west cross-section of such a region.

Some irregularities are seen in the lower F-region from the beginning of the observations until 0300 UT. Starting at 0357 UT the first echoes from an extended region of irregularities are observed at 500 to 600 km height. This disturbance eventually involves the whole F-region between 175 and 670 km. Irregularities in the F-region below 500 km disappear between 0430 UT (500 km level) and 0450 UT (200 km level), while some very weak irregularities above 500 km are observed until 0535 UT. The relatively uniform diffuse background appearing at the first digital level (0 to 6 dB above threshold) was caused by a computer malfunction, and does not indicate the existence of a diffuse background of weak irregularities.

To assess the relation between the airglow depletion and the approximate volume of irregularities resulting in scintillations on the one hand, and the observed backscatter on the other, the volume cross-section shown in Figure 7 is superimposed in dashed lines on the backscatter power map (Figure 8). Using a speed of 92 m sec^{-1}, the arrival time of the airglow depletion at the Jicamarca meridian was estimated to be 0410 UT. At a velocity of 92 m/sec the 165 km wide airglow depletion passed over Jicamarca in exactly 30 minutes. This determines the horizontal extent of the volume cross-indicated in Figure 8. As the figure shows, the estimated volume is in general agreement with the observed backscatter cloud. There is a discrepancy between the shape of the simple rectangle based on the local airglow and scintillation observations and the envelope of the 3-m irregularities shown in the figure. This may be indicative of

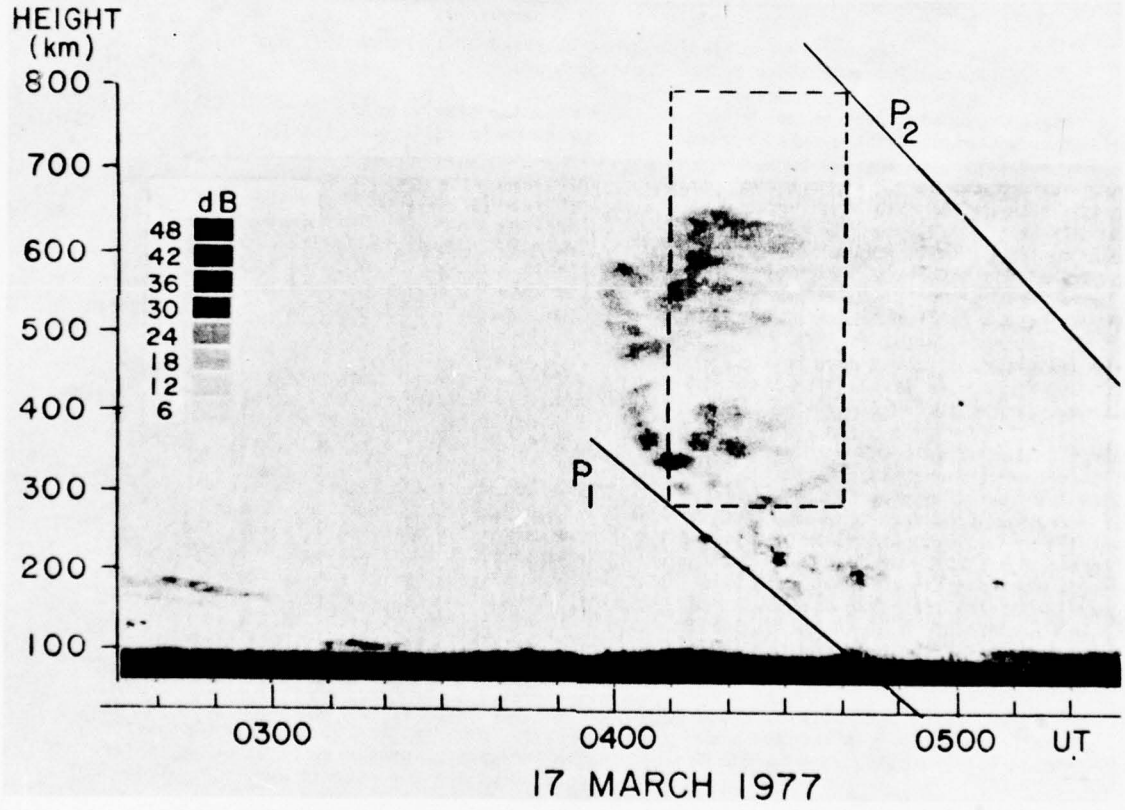


Figure 8. Range time-intensity map of isolated F-region disturbance passing over the Jicamarca radar. The dashed lines represent the irregularity volume determined from airglow and scintillation measurements. P_1 and P_2 denote the trans-ionospheric ray path, through the disturbed region at the beginning and end of the associated scintillation event.

1) changes with altitude of the eastward drift of the ionosphere and/or 2) changes with time and altitude of the upward and relative westward drift velocity of plasma depletion regions (plasma bubbles) with respect to the background ionosphere, as discussed by McClure et al. (1977). Airglow observations, made near the intersection with the 250 km altitude surface, of these middle and upper F-region geomagnetic field lines which cross over Jicamarca, would be useful for comparison with the detailed shape of the region of echoes above Jicamarca.

In Figure 8 we have also shown the position of the ray path from the aircraft to the LES 9 satellite at two selected Universal Times. P1 is the ray path at 0400 UT, the start, and P2 the ray path at 0553 UT, the end of scintillation event. The figure now shows that the crossing of 3m irregularities into the ray path at heights between 175 and 275 km coincides with the onset of the scintillations. The strong 14 db scintillation event coincides approximately with the movement of intense irregularities in the 300-400 km height range into the ray path. And finally, the weak scintillations observed after 0520 UT (see Figure 6) appear to result from the trailing irregularities associated with the weak backscatter seen for about one hour at heights between 500 and 600 km, after the major cloud has passed.

CONCLUSIONS

A new technique of monochromatic, all-sky imaging used onboard an aircraft has revealed the existence of magnetically North-South aligned regions of airglow depletions with E/W dimensions of 50 to 200 km and a North/South extent larger than the 1200 km field of view of the all-sky photometer.

Airglow images, ionosonde and 50 MHz backscatter data have been analyzed to describe the airglow depletion and its relation to the F-region plumes observed at Jicamarca, using a well defined airglow depletion observed on 17 March 1977.

It is concluded that the airglow depletions, the oblique echo/range variations and h'F changes seen by the ionosonde and the 50 MHz backscatter plumes, can all be understood as different aspects of the same phenomenon, a volume of reduced electron density, containing meter to kilometer size irregularities, extending from the lower to the upper F-region causing scintillations on ray paths transiting this volume.

ACKNOWLEDGEMENTS

The authors wish to thank the Jicamarca Radio Observatory personnel for their support in taking and processing the radar information. The success of the airborne missions was due to engineering support provided by R.W. Gowell, J.B. Waaramaa and J. W.F. Lloyd, logistics support by R. Carnevale, and airborne support from the 4950th Test Wing, Wright-Patterson AFB, OH.

This research was supported, in part, by the Air Force Laboratory Independent Research Fund of the Air Force Geophysics Laboratory, Air Force Systems Command.

REFERENCES

Basu, S., J. Aarons, J.P. McClure, C. LaHoz, A. Bushby and R.F. Woodman, Preliminary Comparison of VHF Radar Maps of F-region Irregularities with Scintillations in the Equatorial Region, to appear in J. Atmos. Terr. Phys., Sept. 1977.

Gowell, R.W. and R.W. Whidden, Ionospheric Sounders in Aircraft, AFCRL-68-0369, Instrumentation Papers, No. 144, 1968.

McClure, J.P., W.B. Hanson and J.H. Hoffman, Plasma Bubbles and Irregularities in the Equatorial Ionosphere, J. Geophys. Res., 82, 2650, 1977.

Mende, S.B. and R.H. Eather, Monochromatic All Sky Observations and Auroral Precipitation Patterns, J. Geophys. Res., 81, 3771, 1976.

Weber, E.J., J. Buchau, R.H. Eather and S.B. Mende, North/South Aligned Equatorial Airglow Depletions, J. Geophys. Res., (in press) 1977.

Whitney, H.E., C. Malkk and J. Aarons, A Proposed Index for Measuring Ionospheric Scintillations, Planet. Space Sci., 17, 1069, 1969.

Woodman, R.F. and C. LaHoz, Radar Observations of F Region Equatorial Irregularities, J. Geophys. Res., 81, 5447, 1976.

Preceding Page BLANK - NOT FILMED

TOPSIDE IONOSPHERIC TROUGH MORPHOLOGY AT MID- AND HIGH-LATITUDES

M. Ahmed
Regis College
Weston, MA 02193

and

R.C. Sagalyn
Air Force Geophysics Laboratory
Hanscom AFB, MA 01731

ABSTRACT

The main trough in the topside ionosphere has been studied using the thermal positive ion and electron densities measured over a three year period (1969-1972) by means of spherical electrostatic analyzers aboard the ISIS I and INJUN V satellites in the 560-3600 km altitude range. The trough is found to be a persistent feature at night with an occurrence frequency of approximately 95%. The occurrence frequency decreases to approximately 60% near the dawn-dusk meridian and to approximately 48% near local noon. At altitudes below about 1500 km during quiet to moderate conditions ($Kp \leq 3$) the trough equatorward boundary is found at $L = 3.5 \pm 0.5$ near midnight and $L = 12.5 \pm 1.0$ near local noon. The trough equatorward location on the nightside is in good agreement with published plasmapause locations. Near local noon the trough occurs at the equatorward edge of the magnetospheric cleft and is at significantly higher L values than those reported for the dayside plasmapause. The seasonal variation of the trough location at a given local time is negligible except near sunrise.

With increasing altitude between 1500 and 3600 km, the equatorial boundary of the trough moves to continually lower latitudes during the night hours. The equatorward trough wall becomes a dominant feature of the trough often extending from 15° to 20° in width during quiet magnetic periods. The poleward edge of the trough becomes less well marked with increasing altitude often being defined only by a sharp spike in ionization extending over a few degrees within the auroral zone. The amplitude of the dayside high latitude trough reduces gradually with increasing altitude. However, a second region of dayside plasma depletion is observed between L = 2 and 6 approximately 50% of the time. The equatorward wall of this depletion region probably represents partial flux tube filling in the outer plasmasphere.

INTRODUCTION

Mid-latitude troughs or depressions in the F layer ionization were first reported by Muldrew (1965) and Sharp (1966). Further studies of trough characteristics have been carried out by a number of workers including Miller and Brace (1969), Rycroft and Thomas (1970), Tulunay and Sayers (1971), Taylor et al. (1975) and Grebowsky et al. (1976). Statistical studies of the relation of the trough to the plasmasphere (Thomas and Andrews, 1968, Tulunay and Sayers, 1971, and Grebowsky et al. 1976), have shown that mid-latitude charge density depletions occur near the same L shells as the average plasmapause position on the nightside. Rycroft and Thomas (1970) and Tulunay and Sayers (1971) established that the trough position varies with Kp in a manner similar to the plasmapause dependence upon

magnetic activity. Taylor et al. (1974) have shown that the trough exists in the individual ion species H^+, He^+ and O^+.

Studies of the diurnal, seasonal and altitude variation of the trough characteristics have led to confusing results (Wrenn and Raitt, (1975). Miller (1974), for example, reported that dayside troughs persisted above 2500 km while below they were seldom detectable. There are several reasons for the differences in trough results. These include use of a limited data base, widely varying altitude of the measurements, varying spatial resolutions of the measurement from a few km to nearly 1000 km, difficulties in detecting dayside features due to photoelectrons as well as varying criteria used to define the trough location. Tulunay and Sayers (1971) for example, used the trough minimum, while Brace and Theis (1974) used a density level of 10^3 electrons/cm^3 along the equatorial trough wall.

The present study seeks to contribute new knowledge of the trough characteristics as a function of local time, season and altitude. The trough occurrence frequency is also presented as a function of local time. The study is based on the examination of thirty-seven months of ISIS I positive ion and INJUN V electron probe data. The relation of the trough to the plasmapause is examined at all local times.

THE EXPERIMENT

ISIS I thermal charged particle measurements were obtained with a spherical electrostatic analyzer that measured the thermal ion density, the ion energy distribution from 0 to 50 eV, the satellite potential, and the ratio of the ion mass to the ion temperature. The sensor mounted on a 96 cm boom, consists of three concentric spherical electrodes with radii of 1.90, 2.54 and 3.18 cm respectively. The operation of the probe is based on the motion of charged particles in a central force field (Sagalyn, et al., 1963, Sagalyn and Smiddy, 1967, Smiddy and Stuart, 1969, Whitteker et al., 1972). The sensitivity range of the instrument is $10-10^6$ ions cm^{-3}, in sunlight, however, photoelectron currents limit the lower sensitivity to about 700 ions cm^{-3}. Ion densities were sampled 60 times per second, corresponding to a spatial resolution of 150 m. The ratio of mass to temperature was sampled once per minute, and the energy distribution was samples once every 2 min. The results in this report are based on the ISIS I ion density mode of operation and also on measurements made with a two electrode spherical probe flown on INJUN V with a spatial resolution of 2 km.

DATA BASE

The ISIS I satellite served as an ideal platform for the study of diurnal and seasonal morphology of the trough, since its orbital plane precessed nearly one hour of local time per week, providing a complete 24 hour coverage in about 3 months. Data obtained within 45 days of the equinox and solstice periods were utilized for the seasonal study.

The statistical portion of the study reported here utilizes thermal positive ion density measurements on about 12,000 ISIS I orbits between Febraury 1969 and March 1972. The measurements have a spatial resolution of 150 meters and are well suited for the study of trough characteristics. In addition, thermal ion and electron densities measured by similar instruments aboard the INJUN V satellite on about 3000 orbits between November 1968 and November 1970 were used to improve the data base within a few hours of local noon. The data cover the altitude range 550-3600 km and all local times and seasons.

For the diurnal studies of trough characteristics about 20 to 25 clearly identifiable troughs were available in each hour of local time in each season. Seasonal variations were deduced utilizing data collected in three successive years. Northern hemisphere data obtained during magnetically quiescent and slightly disturbed conditions i.e. Kp $\leq$ 3 were used in the statistical portion of this study.

RESULTS BELOW 1500 km

a. Definition of Trough Parameters

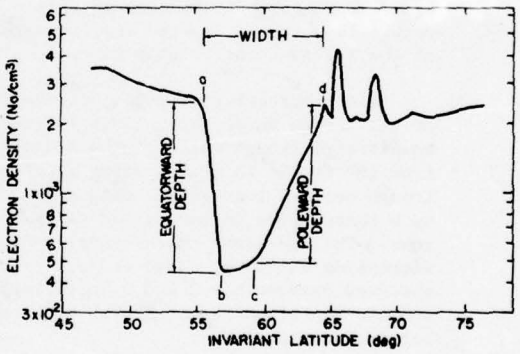


Fig. 1. Example of low altitude trough (<1500 km) where points 'a' and 'b' denote the location of top and base of the equatorial edge respectively. Points 'c' and 'd' denote the location of the base and top of the poleward edge.

A representative low altitude trough is shown in Fig. 1. Point 'a' denotes the location of the trough equatorward edge. It is the point marking the onset of a major decrease in ionization density with increasing latitude.

'b' denotes the base of the equatorward wall, 'c' the base of the trough poleward wall. The top of the poleward edge, point 'd' is the intersection of lines drawn along the trough poleward wall and through the first ionization maximum in the precipitation region. The ratio of the densities at points a/b and d/c represent the trough amplitudes at the equatorward and poleward edges respectively.

While there is considerable variation in the trough amplitude, width and gradient from orbit to orbit as illustrated in Figs. 2, 3 and 4, points 'a' through 'd' can usually be readily measured for altitudes below about 1500 km. The widths of the equatorward and poleward walls typically range from 1° to 4°. The high latitude precipitation region extends over several degrees and is highly structured The trough width and amplitude are consistently smaller on the dayside than on the nightside as illustrated in Figs. 4 and 2, respectively. The equatorward edge of the trough wall point 'a' of Fig. 1, was taken as the trough location for the study of results below 1500 km.

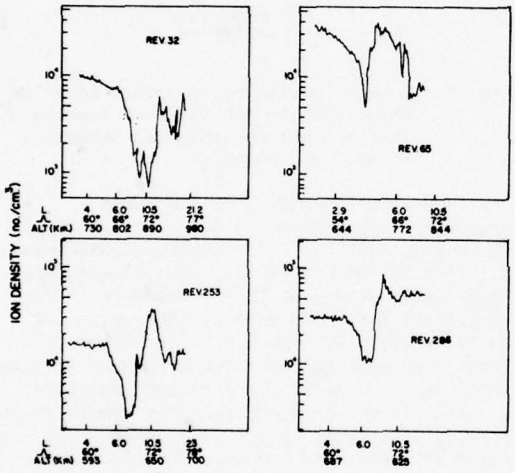


Fig. 2. Nighttime low altitude (<1000 km) trough examples.

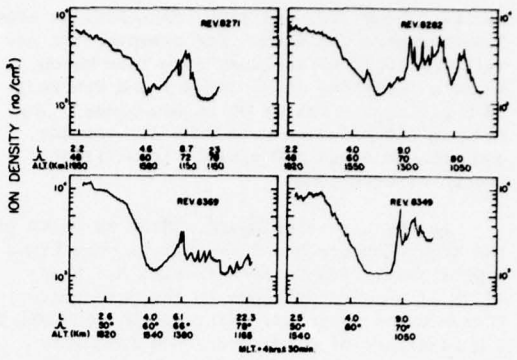


Fig. 3. Examples of troughs between 1000 and 1600 km within 4 hours of midnight.

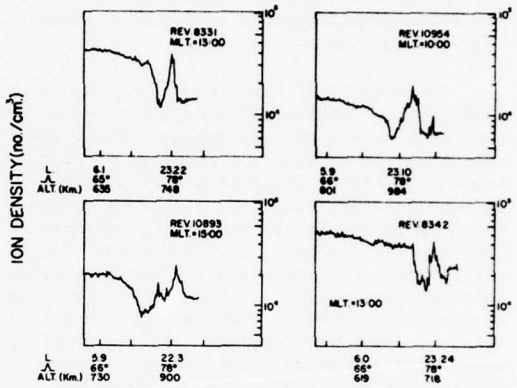


Fig. 4. Low altitude (<1000 km) daytime trough examples within 3 hours of noon.

b. Trough Occurrence Frequency

The trough occurrence frequency as a function of local time is given in Fig. 5 for altitudes below 1500 km.

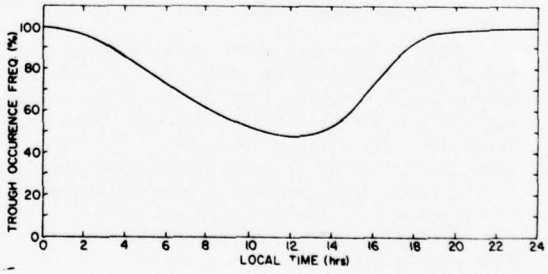


Fig. 5. The trough occurrence frequency versus local time for altitudes ≤1500 km.

For each hour of local time, data from at least 3 months were utilized. For example, the results at 19:00 LT includes data from March, August, September 1969, January and February 1970 giving a total of 65 observations. The results are based on data from all seasons and include about 830 clearly identifiable trough observations.

In the nighttime hours, 19:00 to 05:00 LT the trough occurrence frequency is very high, approximately 96% as seen in Fig. 5. Near 05:00 LT a sharp decrease in the occurrence frequency is observed. After 08:00 LT there is a gradual decrease in occurrence frequency with time reaching a minimum value of approximately 48% near local noon. At about 13:00 LT the occurrence frequency begins to increase reaching the maximum nighttime value at 19:00 LT. It is seen that the afternoon increase in the occurrence frequency is somewhat steeper than the morning decrease.

The results of Fig. 5 represent the first quantitative determination of trough occurrence frequency over a 24 hour period. These results are in agreement with the findings of Tulunay and Sayers (1971) which show a broad maximum during the night hours and a minimum within $\pm$ 3 hours of local noon in the northern winter hemisphere. Taylor et al. (1970) and Tulunay (1973) have reported the existence of persistent daytime troughs. Miller (1974) found no daytime troughs below 2500 km from the ISIS I electron probe measurements. Miller's ISIS I sensor had a spatial resolution of 9° and hence could not resolve the high latitude troughs with widths typically ranging from 2° to 6°.

Brinton et al (1969 and 1970) have shown that the ion composition in the topside ionosphere at mid and high latitudes consists predominantly of O^+ on the dayside. The midday occurrence frequency of 48% shows that the production of O^+ by solar UV radiation frequently dominates over ion depletion mechanisms.

c. Trough Location

Fig. 6 shows the mean location of the trough equatorward edge (point 'a' of Fig. 1) versus local time for each of the four seasons. Each of these four profiles is based upon at least 400 well defined troughs. It is seen that the summer profile is symmetrical within $\pm$ 4 hours of midnight and is located between L = 3.3 and 4.0. In the morning between 04:00 and 07:00 LT, there is a sharp poleward movement with an increase of 3 L units. In the dawn-noon sector, the summer profile gradually moves to higher L values reaching a maximum of L = 12.5 $\pm$ 1.0 around 11:30 LT. Within 4 hours of local noon, the trough is found to be located at the equatorward edge of the cusp precipitation region. In the afternoon sector, the trough moves gradually equatorward to a value of L = 5 near dusk. The summer trough location profile is nearly elliptical in shape except for the LT period, 04:00 to 07:00 LT.

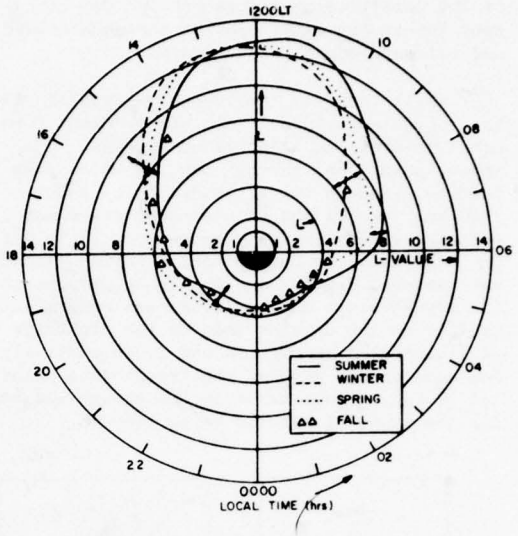


Fig. 6. Diurnal variation of trough location below 1500 km for the four seasons. The bars are the standard deviation of the measurements.

The winter trough location moves gradually inward from L = 5.5 to 3.5 between 18:00 and 04:00 LT. This equatorward movement at night is consistent with the characteristic nighttime movement of the plasmapause in the equatorial plane (Carpenter, 1966). In the 04:00 to 07:00 LT sector, the winter profile shows a gradual movement toward higher L values until 09:00 LT after which a rapid poleward movement is observed locating the trough at its peak value of about L = 12.5 at noon. The rapid movement after 09:00 LT represents the effect of the onset of sunrise in the winter hemisphere. In the noon-dusk sector, the winter trough profile moves gradually from L = 12.5 to 5.5. The winter profile is also elliptical in form.

The spring and fall trough profiles shown in Fig. 6 are similar in form to the summer and winter profiles and generally lie within the envelope defined by the summer and winter locations throughout a 24 hour period. The profiles for all the four seasons approach their highest L values near noon.

The standard deviations of the measured trough locations are shown as bars in Fig. 6; they were deduced using all trough data available in a specific hour of LT in a given season. They are of the order of $\pm$ 1 L unit

during the daytime and $\pm$ 0.4 L near midnight.

The standard deviation calculations show that there is no significant seasonal variation in the trough location except in the 04:00 to 09:00 LT sector, where the effect of the onset of sunrise with season is large.

d. Comparison with Other Trough Measurements

Since the seasonal effects are small, the mean trough location over all seasons was calculated for a comparison with published trough data (Fig. 7). The trough location deduced by Muldrew (1965) from f_0F_2 observations from the Alouette 1 Topside Sounder from September 1962 to March 1963 is also shown in Fig. 7.

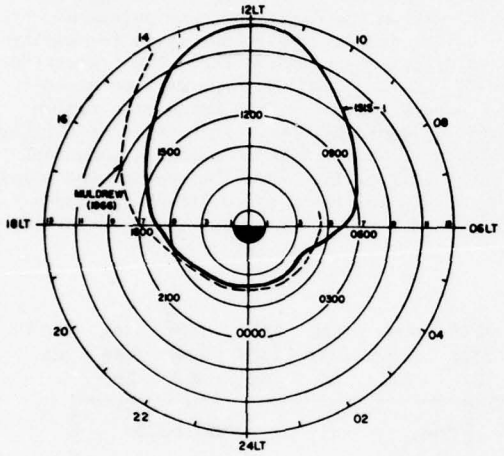


Fig. 7. Comparison of the diurnal variation of the trough location averaged over all seasons with the trough measurements of Muldrew (1965) (<1500 km).

Between 14:00 and 18:00 LT the two profiles have similar shapes although Muldrew's curve is located 1 to 2 L units higher. From 18:00 to 05:00 LT, the two profiles follow one another very closely. It should be noted that there is no "evening bulge" in the trough location in the two results as has been observed in the equatorial plasmapause location by Carpenter (1966), Chappell (1972) and others. The results are also in agreement with the low altitude trough studies of Tulunay and Sayers (1971) and Tulunay and Grebowski (1975) on the nightside. The last two investigations were confined to regions of L < 7 and hence the high latitude daytime troughs would be outside the range of these investigations.

RESULTS ABOVE 1500 km

a. Nightside

The region of significant nightside ionization depletion extends to lower latitudes with increasing altitude. Above 2000 km the equatorial wall of the trough frequently extends 15°-20° in latitude with highly variable shapes. Fig. 8 shows some typical examples of trough density variations. It is seen that there may be a uniform decrease of density with increasing latitude or two or more changes in slope. The high latitude boundary becomes more difficult to define. The poleward edge of the depletion region is marked by one or several sharp spikes in the ionization, each having a width of 1°-2°. The nightside high altitude trough is found on over 95% of the orbits examined.

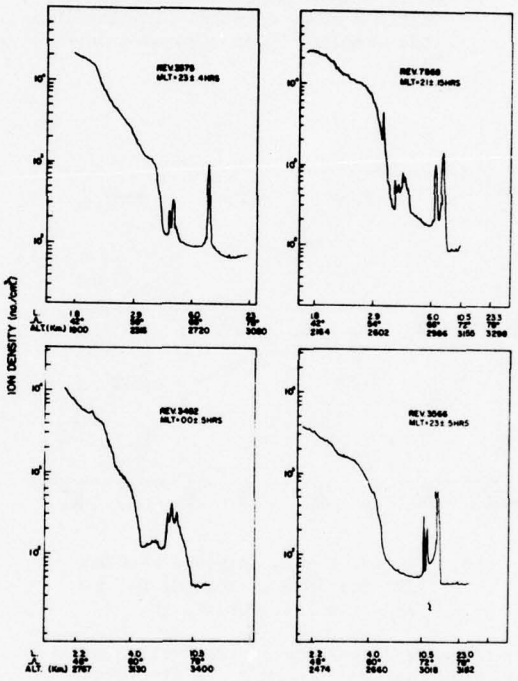


Fig. 8. Examples of nighttime trough measurements at altitudes greater than 2300km.

b. Dayside

Examples of thermal ion density observations near local noon at altitudes greater than 1500 km are given in Figs. 9 and 10. The amplitude of the high latitude trough (hereafter referred to as T_1), which was approximately 3 for altitudes less than 1500 (Fig. 4) gradually reduces to values less than 2 for altitudes greater than 2000 km (Fig. 9).

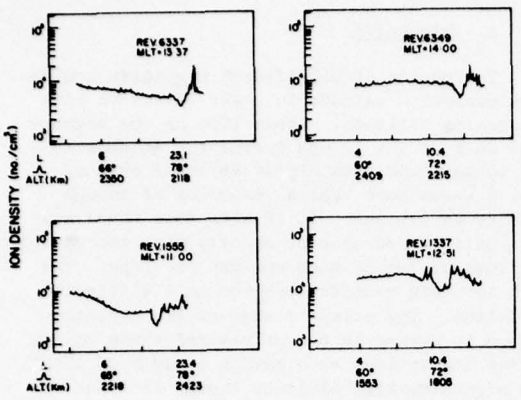


Fig. 9. Daytime high altitude trough examples of T_1 - the high latitude trough, within 2 hours of noon. The low latitude gradient T_2 is also seen on Rev. 1555.

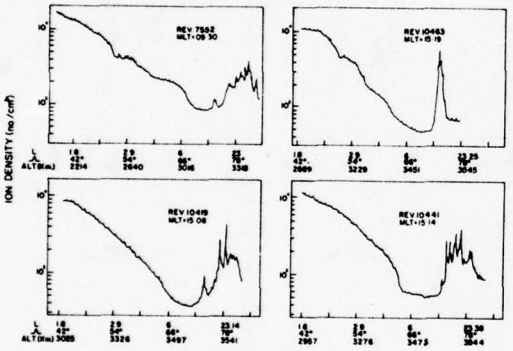


Fig. 10. Daytime trough examples between 2300 and 3500 km showing T_2, the low - mid latitude trough.

The frequent appearance of the smaller amplitude high latitude trough T_1 at altitudes above 1500 is consistent with the findings of Münch et al., (1977) based on INJUN V results. Simultaneous comparison of the trough densities with INJUN particles and electric field measurements showed that T_1 is located at the equatorial edge of the cusp where there are found sharp electric field reversals which indicate shifts in the plasma convection velocity. Increases in the electron temperature by factors of 2 to 3 and a shift from isotropic high energy particles to lower energy anisotropic magnetosheath-like electrons and protons were also observed.

Schunk et al. (1975) have shown that the existence of horizontal electric fields and elevated electron and ion temperatures produce depletions of O^+, a major ion at high latitudes, by increasing the ion loss rate, increasing the ion scale height and by changes in chemical composition. The present results together with the INJUN measurements reported by Münch et al. (1977) strongly support the conclusion of Schunk et al. (1975) that electric fields and enhanced charged particle temperatures make a significant contribution to the formation of the dayside high latitude trough.

Significant daytime gradients are also found to develop between L = 2 and 6 with increasing altitude (Fig. 10). These lower latitude gradients or troughs which we will refer to as T_2, are observed on 50% of the dayside orbits. As on the nightside, the poleward edge of the daytime depletion region is usually marked by spikes in ionization. The transition from T_1 only to T_1 and T_2 type dayside structures occurs gradually in a transition region between 1300 and 2000 km. An example of a fully developed T_1 and T_2 type ionospheric structure is given in Fig. 11. Here the equatorward walls of T_1 and T_2 are found at invariant latitudes of 78.5 and 54°, respectively.

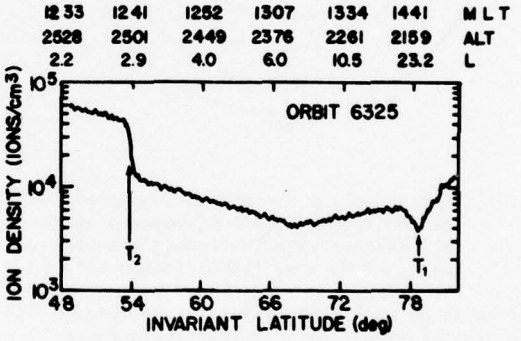


Fig. 11. An observation of both high and low latitude troughs, T_1 and T_2 respectively. Altitude 2100 to 2500 km.

The statistically derived location of the top and base of the "equatorward trough wall" of T_2, vs local time for altitudes above 2000 km is shown in Fig. 12. It is seen that on the nightside the top of the trough wall is consistently located close to L = 2.0 (invariant latitude $\approx 45^\circ$) and its base is found at L = 4.4 ($\Lambda \approx 61^\circ$). On the dayside the base of the ion depletion region, T_2, is found at slightly higher latitudes. At local noon it is located at L = 6.5 ($\Lambda = 67^\circ$). The equatorward wall is the dominant feature of the high altitude ionization depletion region.

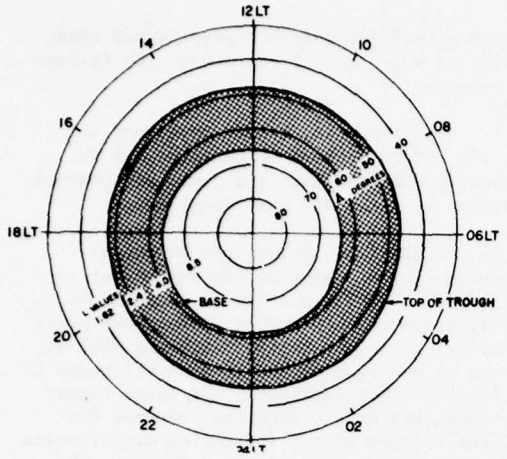


Fig. 12. Mean location of the top and base of the high altitude trough wall (T_2) versus local time for altitudes between 2000 and 3600 km.

As illustrated in Figs. 8 and 10 the ion density frequently changes by two orders of magnitude between the top and the base of the wall. This is much greater than the change in density below 1000 km, either day or night (Figs. 4 and 2). The high latitude trough wall T_2, of Fig. 12 corresponds to the plasmapause reported by Brace and Theis (1974) from ISIS I electron probe measurements above 2500 km. They identified the location of an ionization level of 10^3 electrons/cm^3 along the trough wall as the plasmapause, and obtained a nearly circular plasmapause boundary at about L = 4. As would be expected from the Brace and Theis plasmapause criteria their results lie in the shaded area of Fig. 12. T_2 also corresponds to the high altitude ISIS I dayside trough reported by Miller (1974). The T_2 type of ionization gradients were also observed by an electron sensor aboard the polar orbiting satellite OV3-1 in the 3000-5700 km altitude region between L = 2 and 6 (Bewersdorff and Sagalyn, 1971 and 1972).

We consider that the trough wall of Fig. 12 between about L = 2 and 6.5 is the result of partial filling and/or erosion of the outer plasmasphere. The combined effect of magnetic substorms (Park and Banks, 1974 and 1975) and of diurnal plasma depletions and replenishments prevent the outer shells of the plasmasphere from reaching saturation density.

DISCUSSION: TROUGH LOCATION AND THE PLASMAPAUSE

Nishida (1966 and 1967) first explained the formation of the plasmapause in terms of a magnetospheric convection model. Thomas and Andrews (1968), Rycroft and Thomas (1970), Tulunay (1972) and Tulunay and Grebowsky (1975) have all demonstrated a close relationship between the plasmapause and the mid-latitude trough at night. However, there are disagreements among these workers regarding the details of this association. Nishida and Thomas and Andrews, consider the equatorward trough edge to be the physically more significant part of the trough and have shown it to be correlated with the equatorial plasmapause, while Rycroft and Thomas (1970), Tulunay (1972) and Tulunay and Grebowsky (1975) have shown the trough minimum location to be correlated with the plasmapause. Tulunay and Hughes (1973) have shown that the location of the trough minimum is partially influenced by the location and movement of the auroral precipitation region at night and hence recommend the use of the more precisely measurable trough equatorward edge.

In Fig. 13 the trough location identified as the low latitude edge of the equatorward trough wall, for altitudes below 1500 km is compared with the plasmapause position deduced by Chappell et al. (1972), Carpenter (1966) and Taylor et al. (1970). At night the trough and plasmapause variations are very similar although the ISIS I trough locations are slightly equatorward of the plasmapause position. Thomas and Andrews (1968) obtained similar results. Since the trough equatorward wall is typically 1^o to 4^o wide, the equatorial trough base is located approximately 0.3 to 1 L unit poleward of the results shown. These results strongly suggest that the mid-point of the trough wall is an excellent indicator of the plasmapause during the night hours at low altitudes.

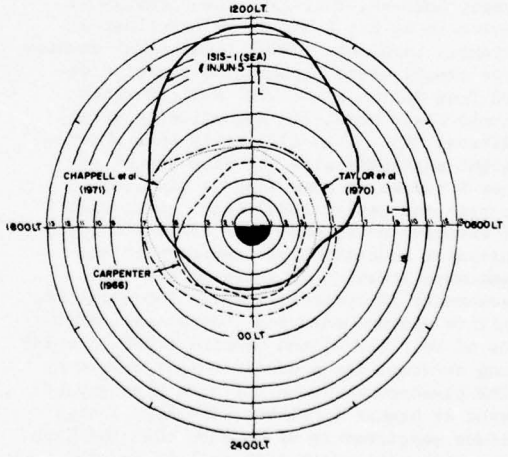


Fig. 13. Comparison of the mean location of the low altitude trough (<1500 km) versus local time with the plasmapause measurements of Carpenter (1966), Taylor et al. (1970) and Chappell et al. (1972).

The daytime trough location below 1500 km deduced from ISIS I and INJUN V measurements shown in Fig. 13 is considerably different from the reported plasmapause profiles. The ISIS I low altitude troughs are found at substantially higher latitudes ($L = 12.5 \pm 1^{o}$), just equatorward of the cusp precipitation region. The trough moves gradually to lower latitudes toward dusk while the plasmapause position lies between L = 4 and 7 from dawn to 1600 LT. The three sets of plasmapause locations in Fig. 13 do not show marked asymmetry between night and day while it is quite pronounced in the ISIS I trough location. The results of Tulunay (1973) and Tulunay and Grebowsky (1975) indicate a similar assymetry.

Examination of the location of the high altitude equatorward trough wall, T_2, (Fig. 12) shows that it is the base which may be reasonably compared with the plasmapause locations shown in Fig. 13. The base located at L = 4.4 near midnight and at L = 6.5 at noon is in good agreement with the plasmapause measurements. However, it should be noted in agreement with the finding of Brace and Theis (1974) that the trough shows no afternoon bulge.

Recent measurements by Gringauz and Bezrukikh (1976) using ion traps aboard Prognoz and Prognoz 2 satellites led them to conclude "a considerably higher latitude for the plasmapause at noon compared to that at midnight as a typical feature of the quiet magnetosphere". Their noon-midnight measurements of May 8 and August 24, 1972, for example, show a difference of approx. 3.5 L in the noon-midnight plasmapause location. On the average, however, they find the plasmapause location to be 1.5 L higher at noon than at midnight. Lemaire's (1976) theoretical studies of the steady state plasmapause position deduced from McIlwain's (1974) E3H convection electric field model for magnetically quiet conditions (Kp = 1 to 2) clearly show a noon-midnight asymmetry with the plasmapause at higher L values at noon than at midnight. Carpenter and Seely (1976) from recent quiet time Whistler drift path observations noted significant noon-midnight asymmetry in the plasmapause location contrary to earlier measurements (Carpenter, 1966). The whistler, satellite measurements and theoretical deductions of Wolf (1974) and Lemaire (1976) provide strong evidence for a noon-midnight asymmetry of the plasmapause, with the noon plasmapause located at higher L values. The ISIS I high altitude measurements of T_2 show that the base of the high altitude trough wall is in good agreement with these recent plasmapause results.

SUMMARY AND CONCLUSIONS

Examination of thermal ion and electron troughs in the topside ionosphere obtained by means of instruments flown on the ISIS-I and INJUN V satellites over a 3 year period under conditions when $Kp \leq 3$ has led to the following results:

1. The trough occurrence frequency is over 90% within 3 hours of midnight, it decreases to 60% near dawn and dusk, and reaches a minimum value of 48% near local noon.

2. At altitudes below 1500 km on the nightside, the midpoint of the equatorial trough wall at about L = 3.8 is found to be in good agreement with reported plasmapause positions. At altitudes between 1500 and 3500 km, the top of the equatorward trough wall moves to continually lower latitudes. At these higher altitudes, the equatorward wall becomes the dominant feature of the ionization distribution often extending 15^{o} to 20^{o} in latitude. The poleward edge of the trough becomes less well defined at high altitudes and is marked by ionization spikes 1^{o} to 2^{o} in width.

3. On the dayside below 1500 km the mean location of the trough T_1 at noon is $L = 12.5 \pm 1.0$, much higher than the dayside plasmapause location. T_1 persists above 1500 km with decreasing amplitude above this level.

4. The diurnal variation of the trough location was not found to vary with season except near sunrise.

5. The ISIS I data and simultaneous INJUN V measurements of electron density, ion & electron temperature, horizontal electric fields and particle measurements show that the high latitude trough, T_1, is located at the equatorward edge of the cusp. It is concluded that electric fields and enhanced thermal electron and ion temperature contribute to the formation of T_1 by increasing ion loss rates, ion scale height, and producing changes in the chemical composition of the region, in agreement with the theoretical analysis of Schunk et al. (1975).

6. At all altitudes above 1500 km a second ionization depletion region or trough T_2, is observed between L = 2 and 6.

7. The base of the high altitude trough wall (T_2 on the dayside) is found to lie between L = 4 and 6 in good agreement with plasmapause locations in the equatorial plane.

REFERENCES

Bewersdorff, A.B. and R.C. Sagalyn, Evidence of an evening ionization anomaly within the plasmasphere, Space Research XI, p. 1289, Akademic-Verlag, Berlin, 1971.

Bewersdorff, A.B., and R.C. Sagalyn, Spatial and temporal variations of the thermal

plasma between 3000 and 5700 km at L = 2 to 4, J. Geophys. Res., 77, 4734, 1972.

Brace, L.H. and R.F. Theis, The behavior of the plasmapause at mid-latitudes, J. Geophys. Res. 79, 1871-1884, 1974.

Brinton, H.C., R.A. Pickett, and H.A. Taylor, Diurnal and seasonal variations of atmospheric ion composition; correlation with solar zenith angle, J. Geophys. Res., 74, 4064, 1969.

Brinton, H.C., J.M. Grebowsky, and H. Mayr, Altitude variation of ion composition in the mid-latitude trough region - Evidence for upward plasma flow, J. Geophys. REs., 76, 3738, 1971.

Carpenter, D.L., Whistler studies of the plasmapause in the magnetosphere, 1. Temporal variations in the position of the knee and some evidence on plasma motions near the knee, J. Geophys. Res., 71, 693, 1966.

Carpenter, D.L. and N.T. Seely, Cross L plasma drifts in the outer plasmasphere: Quiet time patterns and some substorm effects, J. Geophys. Res., 81, 2728-2736, 1976.

Chappell, C.R., Recent satellite measurements of the morphology and dynamics of the plasmasphere, Rev. of Geophys. Space Physics, 10, 951, 1972.

Grebowsky, J.M., N.C. Maynard, Y.K. Tulunay and L.J. Lanzorotti, Coincident observation of ionospheric troughs and the equatorial plasmapause, Planet. Space Science, 24, 1177, 1976.

Gringauz, K.L. and V.V. Bezrukikh, Asymmetry of the earth's plasmasphere in the direction noon-midnight from data of measurements of satellites Prognoz and Prognoz 2, J. Atmos. Terr. Phys., 38, 1071, 1976.

Lemaire, J., Steady state plasmapause positions deduced from McIlwain's electric field models, J. Atmos. Terr. Phys., 38, 1039, 1976.

McIlwain, C.E., Magnetospheric Physics, Edited by B.M. McCormack, Reidel Publishing Co., Dordrecht, Holland, p. 143, 1974.

Miller, N.J., and L.H. Brace, Some winter characteristics of the northern high latitude ionosphere, J. Geophys. Res., 74, 5752, 1969.

Miller, N.J., The dayside mid-latitude plasmatrough, J. Geophys. Res., 79, 3795, 1974.

Muldrew, D.B., F-layer ionization troughs deduced from Alouette data, J. Geophys. Res., 70, 2635, 1965.

Münch, J.W., H.J. Braun, G.R. Pilkington, R.C. Sagalyn, and P.J.L. Wildman, Thermal electron densities and temperatures in the dayside cusp, J.A.T.P., 39, 699, 1977.

Nishida, A., Formation of plasmapause or magnetospheric knee by the combined action of magnetospheric convection and plasma escape from the tail, J. Geophys. Res., 5699, 1966.

Nishida, A., Average structure and storm-time change of the polar topside ionosphere at sunspot minimum, J. Geophys. Res., 72, 6051, 1967.

Park, C.G., and P.M. Banks, Influence of thermal plasma flow on the mid-latitude nighttime F_2 layer; Effects of electric fields and neutral winds inside the plasmasphere, J. Geophys. Res., 79, 4661, 1974.

Park, C.G., and P.M. Banks, Influence of thermal plasma flow on the daytime F_2 layer J. Geophys. Res., 80, 2819, 1975.

Rycroft, M.J. and J.O. Thomas, The magnetospheric plasmapause and the electron density trough at the Alouette I orbit, Planet, Space Sci., 18, 65, 1970.

Sagalyn, R.C., M. Smiddy and J. Wisnia, Measurement and interpretation of ion density distributions in the daytime F regions, J. Geophys. Res., 68, 199, 1963.

Sagalyn, R.C. and M. Smiddy, Charged particle measurements by means of electrostatic probes, electron density and temperature measurements in the ionosphere. COSPAR Tech. Manuals, p. 90, Commun. Space Res., Paris, 1967.

Sagalyn, R.C., M. Smiddy and M. Ahmed, High latitude irregularities in the topside ionosphere based on ISIS-I thermal ion probe data, J. Geophys. REs., 79, 4252, 1974.

Sharp, G.W., Midlatitude trough in the night ionosphere, J. Geophys. Res., 71, 1345, 1966.

Schunk, R.W., W.J. Raitt, and P.M. Banks, Effect of electric fields on the daytime high latitude E and F regions, J. Geophys. Res., 80, 3121, 1975.

Smiddy, M. and R.C. Stuart, An analysis of the behavior of a multigrid spherical sensor in a drifting Maxwellian plasma, Rep. AFCRL-69-0013, Phys. Sci. Res. Paper 364, U.S. Air Force Cambridge Res. Labs., Bedford, MA, 1969.

Taylor, H.A., H.C. Brinton and A.R. Deshmukh, Observations of irregular structure in thermal ion distributions in the dusk side magnetosphere, J. Geophys. Res., 75, 2481, 1970.

Taylor, H.A. and G.R. Cordier, In-situ observations of irregular ionospheric structure associated with the plasmapause, Planet. Space Sci., 22, 1289, 1974.

Taylor, H.A., J.M. Grebowsky, and A.J. Chen, Ion composition irregularities and ionoshperic-plasmaspheric coupling: Observations of a high latitude ion trough, J. Atmos. Terr. Phys., 37, 613, 1975.

Thomas, J.O. and M.K. Andrews, Transpolar Ionospheric Plasma, 1. Plasmasphere Termination, J. Atmos. Terr. Phys., 37, 613, 1975.

Tulunay, Y. and J. Sayers, Characteristics of the mid-latitude trough as determined by the electron density experiment on Ariel III, J. Atmos. Terr. Phys., 33, 1737, 1971.

Tulunay, Y., Magnetically symmetric detection of the mid-latitude electron density trough by Ariel III satellite, J. Atmos. Terr. Phys. 34, 1547, 1972.

Tulunay, Y., Global electron density distributions from the Ariel III satellite at mid-latitudes during quiet magnetic periods, J. Atmos. Terr. Phys., 35, 233, 1973.

Tulunay, Y. and A.R.W. Hughes, A satellite study of the mid-latitude trough in electron density and VLF radio emissions during the magnetic storm of 25-27 May 1967, J. Atmos. Terr. Phys., 35, 1973.

Tulunay, Y. and J.M. Grebowsky, Temporal variations in the dawn and dusk mid-latitude trough positions measured (Ariel III, Ariel IV) and modelled, Ann. Geophys., t. 31, fasc. 1, 29, 1975.

Wolf, R., Calculations of magnetospheric electric fields in magnetospheric physics (Ed. B.M. McCormac, D. Reidel Pub. Col., Dordrecht, Holland), p. 167, 1974.

Wrenn, G.L. and W.J. Raitt, In-situ observations of mid-latitude ionospheric phenomena associated with the plasmapause, Ann. de Geophys., 31, 17, 1975.

ATS-6 OBSERVATIONS OF IONOSPHERIC/PROTONOSPHERIC ELECTRON CONTENT AND FLUX

L. Kersley*, H. Hajeb-Hosseinieh and K.J. Edwards
University College of Wales
Aberystwyth, U.K.

Abstract Measurements of protonospheric content obtained at Aberystwyth from observations of the ATS-6 satellite radio beacon are reported. The monthly median diurnal behavior shows protonospheric contributions of approximately 15 to 20% to the total content along the ray path by day, rising to a predawn maximum of 35% in summer and more than 40% in winter. The results are shown to be typical of those expected from other European stations and differences from earlier American measurements are explained in terms of ionospheric interactions in the conjugate hemisphere. The temporal gradients of protonospheric content provide information on the net integrated ionospheric/protonospheric plasma fluxes and the results obtained confirm the importance of plasma exchange with both local and conjugate ionospheres.

INTRODUCTION

For more than a decade observations of polarization rotation of VHF transmissions from geostationary satellites have provided measurements of the so-called total electron content along the ray path, a parameter of importance in ionospheric group delay corrections. In practice, the weighting effect of the geomagnetic field limits the measurement to the ionospheric part of the path below some arbitrary height generally taken to be about 2500 km; however at times a significant fraction of the total number of electrons may be above this level. The ATS-6 satellite radio beacon group delay transmitter has enabled measurements to be made of the actual total electron content along the path in addition to polarization measurements of what can now be termed Faraday electron content. The difference between these quantities thus provides an estimate of the protonospheric contribution to the columnar electron content. In this paper we present results of ATS-6 observations from a mid-latitude European station, Aberystwyth, U.K. (52.4°N, 4.1°W), for the solar minimum period November 1975 to July 1976 when the geostationary satellite was stationed above 35°E longitude.

EXPERIMENT

The ATS-6 radio beacon experiment has been described by DAVIES et al. (1972) and DAVIES et al. (1975). Two basic measurements are of concern here. First, the polarization rotation of a VHF carrier and secondly the phase of a modulation on the VHF transmission with respect to that of an identical modulation on a coherent UHF carrier.

(a) Polarization Rotation and Faraday Content

Measurement of the phase difference between the ordinary and extraordinary circular modes of the 140.056 MHz carrier allows the polarization rotation (Ω) to be determined. This rotation can be related to ionosphere quantities along the ray path (s) by

$$\Omega = \frac{K}{f^2} \int_s N f_L ds \qquad 1.$$

where f is the wave frequency, K a constant, N electron density and f_L longitudinal gyrofrequency. If a mean value of f_L can be determined representative of conditions along the

* At present: NRC/NAS Senior Resident Research Associate,
Air Force Geophysics Laboratory, Hanscom AFB, MA 01731, U.S.A.

ionospheric path then the above equation can be written

$$\Omega = \frac{K}{f^2 \bar{f}_L} \int_0^S F \, Nds = \frac{K}{f^2 \bar{f}_L} N_F \qquad 2.$$

where N_F is the so-called Faraday content along the ray path. Because of the weighting of the geomagnetic field N_F can be considered as a measure of the ionospheric electron content up to some arbitrary height (h_F) which model studies have shown to be generally between 2000 and 3000 km.

The variation of f_L along the Aberystwyth/ATS-6 path, plotted as a function of height, is shown in Fig. 1. It can be seen that the parameter maximizes at about 200 km and is relatively insensitive to height below about 500 km, a shape which has important consequences for the accuracy of the Faraday and protonospheric content measurements.

A fixed value of $\bar{f}_L = 0.817$ MHz corresponding to a mean ionospheric height of 420 km has been used in the present work. Thus, from Equation 2, the relationship between the measured polarization rotation (in degrees) of the 140.056 MHz carrier and the Faraday electron content (in m^{-2}) becomes

$$N_F = 4.96 \times 10^{14} \, \Omega \qquad 3.$$

(b) Modulation Phase and Total Electron Content

The other angular parameter measured by the Aberystwyth receiver is the phase of a 1 MHz modulation on the 140 MHz carrier with respect to that of an identical modulation on a coherent 360 MHz carrier. The ionospheric modulation phase delay, for ordinary wave components, is given by

$$\phi = -K \int_s \left[\frac{1}{f_2+f_L} - \frac{1}{f_1+f_L} - \frac{1}{f_4+f_L} + \frac{1}{f_3+f_L}\right] N ds \qquad 4.$$

where the suffixes refer to the respective signal frequencies, $f_1 = 140.0560$ MHz, $f_2 = 141.0564$ MHz, $f_3 = 360.1440$ MHz and $f_4 = 361.1444$ MHz.

The longitudinal gyrofrequency is always less than 0.83 MHz for the ATS-6 to Aberystwyth geometry and is thus small compared to the signal frequencies. Hence if an average value $\bar{f}_L$ is chosen for the path the above equation can be written

$$\phi = -K \left[\frac{1}{f_2+\bar{f}_L} - \frac{1}{f_1+\bar{f}_L} - \frac{1}{f_4+\bar{f}_L} + \frac{1}{f_3+\bar{f}_L}\right] \int_s N ds \qquad 5.$$

that is

$$\phi = -K \left[\frac{1}{f_2+\bar{f}_L} - \frac{1}{f_1+\bar{f}_L} - \frac{1}{f_4+\bar{f}_L} + \frac{1}{f_3+\bar{f}_L}\right] N_T \qquad 6.$$

where N_T is the total electron content along the slant path from the satellite to the receiving antennas.

Using $\bar{f}_L = 0.817$ MHz, corresponding to a mean-ionospheric height of 420 km, the total electron content (in m^{-2}) can be obtained from the modulation phase delay (in degrees)

$$N_T = -4.87 \times 10^{14} \, \phi \qquad 7.$$

(c) F-factor

An additional experimental parameter which can be obtained from the ATS-6 angular data is the shape factor or F-factor which is a weighted average electron gyrofrequency along the path. This has been defined by DAVIES et al. (1975) as

$$F = \int_s N f_L \, ds \; / \int_s N \, ds \qquad 8.$$

By substitution from Equations 1 and 5 F can be related to the measured parameters by

$$F = 0.832 \, \frac{\Omega}{\phi} \qquad 9.$$

(d) Protonospheric content

It can be seen that absolute measurements of the total and Faraday contents to a sufficient accuracy will allow the electron contribution from ∿2500 km to the geostationary satellite to be determined. The effective upper boundary is however the plasmapause which is usually well below the geostationary orbit height. The protonospheric (some workers prefer the term plasmaspheric) electron content (N_p) can thus be found from

$$N_p = N_T - N_F \qquad 10.$$

RESULTS

Diurnal plots of median values of N_T, N_F, N_p, N_p/N_T% and F for each of the nine months under study are presented in Fig. 2. The diurnal variations of N_T and N_p are essentially similar in character indicating that the ionospheric contribution dominates the total electron content at least during daytime. By contrast, N_p shows only a small diurnal variation with minimum values in the predawn

hours around 3 x 10^{16} m^{-2} for all months and an afternoon maximum of about 4 x 10^{16} m^{-2} in winter rising to approximately 5 x 10^{16} m^{-2} in summer. The protonospheric content expressed as a percentage of the total has values by day typically in the range 15 to 20% while the predawn maximum of about 35% in summer exceeds 40% in winter. The diurnal variations of F show a predawn minimum about 0.5 MHz while the daytime value is generally in the region of 0.66 MHz.

Some insight can be gained into the physical processes responsible for the observed variations in N_p by considering the temporal rate of change of the parameter. Protonospheric content is a measure of the plasma content of a region of the high plasmasphere above ∿2500 km altitude where production and loss are unimportant and the dominant mechanism for content changes is plasma diffusion up and down the field lines in response to interaction with the underlying ionosphere. The temporal gradient of protonospheric content thus provides a near continuous estimate of the net integrated protonospheric flux responsible for the filling and draining of the region. It should be remembered that the protonospheric content measured in the ATS-6 experiment refers to the slant path to the satellite intersecting flux tubes in the range L∿1.7 to L∿4 on average at the plasmapause. The protonospheric flux estimated from these measurements is thus an integrated parameter in contrast to the more direct measurement essentially along a particular field tube given by the whistler technique (PARK, 1970).

Protonospheric flux measurements (dN_p/dt) estimated from three-hour running mean smoothed hourly values of protonospheric content are presented in Fig. 3. This shows the mean diurnal variation of protonospheric flux for December 1975, January 1976 and June, July 1976 representing winter and summer conditions respectively. In interpreting these fluxes it must be remembered that a given field line interacts with the ionosphere at its terminations in both local and conjugate hemispheres, so that the flux being measured represents the net integrated filling or draining rate of the tubes of interest. To assist in interpretation, the times of sunrise and sunset in both local and conjugate hemispheres at 350 km at the ionospheric base of the L=2 flux tube, which intersects the ATS-6 ray path at ∿5000 km altitude, are marked. In June and July a positive upwards flux is found some hours after sunrise. It should be noted that time constants of the order of hours are probably involved before ionospheric changes can be reflected in protonospheric content, allowing for the O^+-H transition barrier and the travel time of the plasma along the long flux tubes. Following the post sunrise period of upwards flux, for much of the summer day the fluxes do not differ significantly from zero, however after conjugate sunset a strong downwards net flux is observed at a time when the still sunlit ionosphere in the local hemisphere is displaying the late afternoon peak in both maximum density and content. It would thus appear that depletion at this time is essentially to the conjugate ionosphere. In December and January, upwards fluxes are found by day with a post sunset depletion. However, it is interesting to note that net upwards fluxes are also found in the early morning hours apparently associated with the much earlier sunrise in the conjugate summer hemisphere.

DISCUSSION

The protonospheric content variations obtained at Aberystwyth when the ATS-6 satellite was stationed at 35° E differ significantly from those already reported from the earlier American sector phase of ATS-6 operations. Two contrasting features of note are the generally lower magnitudes found in the American observations particularly in summer and a diurnal variation of the earlier data for winter through equinox which minimizes by day (FRITZ, 1976; SOICHER, 1976; JOHANSON and KLOBUCHAR, 1977). In interpreting these differences it must be remembered that the measured protonospheric content changes are largely consequent upon interaction with the ionosphere at the feet of the flux tubes intersecting the ray path. Fig. 4 shows the ionospheric terminations at 350 km altitude in both local and conjugate hemisphere of the field lines crossing the ray path for the Aberystyth observations while the ATS-6 satellite was at 35° E. The important field lines for protonospheric content studies are those with intersections above ∿2500 km up to the plasmapause at say L∿4. It can be inferred from Fig. 4 that because of the convergence of the ray paths towards the satellite the geographic locations of the ionospheric terminations of the relevant field lines will alter by only a relatively small amount

for mid-latitude stations covering a wide range of longitudes. Thus, satellite, rather than observing station, longitude is an important factor in the protonospheric content measurements. Hence, the present observations can be taken as representative of mid-latitude observations from the European sector while the general concurrence of the earlier observations, already referred to, from several American stations is explained. The most apparent difference between the observing situation from Europe presented here and that from America with ATS-6 at 94° W longitude lies in the geographic latitudes of the field line terminations in the conjugate hemisphere. While for the present study the ionospheric regions in the conjugate hemisphere, interacting to contribute towards the observed protonospheric changes, lie at mid-latitudes, for the earlier American work the corresponding locations are at much higher geographic latitudes close to the Antarctic continent. The anomalous behavior of the continuously sunlit Antarctic ionosphere in this longitude sector in local summer (December/January) under the influence of the neutral wind is well documented (KING et al., 1968) and this factor, together with the long winter nights and the generally higher L-shells intersecting the American sector ray paths, can account for the differences between the European and American protonospheric contents (KERSLEY and KLOBUCHAR, 1977). The observed protonospheric fluxes show features which are in broad agreement with the theoretical model studies of MURPHY et al. (1976); namely post dawn upwards fluxes and post sunrise downwards fluxes which maximize and decay. However, the theoretical work has been confined to date to equinoxial studies with assumed equatorial symmetry as opposed to interactions with both hemispheres applicable to the present observations. The magnitudes of the fluxes are generally lower than those reported from whistler studies (PARK, 1970). However, it must be remembered that the latter are obtained from effectively direct measurements of tube contents whereas the present work reports median content changes along a slant path intersecting many field lines, albeit essentially along the flux tubes for the important lower protonospheric part of the range.

CONCLUSIONS

The monthly median protonospheric content shows diurnal variations which reflect the interactions with the underlying ionosphere. The contribution from the protonosphere amounts to some 15-20% of the total content by day, rising by night to a predawn maximum of 35% in summer and more than 40% in winter. It has been shown that observations reported here are expected to be typical of those obtained from other mid-latitude European stations and differences from earlier American measurements are explained in terms of ionospheric interactions in the conjugate hemisphere. The studies of protonospheric flux support the conclusion of the importance of the conjugate region to the interpretation of the data.

Acknowledgement Thanks are expressed to Mr. J. M. Johanson for the computations involved in the preparation of Fig. 4.

REFERENCES

Davies, K., R. B. Fritz and R. N. Grubb, The ATS-F/G radio beacon experiments, J. Environ. Sci., 15, 31-35, 1972.

Davies, K., R. B. Fritz, R. N. Grubb and J. E. Jones, Some early results from the ATS-6 Radio Beacon Experiment, Radio Sci., 10, 785-799, 1975.

Fritz, R. B., ATS-6 Radio Beacon Electron Content Measurements at Boulder, July 1974-May, 1975, Report-UAG-58, World Data Center A, Boulder, U. S. A., 1976.

Johanson, J. M. and J. A. Klobuchar, A comparison of average plasmaspheric electron content at two mid-latitude stations, Paper presented at A. G. U. Spring Meeting, Washington, D. C., U.S.A., June, 1977.

Kersley, L. and J. A. Klobuchar, Comparison of protonospheric electron content measurements from the American and European sectors, submitted to Geophysical Research Letters, 1977.

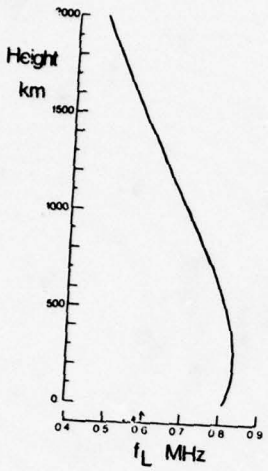
King, J. W., H. Kohl, D. M. Preece and C. Seabrook, An explanation of phenomena occurring in the high latitude ionosphere at certain Universal Times, J. Atmos. Terr.

Phys., 30, 11-23, 1968.

Murphy, J. A., G. J. Bailey and R. J. Moffett, Calculated daily variations of O^+ and H^+ at mid-latitudes - I. Protonospheric replenishment and F-region behavior at sunspot minimum, J. Atmos. Terr. Phys., 38, 351-364, 1976.

Park, C. G., Whistler observations of the interchange of ionization between the ionosphere and the protonosphere, J. Geophys. Res., 75, 4249-60, 1970.

Soicher, H., Diurnal, day-to-day and seasonal variability of N_E, N_T and N_O at Fort Monmouth, New Jersey, in Proceedings of COSPAR Satellite Beacon Symposium, pp. 231-243, Boston University, U. S. A., 1976.



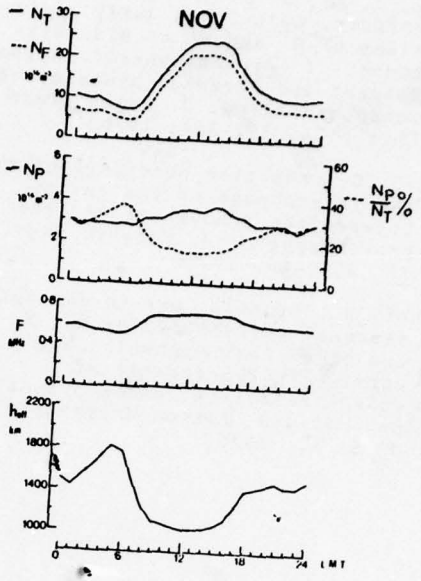
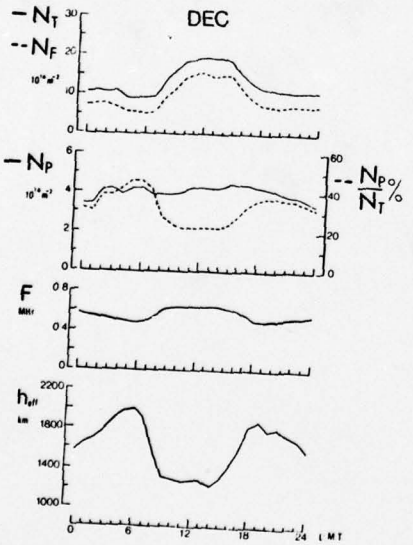


Fig. 1. Height variation of longitudinal gyrofrequency for the ATS-6 to Aberystwyth path below 2000 km.



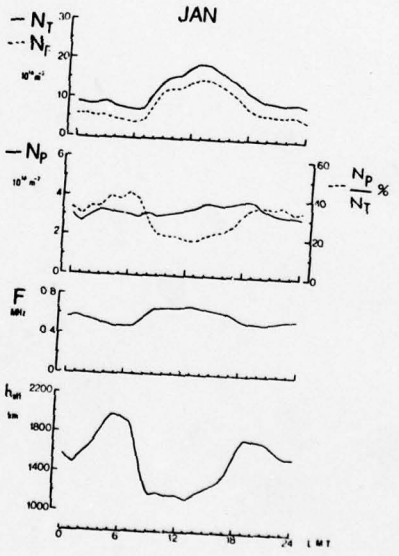


Fig. 2. Monthly median hourly values of N_T, N_F, N_P, N_P/N_T% and F.

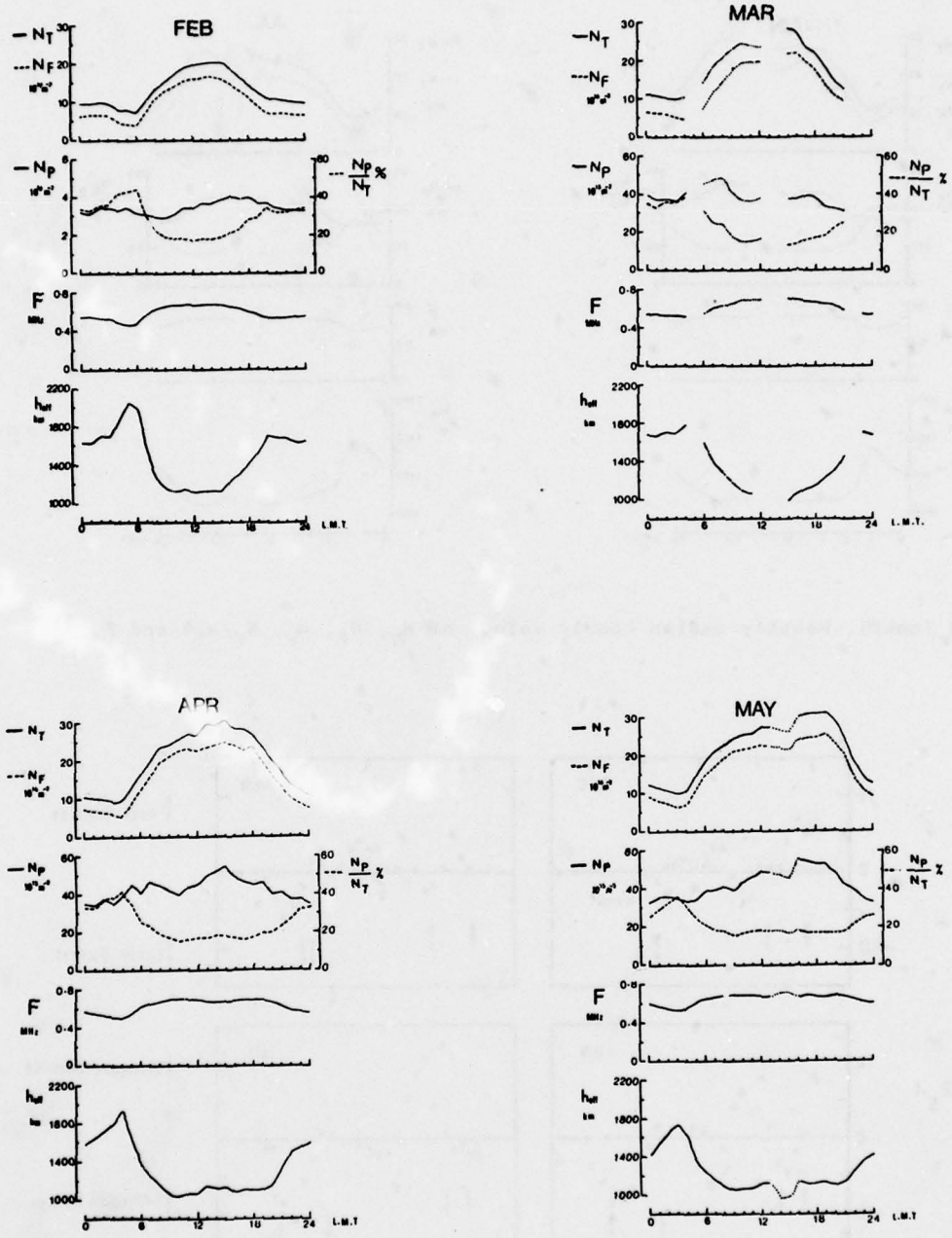


Fig. 2 (cont). Monthly median hourly values of N_T, N_F, N_p, N_p/N_T% and F.

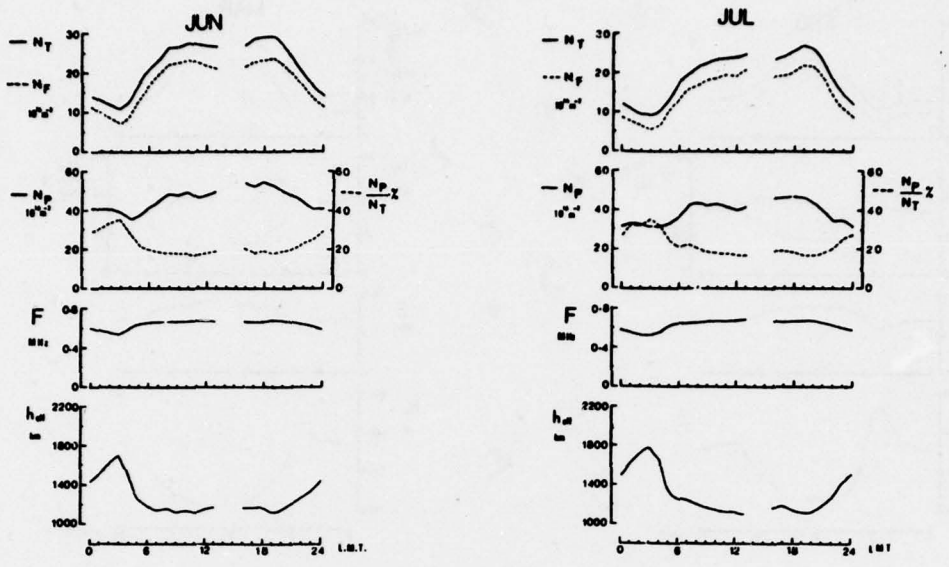


Fig. 2 (cont). Monthly median hourly values of N_T, N_F, N_p, N_p/N_T% and F.

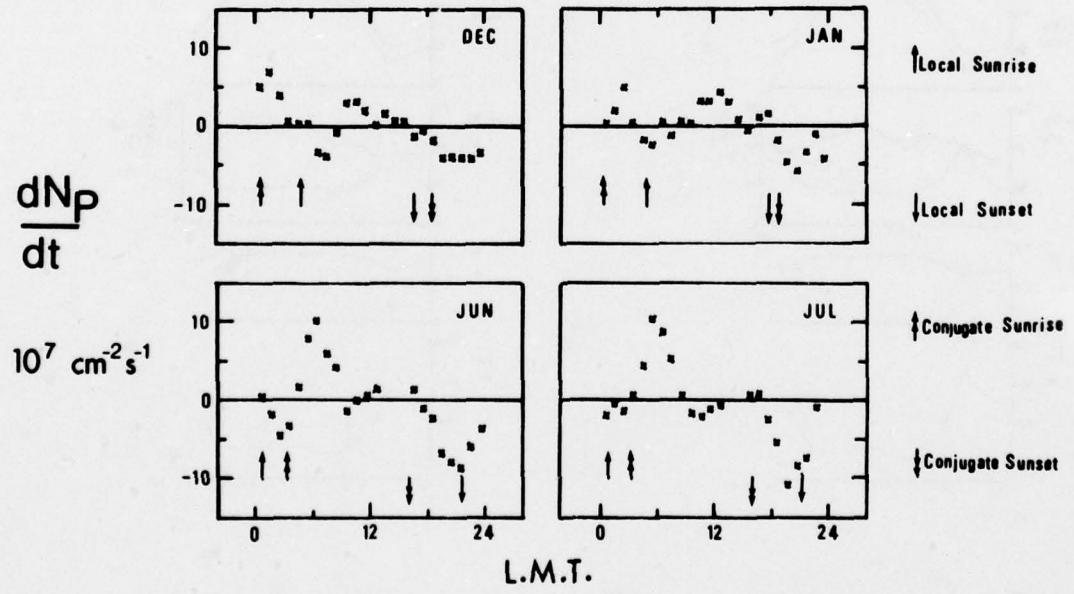


Fig. 3. Diurnal variations of integrated protonospheric flux (dN_p/dt) by month for December 1975, January, June and July, 1976.

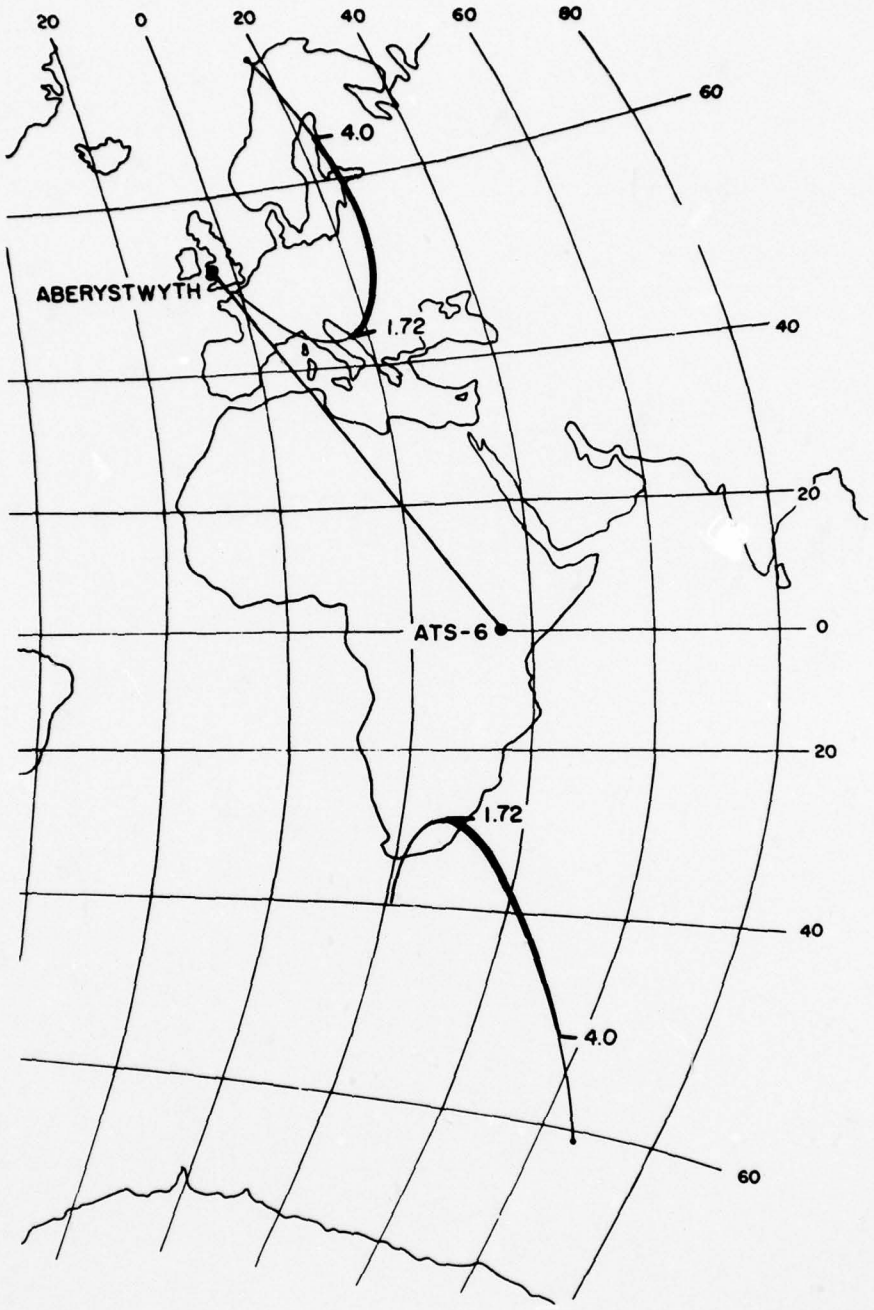


Fig. 4. Terminations at 350 km in both local and conjugate hemispheres of field lines intersecting the ATS-6 to Aberystwyth ray path. The regions of importance to measurements of N_p, corresponding to field line intersections from a height $\sim$ 2500 km to L $\sim$ 4, are marked by the heavier part of the curves.

PRECEDING PAGE BLANK - NOT FILMED

REMOTE IONOSPHERIC MONITORING

Jurgen Buchau and William N. Hall

Air Force Geophysics Laboratory, Hanscom AFB, MA 01731

Bodo W. Reinisch and Sheryl Smith

University of Lowell Center for Atmospheric Research, Lowell, MA 01854

ABSTRACT

A program for the development of automatic real-time monitoring of the ionosphere at a remote observing location is described. The Digisonde 128, a digital sounder in routine operation since 1970, provides digital data suitable for online computer processing. Analytical methods for the detection of ionospheric echoes and the determination of their virtual height, amplitude, and range spread have been developed. For real time application, these methods have been implemented in hardware using microprocessors. The Geomonitor and Geomonitor Display System (GDS) provide the capacility to perform the monitoring at any desired site separated from the remote observing location. The Geomonitor, in addition to analyzing vertical and backscatter digital ionograms, digitizes magnetometer, riometer, radio polarimeter, and satellite scintillation data for transmission to the using site. Compression of the digital ionogram data and the other geophysical and ionospheric data permits transmission over a 600-1200 baud telecommunications link to the GDS. The GDS formats and displays the data for the remote observer and analyzes the data to call attention to disturbances. For each ionogram, lines are printed summarizing the frequency extent of the observed echoes and the variation with height or range of the echo amplitudes. As further data arrive, lines are added to the printouts, resulting in time histories, so-called "ionospheric characteristics" of layer heights, backscatter ranges and critical or top frequencies. In addition to showing regular diurnal variations, the onset, type, and severity of ionospheric disturbances can be determined from these characteristics. To aid in the interpretation of the characteristics, ionograms are reconstituted from the ionospheric data messages. These with displays of the other geophysical and ionospheric data create a comprehensive display for evaluation by the observer.

INTRODUCTION

The high latitude ionosphere, strongly controlled by auroral particle precipitation and especially disturbed during auroral substorms, affects a variety of USAF and DOD systems, as well as military and commercial communications links operating in this environment. To advise the various military users of prevailing conditions, the AF Air Weather Service (AWS) has monitored routinely the state of the local arctic ionosphere and the onset of disturbances from various ground sites as among others Goose Bay, Labrador, Eielson AFB, Alaska, Tromso, Norway. The reports are collected and evaluated by the AF Global Weather Central (AFGWC) and advisories and warnings are being disseminated routinely or on special request through the Space Environment Support System (SESS).

The monitoring of this environment has for a long time been accomplished by trained personnel through hourly reports from the various sites, using a limited selection of geophysical parameters. To automate the process of data analysis and data transmission especially at remote sites, we have developed the Geomonitor (Reinisch and Smith, 1976). This system extracts the essential information from the digital

ionograms, supplied by the Digisonde (Bibl et al, 1970; Bibl and Reinisch, 1978), a digital ionosonde used for vertical incidence and backscatter soundings. Together with properly formatted digitized data from other geophysical sensors messages are formed that can be sent to Air Force Global Weather Central or to other user sites as a final step to remotely monitor the environment of interest. This remote monitoring capability is of special interest at high latitudes, since a.) the auroral effects routinely and severely disturb the ionospheric environment making 24 hour coverage and fast issue of warnings essential, b.) rapdily rising manpower costs and the difficulty to find qualified personnel willing to work for extended periods at these remote, high latitude stations require automation as a cost effective solution.

GOOSE BAY OVAL MONITOR STATION

Requirements for better specifications of the high latitude ionospheric and auroral environment surfaced in the mid- to late sixties, as AF surveillance systems increased their accuracy requirements, the use of an Over-the-Horizon Backscatter System in these disturbed regions began to be contemplated and effects on trans-ionospheric propagation started to become a major concern. AFGL started a large airborne program to improve the understanding of the structure and dynamics of the high latitude ionosphere. Flights between 1967 and 1971 indicated that the auroral oval concept (Feldstein and Starkov, 1967) provided a good ordering frame for various ionospheric phenomena. Airborne investigations of initially the noon sector of the oval (Whalen et al, 1971) and then the more disturbed and complicated night sector (Buchau et al, 1972; Wagner and Pike, 1972) led to a unified picture of the structure of the high latitude environment (Gassmann, 1972) and suggested the feasibility of monitoring this environment from a few selected points. To illustrate the concept, we show in Figure 1 the auroral oval (shaded area) for average magnetic conditions and the location of Goose Bay in relation to the oval in hourly increments. Large scale ionospheric entities ordered by the auroral oval are: a. The FLIZ (F-layer irregularity zone, Pike, 1972) generally colocated with the oval belt, b. The midlatitude F-layer trough (Muldrew, 1965) found south of the equatorward boundary of the night sector of the oval, c. Auroral Es, colocated with the oval belt, d. Auroral E, a particle produced thick E-layer belt coinciding with the oval in the night sector and found just south of the oval in the noon sectors, and e. D region enhancements, during substorms within the night sector, of the oval, and traveling through sunrise around the oval into the noon sector of the oval, where they arrive in a region between 60° and 70° corrected geomagnetic (CG) latitude within .5 to 2 hours after the onset of the substorm (Driatskiy, 1968; Elkins, 1972) and f. The polar cap ionosphere within the oval belt, with auroral, E-layer and F-region phenomena different from those in the adjacent oval. The diameter of the auroral oval and the auroral activity within the oval belt and the polar cap are under strong control of the interplanetary and the earth magnetic field. The equatorward edge of the midnight sector of the oval is found at 70° (CG) latitude under quiet (Q=0) conditions and at 59° CG latitude under very disturbed (Q=8) conditions. All the described ionospheric regimes and phenomena change their locations and/or their intensities as the oval expands or contracts.

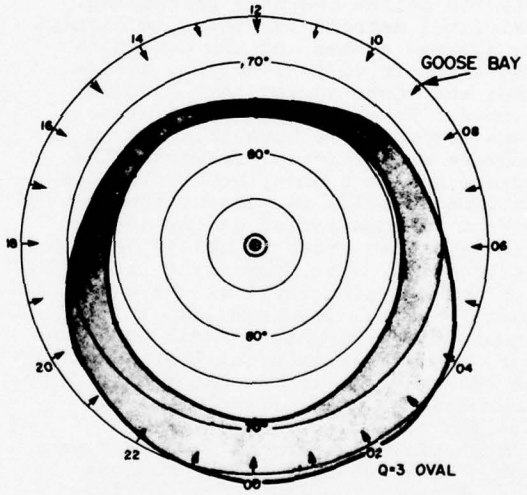


Figure 1 shows the auroral oval in a CG latitude-local time coordinate system. Goose Bay, located at 65° CG latitude, becomes an auroral oval station from 22:30 to 03:30 CGLT. During the other hours of darkness it is an F-layer trough station while in daytime it is between 500 to 1000 km to the south of the equatorward edge of the oval. While under the auroral oval, vertical incidence soundings, and riometer and magnetometer measurements allow the assessment of the state of the auroral ionosphere and the determination of the onset time and severity

of auroral disturbances. In the afternoon and evening hours, backscatter soundings directed towards the oval edge show strong irregularities which are associated with the aurora (Wagner and Pike, 1972) and thus permit the determination of the oval diameter many hours prior to the time, the oval moves over the station. In the early morning and pre-midday hours, Goose Bay is under the influence of the previously mentioned eastward drifting D-region enhancements associated with auroral substorms and monitoring of the existence of auroral disturbances in the midnight sector is possible for many hours.

Based on the evolving monitoring concepts the Air Force Geophysics Laboratory (AFGL) established in 1971 the Goose Bay Ionospheric Observatory. The station was equipped with riometers, magnetometers, satellite receivers for total electron content measurements, and a Digisonde 128 alternatingly connected to two separate transmitting antennas for vertical incidence and backscatter soundings. The Digisonde is a step frequency sounder with a 0.25 to 16 MHz frequency range. Phase coding and coherent integration are used to increase the signal-to-noise ratio. Envelope detection, i.e. power integration, is applied for backscatter soundings, since scatter type reflections or reflections from moving ionization fronts result in random or continuous (Doppler shift) phase changes, respectively, incompatible with a coherent integration scheme.

The two logarithmically compressed quadrature samples are integrated in 128 equidistantly spaced range bins (with selectable ΔZ) determining the amplitude with 6 bit resolution and the phase with 3 bits. The data are recorded on digital magnetic tape and, using an optically weighted font, are printed out on paper. Using available telecopier techniques the digital ionograms can be transmitted via telephone line to any other location for real time assessment of ionospheric conditions at Goose Bay.

Figure 2 shows in its left part a typical daytime ionogram obtained by the Goose Bay Digisonde. For each 1 MHz frequency band, shown between two frequency marks, 2160 characters of amplitude, phase and housekeeping (date-time-frequency, etc.) information is recorded on magnetic tape. The presently standardized 0-10 MHz ionogram requires the storage of 21600 characters. Transmission via telephone line has been accomplished requiring 2 seconds per frequency for a total of 3 minutes 20 seconds for the ionogram shown.

THE GEOMONITOR

In order to reduce the requirements for tape, prepare the data for automatic analysis and limit the amount of data to be transferred by data links to remote users, digital techniques of echo recognition were developed and implemented in the Geomonitor. Microprocessor controlled special electronic circuits achieve the high speed required for the simultaneous processing and display of the digital ionograms and the continuous data stream from various geophysical sensors.

For the processing of the ionograms initially the noise level on each frequency is established. Strong spread F or auroral Es echoes could lead to an overestimate of the noise level, thus suppressing weaker echoes. To circumvent this problem the noise level is determined separately for the lower and the upper 64 height bins by calculating the amplitude distributions for both ranges; the distribution which peaks at a lower amplitude is used to determine the noise level. The noise threshold is set at the positive half point of the distribution and only amplitudes larger than this level are considered as possible echoes. The noise threshold itself is recorded for reference.

The echo detection algorithm scans the 128 height bins on each frequency and detects up to six echoes, two from the E-region (<156 km) and four from the F-region. The selection of echoes is by average pulse amplitude, separately for the two regions. For two different echoes to be recognized as such they must be separated by a dip in amplitude down to the noise threshold. The echo spread is an important parameter in the assessment of the degree of disturbances, and it strongly influences the determination of ionospheric parameters such as foE and foF2. The Geomonitor determines and records, therefore, the spread of the main E and the main F echo.

The accurate heights of the leading edges of all six echoes is determined by sliding a standard pulse along an array of amplitudes with twice the resolution of the initial height steps. The exact virtual height of the echo is found at the position, where the average deviation (Bevington, 1969) between

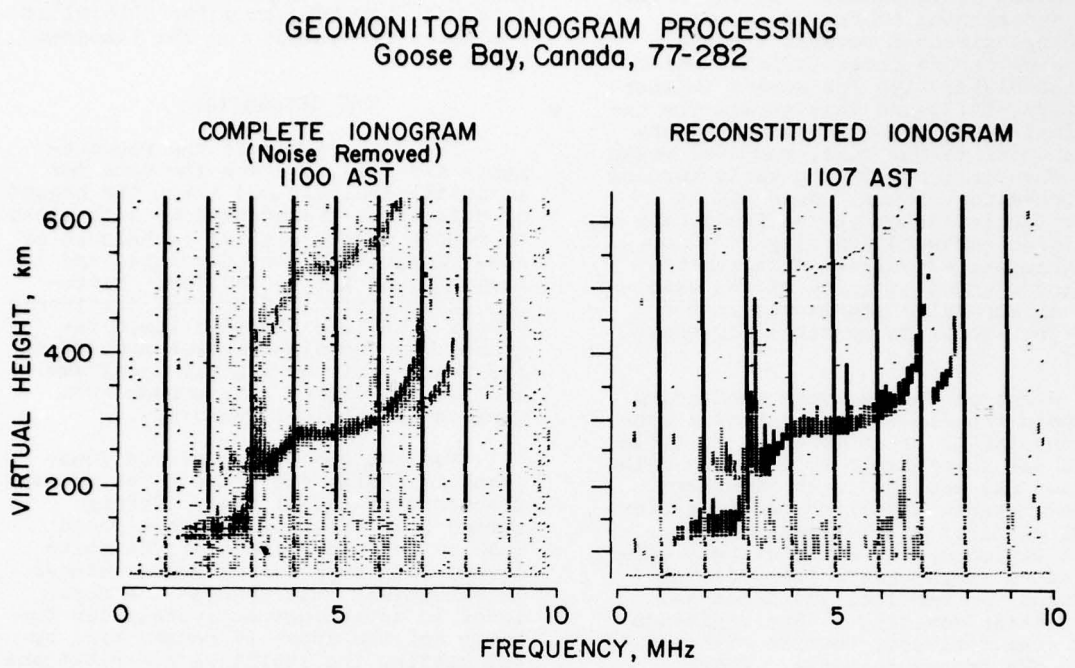


Figure 2. Geomonitor Ionogram Processing

standard pulse and (normalized) data is a minimum. The double-resolution array is generated by linear amplitude interpolation between two adjacent original height bins.

Finally, to investigate the dynamic height variations of the ionospheric layers, the Geomonitor calculates the so-called integrated heights. For each of the 128 height-bins the amplitudes are summed over all frequencies and normalized. This presentation was especially developed for use in the presentation of ionospheric characteristics to be discussed later.

The complement of data, with the addition of the gain setting on each frequency and the housekeeping information, for a standardized total of 128 frequencies, is collated or formatted into one digital record of 2340 characters, a reduction to about 10% of the original data. Evaluations have shown, that the chosen parameters and the number of echoes adequately depict an original ionogram for all routine and most special investigation purposes even under very disturbed conditions. The data are in a format perfectly suited for further processing, as the online determination of critical frequencies, the minimum frequency, layer heights and true height analysis. All these parameters can be determined using minimum computational effort. The development of the techniques to be applied is underway and will be concluded within the near future.

For verification of proper performance of the algorithms the collated ionograms described above are recast into the format of a regular Digisonde ionogram and presented on various displays. Shown in the right section of Figure 2 is such a "reconstituted" ionogram, taken 7 minutes after the one on the left, which is an unprocessed "cleaned" ionogram with amplitudes smaller than the noise level (see above) removed. The example is typical for the performance of the presently used algorithms. The high quality of the reconstituted ionogram is evident, minor problems as raggedness of the spread width will be corrected by refining the respective algorithms.

Sandwiched between the collated ionograms are the so-called "Geophysical Data", also packaged in a 2340 character long record representing 5 minutes of data. Analog signals from the three magnetometer channels, two riometers, satellite signals for Total Electron Content (TEC) and amplitude scintillation measurements are digitized and recorded. Additional analog

AD-A057 411 AIR FORCE GEOPHYSICS LAB HANSCOM AFB MASS F/G 4/1
COMPILATION OF PAPERS PRESENTED BY THE SPACE PHYSICS DIVISION A--ETC(U)
APR 78

UNCLASSIFIED AFGL-TR-78-0080 NL

2 OF 2
AD A057411



END
DATE FILMED
9-78
DDC

data up to a total of 15 can be added as required. Digitization rates presently used are 2 Hz for two scintillation channels and 0.1 Hz for the remaining 13 channels.

In its present operation the Geomonitor produces every five minutes one record of geophysical data and two records for two ionograms of various types (vertical, backscatter, coherent or power integration) as selected at the Digisonde. Reduced operation as, for example, quarter hourly ionograms only is readily possible. The data load of 3 × 2340 or 7020 characters/5 min can be handled by available 600-1200 baud telecommunications links.

DATA PRESENTATION

An important requirement for the analysis of multi-dimensional data under all conditions, but especially important for real time applications, is intelligent presentation that reveals the characteristics of the data set. In the case of ionogram observation, it is the original ionogram itself that gives the scientist the most detailed answer in regard to the momentary conditions of the ionosphere. It does not show, however, the time development of the ionospheric parameters, i.e. the diurnal variations and disturbances, unless a sequence of ionograms is studied simultaneously. Analog methods to present characteristic ionospheric parameters as a function of time, like the critical frequencies of E and F-region and the layer heights, were developed in the fifties (Nakata et al, 1953; Bibl, 1956). Since 1969 Digisondes have produced digital ionograms and we have developed computerized techniques to generate digital characteristics. Use of microprocessor technology in the Geomonitor has made it possible in Goose Bay to print out digital ionospheric characteristics in real time. To extend the usefulness of the display techniques to other users, a Geomonitor Display System which is close to completion, can take the Geomonitor data stream, as arriving via any suitable data link, and present these data in the form of characteristics, and as reconstituted ionograms at any remote site.

Figure 3 is a typical example of three selected characteristics. Shown on top are the integrated heights and ranges derived from backscatter ionograms, below, the F-region characteristic and at the very bottom the E-region characteristic of the vertical incidence ionograms. Each ionogram produces one line in each characteristic.

The height or range characteristic is produced by simply printing out the 128 characters available in each ionogram record, which result from the summation of amplitudes over all frequencies for each height bin separately. Since the ionogram traces are almost horizontal at the minimum heights of the respective layers, the summation results in large numbers at these heights. Similar properties of oblique, oval associated backscatter echoes, result in strong integrated amplitudes at the range of these echoes. Range or height changes with time are thus visible at a glance in this characteristic.

The F-layer characteristic is obtained by sequentially printing the largest of the four F-echoes amplitudes into the respective frequency bin. The presentation thus obtained is an amplitude and frequency vs. time history and, as time progresses, reflects the changes of upper and lower limit of the frequency band reflected from the F-layer. The lower limit is generally a function of occulation by the lower E-layer or of enhanced absorption. The upper limit and its time variation is in daytime a direct measure of the foF2 (the Digisonde uses circularly polarized antennas that suppress the extraordinary component). Spread-F conditions routinely observed at night at Goose Bay make the upper limit a more complicated parameter of the degree of F-region disturbance.

The E-layer characteristic shown in the lowest panel is obtained in an identical fashion by printing the larger amplitude of the two E-echoes into the respective frequency bin. The upper limit of the band of strong amplitudes is equal to foE in those time sectors, where the cosinusoidal time variation shows the solar zenith angle control of the E-ionization. At other times, sharp spikes or deviations from a smooth daytime E-ionization indicate the presence of Es with ftEs > foE.

The daily variations of foF2, foE, h'F and backscatter characteristics for the Goose Bay ionosphere are evident on these hard copy time histories. Comparison with variations of the previous days and with easily produced average curves allows the assessment of current trends as for example enhanced or depressed foF2. The range of auroral backscatter at a given hour in the afternoon or evening can be converted

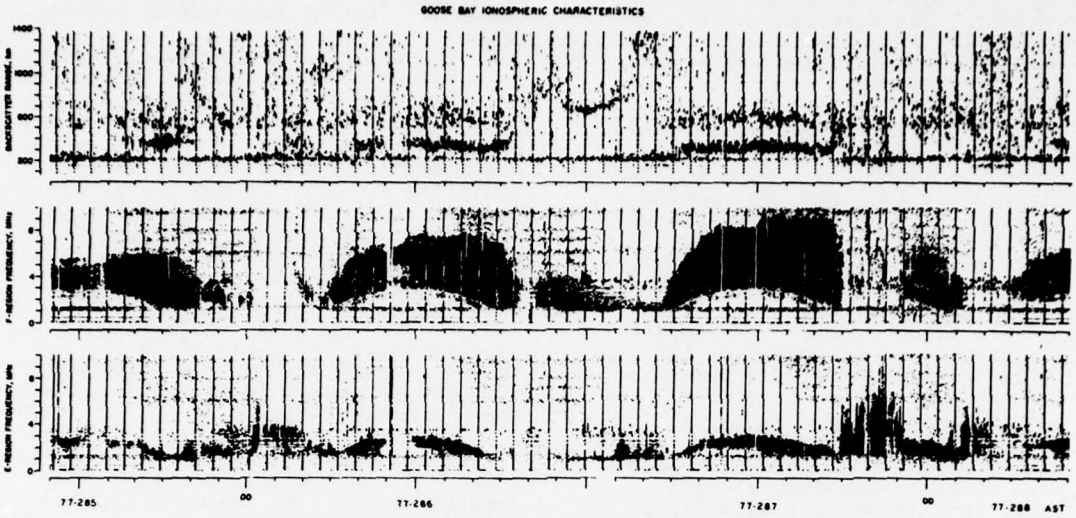


Figure 3. Goose Bay Ionospheric Characteristics

into a specific Q-value. Well established knowledge of oval continuity (Buchau et al, 1970) and the prediction of the circumpolar location of discrete auroral forms (Meng, 1977) from a locally established Q-value makes these backscatter range determinations a powerful measurement. The "anchor point" technique of using a one-point measurement to predict the whole oval has been developed by Gassmann (1973) and is at present successfully used at AFCWC with satellite auroral images providing the input parameter Q_E, the equatorward oval boundary. Of special importance is the ability, to interpret various types of signatures in the characteristics as evidence of auroral oval and ionospheric disturbances. Examples of such signatures are increased minimum frequency resulting from an increase in D-region electron density, the time history of such an increase, the existence of total absorption, sporadic E events, strong spread F occurrence, the sudden depression of foF2, and the early appearance or the rapid advance of backscatter fronts.

The parallel display of properly formatted Geophysical Data provides insight into the nature of the disturbance from different points of view and has to be made an integral part of the assessment of the event prior to issuing of an event report. As the disturbance grows in intensity, ionospheric characteristics become more difficult to interpret either due to the general lack of clear patterns found especially during magnetic storms or due to the strong increase in auroral absorption resulting in total lack of ionospheric echoes. Under these conditions the measurements most important to the preparation of advisories are the riometer and the magnetometer measurements.

The following discussion of the possible real time use of the Geomonitor and Display System in support of an Over-the-Horizon Backscatter Radar (OTH) System operating in this environment demonstrates the approach. The discussion also shows on examples the signatures of specific events and the value of the data compression and characteristic presentation to the investigation of ionospheric phenomena in general.

Let us consider the OTH radar located at a midlatitude location with Goose Bay within the surveillance area. (This is actually the situation of the planned 414L CONUS OTH-B Experimental Radar System, which is scheduled to start tests in 1980 and which will receive Goose Bay Ionospheric Data.) The latitude dependent ionospheric features associated with the auroral ionosphere such as the F-layer trough and the trough wall location, and the time dependent disturbances, such as absorption and sporadic E all have strong impacts on the propagation situation. Limitation of coverage, multipath to one target and azimuth/range errors due to the large gradients are but a few of the related problems.

Assume a station like GBIO with a Geomonitor connected by a communication link to the Geomonitor Display System located in the radar system operations

center. The GDS then provides a comprehensive ionospheric and geophysical data display for use by the radar's ionospheric forecaster. The forecaster assists the radar operators in the frequency management and in determining whether and how the radar is being affected by natural disturbances over part or all of the surveillance area. He also estimates the probability of the disturbance subsiding or continuing. Figure 4 shows a vertical incidence reconstituted ionogram from GBIO at 1000 local time on day 286. An absorption condition exists and only fragments of echoes from the usual daytime layers are seen. More information is available from the characteristics in Figure 3. They show no absorption on this day prior to the event onset and during the previous night. Such time history is indicative of a localized absorption event drifting around from a nightside auroral substorm, and it is likely to be of short duration. The ionospheric forecaster would advise the operators to this effect. Looking at the characteristics at later times that day, we see that the absorption did indeed diminish, disappearing completely in 2 or 3 hours. The ionogram (Figure 5) shortly afterward at 1307 local time on day 286 shows the expected daytime ionospheric layers indicating normal radar system operation.

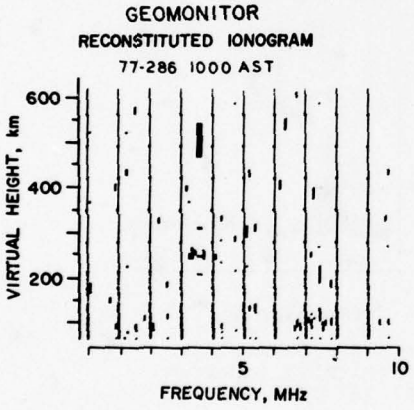


Figure 4. Geomonitor Reconstituted Ionogram 77-286 1000 AST

The vertical incidence ionogram at 0930 local time on day 292 is quite similar to Figure 4, showing complete absorption. The characteristics in Figure 6 show that the E layer echoes had been absorbed throughout the morning, and that absorption had occurred periodically during the previous night; a high level of disturbance is evident

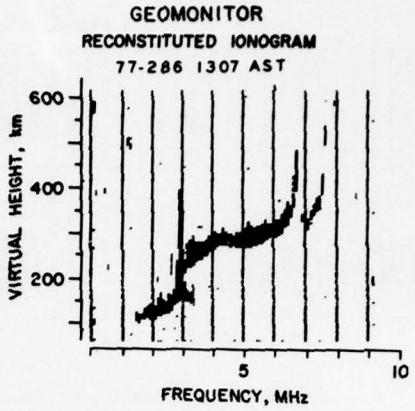


Figure 5. Geomonitor Reconstituted Ionogram 77-286 1307 AST

in the rapid changes in the Es top frequency. This suggests that disturbed conditions will continue with the resulting disturbing effects on the radar system. The ionospheric forecaster would advise the operator on expected future problems. This would permit enhancement of other available means of surveillance if extended outages could not be tolerated. The characteristics later in the day continue to show complete absorption as was inferred above. During short periods, when the absorption subsides, foF2 can be determined as 5.5 MHz, compared to 6.8 MHz on day 286 at the same time. This depression supports the assessment of a continuing disturbance, and aids the frequency management during times when propagation is possible.

The ionogram in Figure 7 shows a typical late afternoon ionosphere at 1637 AST on day 287 with an foF2 of 8.7 MHz. HF propagation would be by F-layer modes. Examination of the backscatter ionogram range characteristic shows that echoes which are associated with the auroral oval have been present as early as 1530 AST with decreasing range throughout the next hours. This indicates that the auroral oval was expanded and that the observatory and thus the OTH coverage area would rotate under the oval early in the evening. The ionogram at 1800 AST in Figure 8 verifies the prediction. The Es layer is well developed, the presence of an Es multiple indicates that absorption is not strong. Thus for selected azimuths, HF propagation would be by E layer modes only. Knowledge that the propagation has changed from F-layer to E-layer modes is impor-

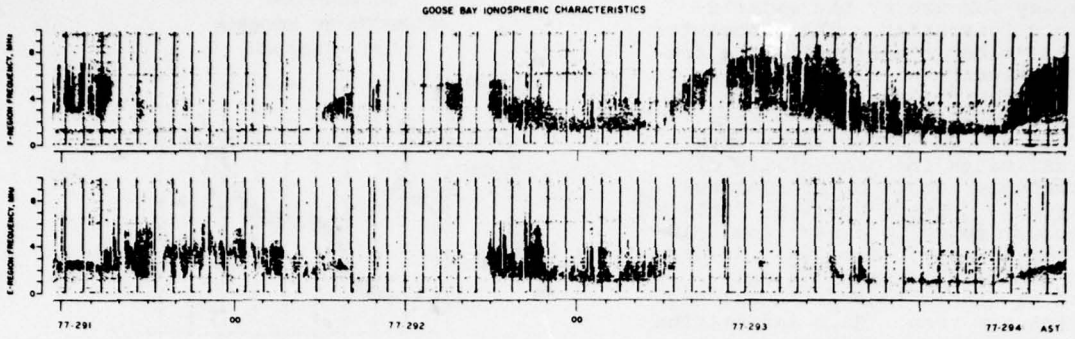


Figure 6. Goose Bay Ionospheric Characteristics, disturbed period

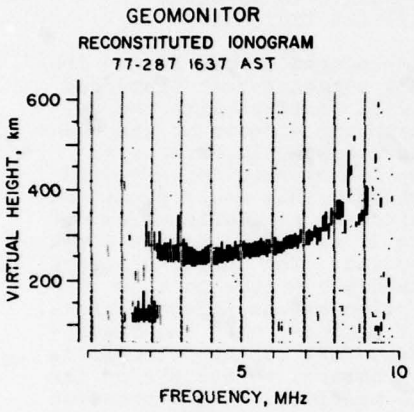


Figure 7. Geomonitor Reconstituted Ionogram 77-287 1637 AST

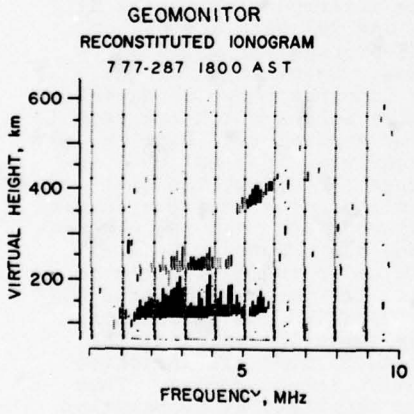


Figure 8. Geomonitor Reconstituted Ionogram 77-287 1800 AST

tant in interpreting the range of targets in the surveillance area. The characteristics show that the Es event continued for several hours. Figure 9 shows that the Es reached 10 MHz at 2052 AST allowing for the use of rather high surveillance frequencies but providing only short (<2200 km) range coverage in the general direction of Goose Bay.

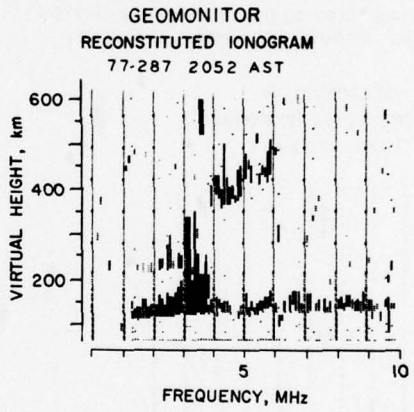


Figure 9. Geomonitor Reconstituted Ionogram 77-287 2052 AST

Another type of behavior of the ionospheric features associated with the auroral ovals occurred on the night of day 286. The backscatter range characteristic showed that the oval stayed well poleward of GBIO throughout the night. The ionogram at 2345 AST in Figure 10 showed the off-vertical echoes from the oval appearing in the vertical ionogram display. The foF2 at this time was approximately 2 MHz, indicating GBIO and thus a large part of the coverage area was in the midlati-

tude ionospheric trough. Knowledge that the auroral oval stayed poleward of Goose Bay and that GBIO was underneath the trough is informative in evaluating the ionosphere effecting the radar surveillance area equatorward of Goose Bay. The reconstituted ionogram at this time would be very important input to the coordinate conversion conducted by the radar to convert azimuth and range information into target ground coordinates, dependent on the reflecting height of the ray path.

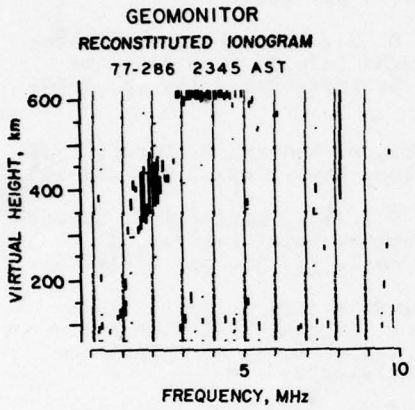


Figure 10. Geomonitor Reconstituted Ionogram 77-286 2345 AST

Notice the contrast in the size of the auroral oval on days 286 and 287. On 286 it remained poleward of GBIO all night, indicating a Q index value of 0. On 287 it arrived overhead at 1800, consistent with a Q index of 8.

SUMMARY

We have described an approach to the remote monitoring of the high latitude ionosphere, which is summarized in Figure 11. Digital vertical incidence and backscatter ionograms are reduced in the Geomonitor by extracting amplitude, height and spread of the ionospheric echoes. The algorithm works remarkably well even under disturbed conditions during an auroral event. Properly formatted digitized magnetometer, riometer and satellite propagation data and the processed ionospheric data are stored on tape, or for real time use, are transmitted over a suitable medium capacity data link to any desired user site. Here a Geomonitor Display System separates the data, presents them as characteristics or time histories of various ionospheric parameters and of the geophysical data for interpretation by an observer. The usefulness to an OTH system has been shown on selected samples. Quiet day curves for the various geophysical data and thresholds for minimum frequency and Es-events can be used in the Geomonitor and the Display System to initiate alarms when deviations of predetermined magnitude occur.

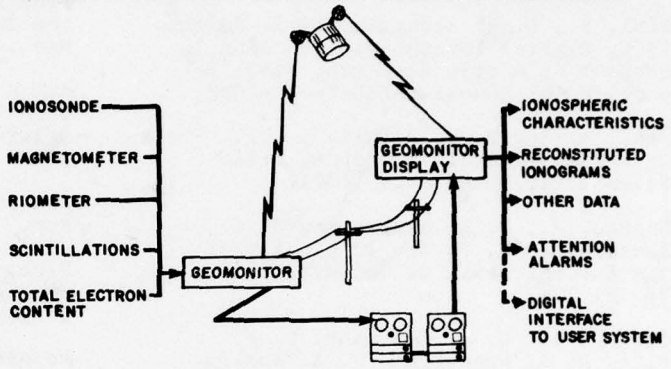


Figure 11. Schematic presentation of data requirements, data flow and display for remote oval monitoring.

The addition of two more monitor sites, one in the European Arctic and one in Alaska could provide inputs into AWS-SESS resulting in a 24 hour continuous coverage of all high latitude disturbances and the continuous determination of the location of the boundary between F-layer trough and auroral oval. Together with the sporadic DMSP satellite auroral images, complete and continuous understanding of the state of this important section of our environment can be achieved. The U. S. Army employs an instrument (Automatic Ionogram Collator) similar to the Geomonitor for their Digisonde operation in Fort Monmouth, N.J. (F. Gorman, private communication). This system could offer the possibility of a mid-latitude expansion of the arctic network.

ACKNOWLEDGEMENTS

The technical support by Messrs. J. B. Waaramaa and R. W. Gowell during the establishment of the Goose Bay Oval Monitor capability is thankfully acknowledged.

REFERENCES

Bevington, P. R., 1956, Data Reduction and Error Analysis for the Physical Sciences, McGraw-Hill.

Bibl, K., 1956, J. Atmos. Terr. Phys., 8, p. 295.

Bibl, K., J. A. Patenaude and B. W. Reinisch, 1970, Digital Integrating Goniometric Ionospheric Sounder Digisonde 128, Final Report, U. of Lowell, AFCRL-71-0002.

Bibl, K., B. W. Reinisch and S. Smith, 1976, Digital Ionospheric Sounding in Support of Arctic Research, Final Report, U. of Lowell, AFGL-TR-76-0037.

Bibl, K. and B. W. Reinisch, 1978, The Universal Digital Ionosonde, Radio Science (accepted July 1977).

Buchau, J., J. A. Whalen and S. I. Akasofu, 1970, On the Continuity of the Auroral Oval, J. Geophys. Res., 75, P. 7147.

Buchau, J., G. J. Gassmann, C. P. Pike, R. A. Wagner and J. A. Whalen, 1972, Precipitation Patterns in the Arctic Ionosphere Determined from Airborne Observations, Ann. Geophys., 28, 2, pp. 443-453.

Driatskiy, V. M., 1968, Diurnal Pattern of Auroral Absorption in the Auroral Zone, Geomagnetism and Aeronomy, VIII, 1, p. 33.

Elkins, T. J., 1972, A Model of Auroral Substorm Absorption, AFCRL-72-0413, Environmental Research Papers, No. 404.

Feldstein, Y. I. and G. V. Starkov, 1967, Dynamics of Auroral Belt and Polar Geomagnetic Disturbances, Planet. Space Sci., 15, pp. 209-229.

Gassmann, G. J., 1973, Analog Model 1972 of the Arctic Ionosphere, AFCRL-TR-73-0151, Air Force Surveys in Geophysics, No. 259.

Ming, C. I., R. H. Holzworth and S. I. Akasofu, 1977, Auroral Circle-Delineating the Polarward Boundary of the Quiet Auroral Belt, J. Geophys. Res., 82, 1, pp. 164-172.

Muldrew, D. B., 1965, F-Layer Ionization Troughs Deduced from Alouette Data, J. Geophys. Res., 70, pp. 2600-2635.

Nakata, Y., M. Kan and H. Kyeda, 1953, Rep. on Ion. Res., Japan, pp. 129-135.

Pike, C. P., 1971, Latitudinal Survey of the Daytime Polar F-Layer, J. Geophys. Res., 76, 31, pp. 7745-7753.

Reinisch, B. W. and S. Smith, 1976, Geomonitor, Digital Real Time Processor for Geophysical Data, AFGL Technical Report TR-76-0292.

Wagner, R. A. and C. P. Pike, 1972, A Discussion of Arctic Ionograms, AGARD-CP-97, AGARD Conference Proceedings "Radar Propagation in the Arctic" held at Lindau/Germany September 1971.

Whalen, J. A., J. Buchau and R. A. Wagner, 1971, Airborne Ionospheric and Optical Measurements of Noontime Aurora, J.A.T.P., 33, pp. 661-678.

ATTEMPTS TO PREDICT TROUGH/PLASMAPAUSE BOUNDARIES IN REAL TIME

M. Mendillo, C. Chacko, and F. Lynch
Department of Astronomy
Boston University
Boston, MA 02215

and

P. J. L. Wildman
Air Force Geophysics Laboratory
L. G. Hanscom AFB
Bedford, MA 01730

1. INTRODUCTION

The nighttime ionospheric trough found near L=4 marks the transition region between the mid-latitude and auroral ionospheres. The latitudinal gradients associated with the trough (particularly on the poleward side) are severe plasma boundaries which impact F-region supported communications systems. Past statistical relations have suggested a close connection between the trough's position (L_T) and the equatorial plasmapause location (L_{pp}). While these relationships generally use local time and the geomagnetic index Kp to specify conditions described, the relatively large uncertainties associated with the correlations have never really suggested that the regression equations could be used as predictors of actual boundary locations.

This paper describes two new approaches for specifying trough and plasmapause locations using satellite-borne auroral photographs and computer-simulated magnetospheric convection patterns. The availability of USAF/DMSP auroral photographs in near real time suggests the possibility of locating the poleward wall of the trough over an extensive geographic area by observing the equatorward edge of the continuous (diffuse) aurora. The concept is tested with case study events employing simultaneous DMSP and ISIS-2 satellite passes in conjunction with a ground-based ionosonde network and a meridianal chain of electron content observatories.

A second scheme tested involves computer modelling of equatorial plasmapause dynamics, initially in an attempt to reproduce satellite probe determinations of the trough/plasmapause location in the topside F-region (h≈800-3200 km). A magnetospheric electric field model keyed to the Kp index is used to compute plasmapause dynamics in the night sector as a way of specifying temporal changes in the L-value of the plasmapause during periods of increasing geomagnetic activity.

2. RELATIONSHIP BETWEEN THE AURORA AND THE TROUGH

The first part of this paper concerns an examination of the detailed relationships between the poleward wall of the F-region trough and the equatorward edge of the continuous (or diffuse aurora). Energetic particle precipitations are known to cause both features, and thus the question arises of whether or not detailed knowledge of the latitudinal pattern of one can be used to predict the detailed structure of the other. The notion of specifying optical auroral features from ionospheric data is not nearly as appealing as the reverse possibility, i.e., using a single optical photograph (obtained during a conventional DMSP or ISIS satellite pass) to specify the location of an important F-region structure over the extensive geographic area covered in the photograph. Since topside sounders or single-height, in-situ satellite probes provide the only routine way of

specifying trough features (along a given satellite track), the concept of using "optical diagnostics" from a single satellite pass to infer F-region structure over a region much more extensive than the sub-satellite track implies a capability broadly equivalent to the unrealistic scheme of having many simultaneous ionospheric sounding satellites pass through a given world region (see Figure 1).

In examining trough morphology, the poleward wall is generally found to be the best-defined feature of all trough characteristics (Pike 1976, Mendillo and Chacko, 1977). Thus, if a consistent relationship exists between the auroral boundary and the poleward wall, and DMSP-type satellites can fix the latitude of the wall over an extensive region, this key reference point can be used to anchor trough models giving latitudinal and height-dependent structure (Rycroft and Thomas, 1970; Feinblum and Horan, 1973; Halcrow, 1976; Mendillo and Chacko, 1977).

We tested this scheme by carrying out ten "case study" investigations using ISIS-2 topside sounder passes in December 1971 for which DMSP auroral photographs were available in near simultaneity. For all ten cases, the temporal separation between the ISIS and DMSP satellite passes fell within the 8 to 40 minute range. The ISIS data were used to determine the N_e latitude gradients (in CGL) at h_{max} near the midnight meridian. Since each ISIS pass crossed (or came very close to) the equatorward edge (ϕ_a) of the continuous aurora, the latitude separation ($\Delta\phi$) between the poleward wall (at ϕ_{pw}) and the aurora could be determined at the longitude or local time (2230-2400 MLT) of the ISIS pass. For ϕ_{pw} corresponding to the foot of the poleward wall, $\Delta\phi = 4.7^{\circ} \pm 1.2^{\circ}$, while for ϕ_{pw} corresponding to the top of the poleward wall, $\Delta\phi = 2.4^{\circ} \pm 1.1^{\circ}$. Apart from the observation that the auroral boundary (via DMSP) is always found poleward of the trough boundary, no systematic relationship between $\Delta\phi$ and magnetic activity (using Kp or AE, for example) could be found. The number of cases examined (ten) was of course small, and the spectral range of the DMSP detector is not ideally suited for high resolution studies. We do, however, believe that the separations observed between the diffuse aurora (as monitored by DMSP) and the poleward wall of the main electron density trough are physically significant quantities.

Given the observed $\Delta\phi$ at the ISIS sub-satellite location, we were interested in determining the longitudinal (or local time) consistency of the separation over the region covered by the DMSP photograph, and indeed beyond. This is not a simple question to answer since no F-region monitoring technique can provide ISIS-type latitude resolution at points to the east and west of a given ISIS pass. We turned to the ground-based network of ionosonde sites (via WDC-A) and to the AFGL chain of total electron content (TEC) observing stations (courtesy of J. A. Klobuchar) for supporting data to estimate the spatial consistency of the trough's location away from the ISIS longitude. Figure 2 shows the network of 24 ionosondes and the 4 TEC sites used in the study.

Two of the case studies are presented in Figures 3 and 4. For the 06UT period on 9 December 1971 (Figure 3), the ISIS pass crosses the DMSP image at $\phi_a \simeq 68^{\circ}$ CGL, with the foot of the trough's poleward wall in foF2 at $\phi_{pw} \simeq 62^{\circ}$ CGL. The ionosonde stations immediately to the east show foF2 $\simeq$ 5MHz to the north of ϕ_a and foF2 $\simeq$ 2MHz equatorward of ϕ_{pw}. Looking further to the east, ionosondes poleward of ϕ_a give foF2 in the 5-6 MHz, again typical of poleward wall values, while sites equatorward of ϕ_{pw} show foF2 values more typical of the trough minimum (i.e., foF2 $\simeq$ 2-3 MHz). The TEC network covers North American, Atlantic Coast longitudes from 73°-53° CGL. The trough in TEC has its minimum near 60°, with 3×10^{12} el/cm^2 consistent with a 2MHz peak. In fixing the trough minimum at $\simeq$ 2MHz near 60°, no inconsistency is found within the DMSP field of view, and indeed as far to the east as the western European foF2 stations in the pre-dawn sector.

In Figure 4, the case of 0600UT on 21 December 1971 is depicted. The ISIS pass occurs several degrees to the west of the DMSP field of view. Once again, the foot of the poleward wall is nearly 5° equatorward of ϕ_a. In the North American sector, the ionosonde and TEC data support a local time consistency of $\Delta\phi \simeq 5^{\circ}$ within (and several hours to the east of) the DMSP field of view. A trough minimum of foF2 $\simeq$ 2MHz near 60° CGL may again be inferred from the satellite track to the west European sector.

In summary, a limited set of "case study" investigations points to the possibility of inferring real-time F-region trough morphology from DMSP auroral images, at least over the longitude span covered by a photograph,

and probably to several hours beyond it.

3. SIMULATION OF PLASMAPAUSE DYNAMICS

Most of the fundamental theoretical studies of the origin and behavior of the equatorial plasmapause (e.g., Nishida, 1966; Brice, 1967; Kavanagh et al., 1968) deal with the application of magnetospheric convection patterns originally suggested by Axford and Hines (1961) to the now classic plasmapause geometry reported by Carpenter (1966). The notion of a contracting plasmapause due to enhanced convection patterns during periods of increased geomagnetic activity is now a widely accepted view, and is, in fact, the scheme generally said to explain why statistical results for the plasmapause location (L_{pp}) vs. an index like Kp seem to provide reasonable descriptions of average behavior (Rycroft and Thomas, 1970; Kohnlein and Raitt, 1977). Yet, these simple statistical patterns of L_{pp} vs. Kp are not expected to provide an actual description of the time dependence of plasmapause changes during a specific storm's Kp-scenario. The real plasmapause cannot adjust instantaneously to a new configuration for each Kp step, and within a given Kp interval, the L_{pp} position must be a function of previous magnetic history.

In an attempt to overcome these two limitations, we decided to use a very simple model for magnetospheric convection keyed to magnetic activity to see if a time-dependent representation for plasmapause distortions in the night sector could be obtained. The convection model is limited to E x B motions in the equatorial plane, using a centered dipole magnetic field and a spatially uniform dawn-dusk magnetospheric electric field. For any given particle in the equatorial plane (specified by a LT and L-value), the instantaneous motion is given by $W = (E \times B)/B^2$, where E is the resultant electric field arising from co-rotation (E_R, directed radially inward) and convection (E_{DD}, directed from dawn to dusk), and B is the dipole field strength. A "fluid" of particles is then followed by keeping track of all the individual motions using a 10-minute time step. The initial distribution of particles was taken to be circular, with a particle at each ½ L-value from L = 1.5 to 5.5, and spaced every 15 minutes of local time. A total of 864 individual points were therefore available to define subsequent transformations (see Figure 5a).

For a given dawn-dusk electric field, a unique plasmapause exists (Kavanagh et al., 1968; Chen, 1970); it defines the boundary between plasma particles which share in the co-rotational field associated with the Earth and those which are lost due to magnetospheric convection. The shape of the resultant plasmapause for such a case is the familiar "tear-drop" described by Chen (1970). Thus, our initial circular distribution of particles becomes distorted into a "tear-drop" configuration due to the E_{DD} field (see Figure 5b). It typically takes about 30 hours of simulation time for a completely stable configuration to develop, i.e., of the original 864 test particles 50-75% are trapped in motion about the Earth in a region defined by the appropriate theoretical "tear-drop" plasmapause associated with E_{DD}. Given this equilibrium plasmapause, we are interested in subsequent transformations caused by a stronger E_{DD} field.

If E_{DD} is increased, the new equilibrium plasmapause position is known in advance since it depends only on the new field strength (Chen, 1970). Our calculations show that it can take typically 8 hours for the new plasmapause to become stable on the nightside. Since geomagnetic activity changes occur on a much smaller time scale, a storm-time scenario for L_{pp} cannot be pictured as a collection of equilibrium configurations.

We decided to by-pass the equilibrium configuration problem by using a dynamic calculation scheme in which the fluid of convecting particles experiences a time-dependent E_{DD} field, and instantaneous L_{pp} (LT,t) locations are obtained by graphical inspection of the fluid's boundary. In an earlier work (Mendillo and Papagiannis, 1971), we developed a model for E_{DD} which showed a quadratic dependence upon Kp. We normalized this model to the "tear-drop plasmapause" which gave $L_{pp}(00LT) = 5$ for Kp = 2 (for which $E_{DD} = 0.14$mv/m). Using our quadratic relation between E_{DD} and Kp, a set of "best estimate" E_{DD}values were now available to describe magnetospheric convection/plasmapause scenarios keyed to observed Kp variations.

To illustrate the procedure, consider the storm period of 21-22 April, 1971. Prior to 1200 UT, magnetic activity was steady for nearly 9 hours, with $\overline{Kp} = 2$. From 1200 UT on, Kp (a 3-hour index) varied as follows: 3, 4, 5, 7, 5, 3, 2, . To follow the nightside L_{pp} variations associated with



this scenario, we first used our simulation program to generate the equilibrium ("tear-drop") particle distribution appropriate to the t=0 point of the scenario. Thus, the initial circular distribution of particles was allowed to evolve to the case: 12:00 UT on 21 April 1971, Kp = 2 (Figure 5b). The electric field model was then used to input new E_{DD} fields in concert with the observed Kp variation. Computer generated plots of the modified particle distributions were made at hourly intervals, and the L_{pp} boundary values for the LT sector in question were scaled from the plots (see Figure 6 for sample outputs 2, 9, 12, and 20 hours into the simulation). For this particular scenario, we examined the 2345 LT values in order to compare the model's predictions with ISIS-1 in-situ probe data for the equatorward edge of the total ion trough in the topside F-region (Wildman et al., 1976). The results are given in Figure 7, together with the "statistical predictions" of the L-value of the plasmapause using the relation given by Rycroft and Thomas (1970).

In examining the results, there are several features to note:
(1) The trough's equatorward edge (measured high in the F-region) is probably a better indicator of the plasmapause location during disturbed times than during quiet periods. Thus, at the t=0 point of the scenario, the difference between the data and the model is the largest.
(2) As the storm progresses (in this case, rather smoothly from Kp = 3→4→5→7), the steady contraction of the plasmapause is reproduced. The statistical results of Rycroft and Thomas (1970) appear as discontinuous jumps every 3 hours (the Kp interval); they also tend to agree with the observed behavior.
(3) Following the storm maximum, i.e., after 00LT on 22 April 1971, the Kp transition 5→3→2 causes a gradual recovery of the plasmapause to higher L-values. There is a definite "sluggishness" built into the model arising from the previously high Kp values. This ability to take previous magnetic history into account is in sharp contrast to the statistical predictions which slow instantaneous adjustments to higher L_{pp} values.

We have tested this procedure for other Kp scenarios and find the "sluggishness" to be a general feature. Thus, we conclude that the empirical model for a convection-dominated plasmapause can be used to simulate nightside dynamics effects in near real-time.

Acknowledgements

We wish to thank the World Data Center A in Boulder for providing the ionosonde values used in this study. Mr. Louis York's efforts with the convection program were greatly appreciated. TEC data were kindly provided by J. A. Klobuchar of AFGL, and we benefited by discussions with L. Snyder, J. Whelan, E. Weber and R. Sagalyn. This work was supported in part by AFGL contracts F-19628-75-C-0044 and F-19628-77-C-0019 to Boston University.

REFERENCES

Axford, W. I. and C. O. Hines, A Unifying Theory of High-Latitude Geophysical Phenomena and Geomagnetic Storms, Can. J. Phys., 39, 1433, 1961.

Brice, N. M., Bulk Motion of the Magnetosphere, J. Geophys. Res., 72, 5193, 1967.

Carpenter, D. L., Whistler Studies of the Plasmapause in the Magnetosphere, 1, Temporal Variations in the Position of the Knee and Some Evidence on Plasma Motions Near the Knee, J. Geophys. Res., 75, 693, 1966.

Chacko, C. and Michael Mendillo, Electron Density Enhancements in the F-Region Beneath the Magnetospheric Cusp, J. Geophys. Res. (November, 1977).

Chen, A. J., Thermal and Quasi-Energetic Plasma Flow in the Magnetosphere-A Theoretical Study, Ph. D. Dissertation, Rice Univ., Houston, Texas, 1970.

Feinblum, D. A. and R. J. Horan, HILON-A Model of the High Latitude Ionospheric F2 Layer and Statistics of Regular Ionospheric Effects at Ft. Churchill, 1968. Bell Labs., Murray Hill, N. J., 1973.

Halcrow, Barry W., F2 Peak Electron Densities in the Main Trough Region of the Ionosphere, Tech. Rept. PSU-IRL-IR-55, IOn. Res. Lab., Penn. State Univ., University Park, PA, 1976.

5511, 1968.

Kohnlein, W, and W. J. Raitt, Position of the Mid-Latitude Trough in the Topside Ionosphere As Deduced From ESRO.4 Observations, Planet. Space Sci., 25, 600, 1977.

Mendillo, Michael and C.C. Chacko, The Base Level Electron Density Trough, J. Geophys. Res. (November, 1977).

Nishida, A., Formation of Plasmapause, or Magnetospheric Plasma Knee, By the Combined Action of Magnetospheric Convection and Plasma Escape From the Tail, J. Geophys. Res., 71,5669, 1966.

Pike, C. P., An Analytical Model of the Main F-Layer Trough, AFGL-TR-76-0098, May, 1976.

Rycroft, M. J. and J. O. Thomas, The Magnetospheric Plasmapause and the Electron Density Trough at the Alouette I Orbit, Planet. Space Sci., 18, 65, 1970.

Wildman, P.J.L., Sagalyn, R.C. and M. Ahmed, Structure and Morphology of the Main Plasma Trough in the Topside Ionosphere, Proc. COSPAR Sym. Geophys. Use of Sat. Beacon Obs., M. Mendillo (ed), Boston University, Boston, MA, June 1976.

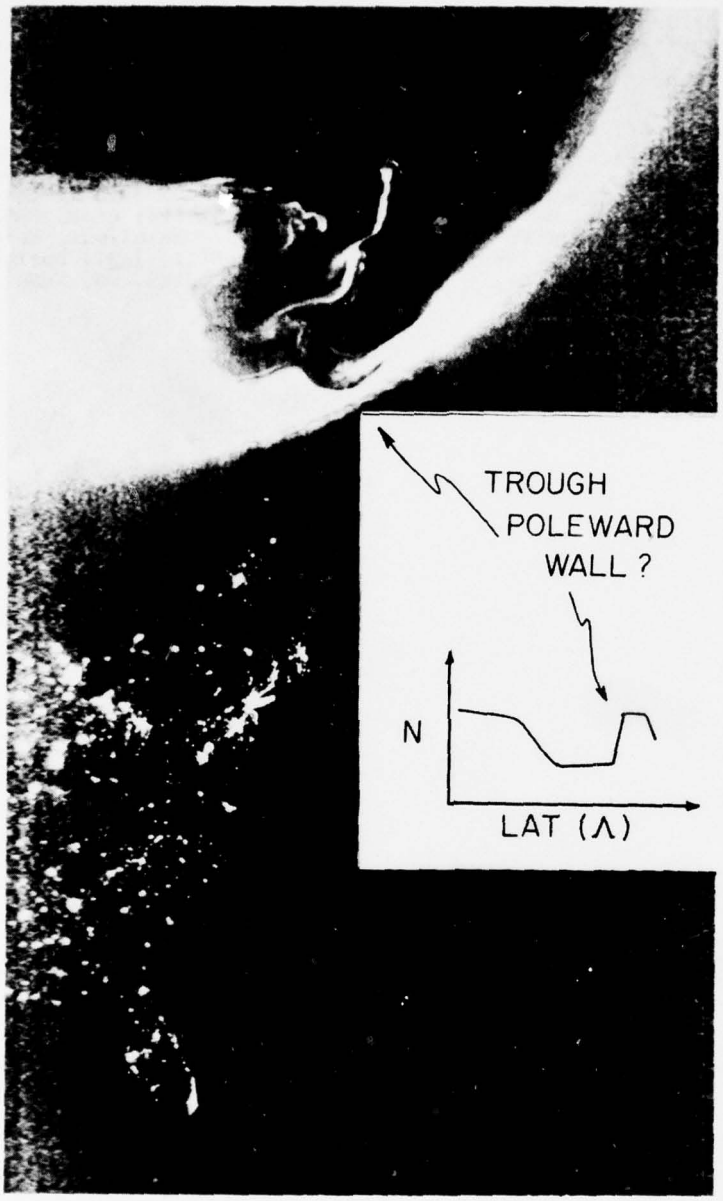


FIGURE 1. Sample DMSP auroral photograph illustrating possible relationship between the equatorward edge of the aurora and the poleward wall of the ionospheric trough.

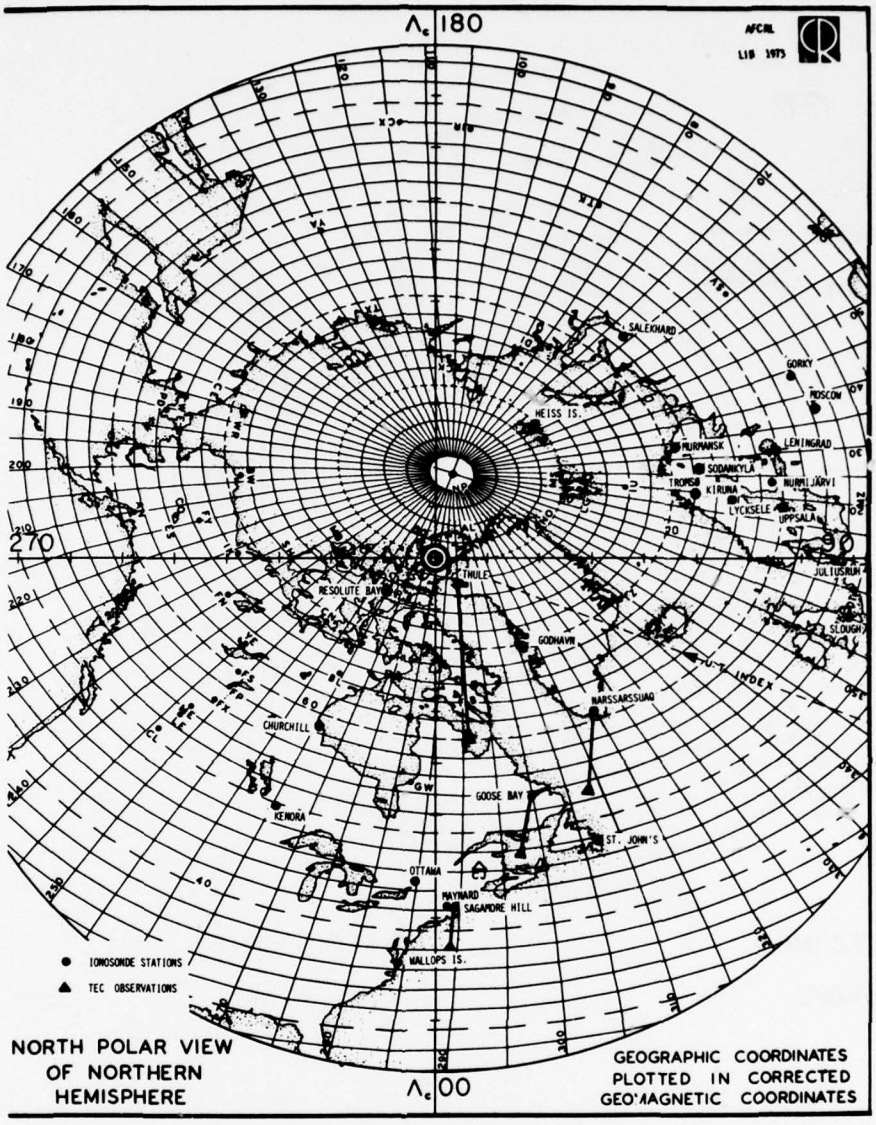


FIGURE 2. Polar view of northern hemisphere with geographic coordinates plotted in Corrected Geomagnetic Coordinates. Ionosonde stations (•) and TEC observing sites (▲) used in "case study" events are indicated. Corrected Geomagnetic Latitudes (CGL) appear as concentric circles on subseguent figures.

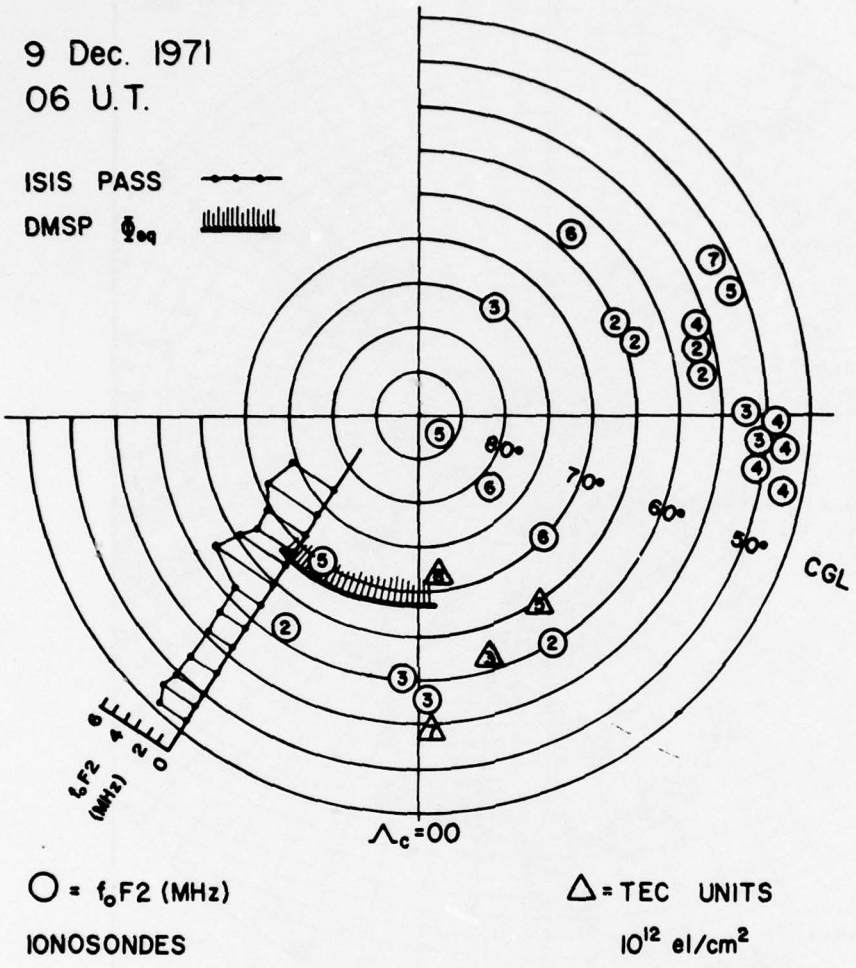


FIGURE 3. North polar view in CGL showing the location of near simultaneous ISIS and DMSP satellite data for 0600 UT on 9 December 1971. Ground-based foF2 values and TEC data at 0600 UT from the network shown in Figure 2 are presented using integer values.

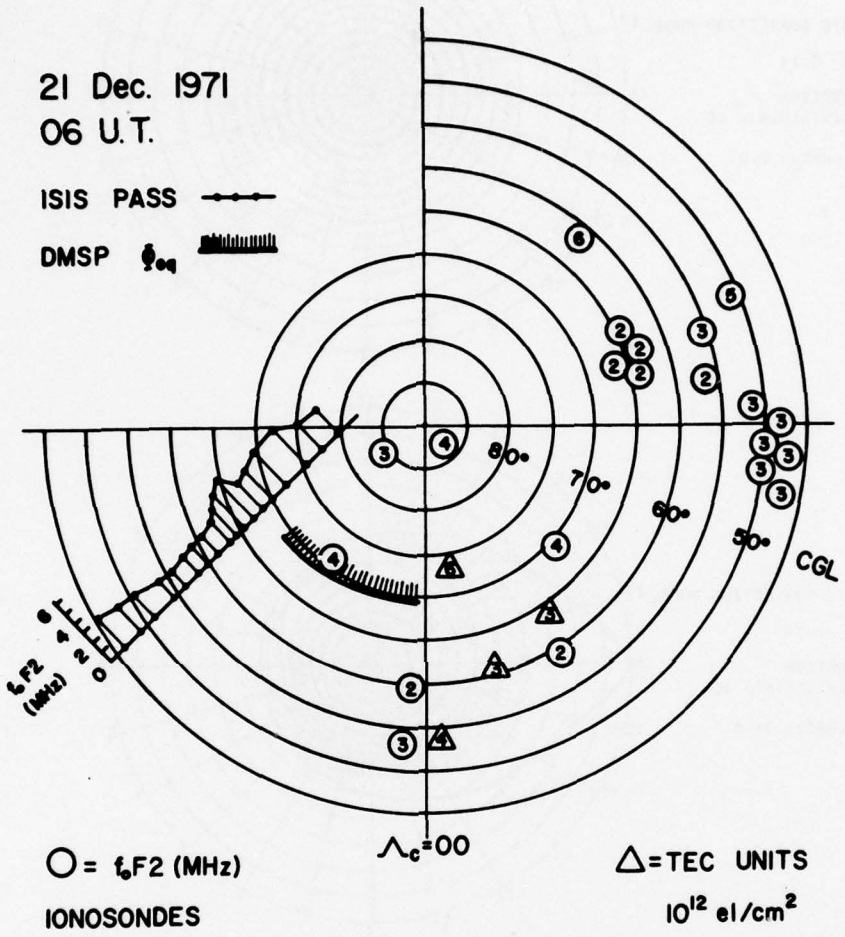


FIGURE 4. North polar view in CGL showing the location of near simultaneous ISIS and DMSP satellite data for 0600 UT on 21 December 1971. Ground-based foF2 values and TEC data at 0600 UT from the network shown in Figure 2 are presented using integer values.

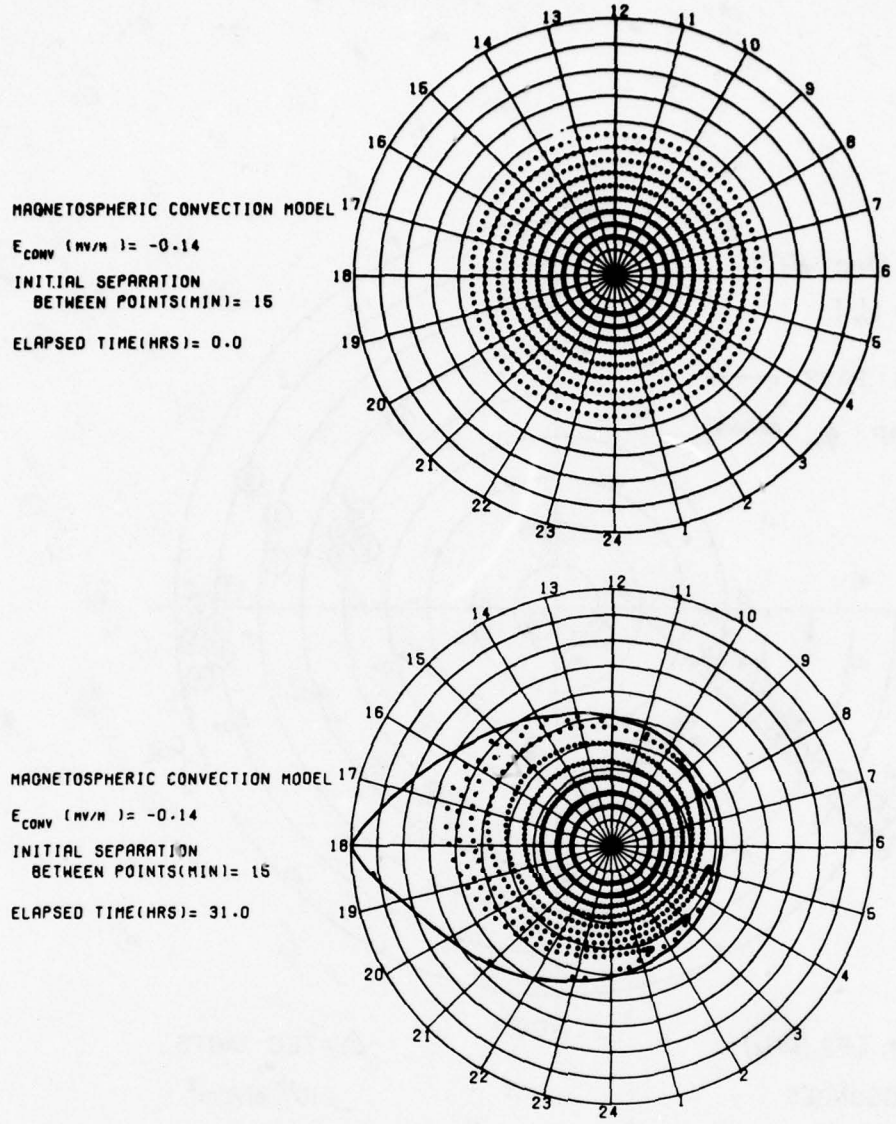


FIGURE 5. (a)Top. Magnetospheric convection model t=0 configuration for transition to a K_p = 2 equilibrium plasmapause (E_{DD} = 0.14 mv/m).

(b)Bottom. Resultant "tear drop" plasmapause for K_p = 2 after 31 hours simulation time. This equilibrium boundary represents the t=0 point for a K_p = 2 scenario beginning with K_p = 2 (e.g., at 1200 UT on 21 April 1971).

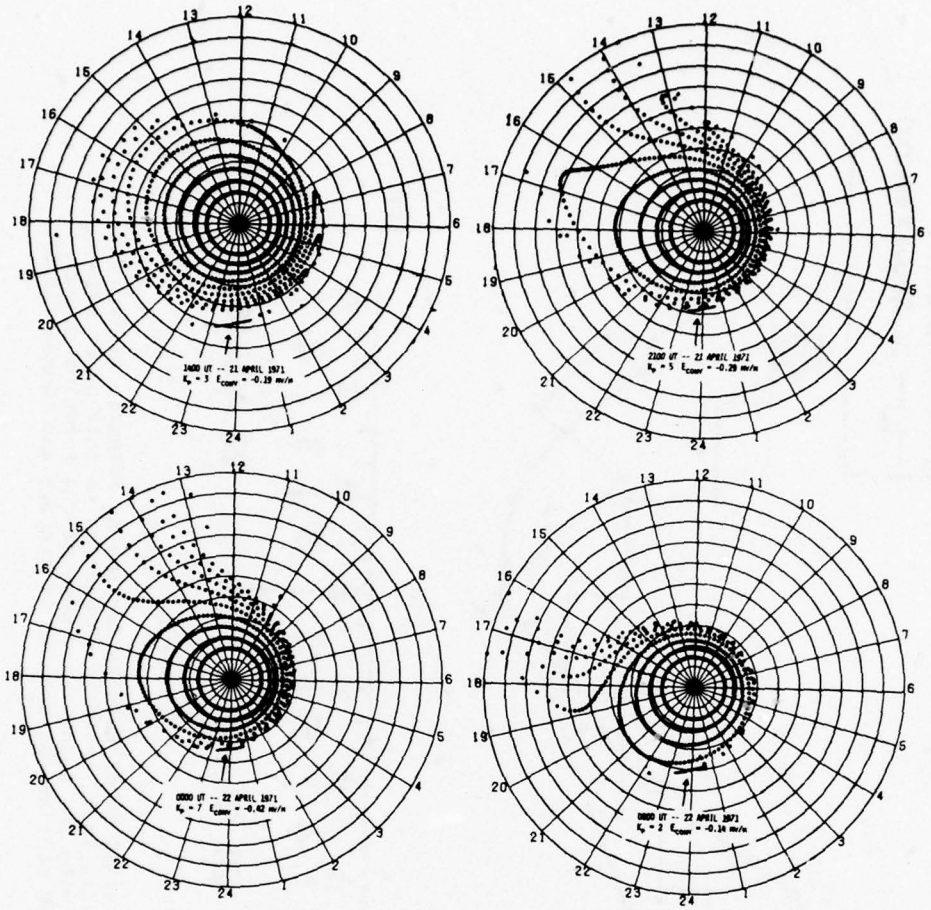


FIGURE 6. Four representative deformations of the plasmasphere depicted in Figure 5(b), at t=2, 9, 12, and 20 hours into the K_p scenario for 21-22 April 1971. The arrows indicate the L_{pp} boundary segments as defined by the particles at 23:45 LT.

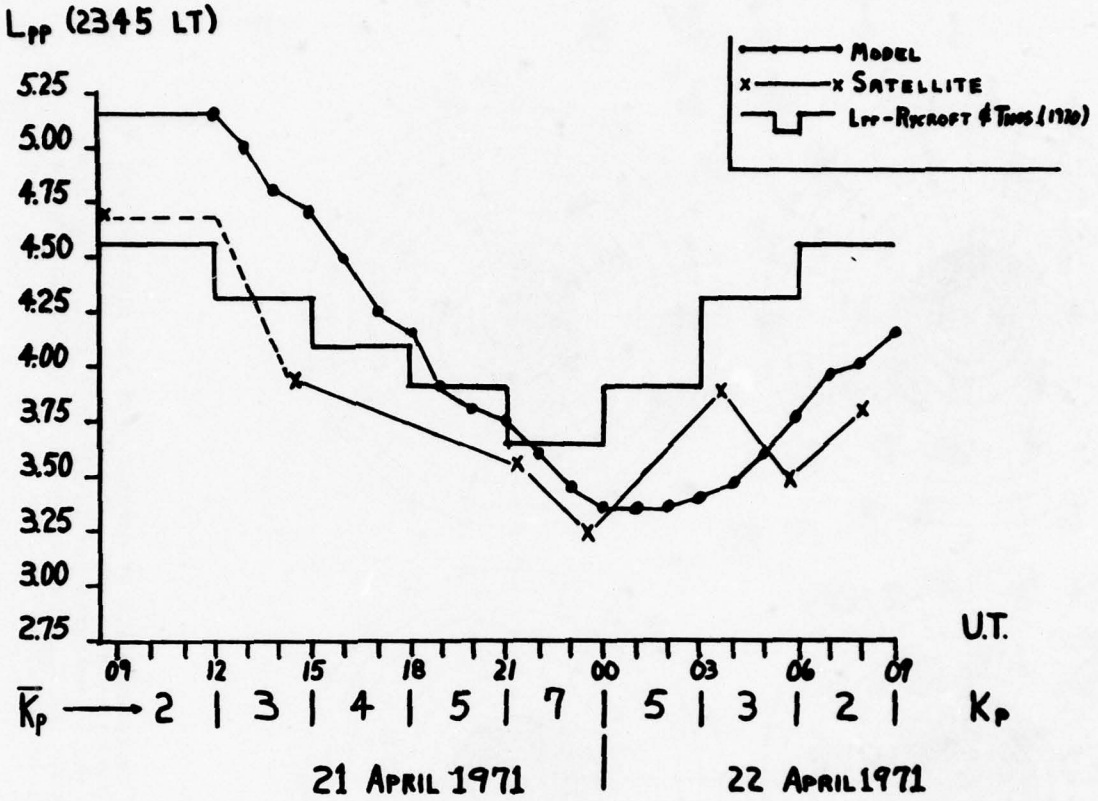


FIGURE 7. Overall Model Results for the K_p scenario of 21-22 April 1971, shown in comparison to ISIS probe data giving the equatorward edge of the F-region trough, and statistical results of Rycroft and Thomas (1970).

THE VARIABILITY OF IONOSPHERIC TIME DELAY

J. M. Johanson
Emmanuel College
Boston, MA 02115

M. J. Buonsanto
Boston University
Boston, MA 02115

and

J. A. Klobuchar
Air Force Geophysics Laboratory
Hanscom AFB, MA 01731

INTRODUCTION

Modern satellite navigation and satellite detection radar systems can be limited in accuracy due to the time delay caused by the ionosphere through which their RF signals must pass. The ionospheric time delay is directly proportional to the number of electrons encountered along the path from satellite to user and is inversely proportional to the square of the system operating frequency. Some systems, for example the NAVSTAR/Global Positioning System, GPS, are able to take advantage of the fact that the ionosphere is a dispersive medium, by measuring the ionospheric time delay at two widely spaced frequencies and thus are able to directly correct for this effect. Other precision ranging systems do not have the two frequency capability, however, and must instead rely upon models of ionospheric time delay to make corrections to increase system accuracy. Such models generally do a good job of predicting the monthly average behavior but, unless they are updated with a nearby measurement within a few hours of their use, do little to predict the day to day changes which occur.

The purpose of this paper is to outline the errors which result when only monthly average time delay values, without updating, are available for corrections to precise ranging systems. With these results systems design engineers will be able to determine how much improvement can be expected by near-real-time updating or by using a direct two frequency time delay measurement as compared with monthly average time delay models used without updating.

THE DATA BASE

Since the total number of electrons along the path from satellite to system user is directly proportional to the ionospheric time delay it is this parameter which was studied from a number of stations to determine the variability of time delay. This total number of electrons, called TEC, was determined from Faraday rotation measurements of linearly polarized VHF radio waves transmitted from geostationary satellites. Since the TEC is generally greatest during the mid-afternoon period, and the corresponding ionospheric time delays will be greatest during that period also, the deivations from average behavior are particualrly important during this part of the day. Further, since these systems must operate during all conditions of solar and geomagnetic activity we made no attempt here to separate magnetically quiet periods from disturbed times. Data for solar maximum years of 1968 and 1969 were reduced separately from the near solar minimum periods.

The Total Electron Content parameter is capable of describing many features of ionospheric behavior. The variability of this parameter may be easily described in terms of the departure from the monthly mean behavior by constructing the standard deviation,

σ. The percentage standard deviation may then be obtained via:

$$\sigma\ (\%) = 100\ \sigma/\bar{x}$$

where $\bar{x}$ is the monthly mean value. From the large quantity of data available, the diurnal, seasonal, solar cycle, and geographic variations of the percentage standard deviations of monthly mean TEC have been determined.

Total Electron Content data from eleven northern mid-latitude monitoring stations whose world-wide distribution is shown in Figure 1 was used in this study of ionospheric time delay. The TEC data base contains solar maximum data from six stations including Edmonton, Alberta, Canada; Aberystwyth, Wales; Hamilton, Massachusetts; Stanford, California; Honolulu, Hawaii; and Hong Kong. Solar minimum data was collected from the following stations: Narssarssuaq, Greenland; Goose Bay, Labrador; Hamilton, Massachusetts; Kennedy Space Flight Center, Florida; Athens, Greece; and Osan, Korea. Many people were responsible for the data used in this paper and they are each noted in the acknowledgements section.

DIURNAL VARIATION

Typical monthly mean diurnal TEC curves are shown in Figure 2 where data from Hamilton, Massachusetts is plotted for the solar maximum month of March 1969 and for the solar minimum month of March 1975 along with their standard deviations. It is clear in Figure 2 that as the TEC decreases, so does the absolute value of the variability with the result that changes in percentage standard deviation are small. Figure 2 also points out the fact that when operating at a frequency of 1.2GHz, one TEC unit corresponds to approximately one nanosecond of time delay. It should be noted that while Figure 2 represents a typical monthly mean diurnal TEC curve for a mid-latitude station, a near-equatorial station may have monthly mean TEC values which are 2 or 3 times greater than those shown in Figure 2. The corresponding magnitude of σ will also be greater for near-equatorial stations.

Figure 3 shows diurnal curves of σ (%) for TEC from six stations during the solar maximum year 1969, except for Hong Kong, for which 1968 data was used. Separate curves for winter (November - February), summer (May - August), and equinox (March, April, September, October) are given. Figure 4 shows similar curves for data from six stations during the period April 1974 through March 1975, a period not far from solar minimum. Figures 3 and 4 indicate lowest σ (%) values during the midday period where the curves are fairly flat, ranging from 15 to 25 percent. One must be careful when comparing Figures 3 and 4 for solar cycle effects because data from only one station, namely Hamilton, Massachusetts, was included in both figures. It may be concluded, however, that no obvious solar cycle dependence of σ (%) is evident. There is also no evidence of a geographical dependence except for the winter nighttime period under solar minimum conditions where a strong latitudinal gradient can be seen.

The data in the two figures seem to fall into one of two categories, the first being those periods exhibiting regular day-to-day variability of approximately 25 percent. The second includes those periods where the extremely high variability can be related to auroral and magnetic storm effects. The Narssarssuaq and Goose Bay nighttime data fall into this second group. At Narssarssuaq, the satellite to station raypath traverses the auroral oval during nighttime and at Goose Bay, the raypath intersects the auroral oval during magnetic storms. We unfortunately have no explanation for the large variability in the Honolulu data, observed especially during the nighttime period in the equinox and winter months.

MONTHLY VARIATIONS

An alternative way of examining the seasonal dependence of σ (%) for the two sets of stations is given in Figure 5. Here the average daytime (12 to 16 hours local time) TEC variability is plotted as a function of month for both the solar maximum and solar minimum periods. Again, we see no evidence of a solar cycle dependence. There is, however, a tendency for the curves to maximize in the equinoctial months. This may be due to the fairly rapid seasonal change between summer and winter diurnal patterns which occurs during those months.

DISTRIBUTION OF PERCENTAGE DIFFERENCES FROM MONTHLY MEAN TEC

Histograms giving the frequency distribution of percentage differences from the monthly mean daytime values of TEC are given in Figures 6 and 7.

Daytime TEC values from Hamilton, June 1971 are plotted in Figure 6 along with a Gaussian curve computed from the standard deviation of the frequency distribution and normalized to the area under the histogram. One can see that the normal curve gives an excellent fit to the data.

Figure 7 shows percentage differences during the daytime period for Hamilton, December 1971. This month includes a massive magnetic storm and may be considered as an example of worst case errors. The December 1971 data was chosen because it includes the greatest absolute deviations from monthly average values ever observed in ten years of observations made at Hamilton. In Figure 7, it can be seen that the normal curve (solid line), calculated in the same way as in Figure 6, is not representative of the data. If we eliminate the three hourly values of December 17, 1971 due to the storm, the standard deviation of the remaining data is greatly reduced, and the resulting normal fit (dashed line) is a better indication of the shape of the residuals.

In the months that we examined, the distribution of errors resulting from use of the monthly mean model were found to be approximately Gaussian. The December 1971 distribution was included only as a worst case example and even here it can be seen that by neglecting 3 hourly values, or 2 percent of the daytime values, the fit is also nearly Gaussian.

CONCLUSIONS

We have presented typical errors that a user of a single frequency system can expect when using monthly mean models, without updating, to correct for ionospheric time delays. If one number were to be chosen as the overall standard deviation of monthly mean time delay, one can assume approximately a 25 percent variability, although slightly higher values can be expected during the nighttime period when absolute time delay values are generally much lower.

There is no evidence of a solar cycle dependence of the percentage standard deviation and only a slight geographic dependence as one approaches the auroral zone. The daytime variability exhibits a peak during the equinox and is much more well behaved than the nighttime variability.

We have shown that the distribution of time delays about the monthly mean is nearly Gaussian for the cases examined.

ACKNOWLEDGEMENTS

Several experimenters were responsible for the data collection from various stations. The authors wish to express their appreciation for use of the data by acknowledging the following: TEC data from Stanford and Edmonton was provided by A.V. da Rosa; from Aberystwyth by L. Kersley; from Hong Kong by G.O. Walker; from Hawaii by H.T. Roelofs; from Narssarssuaq by I. Mikkelsen; and from Athens by D. Matsoukas.

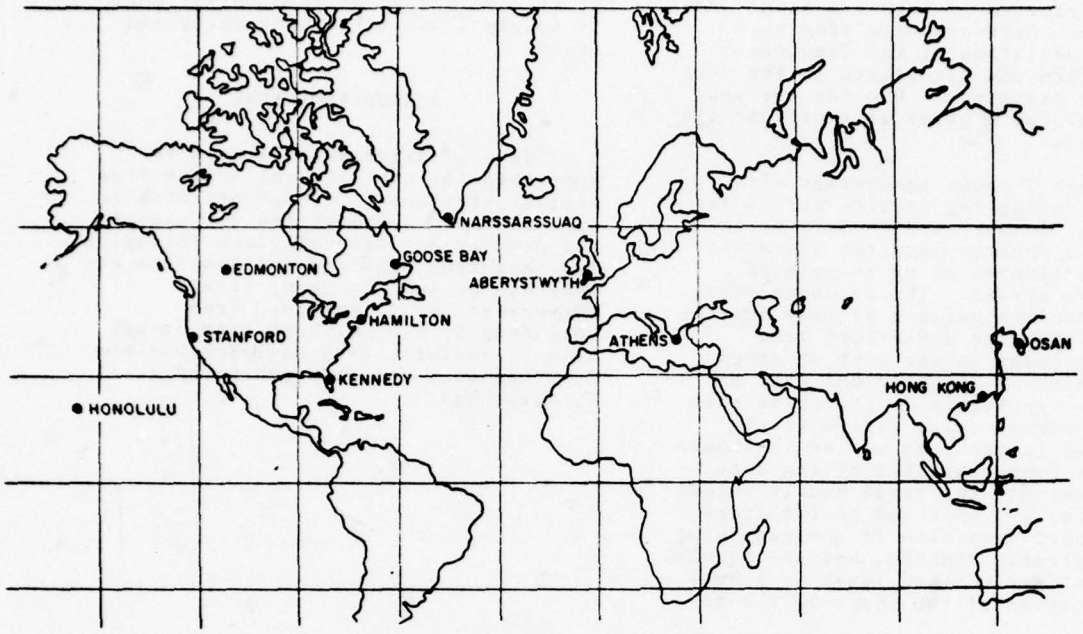


Fig. 1. Location of Ionospheric Monitoring Stations.

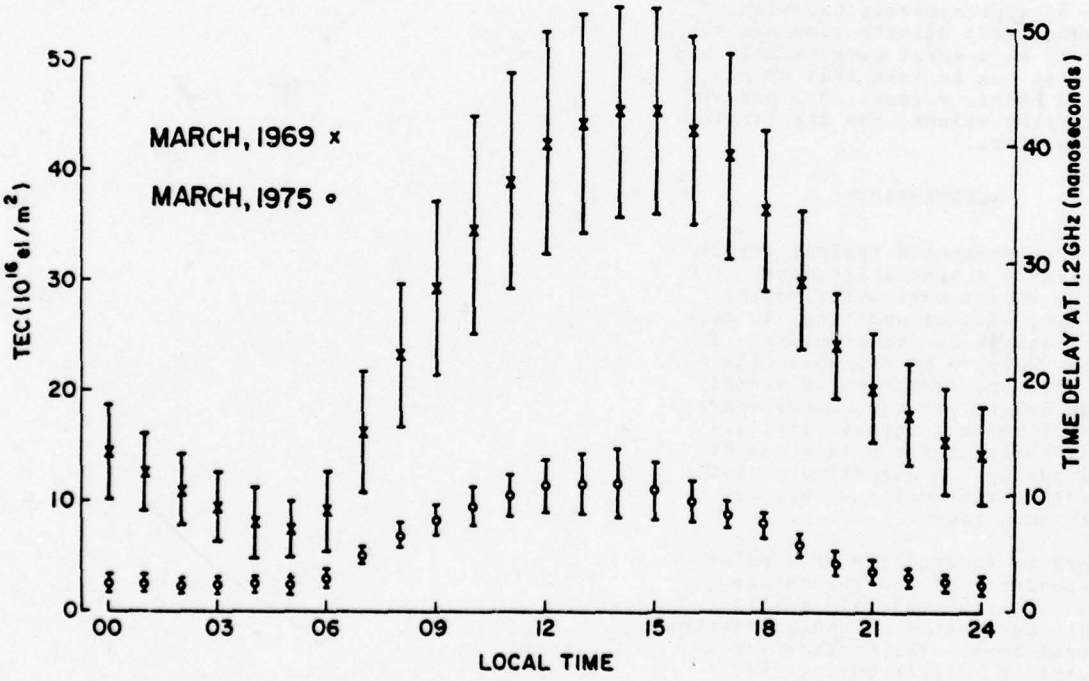
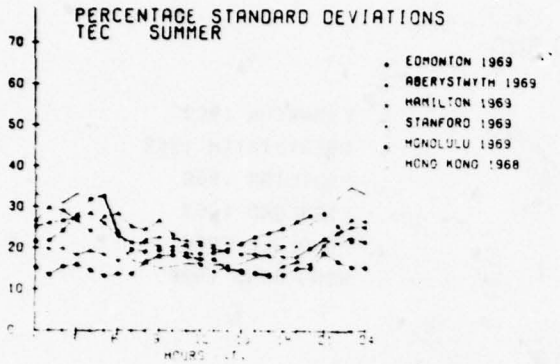
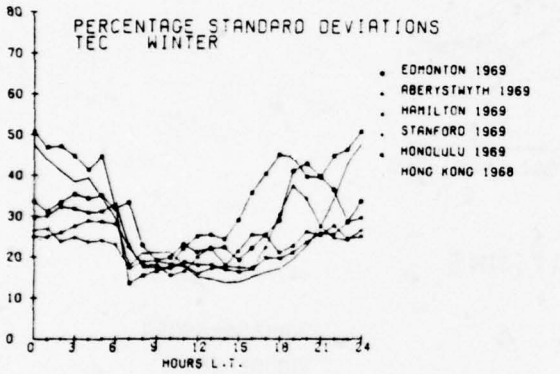


Fig. 2. Typical diurnal monthly mean curves and their standard deviations during solar maximum and minimum conditions observed at Hamilton, Massachusetts.





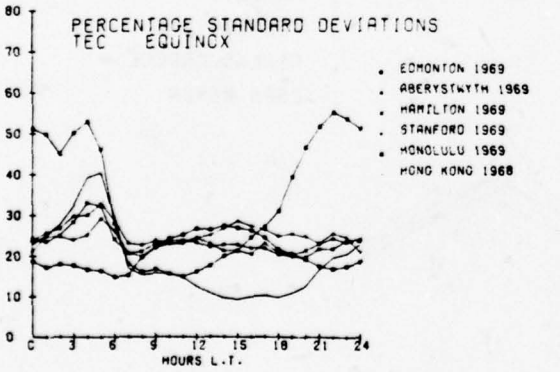
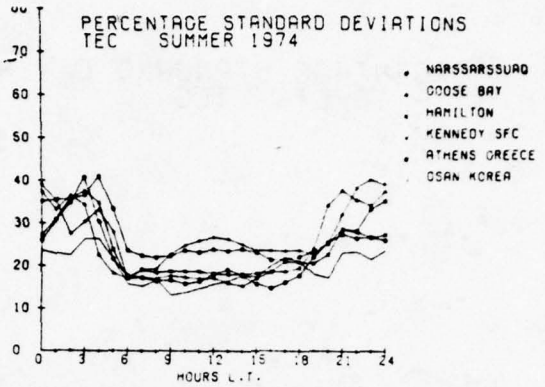
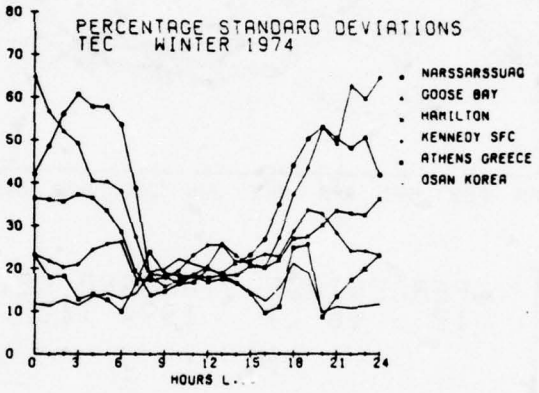


Fig. 3. Diurnal percentage standard deviation TEC curves for six stations during solar maximum.





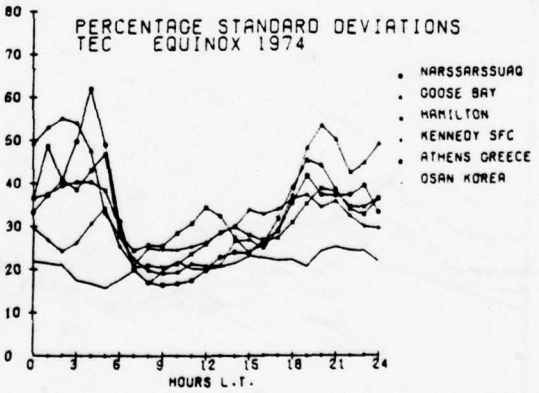
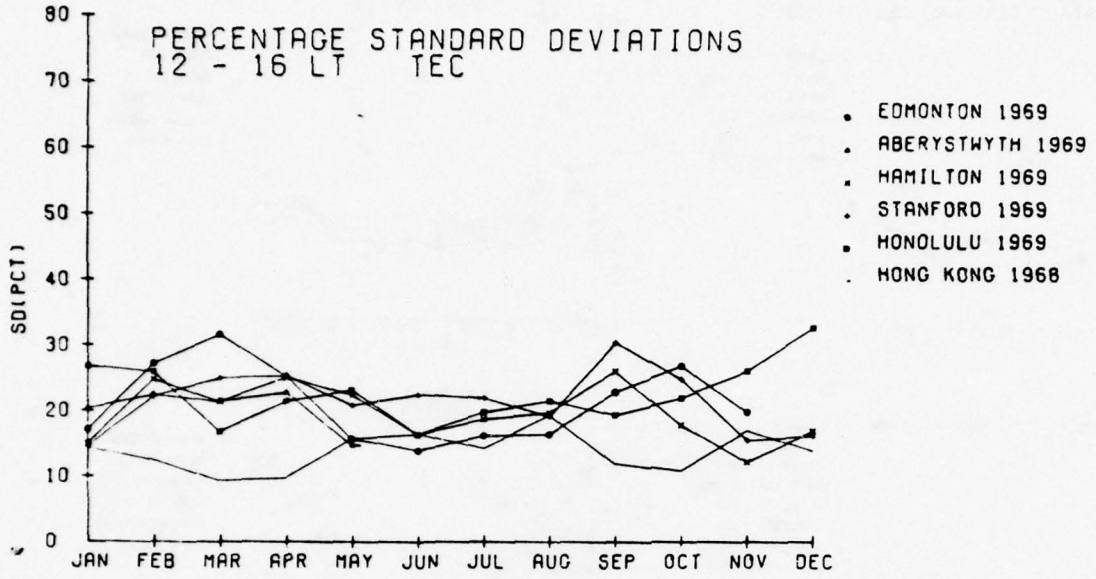


Fig. 4. Diurnal percentage standard deviation TEC curves for six stations during solar minimum.



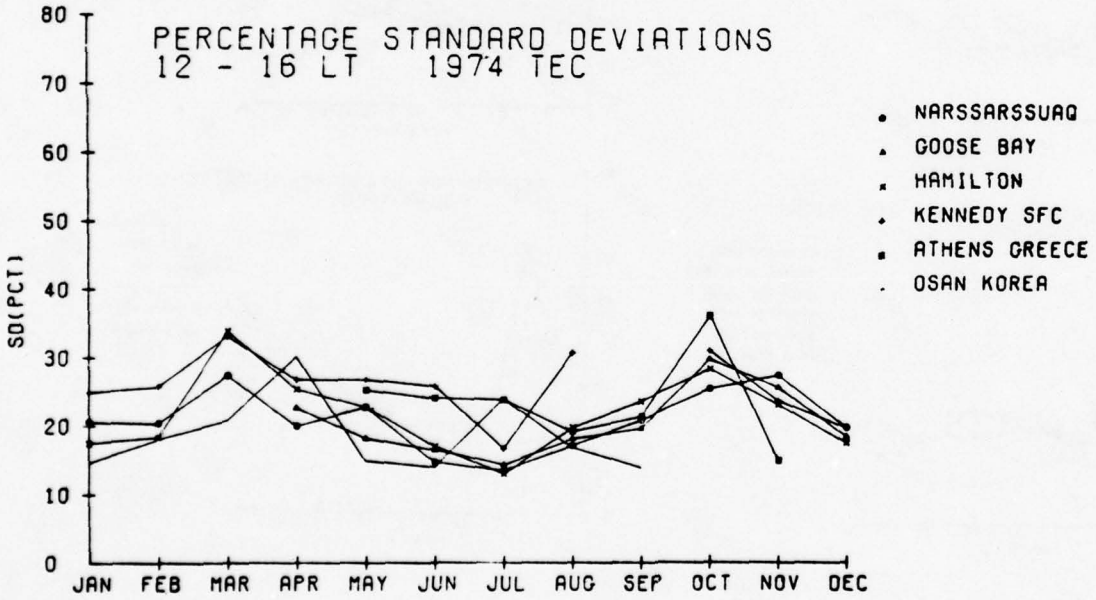


Fig. 5. Daytime percentage standard deviation vs. month for solar maximum and solar minimum conditions.

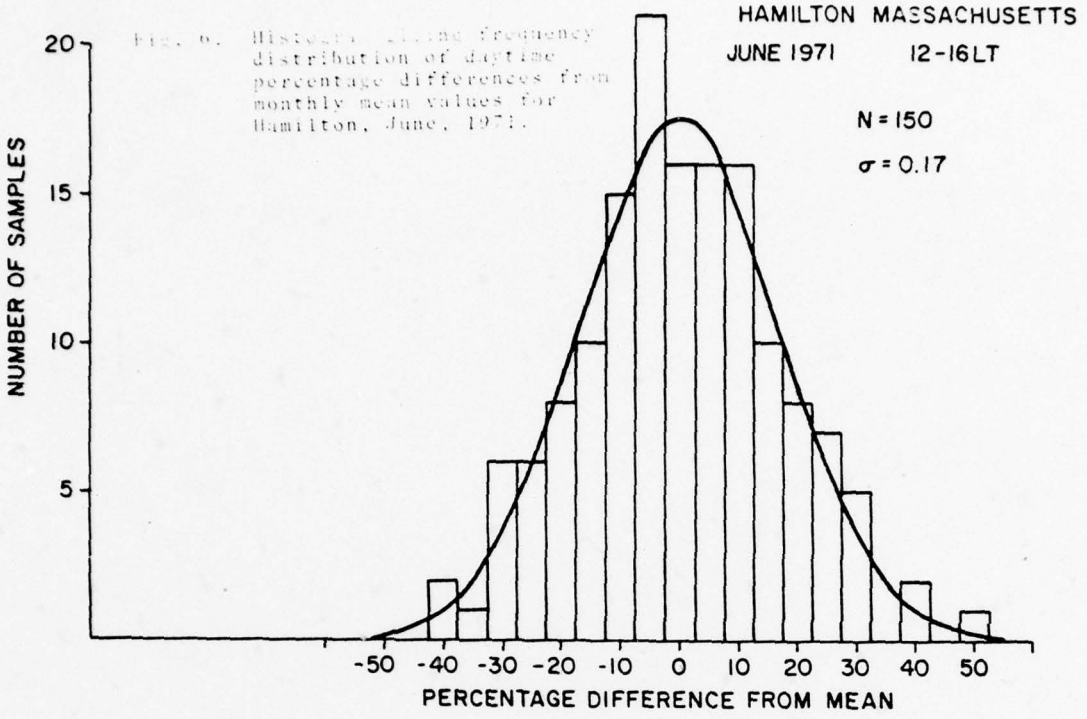


Fig. 6. Histogram giving frequency distribution of daytime percentage differences from monthly mean values for Hamilton, June, 1971.

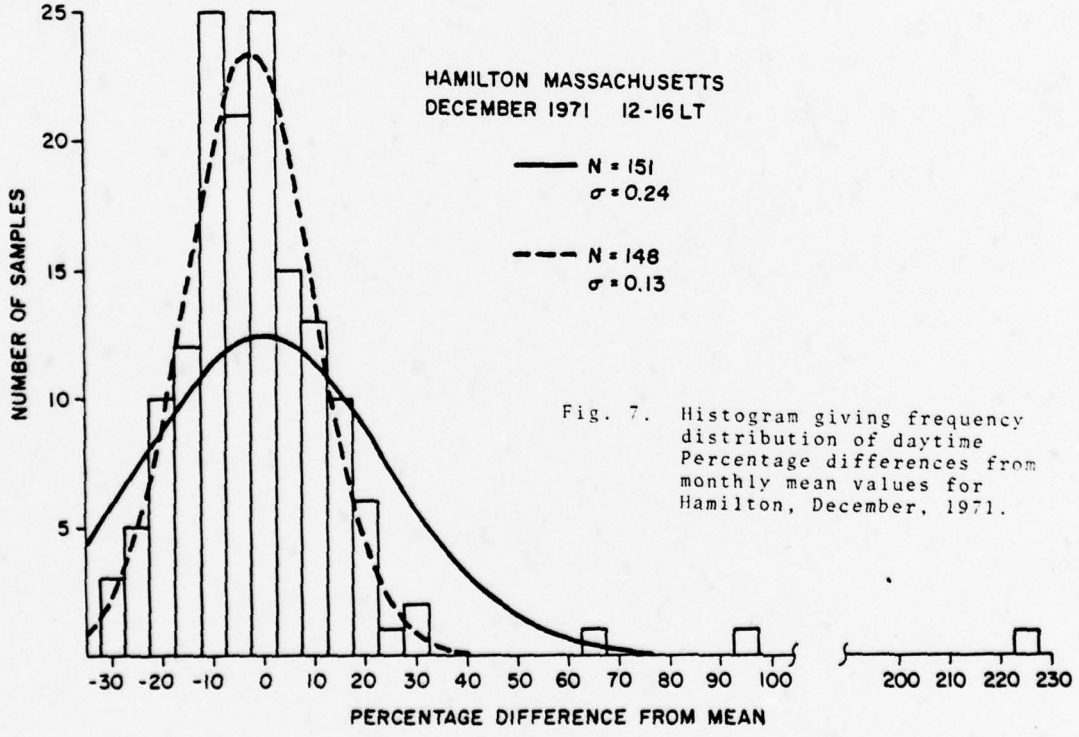


Fig. 7. Histogram giving frequency distribution of daytime Percentage differences from monthly mean values for Hamilton, December, 1971.

PRECEDING PAGE BLANK - NOT FILMED

THE CONTRIBUTION OF THE PLASMASPHERE TO TOTAL TIME DELAY

J.A. Klobuchar
Air Force Geophysics Laboratory
Hanscom AFB, MA 01731

M.J. Buonsanto and M.J. Mendillo
Boston University
Boston, MA 02215

J.M. Johanson
Emmanuel College
Boston, MA 02115

INTRODUCTION

The Total Columnar Electron Content (TEC) of the earth's ionosphere produces group delay of modulation of radio frequency waves which traverse the ionosphere. This group delay can produce significant range errors in advanced systems which require accuracies of a few feet in measured range. The NAVSTAR-Global Positioning System[1] (GPS) is an example of a precise ranging system currently under development by the Department of Defense which will undergo significant ionospheric group delay. Fortunately, the GPS will have two, widely spaced frequencies available from which the group delay of the ionosphere can be directly measured and subtracted from the apparent range to yield the true range from satellite to user. Some users may not choose the sophistication of the two frequency version of the system, however, and may instead choose to use an analytic model representation of the ionospheric time delay. To construct and to test such models and to enable advanced ranging system designers to obtain estimates of the magnitude of the ionospheric group delay error, use has been made of the available Faraday rotation data which is a measure of the TEC to a height of approximately 2,500 kilometers. Since advanced satellite ranging systems will be at orbital heights considerably greater than 2,500 kilometers, 20,000 kilometers in the case of the GPS, it is of interest to determine the additional contribution to ionospheric time delay not measureable from the available Faraday TEC data.

AVAILABLE PLASMASPHERIC ELECTRON CONTENT DATA

There are approximately 1000 station-months of TEC data obtained from the Faraday effect available from representative stations around the world, covering both solar maximum and minimum conditions. Until the launch of the geostationary satellite ATS-6 in mid-1974, there were no simultaneous Faraday and group delay measurements from which the additional contribution to TEC not measureable from the available Faraday TEC data could be determined. The ionospheric beacon transmitter carried on the ATS-6 geostationary satellite, Davies, et al[2], was designed to enable the measurement of simultaneous Faraday rotation and true group delay from its multi-frequency beacon transmissions. This is the first satellite to carry a beacon transmitter specifically designed for simultaneous Faraday and group delay measurements.

The difference between the group delay measurement of slant TEC, minus the Faraday electron content, defined here as a measure of the electrons in the region up to approximately 2,500 kilometers in vertical height, is called the plasmaspheric electron content, N_p. The currently available published monthly mean values of N_p are relatively few and consist of approximately 11 months of data from Boulder, Colorado, Fritz[3], a few months from Ft. Monmouth New Jersey, Soicher[4], one month each from Natal, Brazil and from Kiruna, Sweden, Soicher[5], and nine months of N_p monthly median values from

Aberystwyth, Wales, Hajeb-Hosseinieh[6]. In addition, Soicher[7], Webb and Lanzerotti[8], Poletti-Liuzzi[9], et al and Hajeb-Hosseinieh[6] have published studies of the behavior of N_p during a few magnetic storms, and Klobuchar and Johanson[10] presented a comparison of the monthly average N_p results at Boulder with those from Hamilton, Mass. Since all the available N_p data is from the period later than May 1974 it is representative of solar minimum conditions only.

Kersley[11] has recently pointed out that plasmaspheric electron content measurements taken from stations at nearly the same latitude, but differing in longitude, while viewing the ATS-6 satellite at the same satellite location, actually probe nearly the same plasmaspheric region even though the stations may have relatively large longitudinal differences. This is simply because the ray paths from the ground stations all converge at the satellite at 36,000 kilometers and in the plasmasphere they are also not significantly different. Klobuchar and Johanson indeed showed that the difference in monthly behavior between data sets taken at Hamilton, Mass. and Boulder, Col. was small. In view of this we shall take the Hamilton, Mass. data as being typical of the US region and the data from Aberystwyth, Wales as typical of the European sector.

EXPERIMENTAL RESULTS

With a substantial amount of data available only from Wales from the European sector and with the Hamilton, Mass. data representative of the US data it is of interest to compare the absolute values of the monthly average N_p values versus local time. Data from Hamilton are from July 1974 through May 1975, taken when ATS-6 was at 94°W longitude, while data from Aberystwyth are from November 1975 through July 1976 during which time ATS-6 was located at 35°E longitude. The scale on the left in Figure 1 is in TEC units of $m^{-2} \times 10^{16}$, while the right hand scale is in nanoseconds of group delay at a system operational frequency of 1.6 GHz, the single frequency mode GPS system operational frequency. Also plotted in Figure 1 is the one month's available N_p data from Sao Paulo, Brazil for May 1975 and the one month's available N_p data from Kiruna, Sweden for October 1975.

It is immediately obvious from Figure 1 that the Wales data is significantly higher than the values from the US. Kersley and Klobuchar[12] have attributed the difference between the N_p values in the American and European sectors as being due to the lower geomagnetic latitudes reached by the Aberystwyth ray path to ATS-6 as opposed to the ray from Hamilton, Mass. to ATS-6. At the lower geomagnetic latitudes the scale height at the base of the plasmasphere is predominantly controlled by H^+ ions, with consequent greater scale heights, as opposed to the higher magnetic latitudes where more O^+ ions yield smaller scale heights. The Wales ray path reaches a minimum L shell of 1.7 as opposed to 2.2 for the Hamilton ray path.

While the differences in the diurnal behavior of the two sets of data shown in Figure 1 can be explained by their different minimum geomagnetic latitudes, for the systems engineer it is of more interest to point out that the day-to-night variation for both sets of data is less than the difference between the two data sets. The absolute value of the time delay is small in terms of present system accuracy requirements. In view of the small absolute values of time delay no attempts were made to fit diurnally changing functions to the monthly average data from the station. Simple constant values of 2 nanoseconds for the Wales data and 1 nanosecond for the US representative data are probably sufficient to account for the monthly average values of plasmaspheric electron content.

PLASMASPHERIC GROUP DELAY DURING MAGNETIC STORMS

Major magnetic storms produce electrodynamical effects which cause the emptying of the plasmasphere into the ionosphere and/or the peeling off of the plasmasphere away from the near-earth region. The time for refilling of the plasmasphere has been studied by use of whistler measurements by Park[13], and recently for the N_p data by Soicher[7], Poletti-Liuzzi[9], et al, Webb and Lanzerotti[8], and by Hajeb-Hosseinieh[6]. The time for refilling of the plasmasphere as viewed from the mid-latitudes is on the order of several days. These results from a few representative magnetic storms illustrate that from 3 to 8 days are required for N_p to return to its approximate average value.

CONCLUSIONS

With the limited plasmaspheric

data available thus far the additional contribution to ionospheric group delay not previously available from Faraday rotation measurements of TEC is of the order of 1 to 2 nanoseconds at 1.6 GHz. This value is certainly small compared to the present system operational requirements, but it is an additional amount which can be added to existing models of time delay. The difference between the European and US data is significant and perhaps represents the two limiting cases of N_p from the mid-latitudes as the US longitudes have the highest magnetic latitudes compared to geographic latitudes, while the European magnetic latitudes are lower than their geographic latitudes. Insufficient data are presently available from higher latitudes or from near equatorial latitudes to determine whether either of these regions will have values of N_p significantly different from those in the mid-latitudes. The one month of data available from Kiruna, Sweden compares well with the Aberystwyth data. The Sao Paulo data is at a much lower latitude than any of the other stations, yet it is consistent with the other data sets.

During magnetic storms N_p drops to very small values and takes from 3 to 8 days to recover to the average value. If information on occurrence of magnetic storms is available the model value of N_p can be modified accordingly. Of course, during magnetic storms much greater changes occur in the TEC of the ionosphere and the N_p depletions will be generally insignificant compared to the greater changes from average conditions which occur in the ionosphere. Thus, any TEC model must be capable of representing the ionospheric changes from average conditions, before the much smaller N_p values need be of concern.

All available N_p data are for solar minimum conditions and are from only two representative mid-latitude regions of the world, with small exception. It is expected that the electron content of the plasmasphere will increase with increasing solar activity as does the electron content of the ionosphere. Measurements of N_p using signals from ATS-6 are continuing.

REFERENCES

1. Lassiter, E.M., and B. Parkinson, "The Status of the Development of the NAVSTAR-Global Positioning System", Navigation, Volume XXV, No. 97, pp 13-26, January 1977.

2. Davies, K., R.B. Fritz, R.N. Grubb, and J.E. Jones, "Some Early Results from the ATS-6 Radio Beacon Experiment", Radio Science, Vol. 10, No. 8 and 9, pp 185-799, 1975.

3. Fritz, R.N., "ATS-6 Radio Beacon Electron Content Measurements at Boulder, July 1974-May 1975", Report UAG-58, World Data Center A for Solar-Terrestrial Physics, Boulder, Colorado, September 1976.

4. Soicher, H. "Diurnal, Day-to-Day, and Seasonal Variability of N_f, N_t, and N_p at Fort Monmouth, New Jersey", Cospar Satellite Beacon Symposium, Boston, Ma., Boston University, Ed by M. Mendillo, June 1976.

5. Soicher, H., "Comparative Ionospheric and Plasmaspheric Electron Contents from the Three World Regions", Nature, Vol. 264, pp 46-48, Nov. 4, 1976.

6. Hajeb-Hosseinieh, H., "Ionospheric Studies Using Geostationary Satellites", Thesis submitted to the University of Wales, Aberystwyth, Wales, June 1977.

7. Soicher, H., "Response of Electrons in Ionosphere and Plasmasphere to Mangetic Storms", Nature, Vol. 259, pp 33-35, Jan. 1 & 8, 1976.

8. Webb, D.C. and L.J. Lanzerotti, "Temporal Variations in Total Equatorial Plasmasphere Content and their Relationships to the Ring Current Intensity and the Plasmapause", presented at Spring meeting of Americal Geophysical Union, Washington, D.C. June, 1977.

9. Poletti-Liuzzi, D.A., K.C. Yeh, and C.H. Liu, "Radio Beacon Studies of the Plasmasphere", Journ. of Geophysical Res., Vol. 82, No. 7, pp 1106-1114, March, 1977.

10. Klobuchar, J.A. and J.M. Johanson, "A Comparison of Average Plasmaspheric Electron Content at Two Mid-Latitude Stations", presented at Spring meeting of American Geophysical Union, Washington, D.C., June 1977.

11. Kersley, L., private communication.

12. Kersley, L. and J.A. Klobuchar, "Comparison of Protonospheric Electron Content Measurements from the American and European Sectors", in preparation.

13. Park, C.G., "Some Features of Plasma Distribution in the Plasmasphere Deduced from Antarctic Whistlers", Journ. of Geophys. Res., Vol. 79, No. 1, pp 169-173, January 1, 1974.

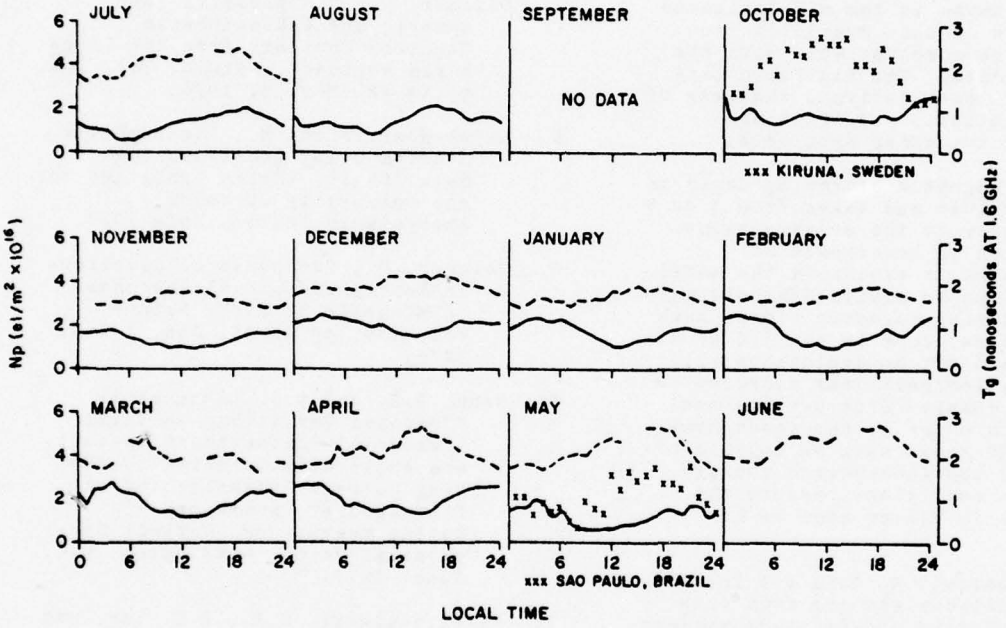


Fig. 1. Monthly average plasmaspheric electron content versus local time for Aberystwyth, Wales (dashed line) and for Hamilton, Mass. (solid line). Also plotted are values from Kiruna, Sweden for October 1975 and from Sao Paulo, Brazil for May 1975. The right hand axis is the equivalent time delay in nanoseconds at 1.6 GHz.

TEMPORAL VARIABILITY OF IONOSPHERIC REFRACTION CORRECTION

D. E. Donatelli
Regis College Research Center
Weston, Massachusetts

R. S. Allen
Air Force Geophysical Laboratory
Hanscom AFB, Mass. 01731

INTRODUCTION

Precision radar and navigation systems now require corrections which consider current ionospheric conditions over their field of view. Techniques are being developed using measurements from calibration satellites to adapt the numerical maps which provide monthly median corrections. These basic maps are derived from a world-wide climatology of ionospheric parameters; their use alone reduces the residual error in range or time delay measurements to 20 to 25 percent of the median correction in daytime and to 30 to 35 percent at night, reflecting the day-to-day variability of the ionosphere about its monthly median values. To reduce this residual, several techniques have been proposed which would scale the maps up or down by a constant percentage, change gradients, and reproduce large local features. This presentation examines the potential effectiveness of such techniques.

Since the refraction corrections are directly proportional to the electron content along the slant path through the ionosphere, measurements of total electron content from Hamilton, Mass. and Goose Bay, Labrador, 30.7°N, 70.7°W, and 47.5°N, 62.2°W geographic, respectively, can be used as calibration measurements for updating median estimates of refraction correction. The data were obtained from measurements of the Faraday rotation of the VHF beacon on the ATS-3 geostationary satellite and were reduced to equivalent vertical electron content (TEC). The years 1970 and 1976 at Hamilton, Mass., taken as representative of solar maximum and minimum, respectively, were used to determine solar cycle and seasonal variations. The data for 1972 from Hamilton, Mass. and Goose Bay, Labrador were used for an initial study of spatial variation in the effectiveness of the updating technique.

EFFECTIVENESS OF AN UPDATING TECHNIQUE

The potential for reduction of residual error while using an updating technique is demonstrated in Figure 1 for March, 1972, with data from Hamilton, Mass. The heavy solid line represents the expected residual error, δR_m, when only the predicted median was used for correction. The light lines depict the time-decay in residual error when a calibration measurement was used. At each calibration time a scaling factor was determined from the ratio of the calibration measurement and the predicted median. This factor was then used to scale the predicted median of the subsequent 12 hours, in 15-minute intervals. There was a 0-error at the time of calibration, shown at every second hour, and these curves show the increase in error with time, as well as the length of time required for the error to approach δRm.

The dashed lines represent the diurnal variation in the residual rms error using a scaling factor determined 30-minutes previously, δR_{30m}, and 1-hour previously, δR_{1h}. After 30 minutes the maximum error increased to about 3 meters and after 1 hour it increased to 5 meters. These residual errors are significantly below the expected residual error of 18 meters for this time of day. This 70-80 percent reduction occurs when refractive effects are greatest and the need for improved accuracy is most critical. Note that a scaling factor should not be used to project an update across either the sunrise or sunset terminator as this may increase error, particularly near sunrise. Unless calibration measurements can be made at these times in 15-30 minute intervals it would be preferable to simply use the climatological prediction.

This applies at any time in which steep gradients in TEC are expected to occur, such as during magnetic disturbances. A "worst case" example of this is noted in Figure 2. On March 8, 1970, a severe magnetic storm occurred, and the effects observed in the TEC data at Hamilton, Mass. were the largest for the total 9 years examined from 1968 through 1976, both for the extremes and rapid changes in TEC.

The ordinate of the upper scale is range correction in meters at 425 Mhz. The predicted median range correction for March, 1970, ΔR, was the range correction the radar would have used on this particular day if no updating procedure existed. The actual range correction that should have been made, ΔR_d, shows that a correction of nearly 195 meters was required at about 1500 hours on that day, more than twice the maximum of 95 meters for ΔR. If an updating technique, such as the one previously described had been used, the range correction made using calibration measurements after 30 minutes would have been ΔR_{30m}, and after 3 hours, ΔR_{3h}.

The ordinate of the lower scale is the absolute error, in meters, that would have been experienced with the corrections presented for this day. The error between: the observations on that day, ΔR_d, and the monthly median, ΔR, is δR_m; between ΔR_d and the 30 minute update, ΔR_{30m}, is δR_{30m}; and between ΔR_d and the 3 hour update, ΔR_{3h}, is δR_{3h}. Using the 30 minute update resulted in a maximum error of less than 50 meters compared to the maximum of nearly 110 meters if only the median had been used. On the other hand, the 3 hour update produced errors on the order of δR_m or greater during this disturbance. The salient feature of this result occurred near 1800 hours when the 3-hour delay caused a large error during the time when a negative gradient was observed. It follows that whenever steep and variable gradients are likely to occur, calibration measurements should be made in intervals no greater than 30 minutes, not only to achieve significant accuracy, but also to avoid introducing errors.

The effectiveness of an updating technique varies seasonally and over solar cycle as well as diurnally. The principal features of these variations are summarized in Figure 3 for the years 1970 and 1976 representing solar maximum and minimum, respectively, at Hamilton, Mass. Included are the maximum values each month for: the predicted median range correction, ΔR; the residual error when the median is used for correction, δRm, which represents the day-to-day variability of the ionosphere; the reduction in residual error when calibration measurements are used in updating techniques each 15 minutes, δR_{15m}; 30 minutes, δR_{30m}; 1 hour, δR_{1h}; and 3 hours, δR_{3h}.

Comparison of ΔR and δR_m showed the 75 percent reduction that can be achieved by simply using a median correction for ionospheric effects. This is possible for both solar maximum and solar minimum conditions, and at all seasons. A further reduction, through use of local measurements in an updating procedure, showed less consistent results. At solar maximum, in daytime, even an update that is 3 hours old will provide a significant reduction in residual error. But at solar minimum, a measurement much more than 1 hour old will provide no significantly greater accuracy than using only the expected median. Whereas the monthly median, ΔR, and the day-to-day variability, δR_m, are a factor of 4 greater at solar maximum than at solar minimum, the residual error using an updating procedure, as shown by δR_{15m}, δR_{30m}, δR_{1h}, and δR_{3h}, varies by only a factor of 2 over the solar cycle. Thus it appears that at solar maximum there are longer period variations that are readily corrected with the updating procedure. The shorter period fluctuations which are superimposed on these long-term variations exist at both solar maximum and solar minimum and impose a limit on the effectiveness of updating techniques.

Seasonally, summer is the time of least day-to-day variability and least residual error after an updating procedure. The greatest residual error appears at the equinoxes and can be considerably reduced with frequent updating, as shown by δR_{15m} and δR_{30m}. It is in winter that updating is least effective. At solar maximum, the residual error can be reduced to a maximum of 25 meters with 15-minute updating, and to 40 meters with 30-minute updating. The maxima occur in winter and at the equinoxes. This becomes even more apparent at solar minimum, where δR_{15m} and δR_{30m} show a definite maximum in winter and minimum in summer.

The same updating procedure was used with data from 1972 for Hamilton, Mass. and Goose Bay, Labrador. The results from both stations are compared in Figure 4, using the same parameters as in Figure 3. It is seen that at both stations the curves for each parameter are comparable; the fact that Goose Bay is a higher latitude station does not appear to be significant. The general results are similar to those described for 1970, at Hamilton in Figure 3, which may be attributed to the fact that the year 1972 was one of increased solar activity. Therefore it is not surprising that the results resemble solar maximum conditions rather than a median which is more representative of the descending phase of the solar cycle.

CONCLUSION

This study has shown that reduction in residual error due to the day-to-day variability of the ionosphere is possible through use of an updating technique coupling local

measurements with climatological predictions of median ionospheric behavior. Reductions of 70 to 80 percent are possible in daytime, particularly during periods of increased solar activity. It has been shown that while the residual error varied by a factor of 4 between solar maximum and minimum, use of the updating procedure reduced this variation to a factor of 2. Therefore, this technique was more effective when the residual error in range correction was greatest.

It has also been shown that caution is required in choosing the length of time a particular scaling factor is used. For an average day, the constraint on this time is set by the sunrise-sunset terminators. A scaling factor may be used for any length of time within the day or nighttime period in which it is determined, but it must not be projected across the terminator.

The large, variable gradients of the sunrise and sunset periods can be equated with those occurring in periods of severe magnetic disturbance. The interpretation of these gradients provided by a median prediction can be improved upon by an updating procedure using calibration intervals of less than 30 minutes. Longer intervals are likely to introduce errors of larger magnitude than the variation from the predicted median.

The temporal decay in effective updating is dependent on the period of the TEC variations. Long period fluctuations, which are readily corrected, are a consistent feature at any site. These include day or nighttime periods that are enhanced or depressed with respect to the median behavior. These periods must be longer than the time interval between calibrative measurements for updating to be effective. Shorter period fluctuations are generally present and the percentage amplitude of these variations is the minimum percentage residual error achievable.

By considering these results with the following factors: range correction is inversely proportional to the radio frequency squared and directly proportional to the total electron content (TEC) along the wave path; TEC, to a first approximation, varies linearly with 12-month running mean, sunspot number and solar flux at 2800 Mhz, it is possible to estimate performance for any system, at any location, at any time.

ACKNOWLEDGEMENTS

The authors would like to thank Mr. J. Klobuchar of the Air Force Geophysics Laboratory for use of the TEC data from Hamilton, Mass. and Goose Bay, Labrador. This work was performed under Air Force Contract F19628-76-C-0255.

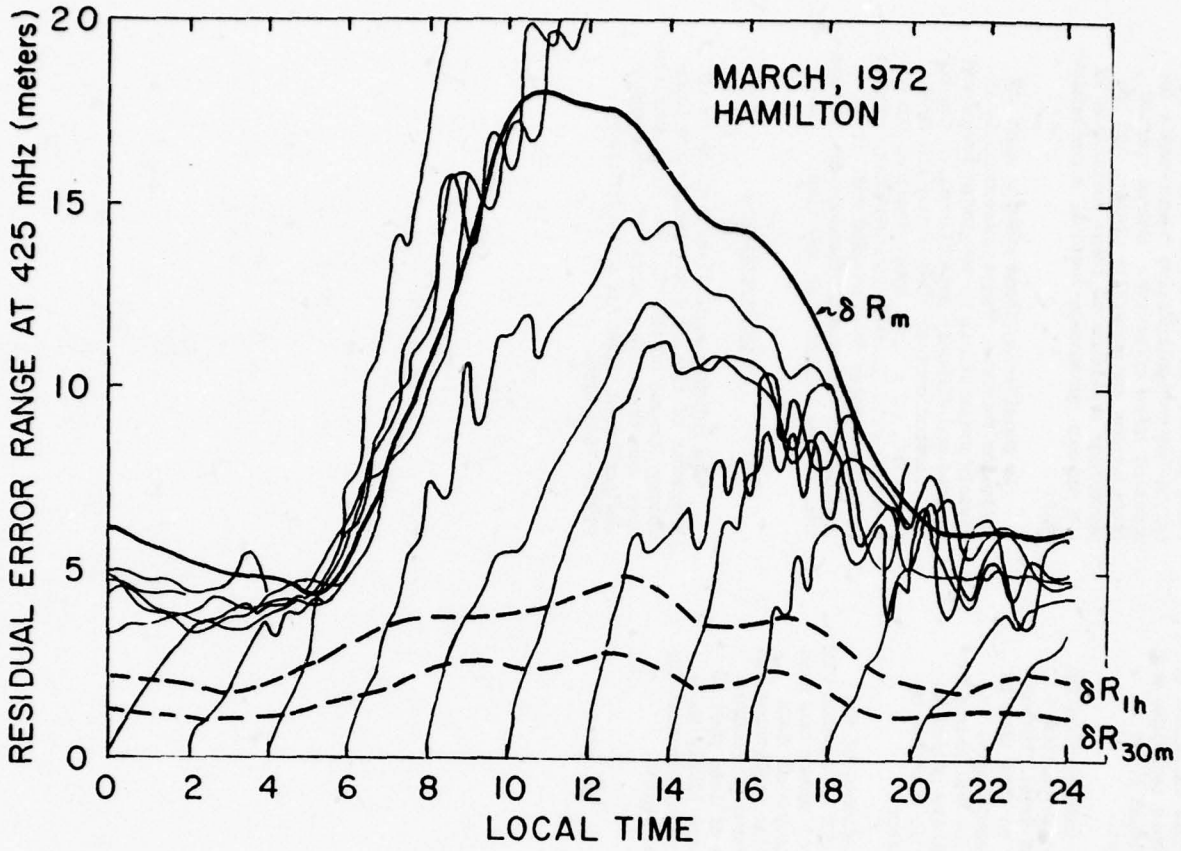


Figure 1. The residual error in range correction using an updating technique ranging from 0-residual error at the time of calibration to the residual error using only the median correction, δR_m, at a time depending primarily on the interval between calibration and subsequent terminator.

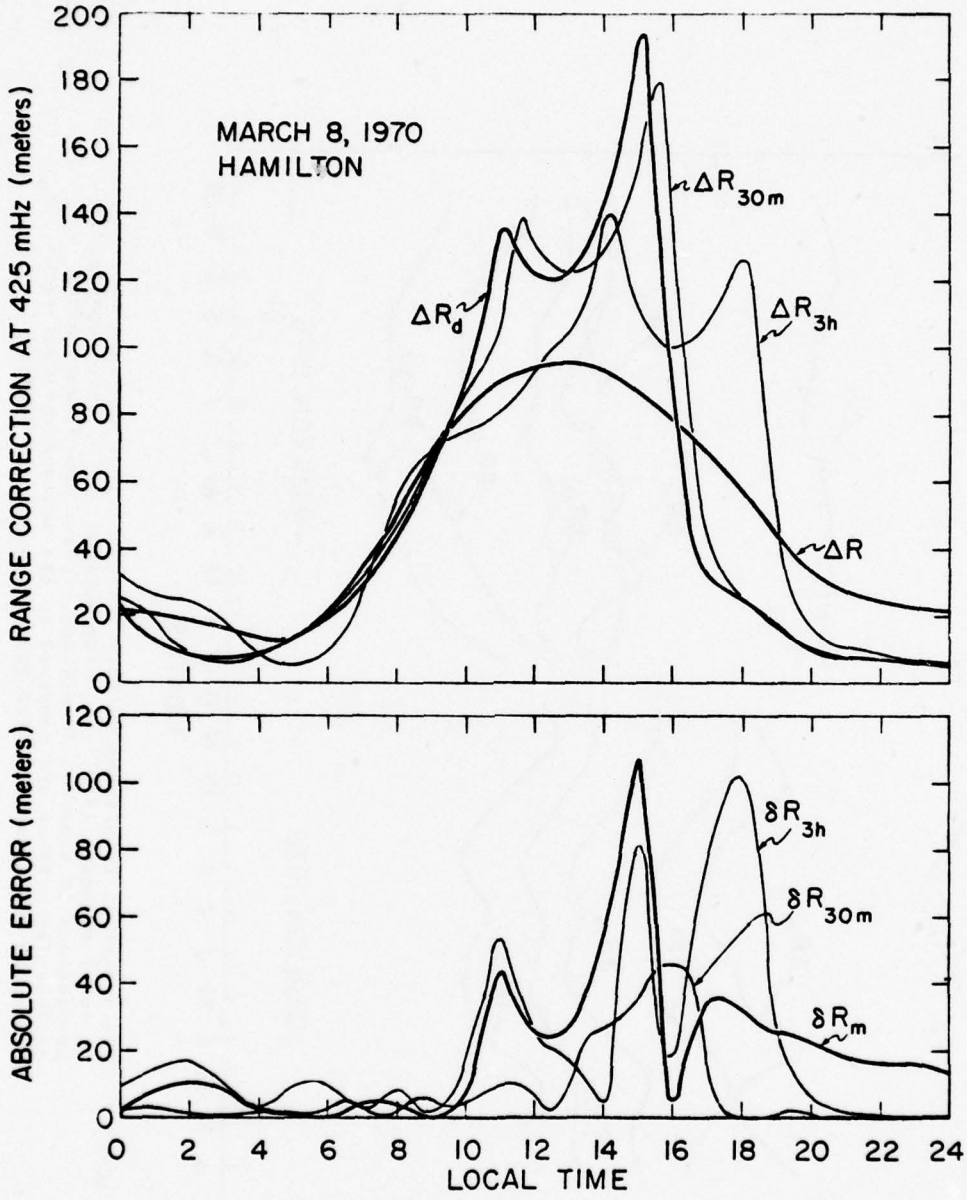


Figure 2. The effectiveness of an updating procedure during a severe magnetic disturbance, comparing the actual required range correction, ΔR_d, with the predicted median, ΔR, and the 30 minute, $\Delta R_{30\,m}$, and 3 hour, $\Delta R_{3\,h}$, updated predictions. The differences in the range correction curves of the upper scale are presented as absolute error on the lower scale.

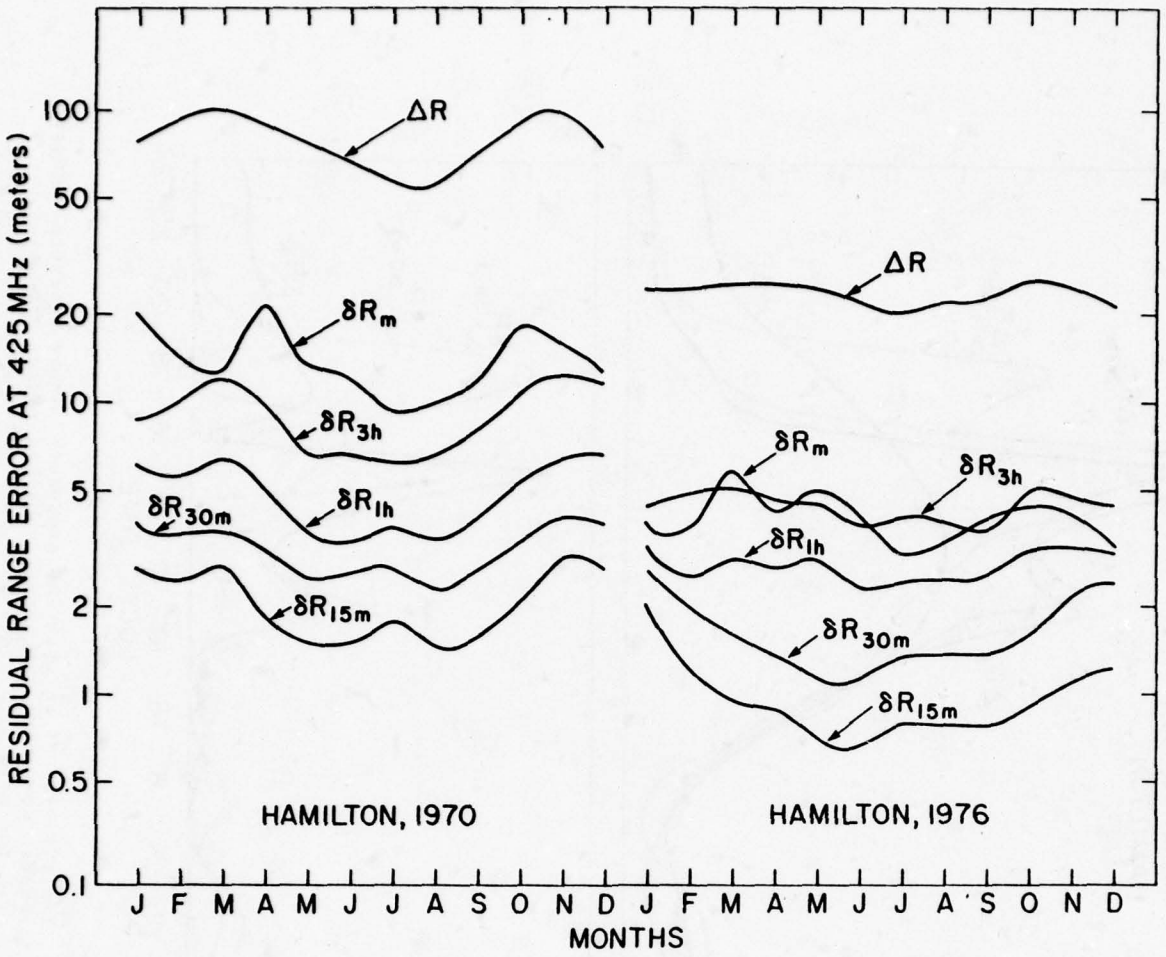


Figure 3. The reduction in maximum monthly residual error in range correction at solar maximum, 1970, and solar minimum, 1976, using updated predictions 15 minutes, 30 minutes, 1 hour and 3 hours after calibration. These are compared to the maximum residual error, δR_m, after the non-updated median correction, ΔR, is applied.

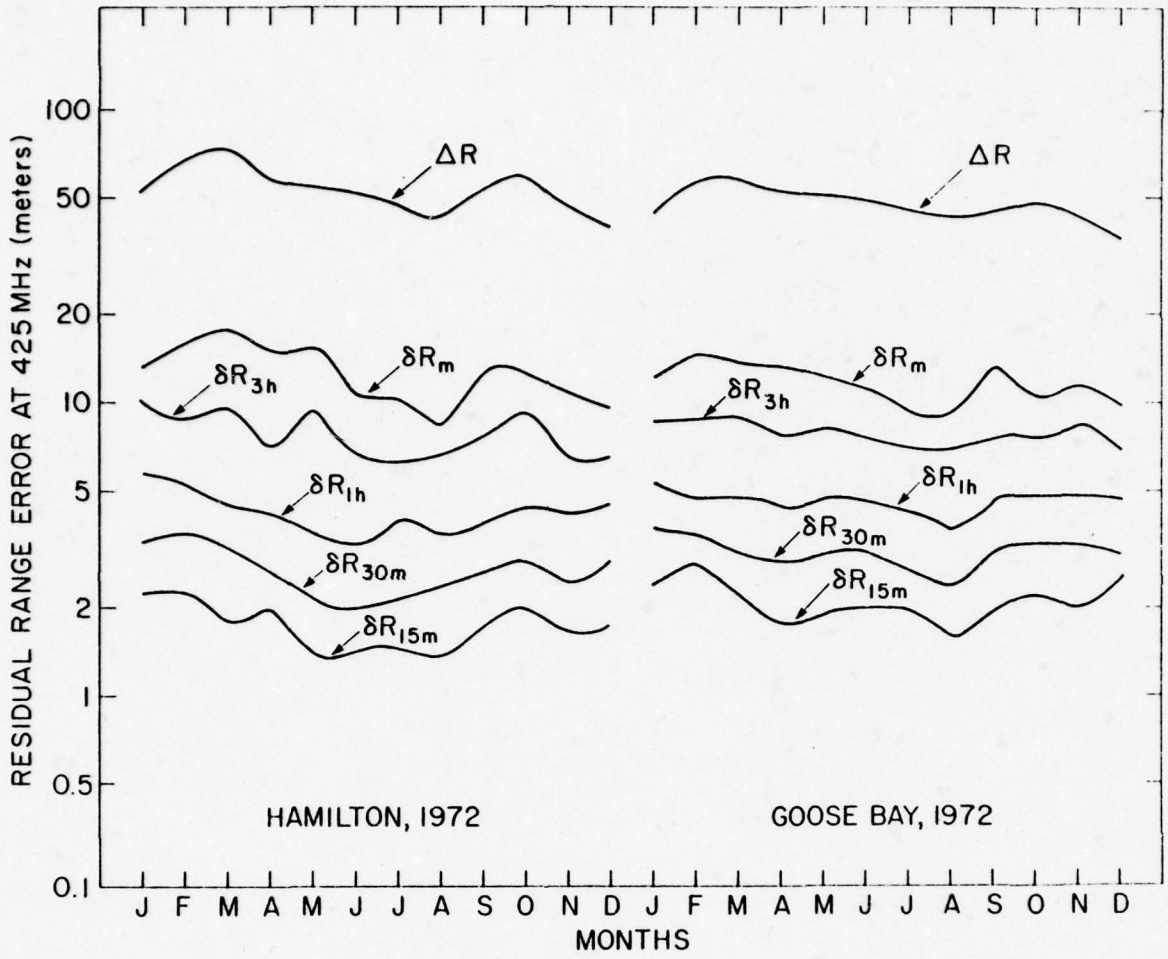


Figure 4. *The reduction in maximum monthly residual error in range correction at two different stations, Hamilton, Mass., and Goose Bay, Labrador, for 1972 using the same parameters as in Figure 3.*

PRECEDING PAGE BLANK - NOT FILMED

ADAPTIVE CORRECTION OF THE EFFECT OF THE IONOSPHERE ON RANGE DETERMINATION BY TERRESTRIAL RADARS

A.H. Katz and M.D. Grossi
Raytheon Company, Wayland, Massachusetts 01778

R.S. Allen
Air Force Geophysics Laboratory, Hanscom Air Force Base, Massachusetts 01731

D.E. Donatelli
Regis College, Weston, Massachusetts 02193

ABSTRACT

An effective correction of the range errors induced by the ionosphere in terrestrial radar systems (the error can be reduced down to 10 ft at UHF) is based on the joint use of an ionospheric model and of a few discrete samples of the dispersive ionospheric medium taken by the radar itself (when dual-frequency ranging is available) or by other means, such as reception at the radar site of dual-frequency emissions from navigation satellites. The scheme makes use of a model of the monthly median ionosphere constructed from existing worldwide climatology (and capable of providing by itself a residual range error not larger than 35 ft) and updates this model with real-time dual-frequency measurements (accurate in themselves to about 4 ft) of the columnar electron content. This is done for directions and at times for which targets of opportunity (such as satellites and target vehicles embedded in the ionosphere) become available. A practical implementation of this real-time adaptive scheme, prepared by the authors, has confirmed that a hybrid hardware-software approach leads to an efficient utilization of radar resources. An experimental evaluation has recently been performed of this novel procedure by using both the data from a precision L-band radar and from ground-based observations of the emissions of the NNSS navigation satellite. This experimental verification has sho shown that the method is both effective in terms of reduction of the ionospheric range errors and advantageous inasmuch as it minimizes the utilization of the radar resources for this scope.

1. INTRODUCTION AND SUMMARY

Precision radar systems require corrections for time or range errors caused by the ionosphere, when that medium is crossed in all or in part by the propagation path. To first order such errors are directly proportional to the integrated electron content along the path to the target. In real time these radar errors may be substantially reduced by predictions of the expected propagation effects using a model of the monthly median ionosphere constructed from existing worldwide climatologies. Such median corrections are shown to have a residual day-to-day r.m.s. variability about the median on the order of 20-25 percent of the median value.

For instance, the expected worst median case (daytime, equinox, sunspot maximum) for range errors experienced by an L-band radar at mid-latitudes is shown in Table 1.

By use of such a model, a goal of 35 ft for the 1-sigma residual range error can be achieved at L-band even during expected worst median conditions. In precision radar systems more stringent requirements exist and the ionospheric induced error must be typically reduced to a few feet.

Table 1
Worst Case Monthly Median Uncorrected Range Errors (ft) at L-Band and Their Variability (1 Sigma)

Target Altitude (km)	Radar Elevation					
	0°		20°		90°	
	Range Error (ft)	Sigma	Range Error (ft)	Sigma	Range Error (ft)	Sigma
1000	147	30	102	20	47	9
400	107	20	74	16	34	7
300	57	11	40	8	18	4

To satisfy such requirements, a real-time adaptive scheme has been developed consisting of a model of the median ionosphere for the particular radar coverage region (derived from more complicated models of worldwide climatology) and of a set of algorithms to provide error corrections for targets at specified coordinates, which together attempt only to deliver an r.m.s. error on the order of 25% of the expected median correction at that location. This estimate is then specified by a dual-frequency dispersive probing of the ionosphere in the target area by the radar itself, using satellites of opportunity or even target vehicles embedded in the ionosphere.

The dual-frequency measurement, with accuracy on the order of 4 feet, is used to derive a normalization factor for the median ionospheric model in the surveillance volume, dependent on the radar range, elevation and altitude of the radar target.

The interval between the model's adaptive updatings by the dual-frequency probing depends on the space and time characteristics of the ionosphere.

At times of low sunspot number, a 10-ft range error specification can be met at mid-latitude by using a spherically symmetric monthly median ionospheric model, stored in the radar processor memory and adapted with dual-frequency measurements made at half hourly intervals. This correction is effective even in the presence of a strong Traveling Ionospheric Disturbance (TID).

At times of high sunspot number, the radar algorithms must consider realistic horizontal gradients modeled by the median ionosphere. The adaptive dual-frequency updating is still sufficient even at these times to meet the 10-ft range error.

During sporadic disturbed periods, such as when impulsive TIDs generated in auroral substorms pass over narrow regions of the radar coverage volume, the space-time cell over which the 10-ft specification can be met by a single normalization will shrink in both space and time, therefore more frequent (in time and space) dual-frequency probing may become necessary.

2. MODEL'S SOFTWARE MECHANIZATION

2.1 General

The range correction model consists of three 33-element vectors. Let's assume, as an example, a radar azimuth span of 130°, an elevation angle span from 0.0° to 80°, and a height span from 0 to 1000 km. Ionospheric range corrections (ΔR) are required at each location in the volume. The value of ΔR is generated by multiplication of the three 33-element matrices (i for height, j for elevation angle, and k for azimuth). ΔR_{ijk} is generated by the following equation:

$$\Delta R_{ijk} = (H_i \; E_j \; A_k) \; C_0(U)$$

where

H_i is a 33-element vector which represents the variation in height referenced to 1000 km at a constant elevation angle (0.0°) and constant azimuth;

E_j is a 33-element vector which represents the variation in elevation angle referenced to 0.0 at a constant azimuth and constant height (1000 km);

A_k is a 33-element vector which represents the variation in azimuth referenced to boresight at a constant height (1000 km) and constant elevation angle (0.0°);

C_0 is a normalization constant which makes the largest value in the H_i vector (which occurs at 1000 km) equal to 1;

U is a factor which updates the model either from a real-time pulse pair measurement from a satellite within the radar coverage or from an ionospheric update service such as the Air Weather Service (AWS) Prediction Service.

Figure 1 provides an example of the median range error predicted as a function of height and elevation angle for an azimuth located at the array boresight. The 33-element elevation and height vectors are determined from this data.

2.2 Height Vector

At radar boresight and 0.0° elevation angle, the range corrections at the radar frequency are determined in 33 steps in height. If we adopt a function I defined as

$$I = K\left[(1 + h/R)^2 - 1\right]$$

it can be shown that

$$I = K\left[(r/R)^2 + 2(r/R)\sin E\right]$$

where h = height of target above earth in kilometers, R is the radius of the earth in kilometers, K is the scaling constant such that I = 33 at h = 1000 km, r is the target range in kilometers, and E is the elevation angle. As r and sin E are normally available in a real-time system, it is relatively straightforward to calculate I. Thus, storing the ionospheric corrections in I space reduces computational requirements. Table 2 shows the value of i, I and the corresponding height for 33 steps along a 0.0 elevation angle. The constant K = 97.46. Note that at h = 0 km, I = 0 and the ionospheric correction is zero. If in the calculation of I we have I = 5.4, the value of H at i = 5.4 is determined by linear interpolation between the value of H at i = 5 and i = 6. The constant C_0 is equal to $1/H_{33}$ and all values of H are divided by H_{33} before entry into the H_i vector.

2.3 Elevation Vector

The elevation vector E are arrayed in (sin E) space where sin E = v cos E_0 + w sin E_0 (E_0 is the tilt of the array from zenith). The 33 elements of the vector are generated in equal increments of sin space from 0.0 (j = 1) to 80 (j = 33) degrees. Table 3 lists the element number "j", the elevation and sin E for the 33 elements. If the calculated sin E from the radar data falls between vector elements, linear interpolation between vector elements will be used.

2.4 Azimuth Vector

The azimuth vector A_k [Kahrilas, 1976] is arrayed in (Tan ΔAz) space where:

$$\text{Tan } \Delta Az = \frac{u}{w \cos E_0 - v \sin E_0}$$

and

$$\Delta Az = Az_0 - Az \quad (Az_0 = \text{radar boresight})$$

ΔAz varies from 0 to 65° off boresight. The use of equal steps in tan ΔAz will lead to a large first step in azimuth from boresight. That is, if a 33-element vector is used the first step in ΔAz space is 7.6° (i.e., 0 to 7.6°). Thus, near the radar boresight, where the greatest accuracy is required, the fewest azimuthal vector elements will be located. However, by using the function $\tan(\Delta Az)/(1 + 0.2 \tan^2(\Delta Az))$, the first step is 4° and further the function provides a fairly uniform spacing in azimuth space. As such, the 33-element azimuth vector is generated in equal steps of $\tan(\Delta Az)/(1 + 0.2 \tan^2(\Delta Az))$ at 0.0° elevation angle (j = 1) and h = 1000 km (i = 33). Table 4 lists the 33 elements of the azimuthal vector including the element number "k", the true azimuth, the difference between true and boresight azimuth, and $(\tan(\Delta Az)/(1 + 0.2 \tan^2(\Delta Az))$ from the

Table 2
Height Vector H_i

i	I	h (km)	H_i
	0	0	
1	1	32.6	
2	2	65.0	
3	3	97.3	Generated By Model
.	.	.	
.	.	.	
31	31	943.3	
32	32	971.7	
33	33	1000.0	

Table 3
Elevation Vector E_j

(j) Vector Element	E	sin E	E_j
1	0.00	0.0000	
2	1.76	0.03078	
3	3.53	0.06156	Generated By Model
.	.	.	
.	.	.	
.	.	.	
31	67.43	0.9234	
32	72.59	0.9542	
33	80.05	0.9849	

Table 4
Azimuth Vector A_k

K	ΔAz (°)	$\frac{\tan(\Delta Az)}{(1 + 0.2 \tan^2(\Delta Az))}$	A_k	
1	-65.0	-1.117		
2	-57.2	-1.047		
3	-52.8	-0.977	Generated By Model	
.	.	.		
.	.	.		
.	.	.		
31	52.8	+0.977		
32	57.2	+1.047		
33	65.0	+1.116		

radar data falls between vector elements, linear interpolation between vector elements will be used.

2.5 Update Procedure

In our study we have considered two update procedures, one adaptive and one non-adaptive. In both cases a single value multiplicatively updates the values of ΔR_{ijk} for all i, j and k. The first update procedure is based on the use of a pulse pair (dual frequency) measurement of the ionosphere by using a satellite of opportunity as the target. This update procedure must be repeated every half-hour. The second procedure is a non-adaptive update approach based on data provided by an ionospheric update service such as AWS. If the dual-frequency measurement is not available or otherwise unacceptable for whatever reason, the AWS update is used instead. In addition, the AWS update is used to ensure that the pulse pair (dual frequency) update does not generate unreasonable corrections.

The update algorithm for the pulse pair (Upp) is

$$Upp = \frac{\Delta b}{\Delta R_{ijk}}$$

where

$$\Delta b = \frac{(R_L - R_H)\, f_H^2\, f_L^2}{f_{OP}^2 (f_H^2 - f_L^2)}$$

R_L is the apparent range to satellite at f_L

R_H is the apparent range to satellite at f_H

f_{OP} is the operating frequency of the radar

Δb is the ionospheric correction factor obtained directly from the pulse pair measurements and ΔR_{ijk} is the prediction of the model at that location.

The Air Weather Service (AWS) provides an update U_{AWS} on a three-hour basis. This number is used in the same manner as the number generated from the dual-frequency measurement except that it

requires an operator-initiated action. The update is defined as the ratio U_{AWS} where

$$U_{AWS} = \frac{\text{AWS Predicted TEC}}{\text{Median TEC}}$$

where TEC is the vertical Total Electron Content. The update U_{AWS} is provided for the "nominal ionospheric characteristic location" for the radar coverage.

Finally, a brief comment on when the update occurs and the time sequence involved in using the vectors from one hour to the next. A given set of vectors will be used from 30 minutes before the hour until 29 minutes, 59 seconds after the hour (e.g. the 00Z deck is used from 2330:00 until 0029:59). If an event occurs during the last few minutes of the half-hour and will continue into the next hour, the new table for the next hour should not be entered until the event has ended.

In addition to updating the model for the one-hour time period which encompasses the pulse-pair measurement, a pulse-pair measurement can also be used to update the model for succeeding hours. However, three hours after the pulse-pair update was obtained, the median model should be used with the AWS update unless a new pulse-pair measurement is made. That is, each pulse-pair update should be considered valid for at most three hours. The update ratio that is obtained during a specific hour can be used to update the set of vectors which represent the following two hours. It must be remembered, however, that the update factor or ratio once calculated does not change even though a new set of vectors representing the next hour is used.

2.6 Software Structure for the Ionospheric Range Correction Procedure

For each hour of the day (24 hours per day) ten computer cards will form the set of inputs required by the model. The 24 sets of ten computer cards will be valid for each day of the month. Each new month will require a new set of cards. Figure 2 shows a listing of the 10 computer cards for April 1977 at 0000Z. The first card is a header card which specifies the month, year, hour (in universal time) and the constant C_0 in feet. The first card also identifies the source of the ionospheric range correction, the elevation coverage sector, and the azimuthal coverage sector. The last 7 columns of each card (columns 74-80) contain the year, month, hour and card number, with the header card Card No. 0. The next three cards contain the height vector H_i. The location of H_i for i = 1 to 33 is noted on Figure 2. In like manner, cards 5, 6 and 7 contain the elevation vector E_j in sin space and cards 8, 9 and 10 contain the azimuth vector A_k in tan space. Figure 3 is a listing of the computer cards which provide the ionospheric range error model for the month of April 1977.

3. VERIFICATION PROCEDURE

3.1 General

Range correction, to the first order, is directly proportional to the integrated electron content along the slant ray path and for an L-band radar tracking a target at 5 degrees elevation angle at a height of 1000 km, the proportionally constant is 7.1 feet for each TEC unit of 10^{16} el/m^2. A recent study of the temporal variability of TEC at a station very similar to the target area of the L-band radar referred to in this paper [Dulong, 1977] can be used to estimate the effectiveness of the updating techniques across the overall radar's operational time.

The average day-to-day variability of the residual range correction after using the monthly median as a predictor will be 20% to 25% of the monthly median at night. The absolute error is about 2 to 3 times greater in daytime than in nighttime.

An evaluation of the effectiveness of the correction method illustrated in this paper was performed using nine years of continuous TEC measurements at Hamilton, Mass., a station very similar to the target area of the radar under evaluation, in geographic and geomagnetic coordinates. This has shown that

one calibration update performed according to our method in the target area can reduce the residual error by 60% when the update is one hour old and by 30% (in daytime) even when the update is three hours old.

3.2 Effect of Local Features

When the highest precision is required, then large local enhancements such as latitudinal gradients over the whole field of view, medium scale traveling disturbances and persistent localized features such as the mid-latitude trough are of concern. To assess their effects, a study is underway using field observations taken with the Navy Navigation Satellite System satellites [Leitinger and Hartmann, 1976]. This can be illustrated by Figure 4. The procedure consists of first determining the equivalent vertical range corrections for the ionosphere along a NNSS track as for 1120 local time, 12 December 1975. This information, plotted versus latitude, is then compared to the prediction of the median expected for the month. Thus, scaling factors are obtained as a function of latitude. These scaling factors are then used to update the median prediction over the whole field of view for the next pass, in this case at 1240 local time. In this way a sequential set of NNSS tracks can be used to simulate first the update calibration and then the actual radar measurement.

As seen in Figure 4, the gradients of the uncorrected median, derived from a smooth climatology of the ionosphere, do not match the actual gradients observed at 1240, resulting in large absolute residual errors in some regions. The adapted prediction, even though it is an hour and twenty minutes old and from a somewhat different longitude region, still significantly reduces the error. Note however that some of the medium scale features of the 1120 ionosphere are either displaced or changed in the 1240 ionosphere, which suggests that there would be the need of some filtering of the spatial information in the update process.

The effect of the mid-latitude trough is sampled in Figure (after Leitinger and Hartmann, 1976). This series of sequential NNSS passes shows that the ionosphere was depressed below the expected medians during the predawn hours and that a deep trough formed near 49° N geographic latitude ($L \approx 4$) at the minimum. The NNSS pass near midnight local time (0005 LT) indicates the start of this feature, which was quite deep four hours later. With such a trough near the horizon of our radar, the residual error with respect to the predicted median would be increased by a factor of about three to account for the slant thickness of the ionosphere.

An on-going study [Allen et al, 1977] suggests that general enhancements of the ionosphere, changes in latitudinal gradients and large local features, may be tracked by local measurements, such as the dual-frequency update, and that they may be extended over the field of view. The density of the updating grid in space and time will be determined by the stringency of the metric requirements of the radar.

3.3 L-Band Radar Data

The proposed approach has been evaluated by comparing L-band radar observations with predicted (and updated) ionospheric range errors. Figure 6 shows the comparison between median predictions and radar observations of ionospheric range error (the radar observations of the ionosphere were obtained using differential time delay from dual-frequency transmission from the radar). In this case the median predicted and radar observations (at the normalization point) were equivalent and no update was required. The difference between the prediction and the observation was in all cases less than 5 ft.

The second example (Figure 7) shows that the median predictions were underpredicting the required range correction. However, updating the median prediction substantially reduces the discrepancy between predicted and measured data.

4. CONCLUSIONS

The effectiveness of the adaptive correction of the deteriorating influence of the ionosphere on the range accuracy

of terrestrial radars [Allen et al, 1976; DuLong et al, 1977; Katz et al, 1977] has been confirmed by experimental findings.

By updating climatological models of the expected ionospheric errors with real-time dual-frequency measurements of the medium, it was shown that L-band radar range errors could be kept at all times below 10 ft with a spatially and temporally rare application of the updating process. This statement holds true even taking into account the presence of localized gradients and features, of difficult inclusion in climatological models. To accommodate then exceptional ionospheric circumstances or more stringent radar range accuracy requirements, our method must simply be applied with a higher spatial and temporal density.

REFERENCES

Allen, R.S., D.D. DuLong, M.D. Grossi, A.H. Katz, Ionospheric Range Error Correction in Precision Radar Systems by Adaptive Probing of the Propagation Medium, AGARD Conf. Proc. #209 on Propagation Limitations of Navigation and Positioning Systems, Istanbul, Turkey, 1976.

Allen, R.S., D.E. Donatelli, G.K. Hartmann, R. Leitinger, Adaptive Mapping of Mid-Latitude Ionosphere, AFGL-TR-77-0176, August 1977.

DuLong, D.D., Reduction of the Uncertainties of Range Correction, AFGL-TR-77-0125, June 1977.

Kahrilas, P.J., Electronic Scanning Radar Systems (ESRS) Design Handbook, Chapter 7, Artech House, Inc., 1976.

Katz, A.H., M.D. Grossi, T.I.S. Boak, Practical Implementation of Adaptive Ionospheric Range Error Correction for High Accuracy Radars, URSI Meeting, San Francisco, Cal., June 1977.

Leitinger, R. and G.K. Hartmann, Time and Latitude Dependence of Ionospheric Electron Content from the Combination of NNSS and ATS-6 Data, COSPAR Symposium Proceedings, Geophysical Use of Satellite Beacon Observation, Boston University, June 1976.

THIS PAGE IS BEST QUALITY PRACTICABLE
FROM COPY FURNISHED TO DDC

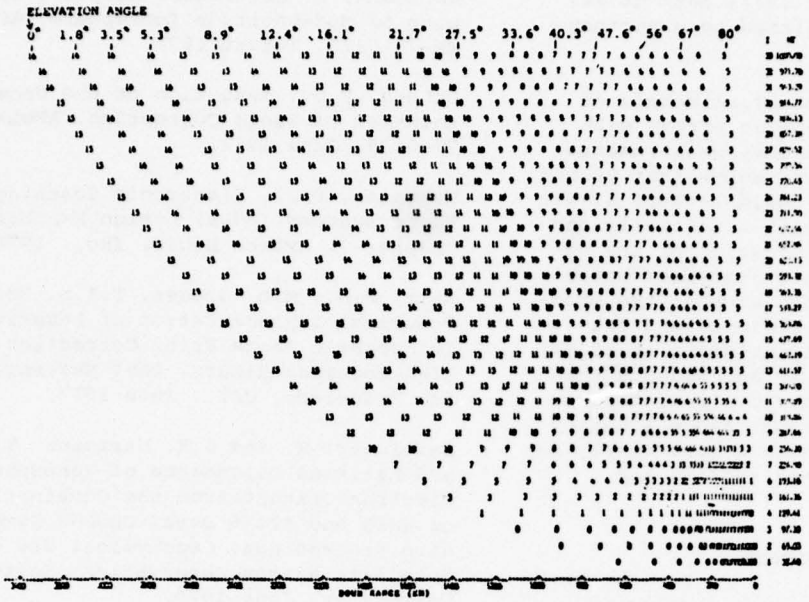
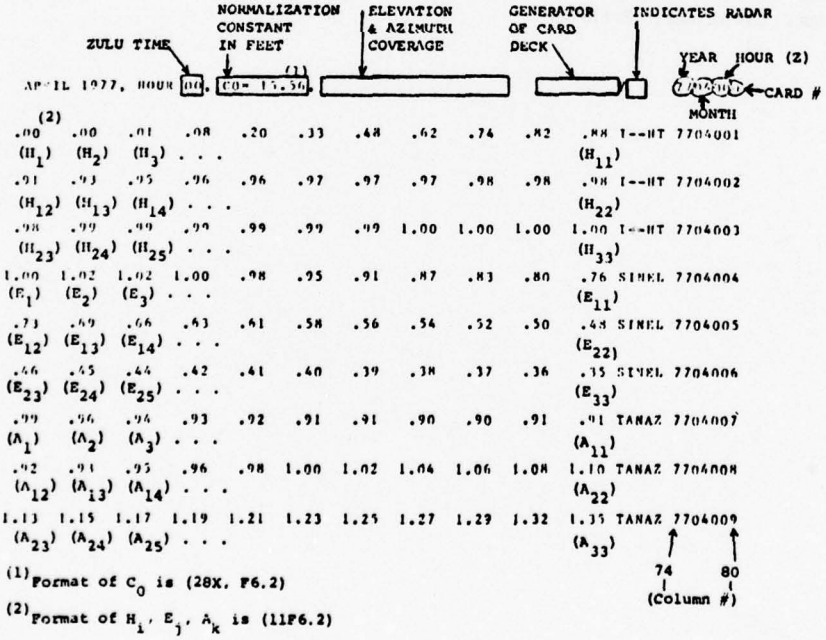


Figure 1 Plot of Range Error (feet) at L-Band Vs Height and Down Range for Selected Elevation Angles for 0000Z, April 1977



(1) Format of C_0 is (28X, F6.2)

(2) Format of H_i, E_j, A_k is (11F6.2)

Figure 2 Listing of Computer Cards for One Hour in April 1977

THIS PAGE IS BEST QUALITY PRACTICABLE
FROM COPY FURNISHED TO DDC

```
  APRIL 1977, HOUR 18, CO=  4.03,                                          7704180
 .00   .00   .00   .00   .01   .02   .03   .05   .08   .22   .40 I--HT 7704181
 .55   .67   .74   .79   .83   .85   .87   .89   .90   .91   .92 I--HT 7704182
 .93   .94   .94   .95   .96   .97   .97   .98   .99   .99  1.00 I--HT 7704183
1.00  1.06  1.15  1.26  1.39  1.51  1.67  1.72  1.69  1.62  1.55 SINEL 7704184
1.49  1.43  1.37  1.32  1.27  1.23  1.19  1.14  1.11  1.07  1.04 SINEL 7704185
1.00   .97   .95   .92   .89   .87   .85   .83   .81   .79   .77 SINEL 7704186
2.28  2.13  2.04  2.00  2.07  2.09  2.08  2.05  2.01  1.98  1.70 TANAZ 7704187
1.38  1.21  1.10  1.04  1.01  1.00  1.00  1.01  1.02  1.04  1.07 TANAZ 7704188
1.09  1.13  1.16  1.20  1.24  1.28  1.32  1.37  1.41  1.45  1.51 TANAZ 7704189
  APRIL 1977, HOUR 19, CO=  8.75,                                          7704190
 .00   .00   .00   .06   .15   .24   .33   .42   .53   .63   .71 I--HT 7704191
 .79   .84   .88   .90   .92   .93   .94   .95   .95   .96   .96 I--HT 7704192
 .97   .97   .97   .98   .98   .98   .99   .99   .99  1.00  1.00 I--HT 7704193
1.00  1.04  1.04  1.03  1.01   .99   .96   .93   .90   .87   .83 SINEL 7704194
 .80   .77   .74   .72   .69   .67   .64   .62   .60   .58   .56 SINEL 7704195
 .55   .53   .51   .50   .49   .47   .46   .45   .44   .43   .42 SINEL 7704196
1.20  1.14  1.11  1.08  1.06  1.03  1.02  1.00  1.00  1.03  1.04 TANAZ 7704197
1.05  1.04  1.04  1.03  1.02  1.00   .97   .94   .90   .87   .85 TANAZ 7704198
 .84   .85   .86   .87   .90   .92   .96  1.00  1.05  1.11  1.20 TANAZ 7704199
  APRIL 1977, HOUR 20, CO=  9.75,                                          7704200
 .00   .00   .01   .09   .21   .36   .50   .63   .72   .79   .84 I--HT 770
 .87   .90   .91   .93   .93   .94   .95   .95   .96   .96   .97 I--
 .97   .97   .98   .98   .98   .99   .99   .99   .99  1.00  1.00          08
1.00  1.01  1.01  1.00   .99   .97   .95   .92   .89   .86                7704209
 .80   .77   .74   .71   .69   .66   .64   .62   .60                  0   7704210
 .54   .53   .51   .50   .48   .47   .46   .45   .43                .88 I--HT 7704211
1.19  1.14  1.11  1.08  1.06  1.04  1.02  1.01                        .97 I--HT 7704212
 .96   .95   .95   .96   .98  1.00  1.02  1.03                   .00  1.00 I--HT 7704213
1.10  1.12  1.15  1.17  1.19  1.22  1.24  1.26                    .90   .87 SINEL 7704214
  APRIL 1977, HOUR 21, CO= 10.51,                                  .59   .57 SINEL 7704215
 .00   .00   .01   .10   .24   .42   .58                          .43   .42 SINEL 7704216
 .91   .92   .93   .94   .95   .95                              1.03  1.02  1.01 TANAZ 7704217
 .97   .98   .98   .98   .99   .99                              1.12  1.15  1.18 TANAZ 7704218
1.00  1.03  1.05  1.06  1.08                                    1.45  1.52  1.59 TANAZ 7704219
 .83   .80   .77                                                          7704220
 .55   .53                      .40   .56   .70   .80   .86   .90 I--HT 7704221
1.20  1.15                .96   .96   .97   .97   .97   .98   .98 I--HT 7704222
1.01                      .99   .99   .99   .99   .99  1.00  1.00  1.00 I--HT 7704223
1.23                1.05  1.04  1.01   .98   .95   .91   .87   .83 SINEL 7704224
           .73   .70   .67   .65   .62   .60   .57   .55   .53 SINEL 7704225
      .50   .48   .47   .45   .44   .43   .42   .41   .40   .39 SINEL 7704226
 .1  1.09  1.07  1.05  1.04  1.03  1.02  1.01  1.00   .99   .99 TANAZ 7704227
 .98   .98   .97   .96   .97  1.00  1.04  1.08  1.11  1.14  1.18 TANAZ 7704228
1.21  1.24  1.28  1.31  1.34  1.37  1.40  1.43  1.46  1.50  1.56 TANAZ 7704229
  APRIL 1977, HOUR 23, CO= 13.95,                                          7704230
 .00   .00   .01   .09   .21   .36   .52   .66   .77   .85   .89 I--HT 7704231
 .92   .94   .95   .96   .96   .97   .97   .97   .98   .98   .98 I--HT 7704232
 .98   .99   .99   .99   .99   .99   .99  1.00  1.00  1.00  1.00 I--HT 7704233
1.00  1.03  1.04  1.03  1.01   .98   .94   .90   .87   .83   .79 SINEL 7704234
 .75   .72   .69   .66   .63   .61   .58   .56   .54   .52   .50 SINEL 7704235
 .49   .47   .45   .44   .43   .41   .40   .39   .38   .37   .36 SINEL 7704236
1.04   .99   .98   .97   .96   .95   .94   .94   .93   .93   .92 TANAZ 7704237
 .92   .92   .93   .95   .97  1.00  1.03  1.05  1.08  1.11  1.13 TANAZ 7704238
1.16  1.18  1.21  1.23  1.25  1.27  1.30  1.32  1.34  1.37  1.43 TANAZ 7704239
```

Figure 3 Example of Listing of Computer Deck for Ionospheric Correction (April 1977)

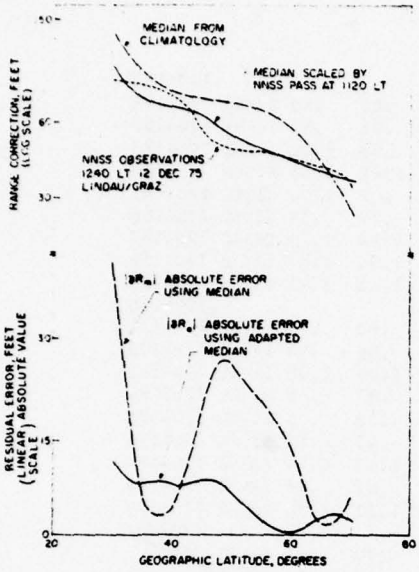


Figure 4 Adaptive Modeling Using Data from NNSS Measurements. 1st pass at 1120 LT is used to scale predicted latitudinal variation at 1120 LT and then the scaled values are predicted forward to 1240 LT.

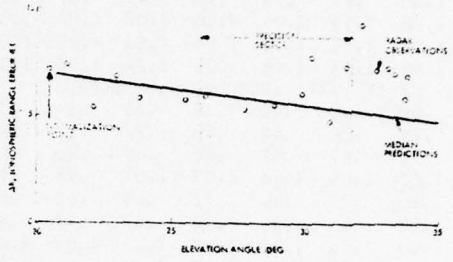


Figure 6 Comparison of L-Band Radar Observations with Predicted Ionospheric Range Errors

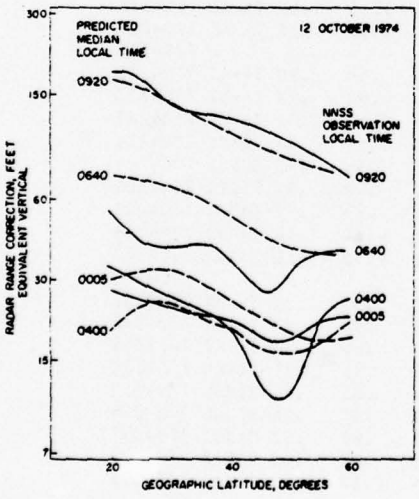


Figure 5 Sample of the Effect of the Trough in Electron Density, Seen Near 49°N Latitude on 12 Oct. 1974 on the Expected Range Correction for an L-band Radar

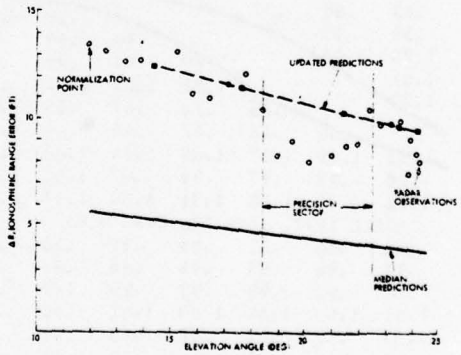


Figure 7 Comparison of L-Band Radar Observations with Predicted and Adaptively Updated Ionospheric Range Errors

ADAPTIVE MAPPING OF IONOSPHERIC FEATURES

R. Leitinger
Institut fur Meteorologie und Geophysik
Universitat Graz, Graz, Austria

R. S. Allen
Air Force Geophysics Laboratory
Hanscom AFB, Mass. 01731

D. E. Donatelli
Regis College Research Center
Weston, Mass.

G. K. Hartmann
Max-Plank-Institut fuer Aeronomie
D-3411 Katlenburg-Lindau 3, FGR

ABSTRACT

Precision navigation and radar systems use local measurements to adapt predictions of refractive effects within their field of view. The intent is to reduce the day to day variability of the refraction correction by tracking local features. To simulate a particular adaptive technique, data from a sequence of passes of the Navy Navigation Satellite System satellites are used to represent both the local measurements of refractive effects and the subsequent system range measurements. This is augmented by measurements of total electron content taken in the same area using VHF beacons on nearly synchronous satellites. Local features such as the nighttime trough and the plasmapause enhancement of the mid latitude ionosphere are tracked by sequential measurements and may be mapped in space and local time across the entire system field of view during quiet daytime geophysical periods. During quiet daytime periods systematic changes in the ionosphere are usefully predicted over a few hours. When the ionosphere is disturbed, very large features can develop in local regions that should only be introduced into the adapted maps if the grid of observations in space and time can resolve their behavior.

INTRODUCTION

The problem being addressed here is generic to modern navigation and radar systems. As their requirements for precision time and range measurements become more stringent, methods must be developed to remove the effects of refraction within the ionosphere. Previously Millman (1974) has shown that, from the first order correction for change in apparent range (ΔR) which is directly proportional to the slant electron content, a correction can be derived for the first order change in elevation angle. Leitinger and Hartman (1977) have shown that for both the range error that affects ranging systems (for navigation purposes, for determination of satellite orbits, etc.) and for the group delay (for dispersion correction of systems), the corrections based on the electron content integrated along the slant path is second order in fineness.

The principle correction, ΔR, may be modeled from existing climatologies of ionospheric parameters (Lewellyn and Bent, 1973), and provided to the system as maps covering the entire field of view.

Since the basic climatology of ionospheric

parameters is dependent only on smoothed solar conditions, these maps can be prepared several months in advance, and when used, will typically remove 50 to 75 percent of the monthly r.m.s. refractive error. For the many systems which require more precise correction, these maps may be adapted by pertinent local measurements to reflect the current solar-terrestrial conditions and major local ionospheric features (DuLong and Allen, 1976). Many local measurements have been proposed: vertical incidence ionosonde data, total electron content derived from beacons of near synchronous satellites, in situ particle measurements from low altitude satellites, etc. The residual refractive error after using any adaptation is dependent on the information within the local measurement and the density of measurements in space and time. These and similar points are discussed in companion presentations (Katz et al, DuLong et al, this Symposium). This working paper will examine some of the promise and problems found when making adapted predictions using slant electron content derived from observations of the Navy Navigation Satellite System (NNSS) satellites.

ADAPTIVE MODELING

To illustrate how refractive effects can be corrected in an adaptive manner, consider a hypothetical radar, figure 1, with a field of view encompassing the ionosphere over Europe. Observations of two radio beacons aboard the NNSS satellites were reduced to provide equivalent vertical electron content for latitude strips representing the satellite tracks within ±8° longtitude of the central stations, Graz, Austria and Lindau, FGR. These NNSS measurements were normalized by referencing to simultaneous electron content data reduced from beacons on the nearly geostationary satellite ATS-6, as observed from Lindau. By converting the NNSS data to radar range correction, the results can be used to adapt maps of median range correction and the reduction in refractive error can be examined over the field of view.

In this presentation we want to ask some basic questions about the usefulness of such an adaptive procedure. Can it predict:

1. enhanced ionospheric conditions?
2. changes in latitudinal gradients?
3. local features?

such that the residual error after adapting for these items is significantly better than the error resulting from use of the monthly median maps alone? We must also ask the question:

4. are the results model dependent?

In simulating a procedure for adaptive modeling, data from the first in a sequence of NNSS passes may be used to normalize the prediction of median range correction to conform to the actual conditions at that time. The scaling used along the latitudinal intervals for this pass would be used to adapt the median along the path at the time of the next NNSS pass. The first pass may be considered a representation of a local ionospheric measurement and the subsequent passes may represent system measurements, such as a radar system measuring the range to a target. The error, after adaptation, δR_a, can be compared to the error using just the median, δR_m, to determine the effectiveness of the adaptive modeling procedure. This may be repeated, using each pass to adapt the model and comparing the predictions of the adapted model at the time of subsequent NNSS passes with the actual observations.

The procedure is illustated in Figure 2 for a pass of NNSS satellite No.5 starting about 11:18 local standard time, 4 Dec 1975 at subionospheric point, 18E Longtitude, 61.5°N Latitude and ending at 20.4°E Lon., 41.5°N Lat. The continous phase variation of the two NNSS radio beacons were reduced to equivalent vertical electron content at 0.5 degree of latitude increments from 41.5°N to 61.5°N. These were converted by multiplying with the constant 2.23 per 10^{16} el/m^2 to give vertical range correction in meters for a 425 Mhz radar. The prediction of the monthly median refraction correction is from a standard Air Force Global Weather Central program using the Bent formulation based on the ITS-78 coefficients. Near the point of closest approach to the ground station, Graz, Austria, at the center of the hypothetical radar coverage area, the ionospheric correction was about 23 percent lower than the predicted median. At the next recorded pass, 1403 L.S.T., the ionospheric correction was still below the predicted median. The technique for making an adapted prediction can now be considered in arbitrary increments.

1. Assume that the monthly median prediction can be scaled by reference to a single point, say the point corresponding to closest approach to the radar, which might have the greatest reliability. This is equivalent to normalizing to a single value derived from a local vertical incidence ionosponde, a measurement along the path to a near-synchronous satellite, etc. As can be seen from the relation between the line labeled "Adapted GWC" and the actual observations along the NNSS track, this may be model dependent.

2. Assume that the diurnal behavior can be defined by the model in a well behaved region, say mid latitudes (47°N in this case) and that the unique daily latitude gradient persists from pass to pass. The latitude gradient could have been derived from in-situ measurements of topside penetration frequencies, from a network of vertical incidence sounders, etc. As shown by the line labeled "Adapted gradient" in figure 2, the gradient at 1403, 2 hrs. 40 minutes later was remarkably the same as that found earlier at 1118. This behavior persisted for the subsequent recorded passes at 1458 and 1610 LST. Note that our linear gradients have minimized the r.m.s. percentage error. Note, also, that there appears to be merit in considering any measurement in real time which could tie the previous

latitude gradient to the current condition to improve on the behavior predicted by the median model. For example, any simultaneous measurement of total electron content along the path could tie the two gradients together.

3. Assume that almost all of the information along the previous pass may be used to predict the current pass. Again this information could have come from sources other than NNSS measurements, such as in-situ data from the DMSP satellites normalized with a local measurement. As a test procedure, observations from the first of a pair of passes were compared to the GWC prediction along the satellite path and the resulting scaling factors were used to scale the GWC prediction at each corresponding point along the subsequent pass. The results of this procedure, labeled "Update", for the 4 December daytime passes contained in figure 3, show that it is ionospherically dependent. During the daytime, measurements consistently show local features of a characteristic ±5 percent amplitude and 3-degree latitude scale size that are effervescent from hour to hour.

A large local feature, which may often be tracked, is the trough at the edge of the auroral zone. At 0241 LST, 2 December 1975, the position of the minimum, determined from the NNSS pass (figure 4), was near 59°N Geographic. In less than two hours, at 0427 LST, the trough had moved southward by about 3 degrees. The minimum in the general trough region and enhancement in the plasmapause region of the standard prediction program was up to a factor of 2 higher than the measured values. The linear gradient, normalized to the expected diurnal behavior at 47°N, greatly reduced the residual error, even though it smoothed both the trough and the enhanced region under the plasmapause.

By using joint observations from Graz, Lindau and Uppsala, Sweden, these features may often be tracked over several days. In the late afternoon through early morning hours in the data for December 11-13, a quiet geomagnetic period, there are well-developed, persistent features, as illustrated by the sequence of figure 5. Near 2000 LST in the region just above 60 degrees latitude (L value between 4 and 6) there is a well developed trough in the ionosphere, a sharp latitude gradient toward the equator and a persistent enhancement close to the region associated with the plasmapause. These can be discerned as smoothed features in the GWC predictions, figure 4, but here they may be tracked throughout the late afternoon and nighttime hours and from day to day.

CONCLUSION

Actual observations made with the Navy Navigation Satellite System (NNSS) satellites have been used to test techniques which adapt maps predicting ionospheric refractive effects over the field of radar or navigation systems. In these techniques each adapted map is then used to predict the local behavior of the refraction correction and the result compared with ensuing NNSS passes.

Systematic changes which represent the daily response of the local ionosphere to solar-terrestrial conditions, such as the general enhancement seen over Europe on 4 December, 1975, are usefully predicted by this technique. A necessary restriction is that a prediction should not be carried across either sunlit terminator as this could increase error.

During quiet geomagnetic periods, those local features with large geophysical scale size and a consistent identification in climatology, such as the nighttime trough and the plasmapause enhancement, seen persistently in the 10-13 December TEC observations from Europe, may be profitably tracked by local measurements. During the daytime some local features may be as large in amplitude but so transitory in either space or time that they are not observed on subsequent passes. In this case it is better to smooth these unknown features prior to adapting the median maps.

ACKNOWLEDGEMENT

The authors would like to thank Dr. A. Hedberg, Ionospheric Observatory, Uppsala, Sweden, for NNSS observations at Uppsala.

REFERENCES

DuLong, D.D. and Allen, R. S. (1976) "Specification of Navigation and Radar Errors caused by the Ionosphere," COSPAR Symposium Proceedings, The Geophysical Use of Satellite Beacon Observations, Boston University.

Leitinger, R. and Hartmann, G.K., (1977) "Time and Latitude dependence of transionospheric propagation errors," Kleinheubacher Bericte, Bd 20, ed FTZ Darmstadt, FRG.

Llwewllyn, S.K. and Bent, R.B. (1973) "Documentation and Description of the Bent Ionospheric Model," AFCRL-TR-73-0657.

Millman, G.H. and Reinsmith, G.M., (1974) "An analysis of the Incoherent Scatter-Faraday Rotation Technique for Ionospheric Propagation Error Correction," General Electric CO., TIS R74EMH2.

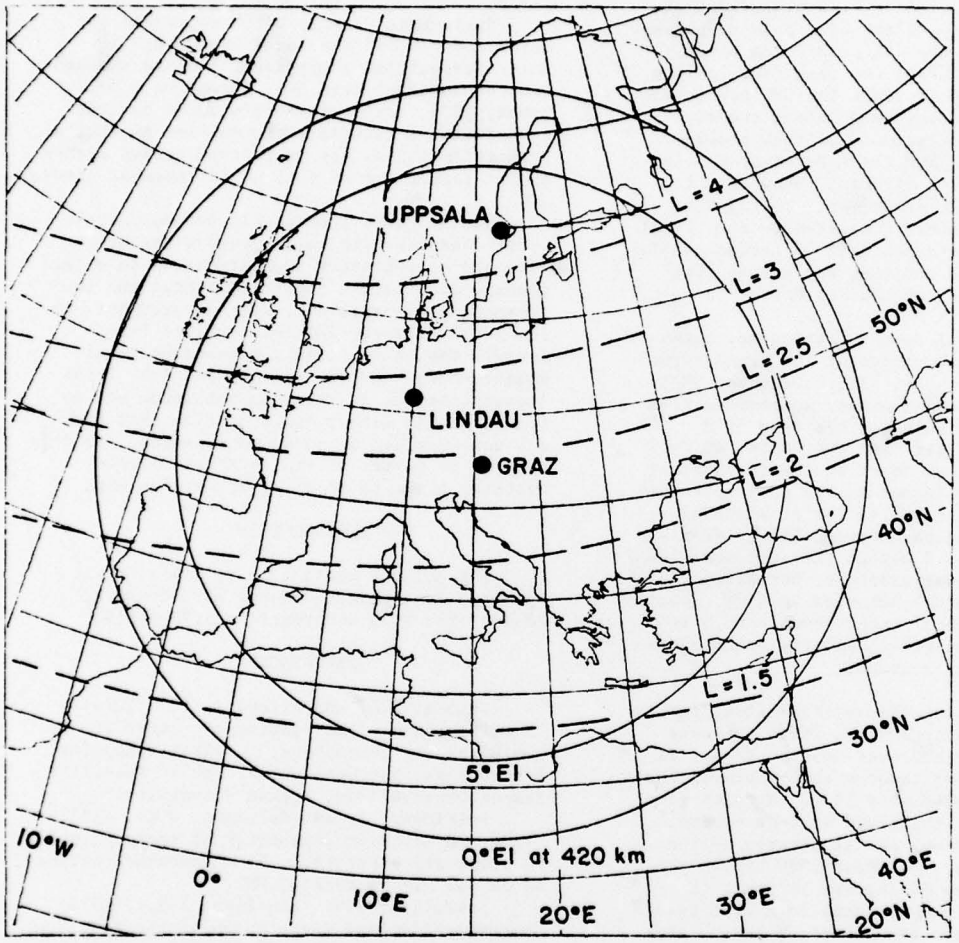


Figure 1. Coverage diagram of a hypothetical radar. Simultaneous measurements of total electron content using NNSS satellites are combined from three stations to represent radar measurements. Coverage extends into the auroral region of the ionosphere.

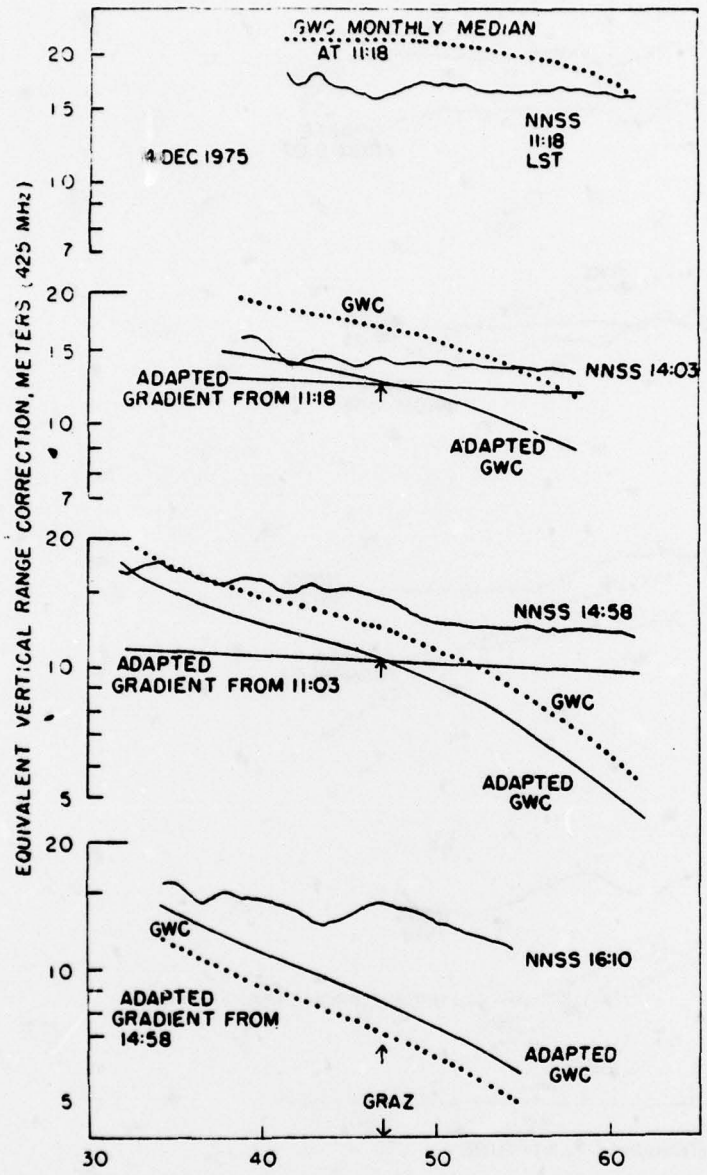


Figure 2. Illustration of adaptive modeling of radar range correction along a series of NNSS tracks. Each pass is predicted by the basic monthly median (GWC); by the GWC prediction scaled by a single observation from the previous pass (labeled Adapted GWC); and by the previously observed latitude gradient predicted forward in tiem at the point of closest approach (labeled Adapted Gradient). Note that general enhancement and simple gradients are usefully predicted.

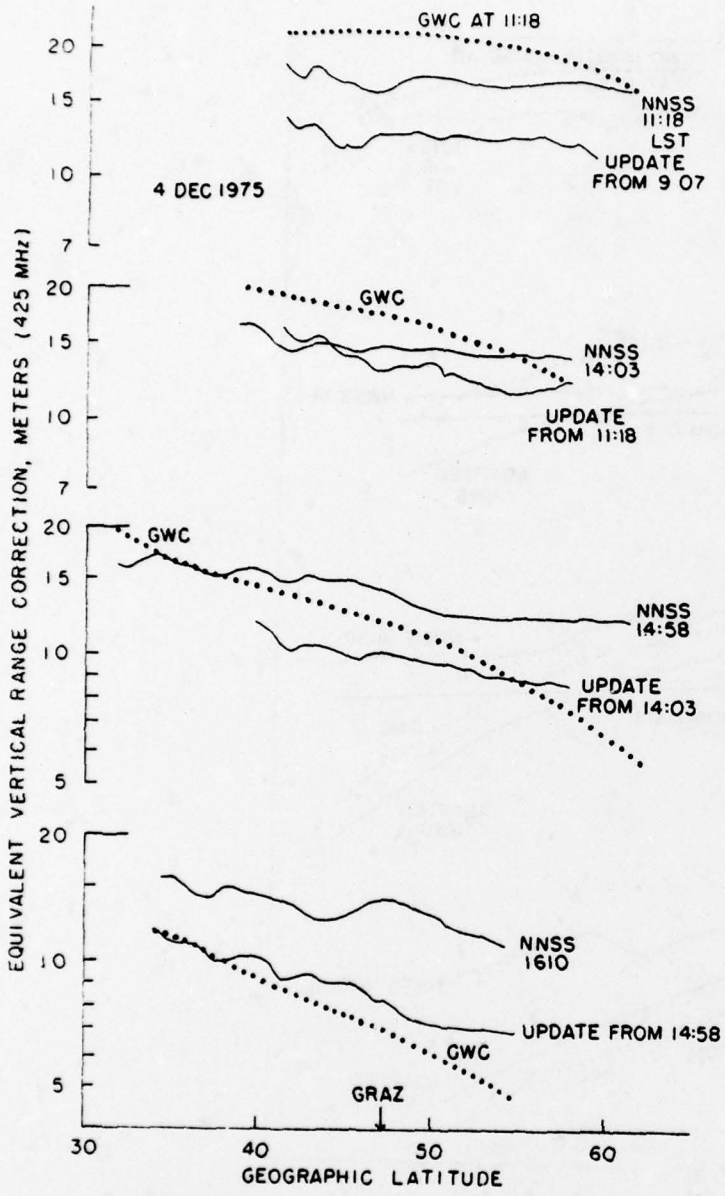


Figure 3. Illustration of adaptive modeling where each point of a previous pass is used to modify the latitude behaviour of the GWC prediction. Local features of 5 to 10 percent amplitude do not reproduce from pass to pass when the inter-pass period exceeds an hour.

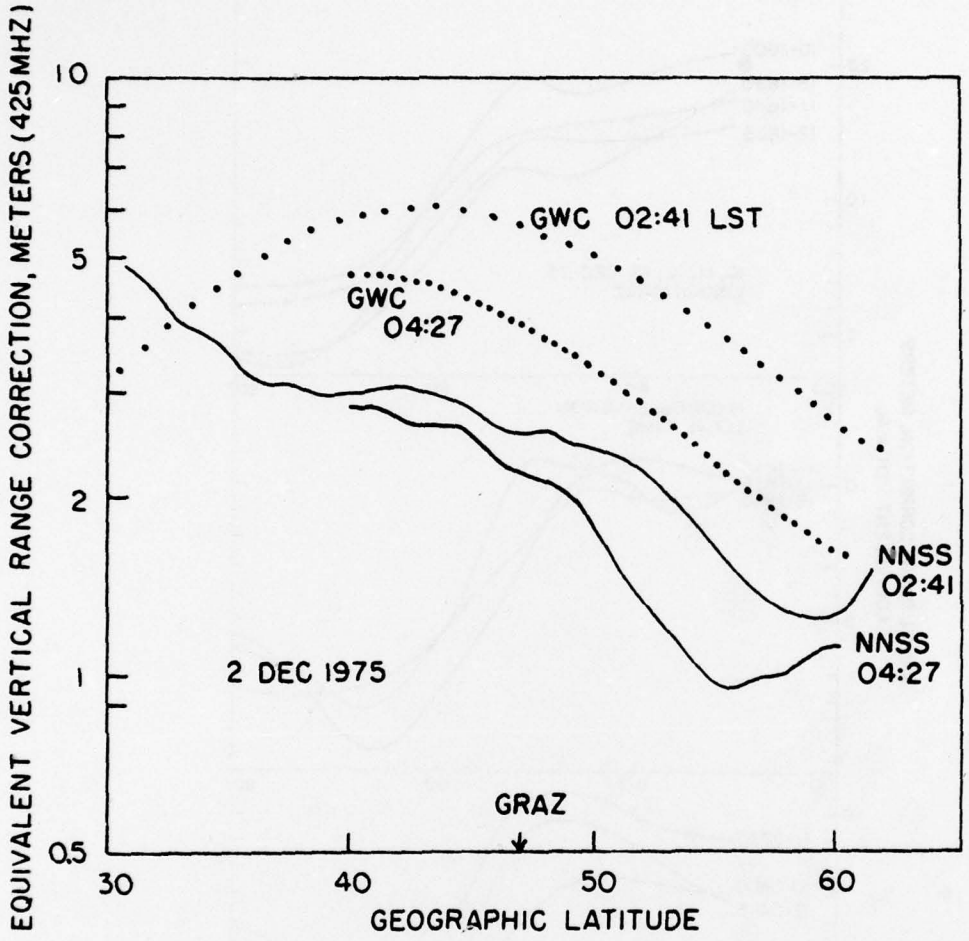


Figure 4. Sample taken 2 Dec 1975 which shows the ability to specify the location and movement of the mid-latitude trough and the plasmapause gradient.

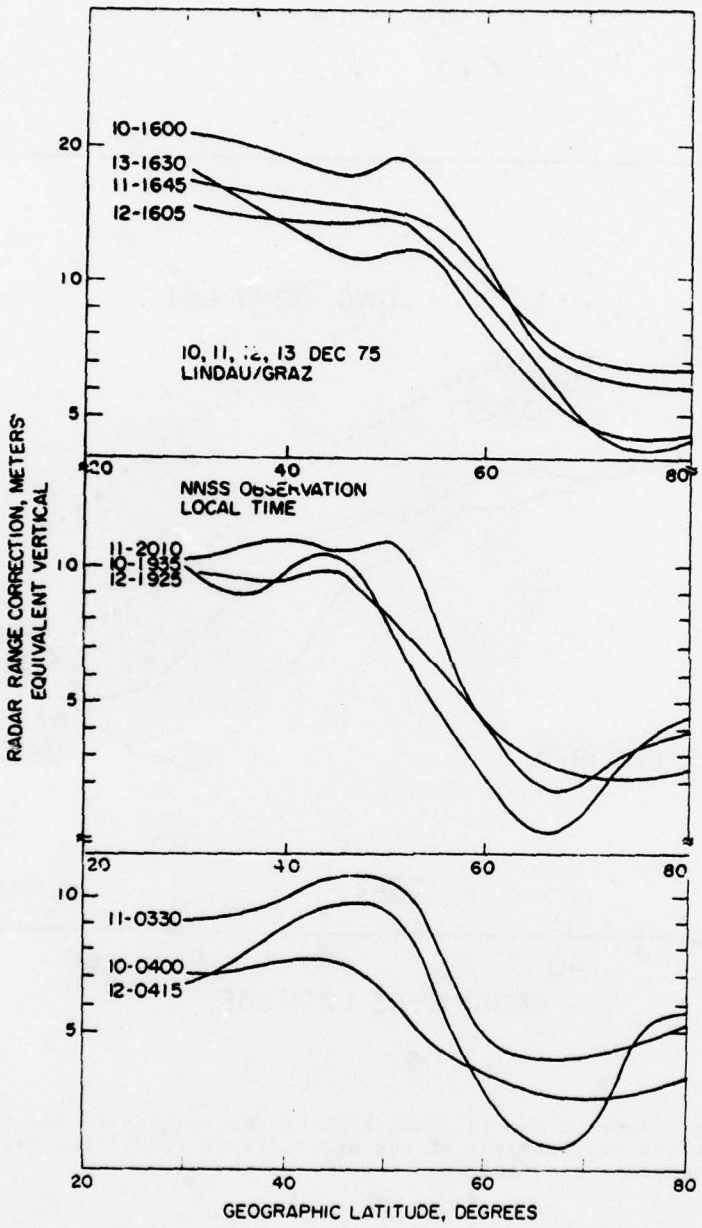


Figure 5. Consecutive days illustrating tracking of the trough, the plasmapause gradient and the plasmapause enhancement from hour to hour and from day to day. Adapted predicitons scaled from such observations could reduce the error of range correction by several meters.

EFFECTS OF IONOSPHERIC SCINTILLATIONS ON SATELLITE COMMUNICATION

Banshidhar, N.M. Vadher, Hari Om Vats, M.R. Deshpande and R.G. Rastogi*
Physical Research Laboratory
Ahmedabad 380009, India.

TEXT

The paper describes some results of the investigations carried out using amplitude recordings of radio beacons from ATS-6 (phase II) at an equatorial station Ootacamund, India. The effect of ionospheric irregularities has been studied in relation with the message length and its reliability for various fade margins at three carrier frequencies 40, 140 and 360 MHz. Out of various schemes to overcome the scintillation effect on communication, the time diversity scheme has been discussed.

From satellite to earth communication the radio waves have to pass through the ionosphere where ionisation irregularities might exist. These irregularities will scatter and distort the signal producing fading. This fading occurs primarily in the equatorial region of the earth, 20° of the magnetic equator. Similar fading occurs in the polar regions also. The fading is more severe during night than day. Nighttime scintillations are attributed to irregularities mostly present in F-region, whereas daytime scintillations are due to E-region irregularities. This morphology has been documented by numerous workers (Aarons et al. 1971, Koster 1972, Crane 1974, Aarons 1976, Rastogi et al. 1977). Here the effect of one specific example of severe scintillation simultaneously on 40, 140 and 360 MHz is discussed.

These amplitude records are shown in Fig.1. The scintillation activity is generally measured as normalized root mean square of power (Briggs and Parkin 1963) known as:

$$S_4 = \frac{1}{\overline{R^2}} \frac{}{(R^2 - \overline{R^2})^2}^{\frac{1}{2}}$$

where R is the instantaneous amplitude, and $\overline{R^2}$ is the average of squares of R.

The records shown in Fig.1 have these S_4 values as 0.97, 0.85 and 0.47 for 40, 140 and 360 MHz respectively. The effect of these scintillations on communication can be visualized by determining the message reliability. Message reliability is measured by determining the number of intervals that completely fit within the signal enhancements or increases above specified calibration levels compared with the total possible number in the sample under investigation (15 minutes) (Whitney and Basu 1977). Fig.2 shows the percentage of messages perfectly received as a function of message length for various fade margins. Here percentage of perfectly received message at 140 MHz reduced to less than 50% for message lengths exceeding 4 seconds and fade margin less than 6 db. Under the same condition, these percentages are 90 and 10 for 360 and 40 MHz respectively. A more realistic view of these effects can be simulated computationally as if a message transmitted from ATS-6 satellite and received by a receiver on the ground having a specified fade margin. One such simulation is shown in Fig.3, where each letter represents a message of 0.4 sec. Here only 140 MHz data from Fig.1 is used. Fig.3a shows the message which would have been received by a receiver having a fade margin of 15 db and Fig.3b shows the same for a fade margin of 4 db only. In Fig.3b 'X's represent non-receivable part of the message. Note that one way to combat scintillations is to increase fade margin.

Without increasing the fade margin, diversity reception also to some extent

* At present: NRC/NAS Senior Resident Research Associate,
Air Force Geophysics Laboratory, Hanscom AFB, MA 01731
U.S.A.

help to get rid of scintillations. Diversity schemes attempt to reduce the effects of fading during a scintillation event by combining two signals that are fading independently. Out of three diversity schemes, viz., space, time and frequency, here only time diversity scheme would be discussed, wherein the same message be sent at two different times separated far enough such that the correlation coefficient to be less than 0.6. For this same sample was processed for correlation analysis. Fig.4 shows the auto-correlation curve for 40, 140 and 360 MHz. The cross-correlation coefficients for these records are 0.030, 0.127 and 0.029 for 40/140 MHz, 140/360 MHz and 40/360 MHz sets respectively. From auto-correlograms of 40, 140 and 360 MHz (Fig.4) the time lags for correlation coefficient 0.6 were obtained and using this time for diversity scheme message reliabilities versus message lengths were obtained for various fade margins. Fig.5 shows the time diversified message reliability plotts for 40 MHz. One can note that the reliability has improved to a considerable amount. These results are preliminary and detailed study is under progress.

Acknowledgements

Grateful thanks are due to Prof. G. Swarup, Radio Astronomy Centre, Ootacamund and Prof.K. Davies, SEL/ NOAA, Boulder, for facilities and collaboration respectively for ATS-6 Ootacamund project. Thanks are also due to Miss Chhaya R. Shah for her sincere programming assistance during the course of this work. This project was supported by DOS and NASA.

References

Aarons J., H.E. Whitney and R.S. Allen, (1971), Global morphology of ionospheric scintillation, Proc. IEEE 59, 159-172.

Aarons J., (1976), Equatorial scintillation: A review, IEEE Trans. Antennas Propagat. (in press).

Briggs B.H. and I.A.Parkin, (1963), On the variation of radio star and satellite scintillations with zenith angle, J. Atmos. Terr. Phys., 25, 339.

Crane R.K., (1974), Morphology ionospheric scintillation, Tech. Note 1974-29, DDC AD-780522 19, MIT,Lincoln Laboratory, Lexeington, MA. 02173.

Koster J.R., (1972), Equatorial scintillations, Planet. Space Sci., 20, 1977-2014.

Rastogi R.G., M.R.Deshpande, Hari Om Vats, K. Davies, R.N. Grubb and J.E. Jones, (1977), Amplitude scintillations of ATS-6 Radio beacon signals within the equatorial electrojet region (Ootacamund, dip 40°N), Pramana, 8, 1-13.

Whitney H.E. and Santimay Basu, (1977), The effect of ionospheric scintillation on VHF/UHF satellite communications, Rad. Sci., 12, 123-133.

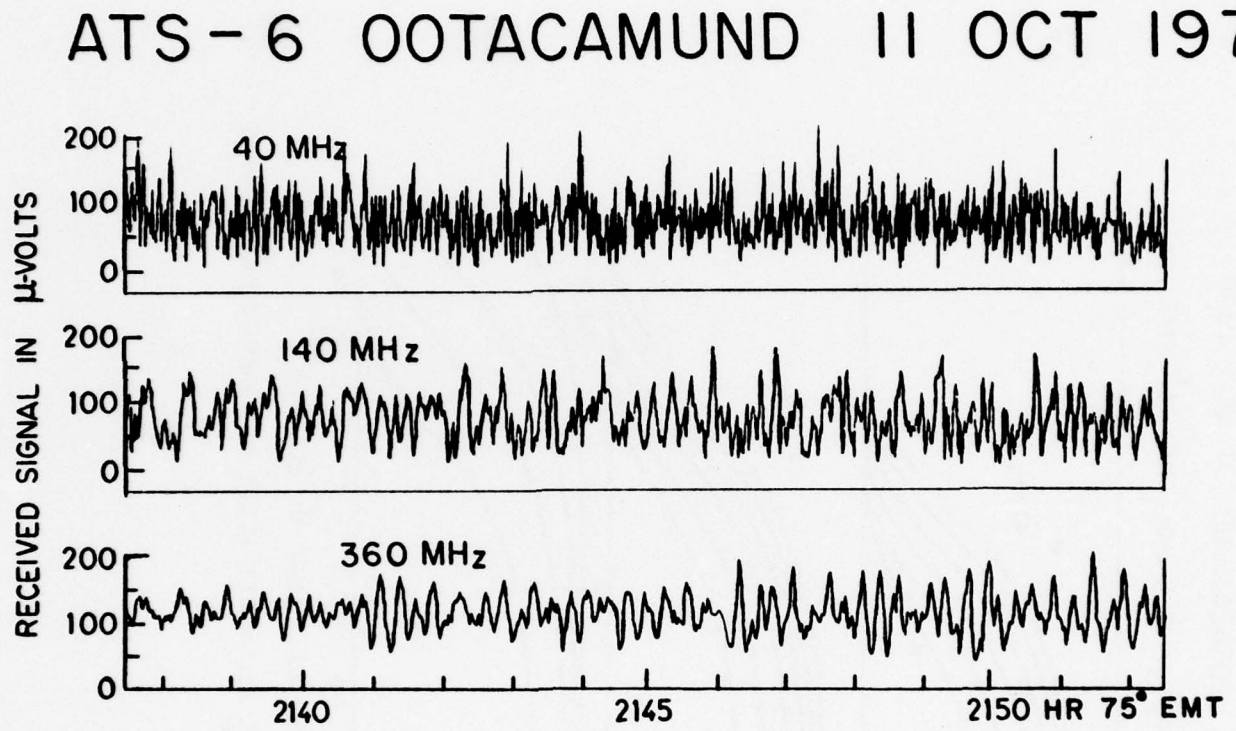


FIG. 1. AMPLITUDE RECORDS

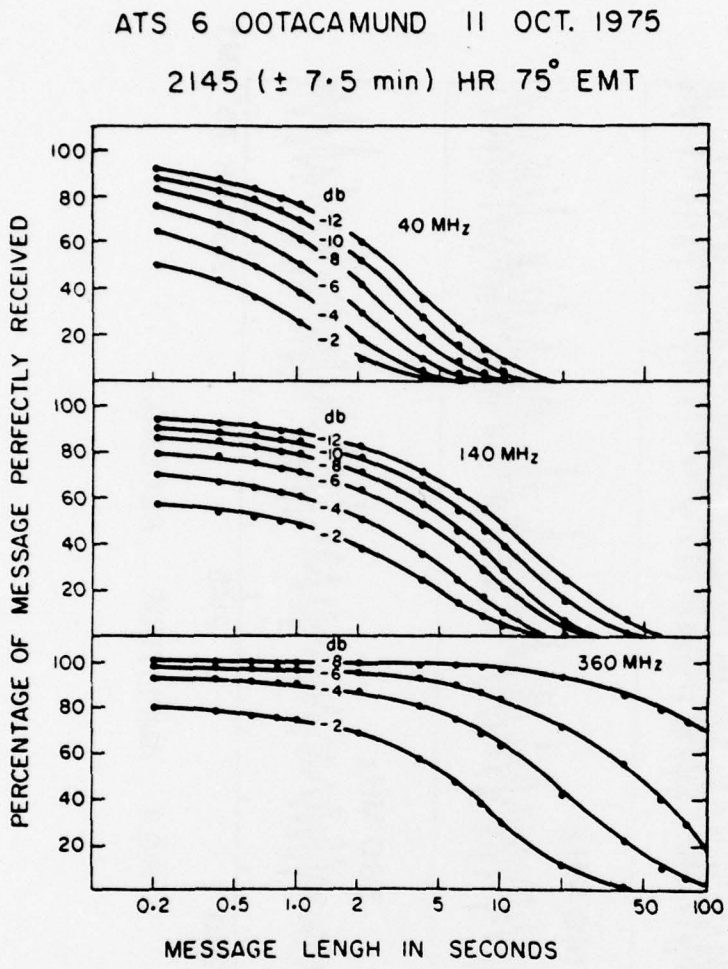


FIG. 2. MESSAGE RELIABLITY PLOTS FOR VARIOUS FADE MARGINS

THIS PAGE IS BEST QUALITY PRACTICABLE
FROM COPY FURNISHED TO DDC

(a)

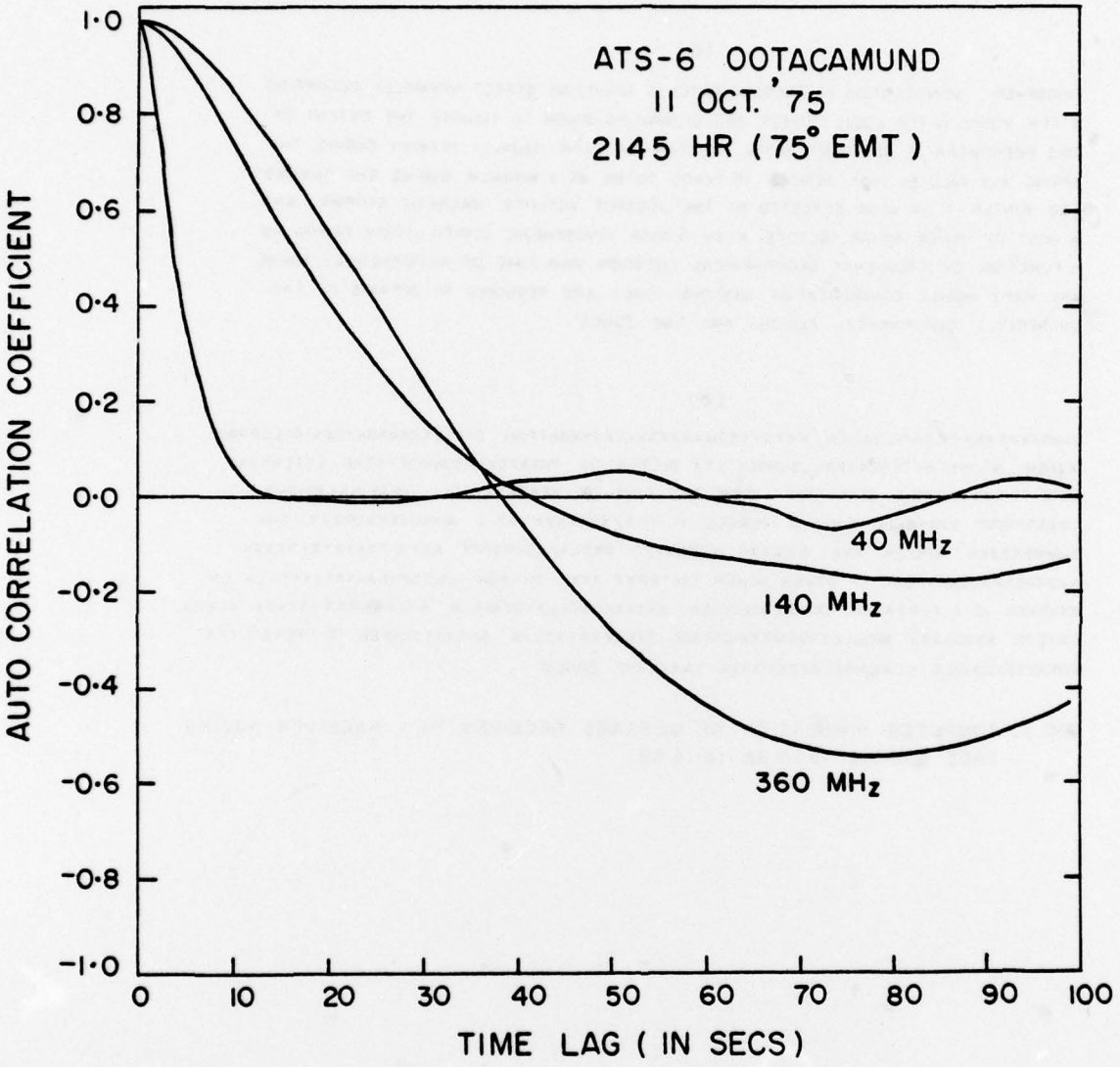
IONOSPHERIC SCINTILLATION IS PREDOMINANTLY A NIGHTTIME EFFECT NORMALLY OCCURRING A FEW HOURS AFTER LOCAL SUNSET AND DISSIPATING PRIOR TO SUNRISE THE EXTENT OF THIS PHENOMENA IS DEPEDENT UPON THE TIME OF YEAR USUALLY PEAKING DURING THE SPRING AND FALL EQUINOX PERIODS IT TENDS TO BE AT A MINIMUM DURING THE SUMMER AND WINTER IT IS ALSO EFFECTED BY THE SUNSPOT ACTIVITY, MAGNETIC STORMS AND A HOST OF OTHER MINOR FACTORS EVEN THOUGH IONOSPHERIC SCINTILLATION FADING IS A FUNCTION OF FREQUENCY GEOGRAPHICAL LOCATION, AND TIME OF OCCURRENCE, THERE ARE MANY MOBILE COMMUNICATION SYSTEMS WHICH ARE REQUIRED TO OPERATE IN THE VULNERABLE GEOGRAPHICAL REGIONS AND TIME ZONES

(b)

IONOXXXERXX SCINTILLATION XXXXXXXOMXXXXXXXXXXXXGHTTIME EFFECXXXXXXXXXX OXCURRING XXFEW HOURS AFTERXXXXXL SUNSET XXX DISSIPATING PRXXXXXXSUNRISEXXTHE EXTENXXXF XXIS PHENOMXXXXIS DEPXXXXT UPON THE TIME OF YEARXXXXXLLY PEAKINXXXXRING XXXXSPRING XXXXXALL EQUINOX PERIODS IT TEXXXXXXXX AT A MINIMXXXXURXXX THE SUMMEXXAND WINTER XXX ISXXXXO XXXXXTED BXXXXXXSUNSPOT XXTIVITYXXXXXXXXXX SXORMSXXANDXXXHOST OF OTHER MINOR FACTORXX XXXX THXXGH IONOSPHEXXXXXXXTILLATION XXXXXXX IS A FUNXXXON OXXFREQUENCYXX GXXXXXPHICALXXOCATXXN, AXXXXXMXXXXXXXXUXXXNCE. XXXERE XXXXXXX MOBILEXXXOMXXXICATION SYSXXXXXXXXH ARXXXEXUIRED TO OPERATEXXX THEXXXXXXRABLE GEXXAPHICAXXXXGIXXX XNXXXXE ZONES

FIG. 3. COMPUTER SIMULATION OF MESSAGE RECEIVED BY A RECEIVER HAVING FADE MARGIN (a) 15 dB (b) 4 dB

FIG. 4. AUTO - CORRELOGRAMS OF AMPLITUDES



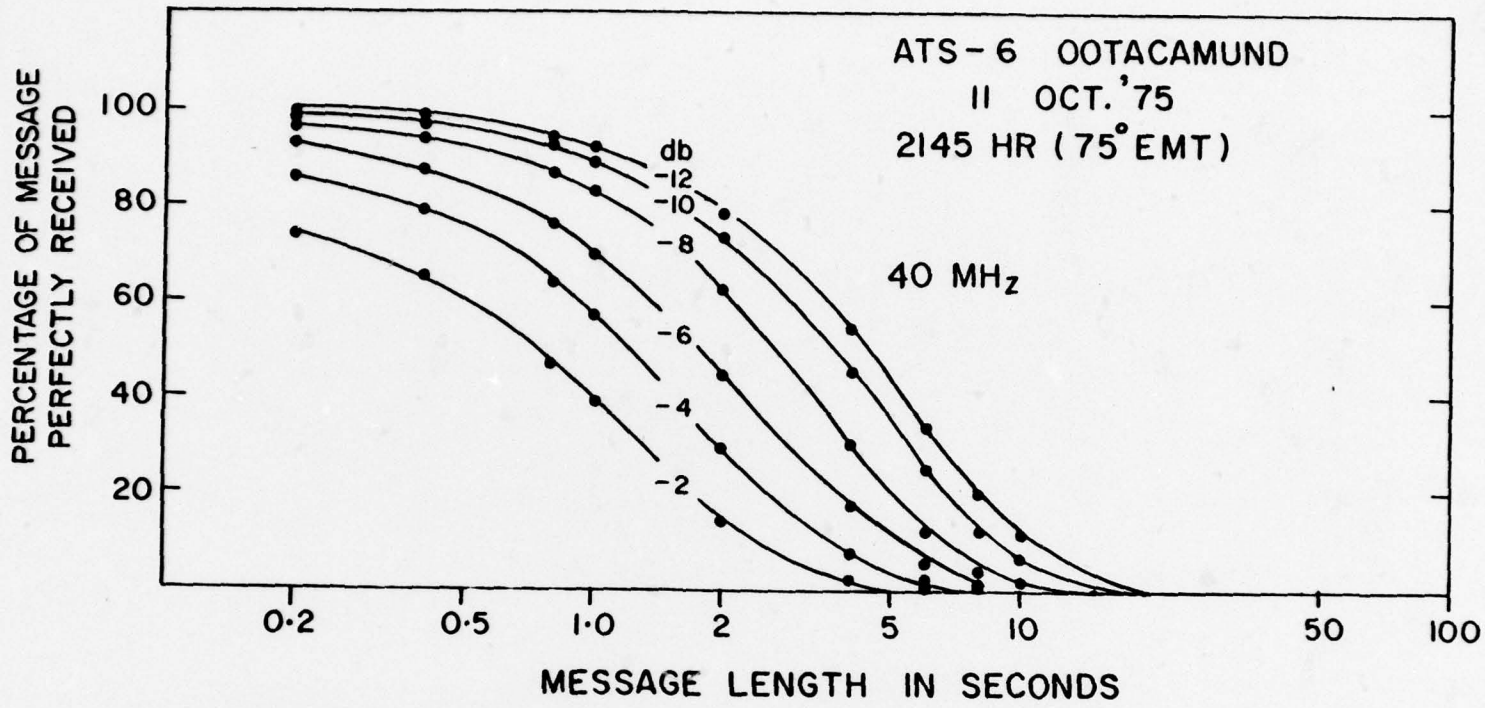


FIG. 5. MASSAGE RELIABLITY PLOTS USING TIME DIVERSITY SCHEME FOR 40 MHz RECORD SHOWN IN FIG. 1.